AVERTISSEMENT

Ce document est le fruit d'un long travail approuvé par le jury de soutenance et mis à disposition de l'ensemble de la communauté universitaire élargie.

Il est soumis à la propriété intellectuelle de l'auteur. Ceci implique une obligation de citation et de référencement lors de l'utilisation de ce document.

D'autre part, toute contrefaçon, plagiat, reproduction illicite encourt une poursuite pénale.

Contact : ddoc-theses-contact@univ-lorraine.fr

LIENS

Code de la Propriété Intellectuelle. articles L 122. 4
Code de la Propriété Intellectuelle. articles L 335.2- L 335.10
http://www.cfcopies.com/V2/leg/leg_droi.php
http://www.culture.gouv.fr/culture/infos-pratiques/droits/protection.htm

UNIVERSITÉ DE LORRAINE
POLYTECHNIQUE MONTRÉAL
UNIVERSITÉ DU QUÉBEC EN ABITIBI-TÉMISCAMINGUE

Thèse en cotutelle

Présentée en vue de l'obtention du grade de :

DOCTEUR DE L'UNIVERSITÉ DE LORRAINE

Spécialité :

Mécanique-Génie Civil

par

Mutaz NUJAIM

COMPORTEMENT GÉOMÉCANIQUE DES BARRICADES ROCHEUSES ET DES REMBLAIS EN PÂTE CIMENTÉS: EXPÉRIMENTATIONS ET MODÉLISATIONS

Geomechanical behaviour of waste rock barricades and cemented paste backfills: experiments and modelling

Soutenue le 11 Décembre 2020 devant la commission d'examen

Membres du jury:

M. Dashnor HOXHA	Professeur, Université d'Orléans, France	Rapporteur
M. Patrice RIVARD	Professeure, Université de Sherbrooke, Canada	Rapporteur
M. Richard SIMON	Professeure, Polytechnique Montréal, Canada	Examinateur
Mme. Mahdia HATTAB	Professeure, Université de Lorraine, France	Examinateur
M. Abdelkabir MAQSOUD	Professeur, UQAT, Canada	Examinateur
M. Serge OUELLET	Ingénieur, Mine Canadian Malartic, Canada	Examinateur
M. Albert GIRAUD	Professeur, ENSG, Nancy, France	Directeur
M. Tikou BELEM	Professeur, UQAT-IRME, Canada	Directeur

DEDICATION

To my parents

To my family and wife

To Yemen

ACKNOWLEDGMENTS

I am extremely thankful for the efforts of the Research Institute on Mines and the Environment (RIME-Université du Québec en Abitibi-Témiscamingue, Canada) and the GeoRessources Laboratory (Université de Lorraine, France) for the establishment of this jointly supervised Ph.D. I would like to express my gratitude to my supervisors for their continued enthusiasm and advice. My sincere appreciation goes to Prof. Tikou BELEM, who has helpfully spent much time discussing different aspects of this thesis and allowed me to present my research results in different events (national and international conferences). This work would not have been possible without his great assistance in preparing the pre-doctoral document (including the literature review and research proposal), papers, and this thesis. His guidance, suggestions, kindness, and support assisted me all through this project. I would also like to thank my supervisor at the Université de Lorraine, Prof. Albert GIRAUD, for his collaboration and help. I am pleased to express my gratitude to Dr. Christophe AUVRAY and the team of the GeoRessources Laboratory of Vandoeuvre-lès-Nancy in France for their help and encouragement. I also appreciate the care and attention I have received at the Université du Québec en Abitibi-Témiscamingue (UQAT) from the professors and staff of the laboratory, as well as the administrators and colleagues.

The authors gratefully acknowledge the financial support from the following organizations: ***i***) Fonds de recherche du Québec sur la Nature et les technologies (FRQNT) – Sustainable Mining Development – Research Partnerships Projects Grant, and ***ii***) Association Scientifique pour la Géologie et ses Applications – ASGA (Vandoeuvre-Lès-Nancy, France).

I would like to express my gratitude to the members of the jury who were kind enough to judge this work, whose comments and observations were very important in improving the thesis. I would also like to thank the members of the steering committee who are:

- Dr. Mountaka Souley, Head of Studies and Research (INERIS, France),
- Prof. Mamert Mbonimpa (RIME-UQAT, Canada), and
- Oumar Dembélé, Mining engineer (Glencore, Mines Raglan)

I want to thank my family (my parents, my brothers, and my sisters) for the support and love they have provided me over these years. Finally, I also very much appreciate the help, advice, and kindness of my friends and colleagues.

RÉSUMÉ

Les métaux précieux (tels que l'or et l'argent), et les métaux de base (tels que le cuivre et d'autres) sont extraits du sous-sol par excavation, en créant des vides de différentes tailles appelés (chantiers d'abattage) qui sont reliés entre eux par des galeries (de circulation et de soutirage). Dans le cas de l'exploitation par chambres-remblayées, ces vides ou chambres sont généralement remplis avec du remblai en pâte cimenté (RPC) qui est un mélange fait des rejets de concentrateur (appelés résidus), d'un agent liant (ex. ciment) et de l'eau de malaxage. Vu que le RPC est déposé à l'état liquide (mélange solide-liquide) dans les chantiers d'abattage, il est nécessaire d'utiliser un ouvrage de retenue afin de le contenir pendant le remblayage. Cet ouvrage de retenue est appelé barricade et peut être construit en bois, en béton, en briques, en béton projeté ou à partir des roches stériles disponibles sous terre et qui sont issues du développement des galeries.

Les barricades construites à partir des roches stériles sont les plus courantes au Québec et au Canada car elles sont économiques, disponibles (sous terre) et favorisent le drainage de l'eau lors du remblayage; ce qui favorise la consolidation gravitaire du RPC, et donc, la réduction de la pression interstitielle. À ce jour, peu d'informations existes sur les caractéristiques réelles in situ de ces barricades (telles que leur granulométrie, leur résistance à la rupture, le mécanisme probable de leur rupture et les dimensions standards utilisées) afin d'appuyer leur conception de manière à assurer la sécurité des travailleurs et des équipements miniers; ce qui contribuerait à la diminution du cycle de minage, et par conséquent, à l'augmentation de la productivité minière.

Les travaux de cette thèse se sont appuyés sur les modélisations physiques et numériques afin de mieux comprendre le comportement géomécanique complexe des barricades de roches stériles. Un modèle physique à l'échelle réduite d'un chantier d'abattage a été développé et construit à partir de plaques en plexiglass translucides, afin de simuler le remblayage dans les mines souterraines. Une méthodologie spécifique a été développée pour l'exécution des essais : instrumentation du modèle réduit à l'aide de capteurs de pression (totale et interstitielle), calibrage des capteurs, remplissage du modèle réduit avec du RPC, suivi en continu des essais avec des caméras haute définition. Les essais réalisés ont permis de mettre en évidence le principal mécanisme probable de rupture des barricades de roches stériles, ainsi que l'estimation de la pression maximale au moment de leur rupture. L'effet de la distribution de la taille des particules de roches stériles sur la stabilité et

l’intégrité des barricades de roches stériles à la suite de la poussée exercée par le RPC a également été analysé.

Une partie des essais réalisés sur le modèle réduit a été modélisée à l’aide du code de calculs numériques Geostudio 2018 (GeoSlope Intl.) par calibrage avec les résultats expérimentaux. Les résultats des simulations réalisées reproduisaient correctement le comportement général observé lors des essais sur le modèle réduit, avec une différence significative au niveau des valeurs des pressions. Des solutions analytiques simplifiées basées sur l’équilibre limite ont également été proposées sur la base des observations expérimentales pour l’analyse de stabilité (par rapport au glissement et au frottement) des barricades de roches stériles. Des recommandations ont été proposées afin de pousser cette étude plus loin en incluant l’effet de différents facteurs (ex. la position de la barricade dans la galerie de soutirage, la viscosité et le seuil d’écoulement du remblai ou son pourcentage de solides, les paramètres de cisaillement des barricades de roches stériles, l’effet d'arche, etc.).

Mots clés: remblais en pâte cimentés, roches stériles, barricades, remblayage, chantier d’abattage, modèle réduit, modèles physiques, modélisation numérique, analyse de stabilité

ABSTRACT

Precious metals (such as gold and silver), and base metals (such as copper and others) are mined from the underground by excavation, creating voids of various sizes called (stope) which are interconnected by galleries or drifts (for circulation and draw point). In the case of cut-and-fill mining, these voids are usually filled with cemented paste backfill (CPB) which is a mixture made of concentrator mill tailings, of a binding agent (e.g., cement) and mixing water. Since the CPB is placed in the liquid state (solid-liquid suspension) in the underground stopes, it is necessary to use a retaining structure to contain it during backfilling. This retaining structure is called a barricade and can be constructed from wood, concrete, bricks, shotcrete or from waste rock available underground and which come from the drift's development.

Barricades built from waste rock are the most common in Quebec and Canada because they are economical, readily available (underground) and promote water drainage during backfilling, which promotes self-weight consolidation of the CPB, and therefore, reduction of pore water pressure. To date, little information exists on the real in situ characteristics of these barricades (such as their grain size distributions, their failure strength, the probable mechanism of their rupture and the standard dimensions used) in order to support their design in a meaningful way to ensure the safety of workers and mining equipment, which would contribute to the reduction of the mining cycle, and consequently, to the increase of mining productivity.

The work of this thesis project was based on physical and numerical modeling to better understand the complex geomechanical behavior of waste rock barricades. A reduced-scale physical model of a mine stope was developed and constructed from translucent plexiglass plates to simulate backfilling in underground mines. A specific methodology was developed for the execution of the tests: instrumentation of the reduced-scale model using pressure sensors (total and pore water), calibration of the sensors, filling of the reduced-scale model with CPB, continuous monitoring of the tests using high-definition cameras. The tests carried out have made it possible to highlight the main probable mechanism of rupture of the waste rock barricades, as well as the estimation of the maximum pressure at the time of their rupture. The effect of waste rock particle size distribution on the stability and integrity of waste rock barricades due to the CPB pressure was also analyzed.

Part of the tests carried out on the reduced-scale model were modeled using the Geostudio 2018 numerical code (GeoSlope Intl.) through calibration with the experimental results. The results of

the simulations performed reproduced well the general behavior observed during the tests on the reduced-scale model, but with a significant difference in the pressure values. Simplified analytical solutions based on limit equilibrium have also been proposed based on experimental observations for the stability analysis (with respect to sliding and friction) of waste rock barricades. Some recommendations were proposed in order to take this study further by including the effect of various factors (e.g., the position of the barricade in the drift or draw point, the viscosity and the shear yield stress of the backfill or its solids mass concentration, the shear parameters of the waste rock barricades, the arching effect, etc.).

Keywords: cemented paste backfills, waste rock, barricades, backfilling, mine stope, scale model, physical models, numerical modelling, stability analysis

TABLE OF CONTENTS

DEDICATION II

ACKNOWLEDGMENTS III

RÉSUMÉ IV

ABSTRACT VI

TABLE OF CONTENTS VIII

LIST OF TABLES XI

LIST OF FIGURES XII

LIST OF APPENDICES XIX

LIST OF SYMBOLS AND ABBREVIATIONS XX

RÉSUMÉ DE LA THÈSE XXVI

CHAPTER 1 INTRODUCTION 1

1.1 Problem statement 2

1.2 Originality 3

1.3 Thesis objectives 4

1.4 Contributions 4

1.5 Methodology 5

1.5.1 Physical modelling 5

1.5.2 Numerical modelling 8

CHAPTER 2 LITERATURE REVIEW 10

2.1 Backfill uses in mining operations 11

2.2 Types of mine backfills 14

2.2.1 Rockfill 14

2.2.2 Hydraulic fill 18

2.2.3 Cemented paste fill 20
2.2.4 Summary of backfill properties 25
2.3 Design and construction of fill barricades 26
2.3.1 Types of barricade 26
2.3.2 Construction of waste rock barricades 28
2.3.3 Barricade design methods 32
2.4 In-situ measurements 36
2.5 Small-scale models of mine stopes 45
2.6 Numerical simulations for vertical backfilled stope stress evaluation 48
CHAPTER 3 EXPERIMENTAL TESTS ON A SMALL-SCALE MODEL OF A MINE STOPE TO STUDY THE BEHAVIOUR OF WASTE ROCK BARRICADES DURING BACKFILLING 54
3.1 Introduction 54
3.2 Small-Scale Model and Equipment Description 57
3.3 Material Characteristics 62
3.3.1 Mine Tailings 62
3.3.2 Waste Rock Barricade 64
3.4 Experimental Setup and Program 65
3.4.1 Setting up the waste rock barricade 65
3.4.2 CPB Mix Design and Preparation 65
3.4.3 Program experimental 68
3.5 Results 69
3.5.1 Stress State after the Placement of the Backfill in the Small-Scale Model 69
3.5.2 Stability and Failure Mechanism of the Waste Rock Barricades 77
3.6 Concluding Remarks 80

CHAPTER 4 ASSESSMENT OF STRESS STATE IN PASTE BACKFILL DURING PROGRESSIVE BACKFILLING: EXPERIMENTS AND MODELLING 82

4.1 Introduction 82

4.2 Experimental & numerical program 85

4.3 Physical & numerical models 85

4.3.1 Physical model 85

4.3.2 Numerical model 87

4.4 Results 90

4.5 Conclusion 97

CHAPTER 5 STABILITY ANALYSIS OF WASTE ROCK BARRICADES USING A SMALL-SCALE MODEL OF MINE STOPE AND ANALYTICAL SOLUTIONS 99

5.1 Introduction 99

5.2 Experimental tests 102

5.3 Results 104

5.4 Concluding and remarks 115

CHAPTER 6 BRIEF DISCUSSION, CONCLUSIONS AND SOME RECOMMANDATIONS 117

6.1 Discussion 117

6.2 Conclusions 119

6.3 Recommendations for further study 121

REFERENCES 125

LIST OF TABLES

Table 2-1: typical backfills in mine stopes (from Hassani & Archibald 1998) 25

Table 2-2: The strength properties of CPB in the field and laboratory (from le Roux et al., 2005). 38

Table 3-1: Geometric characteristics of the three types of stress sensors used on the reduced model. 59

Table 3-2: Characteristics of the mine tailings used in the experimental tests (LaRonde mine tailings). 63

Table 4-1: Characteristics of the pressure sensors used on the reduced model. 86

Table 4-2: Parameters used for the simulations conducted with SIGMA/W (GEO-SLOPE 2018). 89

Table 5-1: Pressure recorded at the failure of the barricade during the experimental tests. 104

LIST OF FIGURES

Figure 1-1: Small-scale model with associated metrology. 6

Figure 2-1: Diagram presenting the underground mining methods (from Brady & Brown, 1985). 11

Figure 2-2: Unsupported mining methods: a) block caving; b) sublevel caving (taken from Copco, 2007).....12

Figure 2-3: Naturally supported methods: a) room-and-pillar method; b) Shrinkage stoping method (from Copco, 2007). 12

Figure 2-4: 3D isometric view of open stope mining (from Potvin et al., 2005). 14

Figure 2-5: Grain size distribution curves of waste rock (from Maknoon, 2016). 15

Figure 2-6: a) Size distribution of waste-rock particles in the Tangshan coal mine (China); b) the deformation modulus and axial stress vs. axial strain of the waste-rock (Zhang et al., 2019). 17

Figure 2-7: a) Hydrocyclone used to remove part of the fine material of the tailings (from Belem et al., 2018); b) Typical grain size distribution curves for hydraulic fills, cemented hydraulic fills, and paste fills in Australia (from Sivakugan et al., 2006b).....18

Figure 2-8: A permeameter for mine backfill application (adapted from Potvin et al., 2005). 20

Figure 2-9: Particle size distribution of full tailings, hydraulic fill, and slimes (adapted from Potvin et al., 2005). 21

Figure 2-10: a) paste fill being deposited into a stope via a pipeline (from Sivakugan et al., 2015); b) a stope underfilling with CPB (Belem et al., 2018). 22

Figure 2-11: Evolution of hydraulic conductivity as a function of curing time for cemented paste backfill with different types of binders (from Godbout et al., 2007). 23

Figure 2-12: Unconfined compressive stress-strain curves of CPB after 112 days of curing for different (a) binder contents and (b) types of binder (from Belem et al., 2000). 24

Figure 2-13: Typical barricades formed from: (a) arched permeable brick wall ; (b) timber; (c) concrete; (d) shotcrete; (e) fibrecrete; (f) waste rock (from Yang, 2016). 27

Figure 2-14: Construction stages of the waste rock barricade (from Gélinas, 2017).....29

Figure 2-15: Wedge model of Mitchell et al. (1982) (Modified by Li & Aubertin 2009c) 30

Figure 2-16: Schematic illustration of a vertical backfilled barricade in fully drained condition (Li & Aubertin, 2009a). 31

Figure 2-17: Diagram of a backfilled vertical stope with a barricade in a submerged condition a) overview (stope and drift); b) cross-sectional view (Li & Aubertin, 2009b).....31

Figure 2-18: a) Schematic view of a backfilled stope with a trapezoidal WRB; b) WRB with various acting forces; c) WRB 's internal translation stability analysis model; d) Variation of the required top length LBT obtained as a function of δ (from Yang, 2016). 35

Figure 2-19: Conceptual model of a trapezoidal WRB (from Gélinas, 2017). 36

Figure 2-20: a) Basic views of cement paste filling in three sequences; b) Semi-stiff metal unit (box) with three TPCs to measure pressure in three directions; c) Instrumentation of the lower wall of the stope and the drawpoint in front of the barricade (from Belem et al., 2004a) 37

Figure 2-21: a) The internal pressures of the paste backfill at the base of the stope; b) Variation of the lateral pressure σx − b on the barricade during the filling (after Belem et al., 2004a)....37

Figure 2-22: a) Self-boring pressure-meter schematics; b) Typical sample quality from thin-walled sampling; c) Excavation of block samples (from le Roux et al., 2005). 38

Figure 2-23: Monitoring and in situ measurement of pore water pressure (u) and total vertical stress (σv) at the stope: a) in KB Mine, b) in SNM Mine (from Helinski et al., 2010).....39

Figure 2-24: a) Stope in Lanfranchi Nickel mine (long section and cross-section); b) Instrumentations (earth pressure cell, piezometer and data-logger) (from Hasan et al., 2014). 40

Figure 2-25: Measurement of stresses at a) location 1; b) location 2; c) location 3 (from Hasan et al., 2014).....40

Figure 2-26: a) Cross-section of the stope with locations of instrument cages, b) Plan shows orientations of the TEPCs, c) Cages hanging in the stope (from Thompson et al., 2009).....41

Figure 2-27: a) Total pressure and pore pressure (PP) for 10 days. The TEPCs are either oriented north (N), east (E) or vertically (V) with stope orientation, b) Total pressure over a period of 240 days from the beginning of the backfill (from Thompson et al., 2009). 42

Figure 2-28: a) Total pressures during the filling for TEPCs on the barricade, in the drift and under the brow, b) Plan shows where the instrumented cages are located, c) Cages photo (from Thompson et al., 2009).....42

Figure 2-29: a) Cross-section showing instrument locations in the 685-stope, b) Detailed instrument plan–cross-section of the 685-stope (from Thompson et al., 2012).....43

Figure 2-30: a) Temperature history for 8.5% and 6.5% CPB binder content in the 685-stope, b) Pressures for two CPB rise-rates in the 715 stope (from Thompson et al., 2012). 44

Figure 2-31: a) TEPCs and piezometers directly attached to the barricade; b) Potentiometers mounted to record barricade deflection; c) Barricade external surfaces (from Thompson et al., 2012).....44

Figure 2-32: 685-Cayeli mine stope: a) TEP, PP, and temperature measurements. The horizontal orientations of the TEP are H1 and H2, and V refers to vertical pressure, b) Displacement of the barricade during backfilling, c) Barricade geometry, TEPCs, piezometer, and displacement array locations (from Thompson et al., 2012).....45

Figure 2-33: General views of a) model fill cast in formwork, b) failure test with a surcharge (from Mitchell et al., 1982). 46

Figure 2-34: a) Stopes geometries with dimensions, b) Photograph of the arching apparatus (taken from Pirapakaran, 2008).....47

Figure 2-35: Schematic view of the three consolidation columns filled with CPB at a) Laronde (LRD) mine backfill plant, b) Louvicourt (LVT) mine backfill plant (from Belem et al., 2016). 48

Figure 2-36: Numerical results of the distribution of (a) vertical and (b) horizontal stresses in FLAC (from Li et al., 2003). 49

Figure 2-37: Vertical and horizontal stresses along the VCL, obtained from numerical simulations and analytical solution ($K = Ka$): a) effective stresses (b) total stresses (Li & Aubertin, 2009c).....49

Figure 2-38: a) Vertical total stresses, b) Horizontal total stresses at the end of backfilling for different k values (from Fahey et al., 2009).....50

Figure 2-39: a) Model of a backfilled stope. Evolution of: b) total vertical stress, c) effective vertical stress and d) PWPs (from El Mkadmi et al., 2013).....51

Figure 2-40: a) Sequentially backfilled stope with drainage at the base, b) Evolution of effective vertical, and c) PWP stress for sequential backfilling (from El Mkadmi et al., 2013). 52

Figure 2-41: a) Illustration of the boundary conditions, dimensions, and materials applied to two backfilled stopes simulations, b) Horizontal (left) and vertical (right) stress distributions at the end of filling for the second stope (from Falaknaz, 2014).....53

Figure 3-1: A small-scale model of a mine stope made of transparent plexiglass, including the measurement tools.....58

Figure 3-2: Experimental protocol and arrangement: (a) strain gauge data acquisition system (20 channels), (b) all pressure sensors used are installed on a plate before calibration, (c) pressure sensors attached to a plate at the base of a bucket for the calibration, (d) calibration procedure of the pressure sensors using water, and (e) dimensions of the model and the different locations of the pressure sensors.....60

Figure 3-3: Calibration of pressure sensors a) DMKY sensors, b) DMTY sensors, c) the sensors at the face of the barricade (PS-D).....62

Figure 3-4: Material characteristics: (a) grain size distribution (GSD) curve of the mine tailings sample, (b) particles' size distribution curves of the waste rock barricade, and (c) barricade total or bulk density as a function of the particle size distribution curve number (from #1 to #7).....63

Figure 3-5: Experimental protocol: (a) paste backfill mixture preparation using a Hobart mixer and backfill ingredients (water, tailings, and binder), (b) setting up the barricade in the drawpoint, and (c) the first layer of the backfill after pouring and self-weight consolidation took place. 68

Figure 3-6: Measurement of pore water pressure of uncemented fill at three locations in the model: (a) for the GSD #1 barricade, and (b) for the GSD #5 barricade. 70

Figure 3-7: Uncemented backfill tests: (a) pouring of the second layer of backfill, (b) the model after self-weight consolidation of the second layer, (c) backfill bleeding water at the top of the filling chamber after each placement of the backfill, and (d) the state of the backfill near the barricade after four days (two layers were continuously poured, once every two days). 71

Figure 3-8: The measurement of the backfill pressure at the base of the stope: (a) for the GSD #1 barricade, and (b) for the GSD #5 barricade. 72

Figure 3-9: The backfill pressure at 20 cm above the base stope: (a) for the GSD #1 barricade, and (b) for the GSD #5 barricade. 73

Figure 3-10: The pressure of the backfill on the barricade: (a) for the GSD #1 barricade, and (b) for the GSD #5 barricade. 74

Figure 3-11: The drainage water collected during the tests. 74

Figure 3-12: The backfill pressure measurement on the upstream side of the barricade. 75

Figure 3-13: Backfill pressure measurement: (a) at the base of the stope, and (b) at 20 cm above the base of the stope. 75

Figure 3-14: The pore water pressure at the base of stope (PWPS1), at 20 cm above the stope (PWPS3), and under the barricade (PWPS4). 76

Figure 3-15: Total pressure measurements: (a) The pore water pressure at the base of stope (PWPS1), in front of the barricade (PWPS2), and at 20 cm above the stope (PWPS3). (b) The total pressure at the base of the stope. (c) The backfill pressure measurement on the upstream side of the barricade. 77

Figure 3-16: The failure mechanism of a waste rock barricade made of GSD #1: (a) the different pressure values in the model at failure, (b) the barricade before the failure (the top largely moved), and (c) the barricade after the collapse. 78

Figure 3-17: The failure mechanism of a barricade made of GSD #5: (a) the different pressure values in the model at failure, (b) the barricade before the failure, (c) the hand piston pushes

water from the backfill into the pores of the barricade, and (d) the barricade after using the hand piston. 79

Figure 3-18: Failure mechanism of a barricade made of the GSD #2: (a) after the filling, (b) during the increase of the pressure using the hand piston, and (c) at failure (at the end of the test). 80

Figure 4-1: Burland Triangle (adapted from Anonymous, 1999). 84

Figure 4-2: Small physical model of the mine stops: a) before backfilling, b) after the first layer is poured, c) after pouring the second layer. 85

Figure 4-3: Measurement of pressure at different points in the physical model [pore water pressure (PWP) and total earth pressure (TEP)]. 86

Figure 4-4: Grain size distribution curves of a) tailings from Laronde mine, b) barricade made of crushed waste rock. 87

Figure 4-5: Numerical model with the boundary conditions: a) steady state (before the backfilling), b) the placement of the first backfill layer, c) the placement of the second layer of the backfill (water table at the top of each layer). 88

Figure 4-6: Hydraulic properties of the backfill used in the simulations: a) permeability function, b) water retention curve (adapted from El Mkadmi et al., 2013). 89

Figure 4-7: Pore water pressures: (a) from the reduced physical model, (b) from the numerical modelling. 90

Figure 4-8: Total stresses on the barricade (horizontal direction): a) on the reduced physical model, b) from numerical modelling. 91

Figure 4-9: Total stresses at the base of stope (horizontal direction, X & vertical direction, Y): a) on the reduced physical model, b) from numerical modelling. 91

Figure 4-10: Stresses at 20 cm above the base of stope: a) on the reduced physical model, b) from numerical modelling. 92

Figure 4-11: Isocontours show the distribution of a) pore water pressure, b) vertical stresses, c) flow and backfill displacements (XY direction) at the end of the tests (after four days). 93

Figure 4-12: The filling chamber (stope) with backfill (C_{w-f} = 70%): a) after backfill placement; b) during self-weight consolidation; c) the front and right views of the top of the stope. 94

Figure 4-13: Total stresses on the barricade (horizontal direction): a) on the reduced physical model, b) from numerical modelling.....95

Figure 4-14: Total stresses at the base of stope (horizontal direction, X & vertical direction, Y): a) on the reduced physical model, b) from numerical modelling.....95

Figure 4-15: Backfill stresses at 20 cm above the base of stope: a) on the reduced physical model, b) from numerical modelling.....95

Figure 4-16: State of the backfill near the barricade at the end of the test (after four days) for a) the uncemented backfill, b&c) the cemented backfill before and after removal of the barricade; d) the barricade-backfill interaction. 96

Figure 5-1: A physical model of mine stope designed to study the behaviour of the waste rock barricades in interaction with the paste backfill.....103

Figure 5-2: Results of the two experimental tests: (a & b) barricade before and at sliding; (c & d) the barricade before and at the collapse of the upper part.....104

Figure 5-3: Sliding analysis of acting forces.....105

Figure 5-4: Shear analysis for a barricade fixed at the drift base using shims.....107

Figure 5-5: Schematic view showing A_3 among the divided areas of the barricade.....109

Figure 5-6: Lateral friction calculation between the barricade and drift walls (second test).....111

Figure 5-7: Displacement of the upper part of the barricade before the collapse. 111

Figure 5-8: Prospective physical model equipped with a piston.....113

Figure 5-9: Different scenarios for the collapse of the barricade.....113

Figure 5-10: a) barricade total density as a function of particle size distribution; b) barricade sliding pressure for all particle size distributions.....114

Figure 5-11: a) Tilt of the backfill slurry surface (Cw=70%) during filling, b) Unfilled portion at the top of the barricade after the drainage and sedimentation process; sand (0/400µm) was used instead of the tailings (see Nujaim et al., 2018).....115

LIST OF APPENDICES

Appendix A – Backfill components 138

Appendix B – Physical relations of mine fill 144

Appendix C - Shear strength of the fill 154

Appendix D - Lateral earth pressure 161

Appendix E - Consolidation of the mine fill 163

Appendix F - Fundamentals of physical modelling 166

Appendix G - Image analysis 172

Appendix H - Use of strain gauges for measuring pressure 176

Appendix I - Fundamentals of numerical modelling 180

Appendix J - Design and optimization of the paste backfill 190

LIST OF SYMBOLS AND ABBREVIATIONS

Symbols

B	width of the stope (m)
C_U	coefficient of uniformity
C_M	calibration factor (Yang et al., 2016)
c	cohesion (kPa)
c'	effective cohesion (kPa)
Cc	compression index
Cr	recompression index
D_{60}, D_{10}	size at which 60% and 10% of particles pass the sieve (mm or μm)
d_{max}	maximum particle size (mm)
E	Young's modulus (MPa or GPa)
E_r	Young's modulus of the rock mass (GPa)
e	void ratio
F	yield function for the constitutive model
G	shear modulus (GPa)
H	height of the stope or opening (m)
H_d	drift/barricade height (m)
H_w	pond height in the stope (m)
I_D	density index (%)
K	earth pressure coefficient
K_a	Rankine's active pressure coefficient
K_p	Rankine's passive pressure coefficient
K_0	at rest earth pressure coefficient
k	hydraulic conductivity (m/s)

k_{sat}	saturated hydraulic conductivity (m/s)
L	stope length (m)
L_B	the average length of the waste rock barricade (m)
L_{BT} *(or* L_T*)*	top length of waste rock barricade (m)
L_{BB} *(or* L_B*)*	the base length of waste rock barricade (m)
L_d	drift/barricade width (m)
l	the distance of the barricade to the drawpoint (m)
M	the critical state line slope in the $p' - q$ plane
n	porosity
$p0$	surcharge pressure on the backfill top surface (kPa)
Q	the total volume of hydraulic fill placed in the stope (m^3)
T	total time needed to drain the pond (s or h)
t	a transient time (s or h)
u	pore water pressure – PWP (kPa)
V	volume (m^3)
W	width of the drift, or weight of the sliding wedge (kN)
α_1	the upstream slope angle of waste rock barricade on the stope side (°)
α_2	the downstream slope angle of waste rock barricade on the drift side (°)
α'	the inclination angle of the failure plane to the horizontal (°)
β	the inclination angle of the stope to the horizontal (°)
θ_w	volumetric water content
ϕ	internal friction angle (°)
ϕ'	effective internal friction angle (°)
δ	interface friction angle (°)
δ'	effective interface friction angle (°)

δc	critical interface friction angle (°)
Ψ	dilation angle (°)
κ	slope of the isotropic over-consolidation (swelling) line (Cam-Clay model)
λ	slope of the isotropic normal consolidation line (Cam-Clay model)
Γ	specific volume at the critical state when p' is 1.0 (Cam-Clay model)
p	average total stress (kPa)
p'	average effective stress (kPa)
p'_c	pre-consolidation pressure (kPa)
p'_x	peak mean stress (kPa)
q	deviatoric stress (kPa)
σ_i^d	deviatoric stress (kPa) in direction i
$J_2,\ J_3$	second and third deviatoric stress invariants
I_1, I_2	the first and the second variants
$d\varepsilon_{ij}^p =$	plastic strain function (elastoplastic model)
V_o	voltage output (V)
V_{EX}	excitation voltage (V)
ΔR	the fractional change in electrical resistance
Δp	differential pressure between two points (kPa)
P_{abs}	the absolute pressure (kPa)
P_{amb}	the amplitude of the atmospheric pressure (kPa)
η_B	Bingham plastic viscosity (Pa.s)
$\dot{\gamma}$	shear rate (s^{-1})
τ_y	shear yield stress (Pa)
τ_w	wall shear stress (Pa) in a pipe of backfill

σ_h	total horizontal stress (kPa)
σ_v	total vertical stress (kPa)
σ'_h	horizontal effective stress (kPa)
σ'_v	vertical effective stress (kPa)
σ_1	major total principal stress (kPa)
σ_3	minor total principal stress (kPa)
σ'_1	major effective principal stress (kPa)
σ'_3	minor effective principal stress (kPa)
γ	unit weight of the backfill (kN/m^3)
γ_w	unit weight of water (kN/m^3)
γ_b	unit weight of the cemented paste backfill (kN/m^3)
γ_{wr}	unit weight of the waste rock (kN/m^3)
γ_r	unit weight of the rock mass (kN/m^3)
γ_{sat}	unit weight of saturated backfill (kN/m^3)
γ_{sub}	unit weight of submerged backfill (kN/m^3)
ν	Poisson’s ratio
ν_r	Poisson’s ratio of rock mass
μ	dynamic viscosity of water
S_T	total shear resistance of the fill
S_μ	shear resistance of fill due to friction
S_i	shear resistance of fill due to interlocking
V_f	volume of fill
V_s	volume of solid particles
V_w	volume of water

V_a	volume of air
V_v	volume of voids
M_f	mass of fill
M_w	mass of water
$M_{w\text{-}add}$	mixing water needed to CPB
M_a	mass of air (null)
M_t	mass of tailings
M_s	mass of solids particles (binder and tailings)
M_b	mass of binder
B_W	mass percentage of binder
B_V	volumetric percentage of binder
$B_{w\text{-}adj}$	adjusted Binder content due to variation in tailings solid particles density
W/C	water-to-cement ratio
w	water content
w_f	water content of the fill
w_t	water content of tailings
θ	volumetric water content
m	moisture content, or the wight of the sliding portion
S_r	degree of saturation
$C_{w\text{-}f}$	solid mass concentration of fill
$C_{w\text{-}t}$	solid mass concentration of tailings
$C_{w\text{-}b}$	solid mass concentration of binder
C_v	solid volume concentration of the fill
L^*	scale factor of the length between the physical model and prototype
T^*	scale factor of time

σ^*	scale factor of stress
ζ^*	scale factor of displacement

Abbreviations

DIC	digital image correlation
CHF	cemented hydraulic fill
CRF	cemented rock fill
CPB	cemented paste backfill
FDM	finite difference method
FEM	finite element method
FLAC	fast lagrangian analysis of continua
FS	factor of safety
FW	footwall
HAR	high aspect ratio
HF	hydraulic fill
HW	hanging wall
LAR	low aspect ratio
OPC	ordinary Portland cement
PWP	pore water pressure
RF	rock fill
RW	rock wall
SBP	self-boring pressure meter
TEP	total earth pressure
UCS	unconfined compressive strength
VCL	vertical centerline
WRB	waste rock barricade

RÉSUMÉ DE LA THÈSE

1. Introduction

Le remblayage des vides souterrains (ou chantiers d'abattage) résultant de l'extraction des métaux (précieux et de base) permet de stabiliser les terrains miniers tout en réduisant la quantité des rejets solides (roches stériles et résidus miniers fins) destinées à l'entreposage en surface dans haldes à stériles et les parcs à résidus. En effet, les rejets solides riches en sulfures et entreposés en surface sont souvent à l'origine de nombreux problèmes environnementaux, tels que le drainage minier acide (DMA) qui résulte de la contamination des eaux à la suite de l'oxydation des sulfures et la précipitation de certains métaux à forte concentration. Il existe trois principaux types de remblai couramment utilisés dans les mines : le remblai hydraulique (à base de résidus fins grano-classés), le remblai rocheux (à base de roches stériles concassées) et le remblai en pâte cimenté – RPC (à base de résidus fins tout venant). Par conséquent, les principaux composants des remblais miniers sont les résidus (grano-classés ou tout-venant), les roches stériles, l'eau de malaxage et l'agent liant. Des adjuvants chimiques peuvent parfois être utilisés afin d'améliorer les performances du remblai ou certaines de leurs propriétés, notamment de fluidité. L'utilisation de chacun des types de remblai dépend à la fois de la méthode de minage choisie (chambre-remblayée, AVOCA, tranches montantes, tranches descendantes, en vrac, etc.) et de la résistance requise selon les besoins de stabilisation des terrains encaissants.

La réutilisation des résidus miniers fins sous forme de remblai en pâte cimenté (RPC) permet de retourner sous terre près de 50% des rejets de concentrateur générés lors du traitement du minerai. La distribution granulométrique et les propriétés physiques des résidus sont importantes à considérer lors de la conception des systèmes de remblayage souterrain (e.g. Potvin et al., 2005). La minéralogie des résidus miniers ainsi que la qualité de l'eau de malaxage (ex. présence de sulfates) peuvent affecter grandement la performance du RPC à court et à long termes (ex. attaque sulfatique et chute de la résistance mécanique). La proportion des résidus fins dans les remblais en pâte cimentés se situe entre 70 et 85% (= 100 × *masse_grains_solides* / *masse_totale_humide* = 100 × M_s / M_h). L'eau de malaxage est généralement de l'eau potable, de lac ou de l'eau de procédé recyclée. Le liant hydraulique ajouté est soit du ciment Portland tout usage ou type GU ou bien du ciment GU incorporant des ajouts minéraux tels que les cendres volantes ou le laitier de hauts fourneaux. La formulation de liant la plus utilisée dans la plupart des mines souterraines est 20%

de ciment Portland GU et 80% de laitier de hauts fourneaux (Belem & Benzaazoua, 2008). Le taux de liant (= *masse_liant* / *masse_résidus_secs*) varie généralement entre 2 à 8% massique.

Les propriétés mécaniques du RPC dépendent non seulement des caractéristiques des résidus, des liants et de l'eau de mélange, mais aussi des propriétés chimiques et de la microstructure des matériaux utilisés. Les RPC peuvent un pourcentage de particules fines ($d \leq 20$ μm) pouvant varier entre 15 et 60% massique selon le degré de broyage du minerai de base. Toutefois, un pourcentage élevé en particules fines pourrait affecter négativement le développement de la résistance mécanique du RPC. Sur le site minier, le RPC est préparé dans une usine de remblai située en surface et est ensuite transporté sous terre vers les chantiers d'abattage via un ligne de pipelines par la gravité ou à l'aide de pompes à déplacement positif.

La transportabilité du RPC dépend de ses propriétés rhéologiques. En effet, le remblai en pâte cimenté est considéré comme non-Newtonien à comportement d'un fluide plastique de Bingham ou pseudo-plastique avec seuil d'écoulement obéissant au modèle de Herschel-Bulkley. En effet, une fois que la contrainte de cisaillement dépasse la contrainte seuil de cisaillement ou seuil d'écoulement, le RPC commence à couler avec une viscosité constante (fluide de Bingham) ou variable (fluide de Herschel-Bulkley). La corrélation entre la contrainte seuil de cisaillement et le pourcentage solide du RPC permet de prédire les besoins en énergie de pompage dans les pipelines de transport. Toutefois, dans l'industrie minière la méthode la plus utilisée pour déterminer les paramètres d'écoulement du RPC est le test d'affaissement au cône d'Abrams (norme ASTM C143) qui est un facteur rhéologique.

Avant la formulation du mélange de remblai, la résistance cible requise du remblai doit être déterminée en fonction de l'utilisation prévue : piliers secondaires de renforcement des épontes (pour empêcher l'effondrement des murs et des toits et pour une récupération compète du minerai, ce qui augmente la productivité) ou plancher de travail. Des barricades sont généralement placées au point de soutirage proche de l'épaulement du chantier d'abattage afin de contenir le RPC à l'intérieur du chantier d'abattage pendant le remblayage. Les barricades peuvent être faites de briques, de blocs de béton, de grille métallique avec du béton projeté, avec généralement un système de drains. Un autre type de barricade consiste à l'utilisation des roches stériles du développement pour construire une berme solide et très perméable, permettant le drainage de l'eau du remblai. Après la mise en place du RPC sous terre dans les chantiers d'abattage, plusieurs

phénomènes peuvent être observés, à savoir le tassement par consolidation gravitaire (dû au drainage), le retrait au niveau des épontes, et l'effet d'arche (Belem et Benzaazoua, 2003).

2. Énoncé de la problématique

Bien que les barricades de roches stériles soient plus économiques car les roches stériles sont réutilisables à souhait et permettent une meilleure gestion des roches stériles de développement des galeries souterraines, elles n'ont pas encore bénéficié d'études exhaustives, de sorte qu'il existe très peu d'options pour leur analyse et leur dimensionnement adéquat (Belem et al., 2020; Li, 2019; Gélinas, 2017 ; Yang, 2016). En effet, l'étude du comportement géomécanique de ces barricades de roches stériles mérite une attention particulière pour permettre leur dimensionnement sûr afin de protéger les travailleurs et les équipements miniers et d'avoir une meilleure maîtrise des opérations de remblayage. Habituellement, une chargeuse-navette équipée d'une plaque de poussée est utilisé pour construire la barricade de roches stériles, généralement de forme trapézoïdale, en formant des couches compactées de roches stériles (Gélinas, 2017 ; Belem et al., 2020). À la fin de la construction de la barricade de roches stériles, une couche de béton projeté est placée sur sa partie aval afin de l'étanchéifier contre les fuites de remblai par débordement (Gélinas, 2017 ; Belem et al., 2020 ; Yang et al., 2016).

De nombreux cas rapportés dans la littérature ont montré que les défaillances des barricades de retenue du RPC ont souvent entrainé de graves conséquences, telles que l'immobilisation ou l'endommagement d'équipements miniers coûteux, des blessures ou même la mort de travailleurs (e.g. Grice, 1998, Sivakugan et al., 2006a, Bussiere, 2007, Helinski et al., 2007, Yumlu & Guresci, 2007, Li & Aubertin, 2009a, Widisinghe et al., 2013, Sivakugan et al., 2015). Les barricades de roches stériles sont peu coûteuses car les roches stériles de développement sont facilement accessibles sous terre. Toutefois, le comportement et les mécanismes de défaillance des barricades de roches stériles sont peu documentés, bien qu'ils soient largement utilisés dans de nombreuses mines souterraines canadiennes. L'analyse de stabilité des barricades de roches stériles nécessite une estimation correcte des pressions totales et de la pression interstitielle dans les chantiers d'abattage remblayés et sur les barricades de roches stériles, en particulier pendant les moments les plus critiques qui sont la mise en place du RPC et immédiatement après le remblayage. Après ces moments critiques, les contraintes totales exercées sur les chantiers et les barricades remblayées diminuent considérablement en raison de plusieurs facteurs (ou phénomènes), tels que le

développement du phénomène d'arche, la dissipation de la pression interstitielle et le durcissement du remblai cimenté.

Dans la littérature, de nombreuses solutions analytiques et des modélisations numériques ont été proposées, dans lesquelles chaque investigation a ses avantages et ses limites (e.g., Li et al., 2003; Li & Aubertin, 2009d, a, c; Li et al., 2009; Li & Aubertin, 2011; Yang, 2016; Gélinas, 2017; Belem et al., 2020). Par conséquent, des études supplémentaires sont nécessaires pour évaluer la pression critique du remblai sur la barricade de roches stériles et la procédure de son dimensionnement approprié. Les solutions développées pour les barricades traditionnelles ne sont pas directement applicables aux barricades de roches stériles, et des études complémentaires sont souhaitables. Il est donc nécessaire de développer de nouvelles approches pour le dimensionnement approprié des barricades de roches stériles en fonction de plusieurs facteurs tels que leur emplacement par rapport l'entrée au bas du chantier, la taille des particules de roches stériles, le degré de compactage, les paramètres de cisaillement des roches stériles de développement ainsi que les paramètres de cisaillement (résistance et frottement) entre la barricade de roches stériles et les épontes latérales de la galerie de soutirage. Des travaux de simulations numériques ont également été réalisés par la méthode des éléments finis afin d'évaluer le comportement hydromécanique des chantiers remblayés et d'apprécier l'interaction entre le RPC et la barricade de roches stériles. Ces simulations ont pris en compte l'effet des propriétés du remblai, de la géométrie et de la profondeur des chantiers, des paramètres des épontes rocheuses ainsi que de la séquence d'excavation et de remblayage (Mkadmi et al., 2012). Des solutions analytiques ont également été proposées pour estimer la pression de remblai dans le chantier et sur la barricade en fonction de la distance du front du point de soutirage (Li & Aubertin, 2009d, a, c; Li & Aubertin, 2011).

Toutefois, une modélisation physique utilisant un modèle transparent à petite échelle n'a jamais été proposée dans la littérature et elle serait nécessaire pour mieux comprendre le comportement géomécanique complexe des barricades de roches stériles et leur mécanisme de rupture. De ce fait, les solutions qui seront proposées pour le dimensionnement des barricades de roches stériles devraient reposer exclusivement sur les observations expérimentales qui tenteront de reproduire des conditions similaires à celles des chantiers miniers réels *in situ*. Une telle approche bénéficierait des solutions expérimentales de plusieurs scénarios critiques différents en laboratoire qui seraient ensuite transposées à l'échelle *in situ* à travers des simulations numériques.

3. Objectifs

L'objectif principal de ce projet de thèse est d'étudier le comportement géomécanique du remblai en pâte cimenté placé dans les chantiers d'abattage de type longitudinal en interaction avec une barricade de roches stériles placée dans le point de soutirage, à une certaine distance de l'épaulement du chantier. Plus précisément, le projet se concentre sur le comportement du remblai en pâte à un âge précoce dans le but d'estimer les pressions générées par le remblai frais et liquide sur la barricade de roches stériles qui serviront pour le dimensionnement des barricades de roches stériles. Les objectifs spécifiques du projet de thèse sont les suivants:

- Étudier les mécanismes de rupture des barricades de roches stériles ayant différentes distributions granulométriques et évaluer l'état des contraintes induites par le remblai en pâte cimenté lors du remblayage.
- Simuler numériquement quelques essais expérimentaux sur modèle réduit en procédant par calibrage (ou calage) avec les résultats expérimentaux obtenus;
- Proposer une solution analytique d'analyse de stabilité par équilibre limite des barricades de roches stériles en s'appuyant sur les observations expérimentales sur modèle réduit.

Ce projet de thèse devra contribuer à mieux répondre aux défis géomécaniques complexes rencontrés dans les chantiers souterrains, notamment lors du dimensionnement des barricades de roches stériles. L'atteinte de ces objectifs permettra d'améliorer l'évaluation de l'état des contraintes dans les chantiers remblayés ainsi que la productivité minière par la réduction des risques associés au remblayage souterrain.

4. Méthodologie

Afin d'atteindre les objectifs du projet de thèse, la méthodologie de recherche adoptée est structurée autour de trois approches: *i*) expérimentale : essais sur modèle physique réduit d'un chantier minier longitudinal, *ii*) numérique : simulations numériques des scénarios expérimentaux (calage de modèle numérique), et *iii*) théorique : développement d'une solution analytique d'analyse de stabilité par l'équilibre limite des barricades de roches stériles.

4.1. Modélisation physique sur modèle réduit d'un chantier d'abattage longitudinal

Des tests en laboratoire et des mesures in situ effectués de manière adéquate peuvent fournir des données précises et fiables qui peuvent être comparées à des solutions analytiques et numériques.

L'utilisation de modèles à échelle réduite est une pratique largement utilisée pour résoudre de nombreux problèmes complexes en géotechnique car ils permettent d'étudier différents scénarios de réponse plus rapidement et avec un meilleur contrôle des détails du modèle physique que ne le permettraient des essais en grandeur nature.

De plus, les données expérimentales sont souhaitables pour les applications d'ingénierie, car les essais en laboratoire facilitent le contrôle ou la mesure des propriétés des matériaux, des géométries des modèles et des conditions de sollicitation. Des modèles physiques réduits (colonnes) ont déjà été utilisés pour étudier la distribution des contraintes verticales dans le remblai (Sivakugan & Widisinghe, 2013, Widisinghe et al., 2013; Widisinghe et al., 2014, Widisinghe, 2014) ou pour étudier la consolidation gravitaire des remblais en pâte cimentés et le développement de leur résistance mécanique (Belem et al., 2016 ; Belem et al., 2006).

Dans ce projet, un modèle physique à l'échelle réduit d'un chantier d'abattage longitudinal a été conçu et fabriqué avec des plaques translucides de plexiglass. Ce modèle réduit a été utilisé pour étudier le comportement géomécanique d'une barricade de roches stériles lors du remblayage avec du remblai en pâte cimenté. Il est question d'évaluer la pression exercée par le remblai sur la barricade de roches stériles, d'analyser l'interaction barricade-remblai pour différentes distributions granulométriques des roches stériles, d'étudier les mécanismes de rupture ou la défaillance mécanique des barricades de roches stériles et d'évaluer la pression maximale à la rupture.

L'un des avantages des modèles physiques à l'échelle est qu'ils sont rapides, reproductibles et les essais peuvent être conduits jusqu'à la rupture. Le choix des propriétés des matériaux est très varié, et divers paramètres peuvent être facilement modifiés pour étudier leur influence. Le modèle réduit doit cependant obéir aux lois de similitude qui garantissent la similitude du comportement mécanique entre le modèle réduit (ou maquette) et son prototype associé (grandeur nature). Ces lois permettent d'appliquer la solution obtenue sur le modèle réduit au problème en grandeur réelle. L'établissement des lois de similitude est basé sur une analyse dimensionnelle en considérant l'invariance des équations générales de la mécanique au changement d'unités. Ces équations sont les équations de la dynamique générale, l'équation de conservation de la masse et les lois de comportement des différents matériaux. Pour satisfaire aux différentes conditions de similarité, l'utilisation d'un modèle de gravité naturelle (1-g) est inutile et ne permet de rester que dans le cadre d'une étude qualitative. De plus, les modèles de laboratoire sont soumis à des effets à grande échelle

qui peuvent perturber les résultats qualitatifs (mécanismes de défaillance) et quantitatifs (déplacements par rapport aux charges) (Garnier, 1997). La modélisation en centrifugeuse basée sur des lois d'échelle permet de maintenir les mêmes niveaux de contrainte et de déformation dans le modèle réduit et le prototype. C'est le principal avantage des essais en centrifugeuse. Les centrifugeuses sont essentielles dans certains cas. Malgré leurs avantages, les modèles de centrifugation ne sont pas sans inconvénients, comme :

- la taille des grains qui n'est pas affectée par l'échelle dimensionnelle (un problème de débit d'eau) ;
- ces modèles nécessitent un dispositif d'installation spécial pendant la rotation ;
- pour les chantiers d’abattage, difficulté à placer le remblai et à surveiller la barricade de roches stériles pendant la rotation de la centrifugeuse ;
- la difficulté à installer les instruments de mesure (capteurs, câbles, etc.).

De plus, la rupture de la barricade de roches stériles pendant l'expérience pourrait endommager les équipements. Par conséquent, tester le modèle en gravité naturelle est plus pratique, moins coûteux et permet de réaliser de nombreux tests. Il peut être nécessaire de reproduire les mêmes essais sur des modèles à différentes échelles pour quantifier les effets d'échelle et extrapoler les résultats obtenus sur le modèle en gravité normale pour la structure à grande échelle. Plusieurs tests ont été réalisés à l'aide du modèle physique à échelle réduit reproduisant différents scénarios d’opérations de remblayage avec du remblai en pâte cimenté pratiquées dans de nombreuses mines canadiennes. Le remblai en pâte cimenté est mis en place et est retenu dans le chantier par une barricade faite de roches stériles concassés placée dans le point de soutirage.

Le modèle physique à échelle réduite a été construit pour reproduire qualitativement et quantitativement le remblayage des chantiers miniers souterrains de type longitudinal. Pour la présente étude, le modèle à échelle réduite simulera le remblayage d'un chantier d’abattage typique dans les mines de la région de l'Abitibi-Témiscamingue (Québec, Canada) avec une échelle de longueur de 1/50 (facteur d'échelle de longueur $L^* = L_{\text{modèle}}/L_{\text{prototype}} = 1/50$). La Figure 0-1 présente le dispositif expérimental du modèle à échelle réduite dans son ensemble.

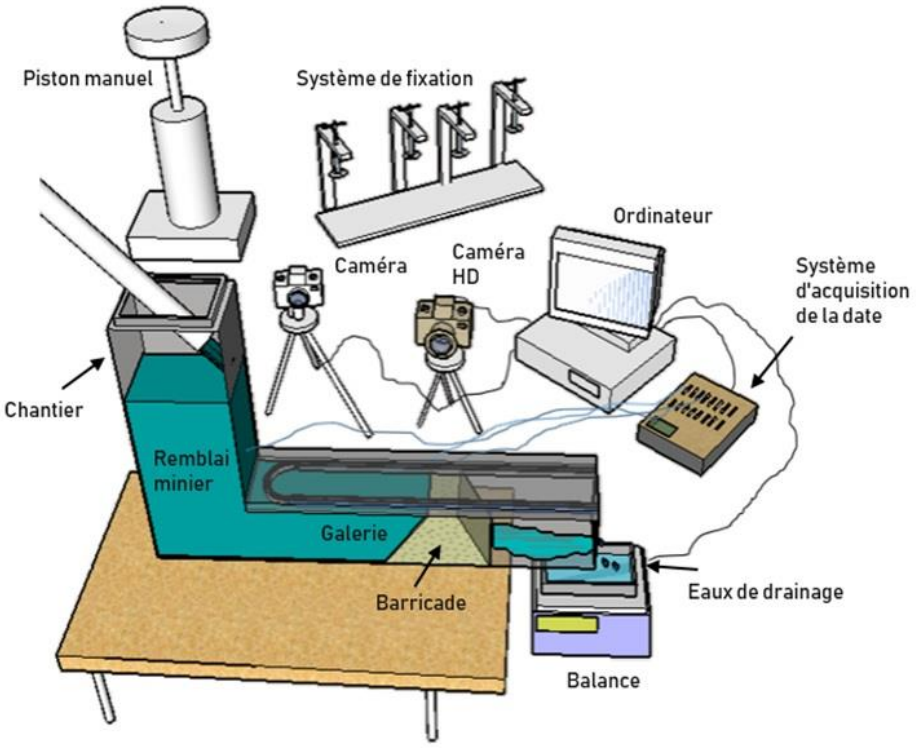


Figure 0-1: Dispositif expérimental avec le modèle physique à échelle réduite d'un chantier d'abattage longitudinal

Le chantier d'abattage (ou chambre de remplissage) est en verre acrylique ou en plexiglas (PMMA) ayant une section longitudinale de 9 x 20 cm et une hauteur de 38 cm (peut être augmentée jusqu'à 100 cm). Le chantier d'abattage est relié à la galerie ou point de soutirage (section de 9 x 9 cm et 63 cm de longueur). Les plaques de plexiglass utilisées ont des propriétés mécaniques suffisantes pour les applications visées. Le choix de ce type de polymère pour cette étude est guidé notamment par sa transparence qui permet d'observer l'interaction barricade-remblai lors du remplissage et après la mise en place du remblai. La pression du remblai dans le chantier et sur la barricade a été mesurée à l'aide de mini-capteurs de pression positionnés à différents endroits. Le modèle physique à échelle réduite est aussi équipé d'un système manuel de chargement externe (piston) pour augmenter la pression sur la barricade jusqu'à sa défaillance ou rupture. Il convient de souligner qu'en raison de contraintes de coûts, les exigences de similitude ont été assouplies et le modèle réduit ne satisfait pas à la similitude de premier ordre. Une caméra haute résolution (2048 x 2048) a été utilisée pour aider à analyser le déplacement de la barricade et son mécanisme de rupture. Le suivi du comportement de la barricade n'a été enregistré qu'en 2D (à travers les parois transparentes

de la galerie), en supposant que les particules au cœur de la barricade ont le même comportement. Une deuxième caméra a également été utilisée pour capter les manipulations lors de la mise en place du remblai (Figure 0-1).

En général, la modélisation physique utilisant des modèles à échelle réduite nécessite le respect des conditions de similitude, y compris i) les équations d'équilibre dynamique (conditions absolues), ii) la loi de comportement du matériau et iii) les conditions aux limites. Les tests expérimentaux sur le modèle physique ont été réalisés en utilisant les matériaux réels du prototype ($\rho_m = \rho_p$) (barricade & remblai), sous gravité normale ($g^* = 1$) et un facteur d'échelle de longueur de 1/50 ($L^* = 1/n$). Selon les règles de similitude, la valeur du module de Young (E_m) et la cohésion (c_m) du matériau utilisé dans le modèle réduit doivent être inférieures (n fois) aux valeurs du prototype, tandis que les paramètres adimensionnels [l'indice des vides (e), l'angle de frottement (ϕ), l'angle de frottement d'interface (δ) et le coefficient de Poisson (v)] du prototype et du modèle réduit doivent être identiques. Les valeurs de déplacements attendus pour la taille réelle du prototype, seront égales à n fois (50) les valeurs mesurées sur le modèle réduit. Dans de nombreux tests géotechniques sur des modèles à échelle réduite, il est nécessaire de maintenir le niveau de contrainte ($\sigma^* = 1$). Dans ce cas, les essais en gravité normale ($g^* = 1$) nécessitent l'utilisation de matériaux équivalents (voir l'annexe F pour plus de détails). Par conséquent, le poids volumique du matériau utilisé dans le modèle réduit doit être n fois inférieur à celui du prototype ou de la structure grandeur nature ($\rho_m = 50\rho_p$). Aussi, le matériau équivalent doit également respecter les règles de comportement pour les grandeurs dimensionnelles ($E^* = c^* = 1$) et les grandeurs adimensionnelles ($\phi^* = \delta^* = \nu^* = 1$). Il est à noter que le respect des lois de similitude est souvent difficile dans de nombreuses situations impliquant des comportements complexes (voir Corté, 1989a; Garnier, 1997). La granulométrie de la barricade de roches stériles peut être respectée (e.g., méthode de la gradation parallèle, facteur d'échelle de taille), mais le poids volumique cible est difficile à atteindre même avec des matériaux équivalents. De plus, les règles de similitude n'ont pas été appliquées au remblai car ses propriétés sont complexes et le comportement change du remplissage au durcissement. En bref, ce type de modélisation n'est pas conforme à toutes les conditions de modélisation physique et des effets d'échelle peuvent se produire, mais il fournit des scénarios similaires pour les opérations de remblayage souterrain et la rupture de barricades difficiles à observer sous terre dans les mines.

La pression en différents points dans le modèle réduit a été mesurée à l'aide de deux types de capteurs de pression dont la capacité variait de 35 à 100 kPa selon le but du test. Les pressions totales (TEP) ont été considérées comme équivalentes aux pressions mesurées par les cellules de pression totale des terres, les pressions interstitielles (PWP) sont considérées comme égales à celles mesurées par les mini-piézomètres, et les contraintes effectives sont la différence entre ces valeurs (σ' = TEP – PWP). Les capteurs de pression ont été étalonnés avant les essais en utilisant de l'eau et en comparant la pression mesurée avec la pression due au poids des terres après la mise en place.

Plusieurs étapes sont nécessaires pour réaliser les essais sur le modèle à échelle réduit: i) préparer le modèle avec les instruments, les matériaux et valider les mesures (étalonnage des capteurs); ii) simuler différents scénarios en faisant varier les propriétés et les séquences de remplissage; iii) enregistrer les pressions et les mouvements relatifs de la barricade lors du remblayage; iv) faire varier la taille des particules de la barricade de roches stériles ou les propriétés de remblayage.

Un moule trapézoïdal a été fabriqué pour former la barricade de roches stériles concassées et compactées. Différentes distributions granulométriques ont été proposées pour étudier le comportement de la barricade en gradation fine ou grossière. Le diamètre des particules de la barricade variait de 0 à 8 mm sur le modèle à échelle réduite, en supposant que ces diamètres de particules varient entre 0 et 400 mm dans la barricade pleine échelle. La méthode de corrélation d'images numériques bidimensionnelles (DIC pour *discrete image correlation*) a été utilisée pour mesurer le déplacement des particules de la barricade ou pour étudier les mécanismes de rupture des barricades de roches stériles. Une fois le remblai préparé à l'aide du mélangeur de laboratoire Hobart, le mélange de remblai est coulé dans le modèle réduit en quelques minutes. Pour certains essais, il a été nécessaire d'augmenter la pression à l'aide du piston manuel jusqu'à ce que la barricade s'effondre pour étudier son mécanisme de défaillance. Pendant le test, les caméras enregistrent l'opération de remplissage et le comportement de la barricade.

4.2. Modélisations numériques

Les simulations numériques sont une autre approche courante pour évaluer l'état de contraintes dans les chantiers remblayés et pour étudier l'effet de différents paramètres (tels que les propriétés physique, hydrique et mécanique, la température et la viscosité du remblai, le taux de remplissage, etc.) sur les pressions interstitielles générées. De nombreuses modélisations numériques ont été réalisées sur le remblayage des mines souterraines (e.g., Li et al., 2003; Li et al., 2007; Pirapakaran

& Sivakugan, 2007; Hassani et al., 2008; Li & Aubertin, 2008; Fahey et al., 2009; Li & Aubertin, 2009d, e; Li et al., 2010; El Mkadmi, 2012; Veenstra, 2013; Emad et al., 2014; Falaknaz, 2014; Yang, 2016). Pour ces simulations numériques, différents codes de calculs par éléments finis tels que FLAC, PHASES^{2}, FLAC^{3D}, PLAXIS et SIGMA/W, ont été utilisés pour évaluer l'état de contraintes et de vérifier les résultats des solutions analytiques.

Dans cette thèse de doctorat, des simulations numériques 2D ont été réalisées à l'aide du logiciel SIGMA/W de GeoStudio 2018 (de GeoSlope International) pour reproduire les interactions entre le remblai et la barricade de roches stériles. Les résultats de ces simulations ont été calés sur les résultats expérimentaux obtenus sur le modèle physique réduit. Plusieurs étapes ont été nécessaires pour compléter ces simulations numériques: i) construire et vérifier la géométrie du modèle de référence numérique basé sur les dimensions du modèle à l'échelle réduite, ii) définir les propriétés physique, hydrique et mécanique des matériaux (en se basant principalement sur des estimations faites par le logiciel, donc non basées sur les propriétés réelles), et iii) définir les conditions aux limites. Avant d'utiliser un modèle défini pour des simulations numériques, une analyse de sensibilité (incluant la taille du maillage) est effectuée pour vérifier la validité et l'adéquation des calculs par le code au problème en question. L'adéquation du code est testée en comparant les résultats obtenus du modèle numérique avec des résultats fiables des tests en laboratoire sur le modèle réduit (ou bien de mesures sur le terrain). El Mkadmi et al. (2012) ont utilisé le code SIGMA/W pour étudier les contraintes développées dans des couches de remblai en pâte cimenté déposées successivement et en suivant l'évolution de l’état des contraintes effectives lors du drainage. Les auteurs se sont d’abord assuré que le code de calcul SIGMA/W pouvait reproduire les solutions connues, y compris les résultats de tests de laboratoire dans des conditions bien contrôlées. En effet, El Mkadmi et al. (2012) ont reproduit les résultats de la littérature d'un test à l'œdomètre en laboratoire sur une argile bleue (déterminer le coefficient de consolidation c_v pour chaque niveau de charge appliquée) (Bowles, 1978, n°13). Une fois que l'adéquation du code a été vérifiée, des simulations numériques plus complexes peuvent être effectuées à grande échelle.

Dans ce projet de thèse, le code SIGMA/W a également été utilisé pour reproduire certains tests expérimentaux (sur le modèle à échelle réduite) pour comparer et confirmer les résultats. La connaissance des écarts entre les résultats numériques et expérimentaux permettrait de mieux interpréter les résultats numériques dans l’optique du dimensionnement d’un système de remblayage. La relation contrainte-déformation la plus simple disponible est la loi linéaire de

Hooke (élasticité isotrope). Le modèle réduit (PMMA) a été modélisé comme un matériau homogène (comportement élastique isotrope et linéaire). Le PMMA a un poids volumique de 11,67 kN/m^3, un module de Young de 3 GPa et un coefficient de Poisson de 0,35. Dans ces simulations numériques, le remplissage du chantier a été très rapide (équivalent à un remblayage instantané), suivi d'un drainage progressif. Vue la taille du modèle réduit, le remblai a été mis en place en deux couches, une couche tous les deux jours (48 heures). Le poids volumique initial du remblai mesuré en laboratoire lors des tests sur le modèle physique avec du remblai non cimenté (70% massique de solides) était de 19,2 kN/m^3. La nappe phréatique est placée à la surface de chaque couche. Une analyse couplée (contrainte-déformation et prenant en compte la pression interstitielle) est ensuite réalisée pendant une durée de 2 jours. Cette analyse nécessite la définition des conditions hydrauliques aux limites (nappe phréatique, drainage, débits hydrauliques, etc.) ainsi que les paramètres hydro-géotechniques de chaque matériau (courbe de rétention d'eau et courbe de conductivité hydraulique saturée en fonction de la succion). Une des conditions aux limites correspondait à une charge hydraulique nulle (h_c = 0 m) du côté aval à la base de la barricade pour simuler l'écoulement de l'eau lors du drainage. Le remblai (pourcentage solide C_w = 70%) se comporte comme un liquide lourd (mélange solide-liquide) pendant le remblayage, donc une forte valeur pour le coefficient de Poisson (ν_b = 0,495), et une faible valeur pour le module de Young (E_b = 10 kPa) du remblai utilisé. La barricade de roches stériles est modélisée comme un milieu élastique linéaire (avec changement de pression interstitielle). Les paramètres hydrauliques de la barricade de roches stériles ont été estimés. La fonction de la teneur en eau volumique a été estimée par le logiciel comme une fonction simple (sable limoneux) avec une teneur en eau saturée de 0,3. De plus, une conductivité hydraulique saturée $k_{sat} = 10^{-4}$ m/s a été utilisée. La densité apparente sèche de la barricade (γ_{wr}) est de 18,9 kN/m^3 (mesurée en laboratoire).

4.3. Développement de solutions analytiques

Des solutions analytiques basée sur les calculs à l'équilibre limite a été développées afin d'évaluer le facteur de sécurité et la stabilité de deux configurations de barricades de roches stériles : i) une barricade placée dans une galerie ayant les parois lisses (faible frottement), ii) une barricade placée sur des cales en silicone alignées et fixées à la base de la galerie afin d'augmenter la friction d'interface (simulation de la rugosité à la base de la galerie).

5. Programme expérimental

Plusieurs tests sont réalisés pour étudier l'état de contrainte lors d'un remblayage séquentiel (deux couches, C_w =70%) d'un mélange de remblai contenant 5% de ciment Portland (type GU) et d'un mélange de remblai sans ciment (résidus uniquement, C_w = 70%). Le mécanisme et la résistance à la rupture de la barricade de roches stériles ont également été étudiés en augmentant la pression au sommet du chantier avec le piston manuel. L'étude de la stabilité des barricades de roches stériles s'est faite à travers deux configurations : i) une barricade placée dans une galerie ayant des parois lisses (très faible frottement), ii) une barricade placée sur des cales en silicone alignées (0,2×0,6 cm chaque 5cm) fixées à la base de la galerie pour augmenter la friction d'interface (surface rugueuse à la base de la galerie). De plus, certains des tests expérimentaux ont été comparés à des simulations numériques avec le code par éléments finis SIGMA/W (GeoSlope International, 2018 R2).

6. Résultats

Un modèle physique à échelle réduite en plexiglass PMMA transparent a été utilisé afin de simuler les chantiers souterrains lors du remblayage. Il a été possible d'observer l'interaction entre la barricade de roches stériles, placée au point de soutirage, et le remblai frais. Le modèle physique transparent a permis également de surveiller la barricade lors de sa saturation, son drainage et sa défaillance probable lorsque le piston manuel est utilisé. Le modèle ne répondait pas à toutes les exigences de similitude et nécessite un développement futur. Les parois intérieures du modèle devraient être pourvues d'une certaine rugosité afin de mieux représenter le frottement à l'interface remblai-éponte rocheuse. Toutefois, les résultats obtenus contribuent à la compréhension du comportement de la barricade de roches stériles et des remblais en pâte (cimentés et non cimentés).

Les résultats obtenus ont confirmé ceux d'une étude antérieure (Gélinas, 2017) à l'effet que la barricade rocheuse doit être construite en suivant une procédure adéquate qui inclut le contrôle de la granulométrie et du degré de compaction des roches stériles de développement. La longueur de la barricade au toit de la galerie de soutirage doit être déterminée en considérant plusieurs facteurs tels que le taux de remblayage, la cure entre deux séquences de remplissage, le type et le pourcentage du liant, etc. L'utilisation de liants est bénéfique et essentielle pour un remblayage rapide. Il a été observé que le remblai en pâte non cimenté se drainait beaucoup et restait saturé pendant plusieurs jours après la mise en place, tandis que le drainage était arrêté pour le remblai

cimenté après plusieurs heures et le remblai commençait à durcir. En effet, le remblai cimenté a consommé l'eau plus rapidement et présentait moins de variation de la déformation volumétrique après la consolidation gravitaire (trois fois moins que pour le remblai non cimenté). Après la mise en place de chaque couche de remblai, un ressuage de l'eau du mélange est observé, puis les processus de consolidation gravitaire et de tassement commencent, accompagnés d'un drainage à travers la barricade. Immédiatement après la mise en place, la pression interstitielle est égale à la pression due au poids du remblai (poids des terres), puis diminue pendant le drainage, rapidement en haut du chantier et près de la barricade, pour devenir négative dans certains cas. Lorsque la barricade contient une grande quantité de matériau fin, la vitesse de drainage diminue et la pression interstitielle augmente et atteint sa valeur maximale au milieu du chantier (dans la couche mise en place). Plusieurs heures après le remblayage, certains capteurs de pression ont indiqué une augmentation significative de la pression totale du remblai cimenté, en particulier pour les capteurs fixés latéralement au milieu du chantier. Il apparaît que pour les simulations numériques, le comportement mécanique ou la loi de comportement du remblai cimenté devra être bien défini en fonction du type et du pourcentage du liant. C’est ce qui garantira un meilleur calage des modèles numériques sur les tests expérimentaux sur le remblai non cimenté. Des travaux de recherche supplémentaires seront nécessaires et prenant en compte la viscosité du remblai, les propriétés des résidus et l'effet d'arche. Cependant, la modélisation numérique est utile pour prédire la pression de remblai cimenté quelques heures après sa mise en place (phase critique). Les modélisations numériques et physiques à l’aide du modèle réduit ont montré qu'une pression négative, en raison de la succion, peut se produire dans différentes zones de désaturation, notamment au sommet du chantier et proche de la barricade.

Les calculs de stabilité basés sur l'équilibre limite ont montré que le frottement latéral entre la barricade de roches stériles et les parois de la galerie, ainsi que la cohésion apparente entre les particules de la barricade, jouent un rôle important dans la résistance à la poussée du remblai avant rupture de la barricade. La bonne qualité de la construction de la barricade et l'utilisation de béton projeté du côté aval augmenteraient sans aucun doute la stabilité de la barricade. Des travaux futurs sont prévus pour étudier l'effet du type de liant et des mécanismes de rupture de la barricade ayant différentes distributions granulométriques. Une boîte de cisaillement spéciale devra être développée ou utilisée pour la détermination des paramètres de cisaillement (angle de frottement de l'interface entre la barricade et les parois du modèle). Des informations plus détaillées sur la

taille des roches stériles utilisées pour la construction des barricades rocheuses et les dimensions des barricades communément utilisées dans l'industrie minière et qui basées sur l'expertise des ingénieurs des mines doivent également être collectées auprès de plusieurs mines.

7. Conclusion

Ce projet présente une étude expérimentale sur un modèle physique réduit d'un chantier d'abattage longitudinal typique, ainsi que des simulations numériques du comportement géomécanique (évaluation de l'état de contraintes dans le remblai en pâte cimenté mis en place dans un chantier d'abattage) et les interactions entre le remblai frais et la barricade de roches stériles. Les résultats de cette thèse peuvent aider à améliorer la conception des systèmes de remblayage souterrain ainsi que le dimensionnement des barricades de roches stériles. Les principales conclusions de cette thèse sont comme suivant :

- La conductivité hydraulique élevée des barricades de roches stériles permet un drainage rapide du chantier. En effet, le drainage du remblai en pâte à 70% de solides a été quantifié *via* la déformation volumique (ε_v) due à sa consolidation gravitaire, qu'il soit cimenté (ε_v = 4,5%) ou non (ε_v = 16%).
- La viscosité du remblai (et/ou son seuil d'écoulement ou de cisaillement) et son paramètre de cisaillement influencent l'état des contraintes dans les chantiers remblayés et le temps qui atteint les consolidations finales.
- Le drainage entraine l'augmentation des contraintes effectives et, après un certain temps écoulé, des zones de désaturation (succion) apparaissent dans la partie supérieure du chantier remblayé et à proximité de la barricade de roches stériles.
- La stabilité d'une barricade de roches stériles dépend de nombreux facteurs, tels que la granulométrie des particules des roches stériles, du degré de leur compactage, ainsi que la rugosité des parois du point de soutirage (résistance au glissement et/ou au frottement entre la barricade et les parois). En effet, cette stabilité semble être contrôlée par la résistance au frottement de l'interface le long de la base de la barricade (parois lisses ou rugueuses). Le glissement global et la rupture par cisaillement ont été observés lors des tests.
- L'interface remblai-parois du modèle physique influence l'état de contraintes dans le remblai mis en place. Plus les surfaces des parois sont rugueuses, plus les forces de

frottement sont importantes, et cela entraîne un transfert d'une partie du poids du remblai vers les côtés (parois).

- L'utilisation d'une barricade trapézoïdale de roches stériles favorise grandement sa stabilité contre le glissement, selon la rugosité des parois du modèle. L'analyse des résultats des tests suggère qu'une attention particulière doit être portée sur la face amont proche du sommet de la barricade en vue de l'analyse de la stabilité globale.
- L'utilisation de ciment pour le remblayage de la première couche (le bouchon), d'une couche de béton projeté sur le pourtour en au sommet de la face aval de la barricade et le compactage des roches stériles de la barricade sont des opérations importantes qui doivent être bien exécutées lors de la construction des barricades rocheuses.
- Les résultats des simulations numériques étaient cohérents avec les tests réalisés sur le modèle physique à l'échelle réduite, mais les ordres de grandeur des pressions mesurées étaient différents (30% supérieur dans les résultats numériques).

Puisque les tests et l'analyse des résultats reposent sur plusieurs hypothèses simplificatrices, il est souhaitable d'améliorer les travaux futurs en utilisant un taux de remplissage plus réaliste, d'autres types de barricades et des surfaces intérieures rugueuses du modèle réduit.

CHAPTER 1 INTRODUCTION

A mine is an excavation in the ground from which ores and minerals are extracted. These must contain enough precious metals. If the orebody is profitable, the engineers identify the best method for mining the earth's ore (open-pit mines or underground mines). The precious minerals must be separated from the gangue by crushing and grinding the ore in order to release the extracted minerals or metals, either gravimetrically or chemically (e.g., by flotation or hydrometallurgical processes). The ore is crushed to a grain size typical of silty material, with most particles varying from 2 to 80 mm (Bussiere, 2007). Two products are obtained at the end of the mineral separation process: the valuable portion (precious metals) and the residue of the mineral separation process (tailings), which does not have any economic value. Many mines need to manage a significant amount of tailings because mineral quantities are low compared to the mined volume of ore. Tailings are usually transported as a slurry from the mine concentrator to a specific area called a tailings impoundment, which is partially or completely enclosed by dikes that hold both the solid tailings and the mill effluent. The key geoenvironmental issues associated with the disposal of tailings are the physical stability of the impoundments and the geochemical stability of the solid and liquid waste generated, which can result in water pollution. Mines can have a significant impact on groundwater quality and surface water quality. The tailings can be sources of environmental pollution because acid mine drainage (AMD) or acid rock drainage, collectively called acid drainage (AD), is formed when certain sulphide minerals in rocks are exposed to oxidizing conditions.

The solid waste materials can be used in underground stopes to control ground movement and provide a safer workplace for workers and equipment. The reuse of mining waste as backfilling material for underground mine stopes is considered an environmentally friendly way to manage waste, as it reduces the amount of waste that is disposed of on the surface. Therefore, the environmental and economic benefits of returning part of the tailings or waste rock underground are part of the rationale behind backfilling (Hassani & Archibald, 1998; Belem & Benzaazoua, 2008). Three types of backfill commonly used in the mining industry are rock backfill, hydraulic backfill, and paste backfill. With the development and advancement of dewatering technologies to increase the solid content of tailings to levels between 70% and 85%, underground paste backfill is now commonly used by the mining industry. Recently, paste technology has been suggested to

replace traditional slurry surface deposition primarily for environmental reasons (Hassani & Archibald, 1998; Potvin et al., 2005; Bussiere, 2007; Belem & Benzaazoua, 2008). To produce paste fill, tailings slurry (typically 25% to 45% by solid weight) is first sent to a thickener to raise its solid content to around 60% to 65% and later pumped to filter discs that produce a filter cake. The filter cake is delivered to the paste plant where water (fresh or processed) is applied to the paste conditioner to create a paste of the desired consistency (usually a paste with a solid content of 70% to 85 %). The consistency of the paste is relatively like that of wet concrete (Newtonian flow behaviour). Making the paste fill by adding a small dosage of binder, in the range of 2% to 10% binder (mass cement / mass solids) is common practice to increase strength.

Underground backfilling requires the construction of a retaining structure (termed barricade), which is installed in the drawpoint to hold the backfill in place until it cures and forms a plug. Because of this process, barricade stability plays an important role in the success of backfill operations. Depending on the type of backfill used, the barricade is usually made of permeable brick, fibrecrete, concrete (hydraulic fill), timber frame (hydraulic & paste fill), shotcrete (hydraulic & paste fill), or waste rock (paste fill). Waste rock barricades are economically efficient because waste rock can easily be obtained underground. However, a waste rock barricade design remains a major challenge encountered in underground stope filling, and more investigations are needed to evaluate the critical backfill pressure exerted on the barricade.

1.1 Problem statement

Numerous cases reported in the literature have shown that barricade failures often lead to serious consequences, such as the immobilization or damage of expensive mining equipment, injuries or even death of mine personnel (e.g. Grice, 1998, Sivakugan et al., 2006a, Bussiere, 2007, Helinski et al., 2007, Yumlu & Guresci, 2007, Li & Aubertin, 2009a, Widisinghe et al., 2013, Sivakugan et al., 2015).

Waste rock barricades are cost-effective because they are readily available and produced underground (from the development of access galleries). The behaviour and failure mechanisms of waste rock barricades are poorly documented, although they are widely used in many Canadian underground mines. Analysis of barricade stability requires a correct estimate of pore water and total pressures in backfilled stopes and on barricades, particularly at the most critical times that occur during the backfilling and shortly thereafter. After these critical moments, the total stresses

on backfilled stopes and barricades can decrease drastically due to several factors (or phenomena), such as the development of the arching phenomenon, pore water pressure dissipation, and the cemented backfill hardening. Through the literature, numerous analytical solutions, numerical modelling, and in situ measurements have been proposed, in which each investigation has its advantages and limitations, but further investigations are needed to assess the critical backfill pressure on the barricade and its design procedure. Few researchers published their work conducted on this subject (e.g., Li et al., 2003; Li & Aubertin, 2009d, a, c; Li et al., 2009; Li & Aubertin, 2011; Yang, 2016).

The solutions developed for traditional barricades are not directly applicable to waste rock barricades, and further studies are required to assess the critical backfill pressure exerted on the barricade and its design. It is, therefore, necessary to develop new methods to determine the appropriate size of waste rock barricade based on several factors, such as its location from the stope brow, the particle size of the waste rock particles and the degree of compaction, as well as the frictional resistance between the barricade and the drawpoint sidewalls.

1.2 Originality

Laboratory tests and in situ measurements, when performed adequately, can provide accurate and reliable data that can be compared to analytical and numerical solutions. The use of small-scale models is commonly spread to solve many geotechnical and complex problems since they allow for faster analysis of the predicted reaction patterns and better control of the parameters of the experiment than would be possible with full-scale experiments (e.g., in situ measurements).

Experimental data is desirable for engineering applications because laboratory testing makes it easier to control or measure material properties, model geometries, and load conditions. Many reduced physical models for the mining sites (stopes) have been used to study the distribution of vertical stresses (Sivakugan & Widisinghe, 2013, Widisinghe et al., 2013; Widisinghe et al., 2014, Widisinghe, 2014) or to study the consolidation of the self-weight and the development of the pressure resistance in the mine filling factories (Belem et al., 2016). All the previous physical models did not address the waste rock barricades and their interaction with the paste backfill. Furthermore, several analytical solutions have been proposed for designing the waste rock barricades, but these solutions have not been tested experimentally. The numerical simulations

conducted to study the state of stress on the backfill in the mine stopes were not also compared to experimental studies.

In this project, an experimental set-up is used to study the geomechanical behaviour of a mine stope during the underground filling of a cemented paste backfill supported by a waste rock barricade placed in a drift (gallery). This study includes some issues such as the pressure exerted by the backfill on the barricade, the barricade-backfill interaction for different size particle distributions, the resistance, and the mechanical failure of waste rock barricades. This project included an experimental-numerical comparative study of the stress state of the backfill at different locations on the stope. It also contributes to better addressing major geomechanical challenges encountered in underground stopes, including the design of retaining structures (barricades). The limit equilibrium calculation for the experimental tests on the barricades showed the importance of several points practiced in the mines such as the use of the shotcrete layer.

1.3 Thesis objectives

The general objective of this research is to investigate the geomechanical behaviour of backfill placed in vertical mine stopes and its interaction with a waste barricade placed in the drift. More specifically, the project focuses on the behaviour of the backfill, and on the stress state within the backfilling and drainage.

The following sub-objectives are specifically addressed:

- Evaluate the state of the stresses induced by cemented backfill during backfilling;
- Study the failure mechanisms of waste rock barricades in different grain size distributions (GSDs) in order to size the waste rock barricades to retain the cemented paste backfill during the filling of the mine stope;
- Compare the experimental tests conducted on the physical model with the numerical modelling results.

1.4 Contributions

The following papers have been published during this project:

Nujaim M., Belem T., Giraud A. (2020). Experimental tests on a small-scale model of mine stope to study the behavior of waste rock barricades during backfilling. *Minerals*, 10, 941.

Nujaim et al. (2019a). *Small-scale model preliminary testing on the interaction between paste backfills and waste rock barricades*. Proc. ISRM 14th International Congress on Rock Mechanics, September 13-18, Foz do Iguassu, Brazil, 8p.

Nujaim et al. (2019b). *Use of a reduced scale physical model of a mine stope for assessing waste rock barricades potential instabilities due to early age pastefill pressure*. Proc. of GeoSt.John's 2019, the 72nd Canadian Geotechnical Conference, St. John's, Newfoundland and Labrador, Canada, September 29 - October 2, 2019, 8 p.

Nujaim et al. (2018a). *Geomechanical behaviour of a rock barricade and cemented paste backfill: Laboratory experiments on a reduced-scale model*. Geomechanics and Geodynamics of Rock Masses, Volume 1: Proceedings of the 2018 European Rock Mechanics Symposium, Saint Petersburg, Russian Federation, 2018/5, CRC Press, p. 339.

Nujaim et al. (2018b). *Experimental tests on waste barricades used to retain paste backfill using an innovative experimental set-up*. CIM 2018, Vancouver, Canada, 8p.

Nujaim et al. (2016). "Comportement géomécanique d'une barricade rocheuse et du remblai en pâte cimenté : Essais en laboratoire". Réunion des sciences de la terre RST2016, 25ième édition, Caen, France.

1.5 Methodology

This study is structured along two axes to achieve the objectives of this project: i) experimental tests, and ii) numerical simulations.

1.5.1 Physical modelling

In this part, several tests conducted using a reduced physical model reproduce the backfilling operations of the paste fill (into a stope) that are practiced in some Canadian mines. The paste fill in the stope is supported by a barricade made of crushed waste rock placed in the access of the drift.

The small-scale model was built for qualitatively reproducing underground longitudinal-type stope backfilling in conjunction with the waste rock barricades. For this current study, the small-scale model simulates the backfilling of a typical mine stope in the Abitibi region (Quebec, Canada), with a considered length scale of 1/50 (length-scale factor $L^* = L_{model}/L_{stope} = 1/50$). Figure 1-1 shows the experimental setup of the small-scale model.

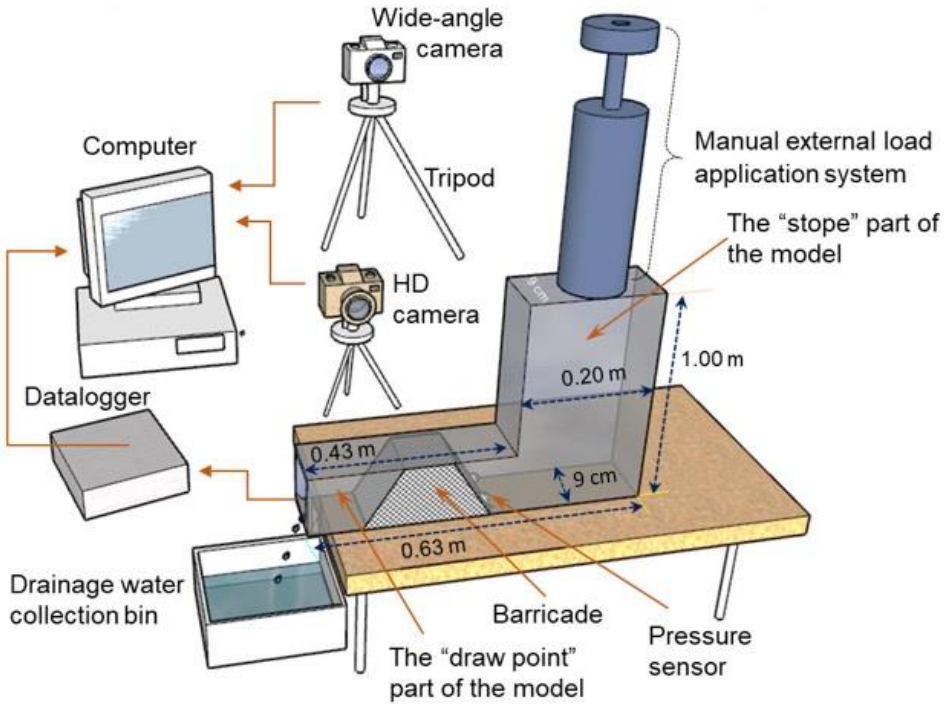


Figure 1-1: Small-scale model with associated metrology.

The stope (or filling chamber) is made of acrylic glass or Plexiglas (PMMA), with a horizontal section of 9 × 20 cm and a height of 38 cm, which can be increased up to 100 cm. The stope is connected to the drift (a section of 9×9 cm and 63 cm of length). The reason for selection of this type of polymer for this study is notably its transparency, which makes it possible to observe the barricade-fill interaction during filling and after the placement of the fill. The backfill pressure in the stope and on the barricade was measured using mini-pressure sensors positioned at different locations. The physical model is equipped with a manual external loading system (piston) to increase the pressure on the barricade until its failure. It should be emphasized that due to cost constraints, the similitude requirements have been lowered, and the scale model will not satisfy the first-order similarity. A high-resolution camera (2048 x 2048 pixels) was used to help analyze the displacement of the barricade and its breaking mechanism. The monitoring of the barricade was only recorded in 2D (through the transparent walls of the gallery), assuming the particles at the core of the barricade have the same behaviour. The method of indirect measurement of displacement using image processing by the digital image correlation method and its basic work is presented in Appendix G. A second camera was also used to capture the manipulations during backfill placement (Fig. 1-1).

In general, physical modelling using small-scale models requires compliance with similarity conditions, including *i)* dynamic equilibrium equations (absolute conditions), *ii)* constitutive law of the material, and *iii)* boundary conditions. The experimental tests on the physical model are performed using the real materials of the prototype ($\rho_m = \rho_p$) (barricade & backfill), under normal gravity ($g^* = 1$) and a length scale factor of 1/50 ($L^* = 1/n$). According to the similarity rules, Young's modulus value (E_m) and the cohesion (c_m) of the material used on the reduced model should be lower (n times) than of the values of the prototype, while the dimensionless parameters [void ratio (e), friction angle (ϕ), interface friction angle (δ), and Poisson's ratio (v)] of the prototype and the reduced model should be identical. The expected displacements values for the actual size of the prototype will equal n times (50) the values measured on the reduced model. In many geotechnical tests on small-scale models, it is necessary to maintain the level of stress ($\sigma^* = 1$). In this case, the tests under normal gravity ($g^* = 1$) require the use of equivalent materials. Consequently, the unit weight of the material used on the reduced model must be n times less that of the prototype or full-scale structure ($\rho_m = 50\rho_p$). The equivalent material should also meet the behaviour rules for the dimensional quantities ($E^* = c^* = 1$) and the dimensionless quantities ($\phi^* = \delta^* = v^* = 1$). It should be noted that compliance with similarity laws is often difficult in many situations involving complex behaviours (see Corté, 1989a). The grain size of the barricade can be respected (e.g., parallel gradation, size scale factor), but the target unit weight is difficult to achieve even with equivalent materials. In addition, similarity rules were not applied to the backfill because its properties are complex, and its behaviour changes over time, from filling to hardening. In short, this type of modelling does not conform to all physical modelling conditions, and scale effects can occur, but it does provide similar scenarios for underground backfilling operations and the failure of hard-to-see barricades in mines. Appendix F provides more details on the rules of similarity and the fundamentals of physical modelling in geotechnical engineering.

The pressure at different points in the model was measured using two types of pressure sensors that ranged in capacity from 35 to 100 kPa, depending on the purpose of the test. Total stresses have been equivalent to the pressures measured by total earth pressure cells (TEP), pore water pressures (PWP) are considered to be equal to those measured by mini-piezometers, and effective stresses are the difference between their values (TEP-PWP). The pressure sensors were calibrated before the test by using water and comparing the measured pressure to the backfill overburden after

placement. Appendix H presents some details about the pressure types and the use of strain gauge for pressure measurement.

Several steps are required to carry out small-scale model testing: (i) implement the model with instruments, materials and validate measurements; (ii) simulate different scenarios by varying the properties and filling sequences; (iii) record the pressures and relative movements of the barricade during backfilling; and iv) varying the size of the barricade particles or the backfilling properties.

A trapezoidal mould was made to form the barricade in the drift from crushed and compacted waste rock. Different grain size distributions were proposed to study the behaviour of the barricade in fine or coarse gradation. The diameter of particles of the barricade ranged from 0mm to 8 mm on the reduced-scale model, assuming these particle diameters vary between 0mm and 400 mm in the full-scale barricade. The two-dimensional digital image correlation method (2D DIC) was used to measure the displacement of the barricade particles and to study the barricade mechanisms of failure.

The calculation of the ingredients (water, binder, and tailings) for the cemented paste backfill (CPB) was performed by estimating the volume of backfill required to fill the scale model stope, the required binder ratio (B_w), and the targeted final solid mass content of the CPB. The design and dosing of the backfill mix were carried out according to several relationships from the mine backfill course (Belem et al., 2018). The physical relations required to design the paste backfill are in appendix B for more details. After the backfill had been prepared using the Hobart laboratory mixer, the backfill mixture was poured into the model in just a few minutes. For some of the tests, it was necessary to increase the pressure using the manual piston until the barricade collapsed to study its failure mechanism. During the test, the cameras recorded the filling operation and the behaviour of the barricade. Chapter 3 includes more details on the small-scale model and the methodology used.

1.5.2 Numerical modelling

Numerical simulations are another common approach to evaluate the stress state of backfilled stopes and to study the effect of different parameters (such as backfill properties, filling rate, and pore water pressures). Several numerical modelling was carried out on underground mines backfilling (e.g., Li et al., 2003; Li et al., 2007; Pirapakaran & Sivakugan, 2007; Hassani et al.,

2008; Li & Aubertin, 2008; Fahey et al., 2009; Li & Aubertin, 2009d, e; Li et al., 2010; El Mkadmi, 2012; Veenstra, 2013; Emad et al., 2014; Falaknaz, 2014; Yang, 2016).

Many different Finite Element software, such as FLAC, PHASES2, FLAC3D, PLAXIS, and SIGMA/W, have been used to evaluate the stress state and verify the results of analytical solutions. The previous authors addressed various aspects to explain the impact of key factors, including stope geometry, drainage (and consolidation), filling rates, arching effect, cementing effect on stress distribution in backfilled stopes, and the evolution of effective stresses during pore water pressure dissipation.

In the second part, numerical (2D) simulations using the GeoStudio2018 (SIGMA/W) software are used to model the interactions between the backfill and the barricade. Simulation results were compared with experimental results obtained on the physical model. Several steps were necessary to complete this part: (i) construct and verify a numerical reference model based on the dimensions of the laboratory scale model, (ii) define material properties and behaviour, and (iii) define boundary conditions. SIGMA/W can execute stress-strain analysis for various types of geotechnical problems and soil-structure interactions in which boundary conditions can change over time. SIGMA/W requires the definition of the water retention curve and hydraulic conductivity function to conduct a coupled analysis (stress-strain and PWP) to study the development of the effective stresses during the dissipation of the pore water pressure. The geotechnical input parameters for numerical simulations depend essentially on the chosen constituent model and the type of analysis. Several studies can be used in order to define the backfill behaviour and its properties (e.g., Aubertin et al., 1996; Belem et al., 2000; Godbout et al., 2004; Fall et al., 2007; Godbout et al., 2007; Pirapakaran, 2008; Veenstra, 2013). The fundamentals of numerical modelling and several constitutive models used in geotechnical engineering are widely discussed in appendix I.

CHAPTER 2 LITERATURE REVIEW

This literature review presents several aspects that cover the different research objectives focused on the uses of mine backfills in mining operations and the main materials of backfills. The typical backfills used to fill the underground voids (stopes), i.e., rockfill, hydraulic fill and paste fill, are reviewed according to their properties (physical, hydraulic, and mechanical).

A brief review of the popular barricades used for retaining backfill in stope is presented with some analytical relations used to size the waste rock barricades. This literature review also presents some in-situ measurement data collected in several mines, several reduced models of mine stopes used to study different objectives, and some numerical simulations conducted to study the stress state in backfilled stopes and drifts.

Several aspects related to cemented paste fill are addressed in separate appendices, such as the main components of the backfill (appendix A), physical relationships (Appendix B), shear strength (Appendix C), the lateral pressure of the backfill (Appendix D), and the self-weight consolidation (Appendix E). For those who wish to read more about these different aspects, they can refer to the appendices at the end of the thesis, which were necessary for the realization of this work.

The use of small-scale models in geotechnical engineering, considering similarity rules and selecting appropriate materials for simulation, is summarized in Appendix F. The physical modelling required monitoring with a high-resolution camera during the tests. The use of image analysis to measure the displacement using the digital image correlation method is discussed in appendix G. The types of pressure and the use of strain gauge transducers in laboratory tests are explained in Appendix H. Finally, the fundamentals of numerical modelling in geotechnics are also presented in Appendix I. This appendix includes some of the constitutive models (laws of behaviours) used in the geotechnical modelling, as well as the main steps required to perform appropriate simulations.

Appendix J includes the paste fill design for underground mine applications (horizontal or vertical stress, development opening through backfill mass, and using the paste fill as a working platform for mining equipment and personnel). This appendix comprises the design of the optimal backfill mix by understanding the different factors that optimize the backfill prior to its transport to the underground.

2.1 Backfill uses in mining operations

Mining aims to extract valuable minerals from ground resources, which usually creates voids. The primary function of mine backfills is to help manage the mining operations that create voids. Backfilling is one of the techniques used to improve the flexibility of ore extraction strategies and mostly allows better recovery of orebodies (Potvin et al., 2005; Belem & Benzaazoua, 2008). The use of various backfill types, their specific functions, and their technical aspects are intimately associated with methods of extraction, extraction strategies, and sequences of the extraction process. In practice, the choice of an exploitation method depends largely on the characteristics of the deposit and the rock mass. Mining methods are divided into surface mining methods (e.g., open-pit mining, strip mining) and underground mining methods (Hartman & Britton, 1992; Darling, 2011). Brady & Brown (1985) proposed to divide mining methods into three main categories, as shown in Figure 2-1.

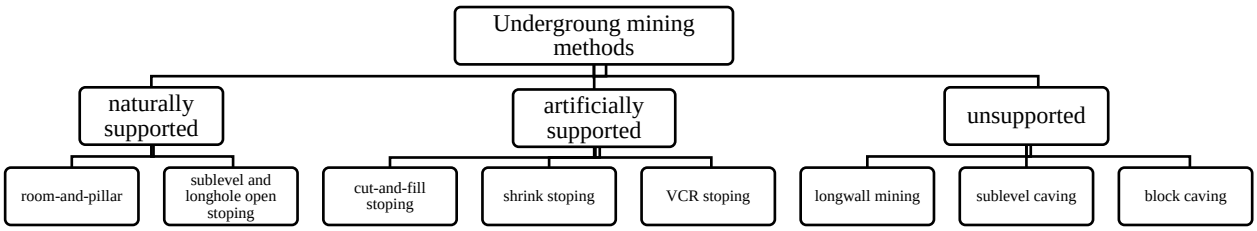


Figure 2-1: Diagram presenting the underground mining methods (from Brady & Brown, 1985).

Underground methods involve the self-supported methods (as vertical crater retreat, vertical crater retreat, sublevel stoping, shrinkage stoping), artificially supported methods (cut-and-fill mining), and unsupported caving methods (longwall mining, sublevel caving, and block caving). Below is a brief explanation of the previous methods:

- *Unsupported (caving) methods*: they allow the ground to collapse under its weight, sometimes reaching the ground surface. These include techniques of block caving in which the orebodies are undercut, inducing the caving of the ore. Unsupported methods also include sublevel caving methods where the hanging wall progressively caves into fill the mined-out voids produced by ore extraction (Fig. 2-2). Caving methods do not require backfilling, as the mine voids are filled with caved country rock (Potvin et al., 2005).

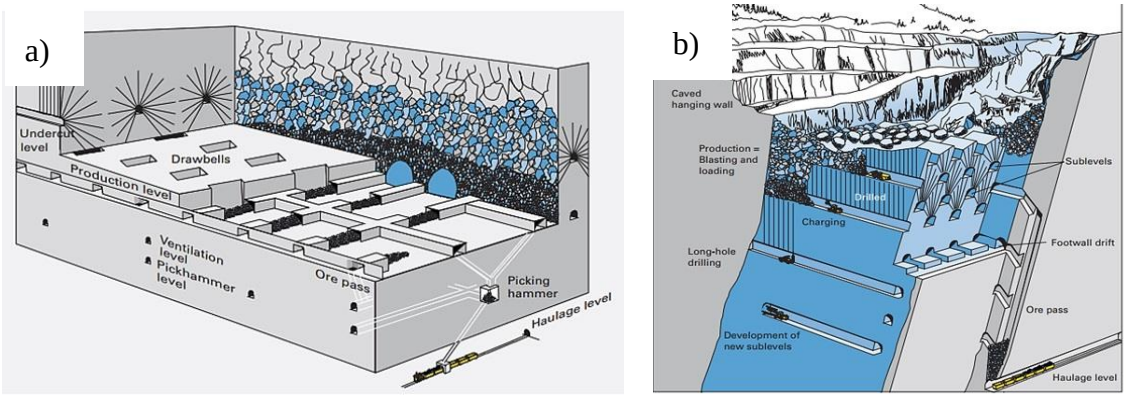


Figure 2-2: Unsupported mining methods: a) block caving; b) sublevel caving (taken from Copco, 2007).

- *Naturally supported methods*: pillars are left (lost in most cases) to stabilize the rock walls or to control the stability of the extracted areas (voids). Generally, this process results in less gold being extracted and is often used for low-grade deposits where higher mineral recovery does not justify the cost of backfilling. This includes the method of room-and-pillar, but in some cases, it is necessary to recover the ore pillars; this involves placing cemented or uncemented fill between the pillars up to the back of a room. In general, backfilling is less efficient in the extraction of shallow dipping ores since backfill transport by gravity is less feasible (Potvin et al., 2005). Shrinkage and some variation of open stope mining can also rely on naturally supported methods, using crown and rib pillars to separate stopping blocks (Fig. 2-3).

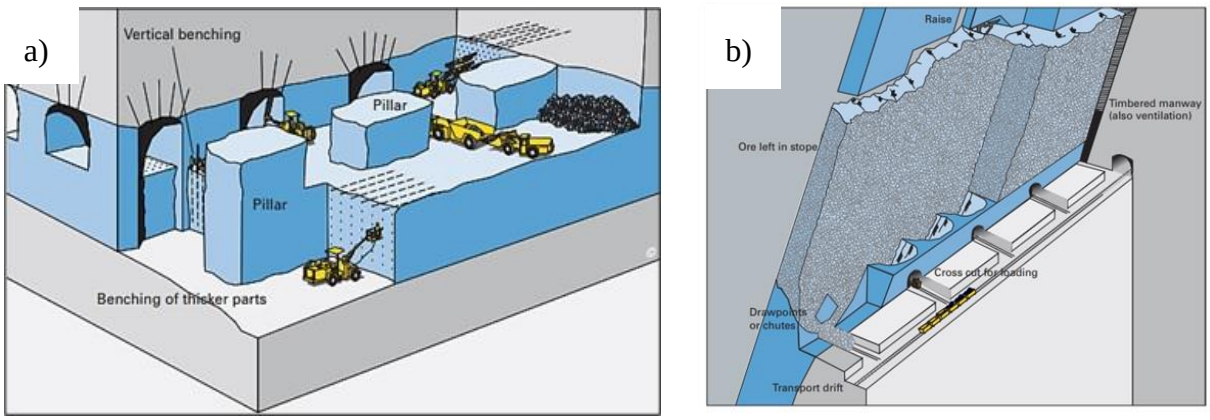


Figure 2-3: Naturally supported methods: a) room-and-pillar method; b) Shrinkage stoping method (from Copco, 2007).

- *Artificially supported methods*: the backfill is used (often in combination with temporary or/and permanent pillars) to control rock wall stability and limit voids exposure so as not to exceed critical stable dimensions (Brady & Brown, 1985; Potvin et al., 2005). This includes a variation of cut-and-fill and open stope mining methods. As underground mining approaches deeper stages, stable void exposure becomes smaller, and reliance on an effective method of fill distribution (delivery system) is emphasized. Mine fill generally applies to artificially supported strategies. If the rock mass and ore conditions do not allow large stopes to be created, the mined-out voids must be filled at the same time as the extraction. Generally, the voids are filled with cemented or uncemented fill that serves as a working floor (platform) or roof for subsequent extraction and stabilizes the rock mass as well. As part of these methods, a wide range of filling applications have been used to meet various engineering objectives. Potvin et al. (2005) summarised the main function of fill in artificially supported mining methods as following:

  i) *Waste disposal:* filling of the underground voids (stopes) reduces the amount of mine waste disposal on the surface and can be an ecological and responsible solution to manage the mine waste.

  ii) *Ensuring long-term regional stability:* the stability of underground excavation is controlled by several variables (e.g., spam, time, and ground conditions). Over time, the risk of collapse increases in open excavations, as many cases have been documented when filling was not used, and crown pillars failed. After excavation, the backfill occupies the mining voids, which in turn reduces the risk of instability. It prevents the opening of joint discontinuities, increases the friction along the weak planes. Consequently, the propagation of the rupture is stopped with mobilization of the shear strength of the rock mass. The bulk filling also helps to reduce the convergence of walls, which will have a positive effect on the mine's regional stability.

  iii) *Limiting excavation exposure:* using cemented fill to reduce voids can lead to highly productive and flexible extraction sequences, particularly when large deposits of reasonable quality are mined. Ore deposits may be divided into stopes, while others can be mined simultaneously (Fig.2-4). There may be another series of stopes in pre-production (drilling) and another series in post-production (filling).

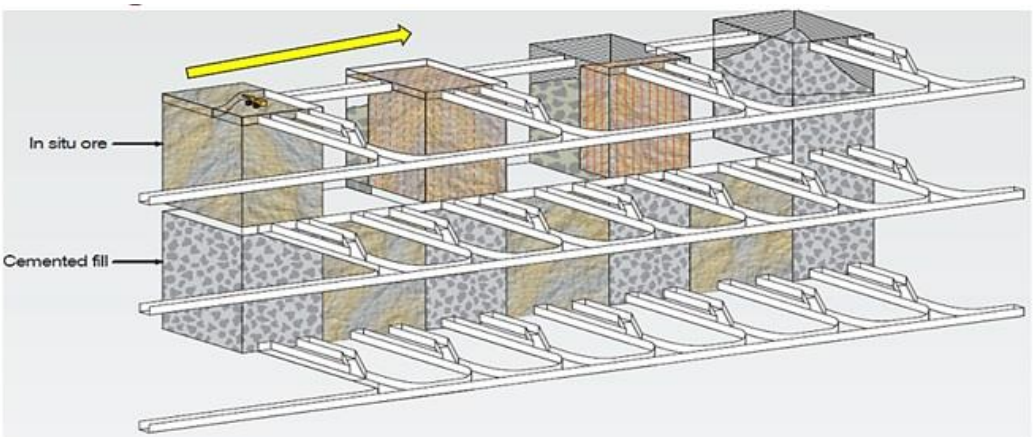


Figure 2-4: 3D isometric view of open stope mining (from Potvin et al., 2005).

2.2 Types of mine backfills

As explained above, safety and environmental factors have led mining companies to consider backfilling mine wastes to prevent the mine from collapse during later and deeper mining phases, ground subsidence during mine abandonment, and environmental pollution. Mine waste surface disposal (i.e. waste rock and tailings) can be minimized by backfilling, which can help prevent acid mine drainage generation (Aubertin et al., 2002; Bussiere, 2007; Belem et al., 2000; Benzaazoua et al., 2004; Belem & Benzaazoua, 2008).

Underground extraction of economic minerals creates voids of various shapes (termed stopes). These voids create risks of instability for the mining of adjacent pillars that contain beneficial minerals. Underground voids also pose the risk of infrastructure subsidence on the ground during development or after the abandonment of mines. During the history of mining technology, various techniques have been developed to fill underground cavities. Common practical methods for waste disposal are rock backfill, hydraulic backfill, and cemented paste backfill. The implementation of any such approach depends on financial considerations and other goals, such as mining development or abandonment.

2.2.1 Rockfill

Rockfill (RF) consists of waste rock from mining development or surface quarry (e.g., Yu, 1989& Dismuke & Diment, 1996; Farsangi, 1997; Potvin et al., 2005). A truck or a conveyor transports RF to fill underground stopes. Rockfill acts as a working floor (when side and base exposures are

not required) and provides ground stability and active support when exposed during the extraction of adjacent stopes (Hassani & Archibald, 1998; Liston, 2014).

Cemented Rockfill (CRF) is mixed with binders, which can be Portland cement, slag, and fly ash, with a percentage ranging from 1% to 8% (solid weight). The RF can also be modified by optimizing the grain size (such as grinding or adding fine-grain materials) depending on its applications (Hassani & Archibald, 1998; Kuganathan, 2005b).

2.2.1.1 Physical properties of rockfill

It is not easy to obtain an accurate particle size distribution of waste rock in piles where heterogeneity, segregation, and the presence of large rocks make measurement difficult (Maknoon, 2016). Various methods can be used to estimate the particle size distribution, such as sampling and laboratory measurements, in situ determination, and image analysis of photographs (McLemore et al., 2009). Typical waste rock shows a wide gradation curve (from silt to boulders size) with a coefficient of uniformity ($CU = D_{60}/D_{10}$) of 20 or more (Barbour et al., 2001; Aubertin et al., 2002). Maknoon (2016) collected different grain size distributions of waste rock (measured in the laboratory or in situ). The distributions showed that the size of particles ranged from 75 µm to about 10 cm and above (Fig. 2-5). The typical angle of repose of waste rock is near 37° (± 3°), which may differ with the physical characteristics of the waste rock (Farsangi, 1997; Aubertin, 2013).

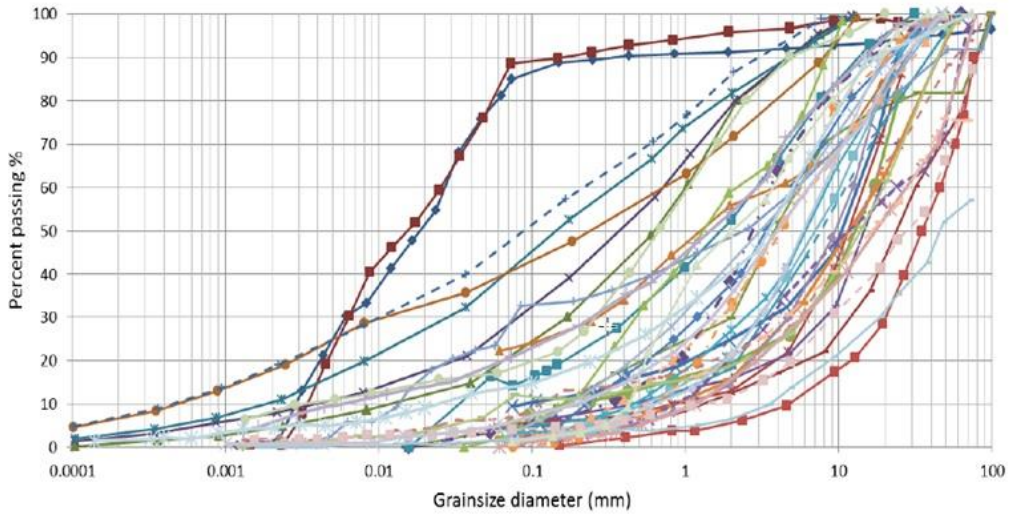


Figure 2-5: Grain size distribution curves of waste rock (from Maknoon, 2016).

The Talbot grading has been adopted to design the optimal particle size distribution for RF, which gives the maximum in-situ density (Kuganathan, 2005b). The typical RF particle size used can vary from 1 to 100 mm and should be optimized to minimize the void ratio and maximize the density in situ. Thus, the addition of binder and/or fine-grained materials increases the strength of the filling which can be associated with a decrease in the final void ratio (or porosity). However, RF optimization remains difficult, and the particle size distribution varies from one operation to another. Segregation usually occurs during the RF filling operation when the RF is placed in a stope by trucks or raises (Hassani & Archibald, 1998; Potvin et al., 2005; Belem et al., 2018). Different factors produce RF with different layers, such as ejection velocity, the trajectory of movement, and settlement effects between coarse and fine aggregates. The degree of segregation varies depending on the filling method, elevation height and length, aggregate size, stope geometry, and free-fall height (Yu, 1989; Annor, 1999; Belem et al., 2018).

2.2.1.2 Mechanical properties of rockfill

The angle of friction of the uncemented rockfill material can vary from 35° to 55°, depending on the relative density (Kuganathan, 2005b). Large-scale tests indicated that the internal friction angle of the waste rock is between 21° and 62°, with typical values ranging from 34° to 45° (Aubertin, 2013).

It is of critical importance that the waste-rock material modulus is carefully and effectively analyzed in underground backfill mining. Zhang et al. (2019) conducted a series of laboratory-based compression tests on waste-rock samples in the Tangshan coal mine (China) and compared the results to field tests and numerical modelling using FLAC. They stated that waste material used in underground backfill mining has a granular texture and, when compressed, acquires non-linear deformation characteristics (Fig. 2-6). They also reported that the deformation modulus of waste rock determined by a laboratory compression test differs significantly from the real deformation modulus in the field due to the full confining impact of the loading steel cylinder. The waste rock deformation modulus exponentially increased with an increase in axial strain. The exponential equation to fit the relationship between the deformation modulus and the strain in the field as follows:

$$E = 3.6915e^{18.94\varepsilon} \tag{2-1}$$

It has been stated (by Lee et al., 2009) that the stress-strain behaviour of crushed rock is nonlinear, inelastic, and stress-dependent during large-scale direct shear tests. The stress-strain characteristics of crushed waste-rock material are generally dependent on the grain size, gradation, degree of saturation, uniformity, breakage, etc.

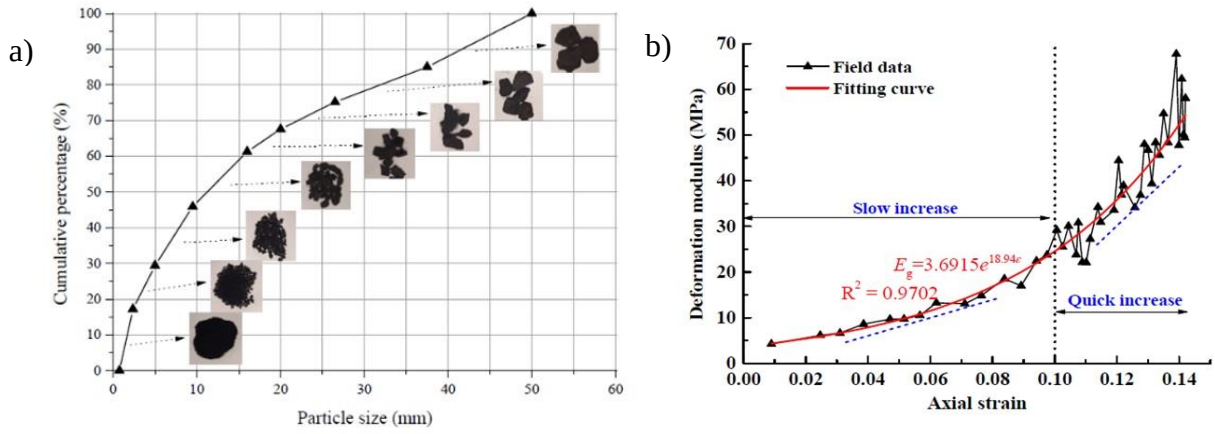


Figure 2-6: a) Size distribution of waste-rock particles in the Tangshan coal mine (China); b) the deformation modulus and axial stress vs. axial strain of the waste-rock (Zhang et al., 2019).

Generally, the fill elasticity modulus increases with the content of the binder (Pierce et al., 1998). The elastic modulus of cemented rockfill varies between 2.0 and 3.8 GPa according to some in-situ and laboratory tests (Yu & Counter, 1983). Usually, the cemented rockfill elastic modulus is much higher than that of cemented hydraulic fill and paste fill (Zhu, 2002).

The unconfined compressive strength (UCS) of RF is close to zero because it is a non-cohesive material, and it can be much higher with the addition of binders and fine-grained materials. The in-situ UCS of CRF can range from less than 1 MPa to more than 10 MPa (Hedley, 1995; Annor, 1999).

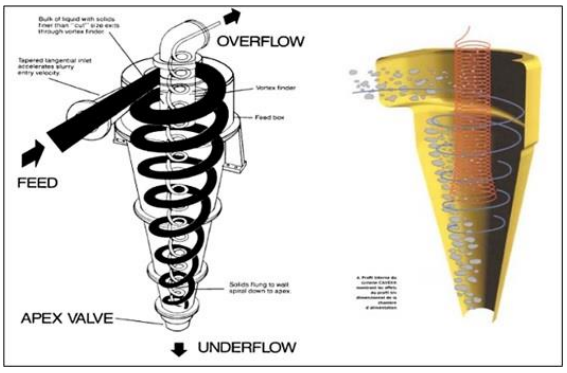
2.2.1.3 Hydraulic properties of rockfill

The hydraulic conductivity represents the average velocity when water flows through the fill mass under constant hydraulic gradient. It is affected by particle size distribution, particle shape, void ratio, and so on (Potvin et al. 2005). Infiltration tests on the waste rock pile at Tio mine showed that the hydraulic conductivity ranges from 4×10^{-5} to 3×10^{-3} m/s (Lessard, 2011).

2.2.2 Hydraulic fill

Hydraulic fill (HF) consists of classified mill tailings and/or natural sand and contains a large amount of water that drains after placement. HF is slurry, with low solids content ($C_{w\text{-}f}$ = 60% to 75%), transported to underground stopes through boreholes and pipelines (Hassani & Archibald, 1998; Potvin et al., 2005). It is usually prepared with about 70% of solid content for traditional transport (Hassani & Archibald, 1998; Grice, 2001). A portion of the fine materials is eliminated, usually by hydrocyclone (Fig. 2-7a), to avoid inadequate drainage (particle size ≤ 10 µm does not exceed 10%). Below, the figure 2-7b represents a typical particle size spindle of tailings that can be used for the hydraulic fill preparation. Normally, the particle size of HF varies from 1 to 1000 µm (with an average of around 100 µm). The principal advantage of hydraulic backfill is its simplicity and low cost of production and delivery (Pirapakaran & Sivakugan, 2007)

a)



b)

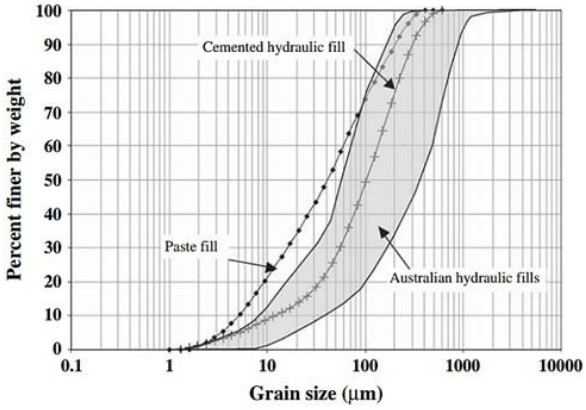


Figure 2-7: a) Hydrocyclone used to remove part of the fine material of the tailings (from Belem et al., 2018); b) Typical grain size distribution curves for hydraulic fills, cemented hydraulic fills, and paste fills in Australia (from Sivakugan et al., 2006b).

2.2.2.1 Physical properties of hydraulic fill

Rankine (2005) indicated that the HF relative density could change from 2.8 to 4.5, and the density index (I_D) between 50% and 80%. The settled fill porosity (n) varies from 0.37 to 0.48, and the void ratio (e) of 0.58 to 0.93.

The uniformity coefficient ($C_U = D_{60}/D_{10}$) is usually used to describe the spread of the particle size distribution. Bussiere (2007) reported that the C_U of full-tailings samples can range from 8 to

18. For HF, C_U normally varies between 5 and 10 (Kuganathan, 2005a), pointing to a relatively narrow spread.

Segregation can happen within the HF, where fine particles (including binders) can be driven by water flow and concentrated in layers, resulting in a heterogeneous mass (anisotropy) with strength zoning (Belem et al., 2018).

2.2.2.2 Hydraulic properties of hydraulic fill

The laboratory tests are used to measure HF's hydraulic conductivity. The constant head infiltration test is commonly used with coarse-grained materials. The falling head infiltration test is also used for relatively low permeability fills (Rankine, 2005). Figure 2-8 shows a set up used for the constant head permeability test. The sample is subjected to a constant water head (the difference between its ends). The water flow rate through the sample of fill is measured. The constant head permeability of the fill is given by:

$$k = \frac{aL}{At} \ln \frac{h_0}{h_1} \tag{2-2}$$

Where k = coefficient of permeability; a = area of the burette; L = length of fill sample; A = area of the fill sample; h_0 = initial height of water; h_1 = final height of water = h0 – Δh; t = time required getting head drop of Δh.

High permeability is important for slurry backfill to achieve rapid drainage and self-weight consolidation and to prevent the potentially dangerous build-up of hydrostatic pressure in underground stopes (Sveinson, 1999). The in-situ hydraulic conductivity of uncemented HF usually ranges from 10^{-6} to 10^{-5} m/s (Grice, 2001). Rankine (2005) reported that the hydraulic conductivity of Australian hydraulic fills typically ranges from 2.78 $\times 10^{-6}$ to 8.33 $\times 10^{-6}$ m/s. Alternatively, some functions, based on the Kozeny-Carman equation for granular materials, can be used to predict the hydraulic conductivity of HF indirectly from grain size curves (Aubertin et al., 1996; Mbonimpa et al., 2002; Chapuis & Aubertin, 2003).

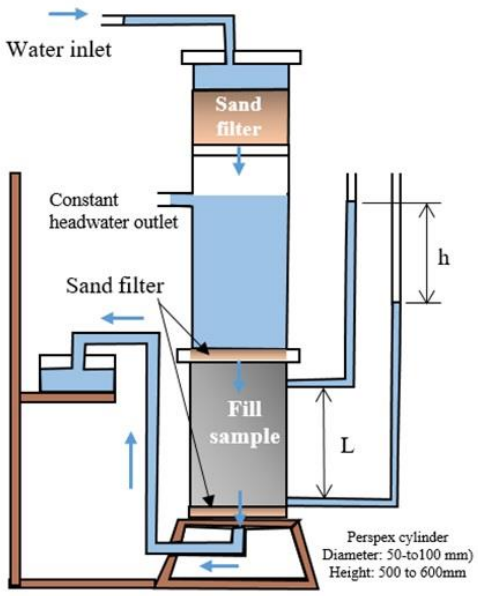


Figure 2-8: A permeameter for mine backfill application (adapted from Potvin et al., 2005).

2.2.2.3 Mechanical properties of hydraulic fill

Usually, the friction angle of uncemented HF ranges from 35° to 37°, and some cemented hydraulic fills (CHF) range from about 30° to 48° (Askew et al., 1978; Bloss, 1992). CHF's cohesion is closely associated with several factors (e.g., binder type, binder content, and curing time). Askew et al. (1978) stated that CHF's cohesion could rise from 0.1 MPa to 1.5 MPa as the cement content rises from 3 to 17% for a curing time of 112 days. A value of 150 MPa for CHF elastic modulus was reported (Leahy & Cowling, 1978). Furthermore, UCS of the hydraulic fill is positively related to the binder content based on the test results for several mines. Also, CHF's mechanical properties are primarily affected by segregation, erosion piping, arching effect, etc. The mechanism of erosion piping is reported in Cowling et al. (1988), Grice (1989), Bloss & Chen (1998), and Potvin et al. (2005).

2.2.3 Cemented paste fill

As the tailings become gradually finer through better recovery at the processing plants, the disposal of these finer tailings as hydraulic backfill is quite limited. Cemented paste backfill (CPB) was developed to solve this problem by using the entire tailings as mine backfill (Potvin et al., 2005; Belem et al., 2018). The initial use of paste backfills at the Grund mine in Germany in the 1980s

then grew rapidly and spread around the world. CPB is a high-density (75-85% solids content) mixture of tailings, binders (Portland cement, slag, fly ash, gypsum, etc.) and water and must contain adequate fines to achieve a viscous paste behaviour (Hassani & Archibald, 1998). Appendix A provides an extensive review of the main components of backfill.

2.2.3.1 Physical properties of CPB

Figure 2-9 presents the particle size distribution (particle size ranges from 1-1000 µm) for typical copper tailings (curve A), cyclone underflow (HF, curve B), and the cyclone overflow (slimes).

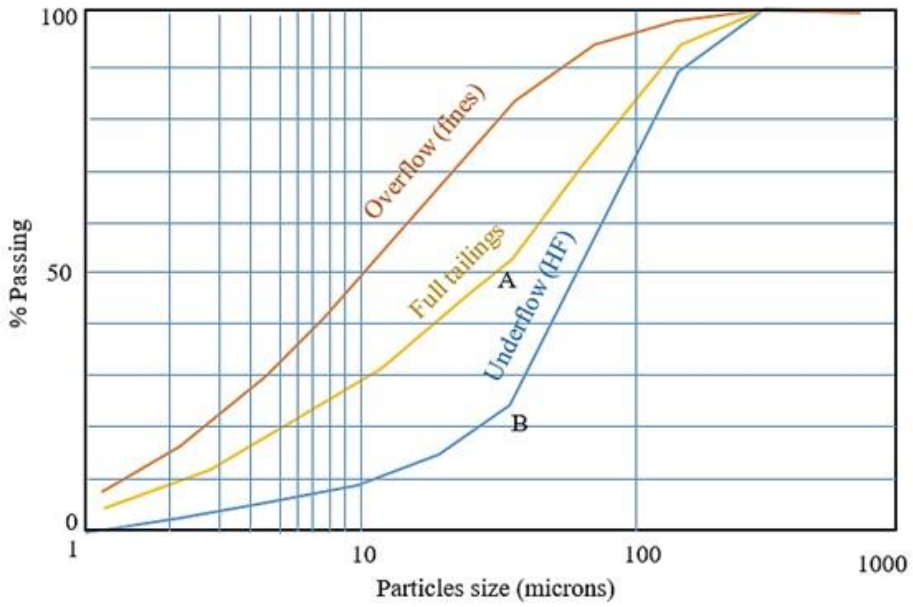


Figure 2-9: Particle size distribution of full tailings, hydraulic fill, and slimes (adapted from Potvin et al., 2005).

Kuganathan (2005) reported that the CPB has a uniformity coefficient (C_U) ranging from 10 to more than 20 in some cases, indicating widespread and well-graded material due to the use of full tailings. The fines (≤ 20 µm) in CPB should be not less than 15% (by weight) to obtain sufficient viscosity (Brackebusch, 1994; Potvin et al. 2005). The slump test is usually used to measure the workability of concrete, but it has also been adapted to control the consistency of paste in the mining industry (Clayton et al., 2003; Belem & Benzaazoua, 2008). The CPB should typically have a slump of less than 230 mm to behave like a non-Newtonian fluid (Potvin et al., 2005). Empirical

correlations between the slump and yield strength were established to quickly assess the rheological properties of the CPB (Belem & Benzaazoua, 2008).

2.2.3.2 Rheological properties of CPB

CPB transportation (Fig. 2-10) is mainly controlled by its rheological properties. Similar to fresh concrete, CPB is classified as a Bingham plastic fluid (Boger et al., 2006; Potvin et al. 2005).

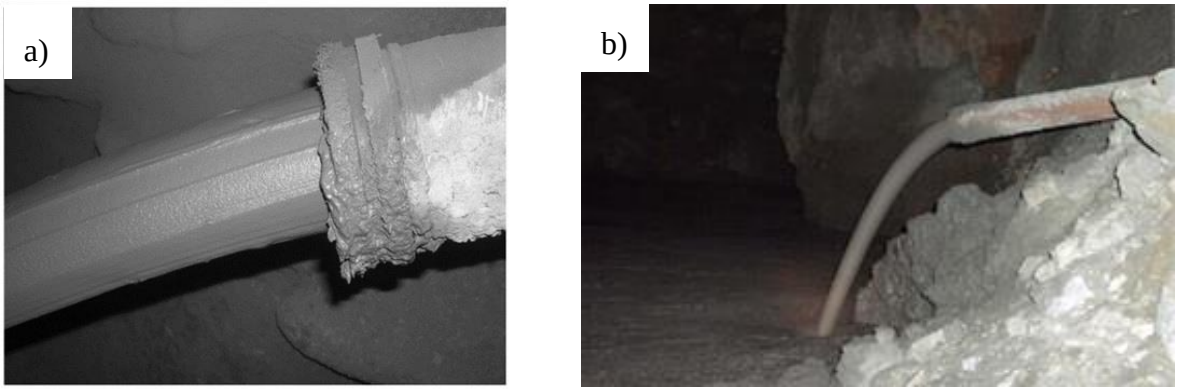


Figure 2-10: a) paste fill being deposited into a stope via a pipeline (from Sivakugan et al., 2015); b) a stope underfilling with CPB (Belem et al., 2018).

For such type of fluid, it has an elastic behaviour when the applied shear stress is lower than its yield shear stress, and the deformation is reversible. Once the applied shear stress exceeds the yield shear stress, the CPB starts to flow at a constant (or variable) viscosity. The yield shear stress is the minimum shear stress required to initiate paste flow. It is a key parameter for CPB and tailings transportation design. Generally, the yield shear stress of CPB is affected by several factors such as the solids content, water content, content and type of binder, stage of hydration, and pore fluid chemistry (Sofra & Boger, 2001; Simon & Grabinsky, 2013; Belem et al., 2018).

Certain relationships are correlated between yield stress and solids content to predict pumping energy requirements in pipeline transportation. (Sofra & Boger, 2001). The common methods used to measure the rheological parameters of the CPB are the slump test (e.g., Pashias et al., 1996; Clayton et al., 2003; Boger et al., 2006) and vane tests (e.g., Simon & Grabinsky, 2013). Usually, the yield stress (η_0) ranges from 100 to 800 Pa (Boger et al., 2006; Cooke, 2006). Other studies (e.g., Saebimoghaddam, 2005) indicated that the yield shear stress of CPB could reach up to 1100 Pa and 1250 Pa, respectively.

2.2.3.3 Hydraulic properties of CPB

Due to a large amount of fines materials in the CPB (full tailings), the hydraulic conductivity is much lower than that of the HF tailings (a hydrocyclone is usually used to remove part of the fines). The hydraulic conductivity of homogenous hard rock tailings and CPB typically ranges from 10^{-8} to 10^{-6} m/s (Aubertin et al., 1996; Bussiere, 2007; Godbout et al., 2007; Fall et al., 2009).

Usually, the falling head infiltration test is used to specifically measure the hydraulic conductivity of materials such as CPB. The results of some laboratory tests demonstrated that the hydraulic conductivity of the CPB is greatly influenced by several factors such as binder type/proportion, water-to-cement ratio, fineness of the tailings, sulphate content, curing time and temperature, stress level, and mechanical damage (Godbout et al., 2007; Fall et al., 2009). A higher binder content and longer curing time can lead to a further reduction in hydraulic conductivity (Belem et al., 2001).

Godbout et al. (2007) reported that the hydraulic conductivity of the uncemented paste backfill remains practically constant up to 28 days. Their results also showed that a backfill containing 80% Portland cement mixed with 20% slag resulted in a greater decrease in hydraulic conductivity compared to a backfill containing 70% Portland cement mixed with 30% fly ash. Godbout et al. (2007) and Fall et al. (2009) stated that the largest decrease of the CPB's hydraulic conductivity was observed at the early ages of curing (0-7 days). Figure 2-11 shows the effect of the type of binder on the evolution of hydraulic conductivity as a function of curing time.

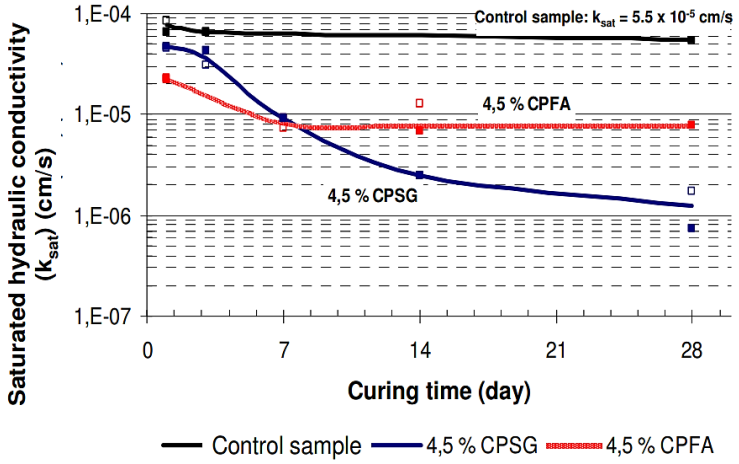


Figure 2-11: Evolution of hydraulic conductivity as a function of curing time for cemented paste backfill with different types of binders (from Godbout et al., 2007).

CPB has very low permeability and behaves as a material between silt and clay. The drainage and consolidation phase of the CPB takes a long time, so there is less water bleeding in backfilled stopes.

2.2.3.4 Mechanical properties of CPB

Experimental results indicated that under uniaxial compression (Appendix C for more details), the CPB exhibits elastoplasticity with strain-softening behaviour (Klein & Simon, 2006). Belem et al. (2000) demonstrated that the UCS of the CPB increases as the binder content increases and that the proportion of paste mixture plays a major role in the mechanical properties. The elastic modulus of the backfill increases with the binder content (Fig. 2-12).

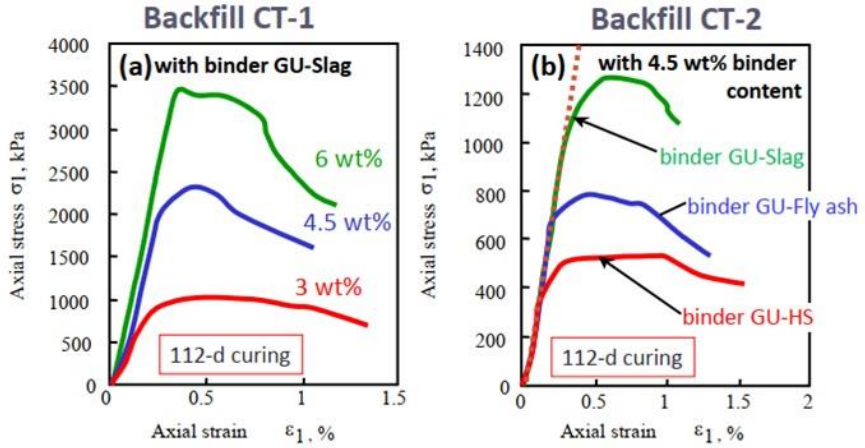


Figure 2-12: Unconfined compressive stress-strain curves of CPB after 112 days of curing for different (a) binder contents and (b) types of binder (from Belem et al., 2000).

Leahy & Cowling (1978) reported a modulus of elasticity of 280 MPa for CPB. In situ tests (Barrett & Cowling, 1980) showed that the modulus of elasticity of the CPB reached 695 MPa. Laboratory experiments performed with hydration cells showed that stress conditions and temperature during the curing have a substantial effect on the mechanical behaviour of CPB (Helinski et al., 2007; Walske et al., 2015). Walske et al. (2015) stated that with high curing temperature and effective stress generation, the strength of the CPB increases.

More information on the components of the mine backfill is summarized in Appendix A at the end of the thesis. The physical and mechanical characteristics of the backfill (calculations or measurements) have been placed in appendices B and C, respectively. Also, the concept of lateral earth pressure and backfill consolidation are demonstrated in appendices D and E, respectively.

2.2.4 Summary of backfill properties

Table 2-1 summarizes the main characteristics and behaviours of mine backfills.

Table 2-1: typical backfills in mine stopes (from Hassani & Archibald 1998)

Properties	Hydraulic fill	Pate fill	Rockfill
Placement state	60% to 70% solid (by weight)	70% to 85% solid (by weight)	Dry
Underground support system	Borehole/Pipeline via gravity	Borehole/Pipeline via gravity, can be pumped	Raise, mobile equipment, separate cement system
Binder application	Cemented or uncemented	Cemented only	Cemented or uncemented
Water and cement ratio (w/c)	High w/c ratio, low binder strength	Low to high w/c ratio, Low to high binder strength	Low w/c ratio, high binder strength
Placement rate	100 to 200 tonne/hr	50 to 200 tonne/hr	100 to 400 tonne/hr
Segregation	Slurry settlement and segregation, low strength development	No segregation	Stockpile and placement segregation, reduced strength and stiffness
Stiffness	Low stiffness	Low or high stiffness	High stiffness if placed correctly
Tight filling	Cannot tight fill	Easy to tight fill	Difficult to tight fill
Binder quantity	Require a large quantity of binder	Usually, a lower quantity of binder required	Moderate binder quantities
Barricades	Expensive	Inexpensive	Not necessary
Water runoff	Excessive water runoff	Negligible water runoff	No water runoff
Capital costs	Low capital costs	Higher than for hydraulic fill	Moderate capital costs
Operating costs	Low distributions costs, lower cost for an uncemented fill	Lowest cost for a cemented fill	High operating costs

2.3 Design and construction of fill barricades

2.3.1 Types of barricade

Usually, the terms barricades and bulkheads are used interchangeably. Grice (1998) proposed that hydraulic fill walls be called barricades to indicate low loading and porous structures. Bulkheads would cover all high-pressure non-draining structures. Barriers are installed in the entrance drifts near drawpoints to hold initially saturated fills (hydraulic and pasty fills). Usually, the hydraulic conductivity of the barricade should be larger than that of the fill to ensure good drainage (Potvin et al., 2005; Yang, 2016).

In various mining districts, several different design barricades have evolved. A list of parietals includes (see Potvin et al., 2005):

- *Arched impermeable concrete masonry blockwork (up to 1m thick over spans of 4m x 4m with sealing grout, hatchways, and drainage pipes);*
- *Arched porous concrete block walls (up to 0.39m thick over spans of 6.5m wide by 5.5m high);*
- *Planar impermeable reinforced fibrecrete walls (up to 0.5m thick over spans of 6.5m wide and 5.5m high);*
- *Planar porous concrete block walls (up to 0.46m thick over a span of 4m x 4m),*
- *Arched impermeable reinforced fibrecrete walls (up to 0.5m thick over spans of 6.5m wide and 5.5m high);*
- *Timber and permeable barricades,*
- *Prefabricated steel and mesh formwork with geotextile woven, to form a frame onto which fibrecrete is sprayed, with permeable drainage windows (holey fences), and*
- *Waste-rock barricades with very limited use with very low lift height in some cut-and-fill operations.*

To satisfy the functional requirement, there are several technological or engineering solutions; choosing one over the other might occur due to local skills, contract materials, and economics. Figure 2-13 is a photograph of various types of barricades.

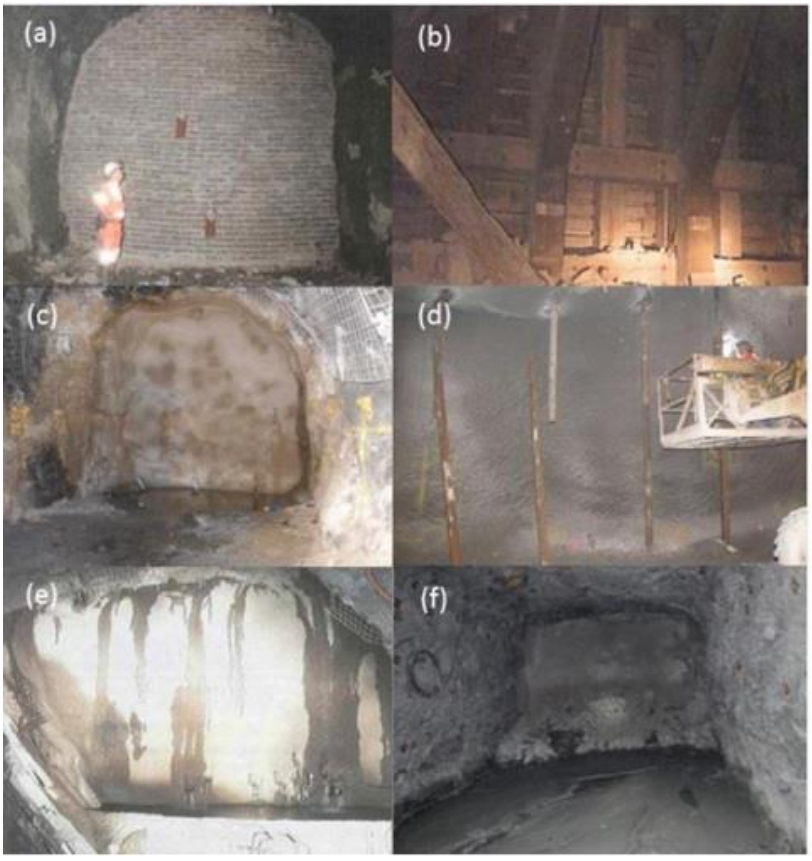


Figure 2-13: Typical barricades formed from: (a) arched permeable brick wall ; (b) timber; (c) concrete; (d) shotcrete; (e) fibrecrete; (f) waste rock (from Yang, 2016).

Several issues must be considered in the design and construction of hydraulic fill barricades (see Potvin et al., 2005; Belem et al., 2018), including the followings:

- The opening dimensions and shape: there is a growing trend towards larger openings for large mining machinery, but strong structures are easier to build in small openings.
- Barricade position from the brow of the stope: Mitchel et al. (1975) and Kuganathan (2002) showed higher loading conditions for barricades built closer to the brow. Both papers show that a long distance from the brow decreases the drainage.
- The design phase of the built wall should consider the magnitude and direction of the expected loading conditions and the wall capacity to transmit such stresses around the rock interface. The rock conditions on the barricade interface will have a significant impact on the wall capacity.

- The quality of the materials, the construction methods, the skills, and the expertise of the workers contribute to the stability of the barricades.
- For secure barricade design, the engineers must consider the period between the completion of the wall construction and the start of the deposition as well as the actual capacity of the wall at the time. The filling loads applied to the barricade must be less than the design strength.
- The excess transport water supplied with the hydraulic fill must be able to drain freely from the fill and stope. Maximizing the density of slurry placement and removing flushing water to the stope would reduce the excess water.

2.3.2 Construction of waste rock barricades

The design of rock waste barricades to retain fresh paste backfill columns must be done rigorously. As these studies are carried out on waste rock barricades, the stages of their construction are explained only among other types, but few data are available to describe their characteristics. Figure 2-14 simply shows the stages of the construction of the barricades at Laronde mine (Gélinas, 2017), which includes the following steps:

- The bulldozer is used to form a pile of wastes rock with a height of up to 3.5 m.
- To close the remaining space between the rock pile and the roof of the drift, a push-plate is installed at the front of the bulldozer to lift the material to the top (about 4.5 m).
- Pushing the waste rock upwards to fill the space between the drift roof and the pile requires the expertise of the operator responsible for the construction of the barricade.
- The waste rock continues to be pushed with a compacting procedure until the front part of the barricade is completed.
- Once the front part is built, the barricade dimensions are determined (usually the length at the top is 3.5 m), then the remaining part of the barricade is finished with the required dimensions.
- Once the construction of the barricade is completed, a layer of shotcrete is sprayed in the downstream part to close the gaps and prevent the collapse of the barricade.

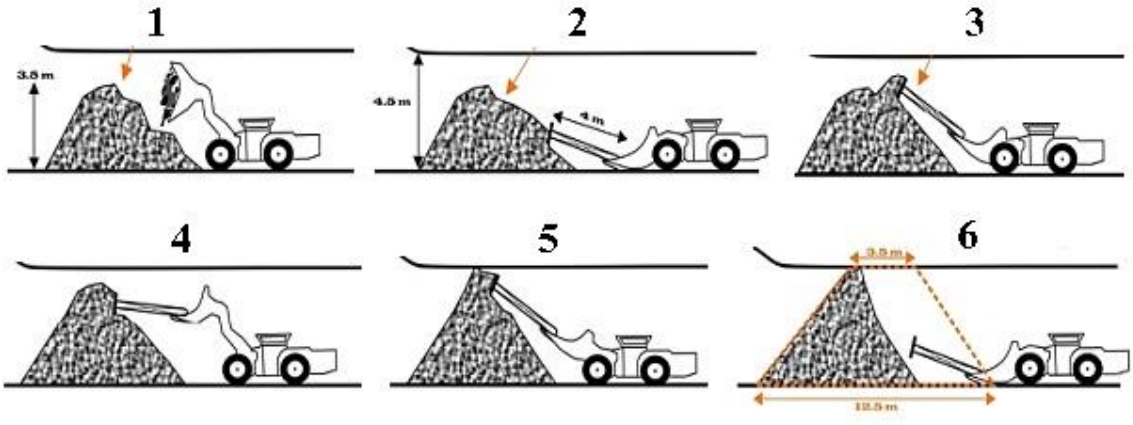


Figure 2-14: Construction stages of the waste rock barricade (from Gélinas, 2017).

2.3.2.1 Analytical solutions for estimating backfill pressures on barricades

The load on a barricade is determined by the pressure of the backfill in the stope and drift. The capacity of the barricade (strength) depends on the material, shape, size, and construction. Mitchell et al. (1975) proposed a simple relation based on the overburden pressure without considering the arching effect to calculate the load on a barricade:

$$F_h = \frac{1}{2}\gamma_f H^2 L_d K_0 \tag{2-3}$$

Where F_h (m) is the horizontal load applied on the barricade; γ_f (kN/m^3) is the unit weight of the backfill; H (m) is the total fill height in the stope; L_d (m) is the drift width; and K_0 is the at-rest reaction coefficient.

Smith & Mitchell (1982) and Mitchell & Roettger (1984) gave an empirical solution considering the arching effect to estimate the horizontal stress σ_h(kPa) on a barricade located at a distance l (m) from the brow:

$$\sigma_h = 0.4\gamma_f H\left(1 - 0.6\frac{l}{L_d}\right) \tag{2-4}$$

This solution supposes that the horizontal stress increases linearly with stope backfill height H (m). Mitchell et al. (1982) and Mitchell (1983) regarded the limit equilibrium of a 3D wedge of backfill (Fig. 2-15). The horizontal load on the barricade is given by:

$$F_h = \frac{[P_0 + L_s(H_d - L_s \tan\alpha/2)(\gamma_f W_d - 2C_b)](\sin\alpha - \cos\alpha \tan\emptyset) - cW_d L_s/\cos\alpha}{\sin\alpha \tan\emptyset + \cos\alpha} \quad (2\text{-}5)$$

Where L_s (m) is the stope length; H_d (m) is the drift height; W_d (m) is the drift width; w (m) is the weight of the wedge; P_0 (kN) is the surcharge above backfill; N (kN) and T (kN) are the normal and shear forces along the sliding plane; C_b (kPa) is the cohesion between the fill and walls; F_h (kN) is the force of a smooth barricade to maintain wedge equilibrium.

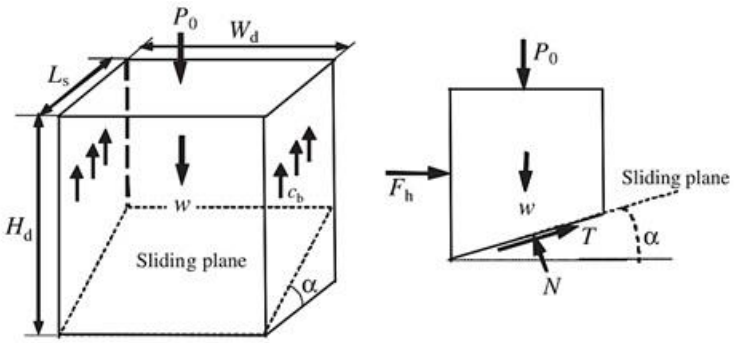


Figure 2-15: Wedge model of Mitchell et al. (1982) (Modified by Li & Aubertin 2009c)

Another solution (see Kuganathan, 2002) is proposed to estimate the horizontal stress σ_h in the drift onto the barricade given by:

$$\sigma_h = \sigma_0 \, exp\left(-\frac{PK_0 \tan\emptyset}{A} l\right) \quad (2\text{-}6)$$

Where σ_0 is the horizontal stress at the drawpoint obtained from Terzaghi's arching theory; P is the perimeter of the drift; A is the cross-section of the barricade.

Li & Aubertin (2009) proposed a 3D analytical solution for fully drained conditions (Fig. 2-16), which is given by:

$$\sigma_h = \left[\frac{h}{H_d}\sigma_{hT0} + \left(1 - \frac{h}{H_d}\right)\sigma_{hB0}\right] exp\left[-l\frac{2\tan\delta}{K_{dl}}\left(\frac{1}{H_d} + \frac{K_{dt}}{W_d}\right)\right] \quad (2\text{-}7)$$

Where the earth pressure coefficients K_{dl} or K_{dt} is the ratio of the horizontal stress in the longitudinal or transverse direction over the vertical stress, respectively.

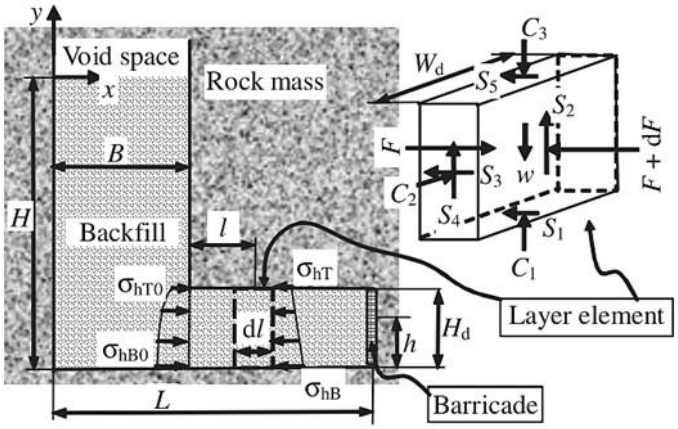


Figure 2-16: Schematic illustration of a vertical backfilled barricade in fully drained condition (Li & Aubertin, 2009a).

Li & Aubertin (2009) also proposed a solution to consider the pressure on the barricade induced by submerged fill (Fig. 2-17). The solution refers to submerged conditions after the installation of the backfill, where the PWP is equivalent to hydrostatic pressure (the excess PWP dissipation is complete). The arching theory was applied to the barricade drift. The horizontal stress in the direction of the drift axis at elevation h (m) is:

$$\sigma'_h = \left[\frac{h}{H_d}\sigma'_{hT0} + \left(1 - \frac{h}{H_d}\right)\sigma'_{hB0}\right] exp\left[-l\frac{2\tan\delta_{sat}}{K_{dl}}\left(\frac{1}{H_d} + \frac{K_{dt}}{W_d}\right)\right] \qquad (2\text{-}8)$$

Where l (m) is the distance between the vertical layer element and the drawpoint; σ_{hT0}(kPa) and σ_{hB0} (kPa) are the horizontal normal stresses at the top and base of the drift at the drawpoint, which are calculated using Li et al. (2005) solution.

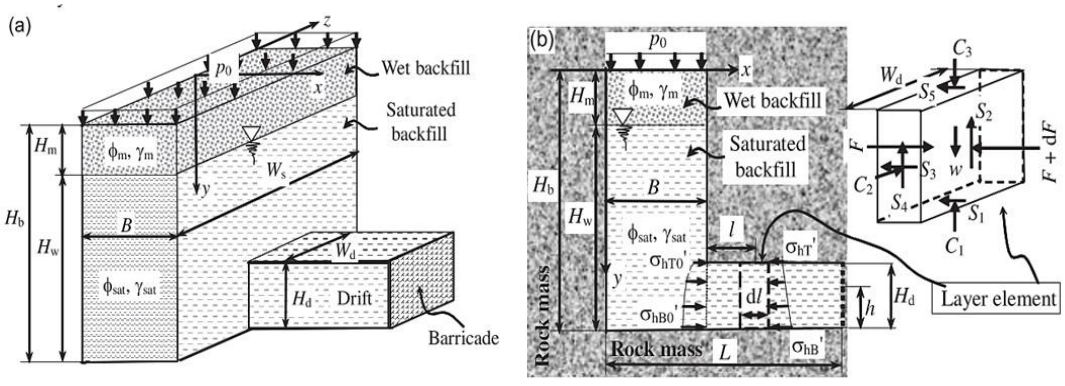


Figure 2-17: Diagram of a backfilled vertical stope with a barricade in a submerged condition a) overview (stope and drift); b) cross-sectional view (Li & Aubertin, 2009b).

For submerged backfill (Li & Aubertin, 2009b) is observed that effective stresses in drifts are less than those produced in drained conditions, whereas PWP can greatly increase total stress in barricades.

2.3.3 Barricade design methods

As previously stated, barricades are made mainly of bricks, concrete blocks, shotcrete, and fibrecrete. The design methods of these traditional barricades are mainly based on the bending failure mechanism (Duffield et al., 2003). Beer (1986) assumed that the barricade is a square slab that breaks with tension cracks developing along the diagonal lines and the rock barricade. The relationship proposed for the estimation of the maximum load on the barricade is given by:

$$w_p = \frac{24 m_p}{b^2} \tag{2-9a}$$

$$m_p = \sigma_c \frac{t^2}{8} \tag{2-34b}$$

Where w_p (MPa) is the ultimate uniformly distributed pressure; w_p (MNm/m) is the ultimate moment capacity per unit length; σ_c (MPa) is the UCS of the mortar; b (m) and t (m) are the width and thickness of the barricade, respectively. This equation has an implied safety factor of 1,72 based on the analysis of a controlled barricade failure experiment at Mont Isa mine.

Constructing underground waste rock barricades can also help reduce mine waste disposal on the surface; nonetheless, traditional design methods based on simply supported slabs are not applicable to waste rock barricades (Yang, 2016).

Li & Aubertin (2011) suggested a rectangular block analysis method to estimate the length of waste rock barricade (WRB) to fully drained and submerged conditions (partially to fully). For completely drained backfill, the minimum required WRB length (LB) (with FS=1) is the following:

$$L_B = \frac{\mathcal{P}}{\gamma_{wr}(1 + KH_d/L_d)\tan\delta} = \frac{P}{\gamma_{wr} H_d (L_d + KH_d)\tan\delta} \tag{2-10}$$

Where $\mathcal{P}$(kPa) is the average backfill pressure on the barricade (the pressure is distributed linearly on the barricade from top to bottom); $P = (\mathcal{P} H_d L_d)$ is the force applied on the barricades by the backfill (kN); γ_{wr} (kN/m^3) is the unit weight of waste rock ($\mathcal{P}$ or load P can be obtained from the

solution proposed by Li & Aubertin, 2009a); δ (°) is the friction angle along the interfaces between the waste rock and the drift walls and floor; K (-) is the earth pressure coefficient within the waste rock along the transversal direction of the drift; L_d and H_d are the width and height of the drift.

In practice, WRB (waste rock barricades) constructed in drifts have a shape that is close to a trapezoid. Modified solutions have been proposed (and validated using FLAC) by Yang et al. (2014, 2016) to improve the design of WRB (Fig. 2-18). The proposed solution addresses the design of trapezoidal WRB designed to retain CPB in the early hours (i.e., critical period) after deposition. The solution considers both global and local stability of the barricade and is based on several assumptions, including the following:

- Due to the large contrast in hydraulic conductivity between CPB and waste rock, the impact of pore - water pressures within WRB is ignored;
- The frictional strength between the top of the barricade and the roof of drift (back) is ignored, as a gap may exist above the barricade;
- The vertical stress of the barricade is considered with the overburden (vertical arching along the vertical sidewalls of the barricade is ignored due to the limited height of the drifts);
- The horizontal stress on both walls of the drift is only presumed to be due to the overburden pressure of the waste rock (without taking into account the backfill pressure effect);
- The angle of friction along the drift walls equals the angle of friction between the waste rock and the floor of the drift δ. When the interfaces are rough, the value of angle (δ) can be taken as the internal friction angle of the waste rock $\emptyset'$(°). However, $\delta < \emptyset'$should be used if the side walls have a smooth surface (or coated by a fine-grained material layer).

The global and internal (local) stability of the barricades is given by:

For $\delta \leq \delta_c$

$$L_{BT} = \frac{\gamma_b \left(H - \frac{H_d}{2}\right)\left(\frac{FS}{\tan\delta} - \frac{1}{\tan\alpha 1}\right) - \gamma_{wr} H_d \left(\frac{1}{2} + K\frac{H_d}{3L_d}\right)\left(\frac{1}{\tan\alpha 1} + \frac{1}{\tan\alpha 2}\right)}{\gamma_{wr}\left(1 + K\frac{H_d}{L_d}\right)} \quad (2\text{-}11a)$$

For $\delta > \delta_c$

$$L_{BT} = \frac{\gamma_b}{\gamma_{wr}}\,(H - H_d)\left(\frac{C_M \times FS}{\tan \emptyset'} - \frac{1}{\tan \alpha 1}\right) \quad \text{(2-36b)}$$

Where H (m) is the backfill height in the stope; H_d (m) and L_d (m) represent the drift height and width, respectively; L_{BT} (m) is the top length of WRB and L_{BB} (m), the base length; α1 (°) is the upstream slope angle of WRB on the stope side; α2 (°) is the downstream slope angle; C_M calibration factor to avoid a negative value of the required L_{BT} (can be taken as 1.5); ϕ' internal friction angle of the waste rock (ranges between 34° and 45° (McLemore et al. 2009; Aubertin 2013)); δ is the friction angle between the waste rock and drift floor; γ_{wr} (kN/m^3) is the unit weight of the waste rock; *FS* is the factor of safety; and K (-) is the earth pressure coefficient in the waste rock along the transversal direction of the gallery.

δ_c is the critical interface friction angle that marks the change in the controlling failure mechanism, from a global (smaller δ) to local stability of the WRB, and is given by:

$$\delta_c = \tan^{-1}\frac{FS(2H - H_d)\tan \alpha 1}{H_d + 2(H - H_d)\left[\frac{C_M \times FS \tan \alpha 1}{\tan \emptyset'}\left(1 + K\frac{H_d}{L_d}\right) - K\frac{H_d}{L_d}\right] + \frac{\gamma_{wr}}{\gamma_b}H_d\left(1 + K\frac{2H_d}{3L_d}\right)\left(1 + \frac{\tan \alpha 1}{\tan \alpha 2}\right)} \quad \text{(2-12)}$$

The barricade length at the base is given by:

$$L_{BB} = L_{BT} + H_d\left(\frac{1}{tan\,\alpha 1} + \frac{1}{tan\,\alpha 2}\right) \quad \text{(2-13)}$$

Therefore, the corresponding volume of WRB is then given by:

$$V = H_d L_d\left(L_{BT} + \frac{H_d}{2\,tan\,\alpha 1} + \frac{H_d}{2\,tan\,\alpha 2}\right) \quad \text{(2-14)}$$

A sample 2D (plane-strain) solution is also proposed by Yang et al. (2016) and given by:

For $\delta \leq \delta_c$,

$$L_{BT} = \frac{\gamma_b}{\gamma_{wr}}\left(H - \frac{H_d}{2}\right)\left(\frac{FS}{\tan \delta} - \frac{1}{\tan \alpha 1}\right) - \frac{H_d}{2}\left(\frac{1}{tan\,\alpha 1} + \frac{1}{tan\,\alpha 2}\right) \quad \text{(2-15a)}$$

For $> \delta_c$,

$$L_{BT} = \frac{\gamma_b}{\gamma_{wr}} (H - H_d) \left(\frac{C_M \times FS}{tan\, \emptyset'} - \frac{1}{tan\, \alpha 1} \right) \quad (2\text{-}40b)$$

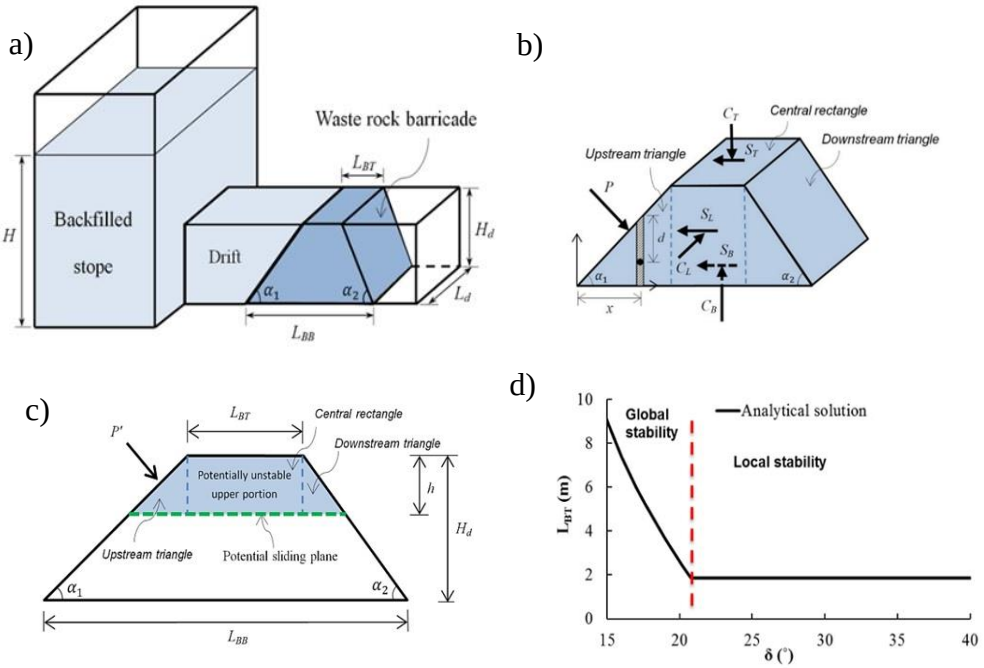


Figure 2-18: a) Schematic view of a backfilled stope with a trapezoidal WRB; b) WRB with various acting forces; c) WRB 's internal translation stability analysis model; d) Variation of the required top length L_{BT} obtained as a function of δ (from Yang, 2016).

Gelinas (2017) proposed an empirical model to size the waste rock barricades (Fig. 2-19). A dimensionless formula for calculating the barricade top length (L_{BT}) is given as follows:

$$L_{BT} = F_p \frac{\gamma_f}{2\,\gamma_{wr}} \tan\left(R \log_{10} \frac{S}{(\gamma_{wr} h)} + \emptyset_R \right)^{-1} \quad (2\text{-}16)$$

Where F_p= pressure factor (two constants were suggested: 3m if the height of stope < 15m and 6m if the height of stope > 15m); $\gamma_f =$ the density of CPB, which generally varies between 18 and 26 kN/m^3; $\gamma_{wr} =$ stack density of waste rock (22 kN/m^3 average value according to the literature); $R =$ The equivalent roughness of the particles (suggest using 15 if porosity is not identified after consolidation); $\emptyset_R =$ the internal friction angle of the waste rock ($\approx 30°$); $h =$ the height of the barricade (between 3.9 and 5 m); and $S =$the compressive strength of the waste rock stack (MPa).

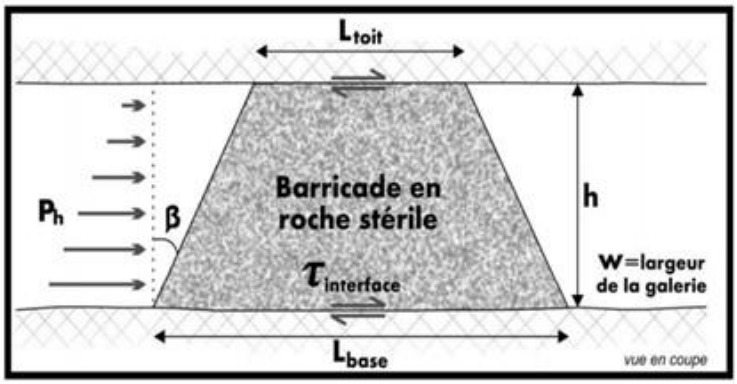


Figure 2-19: Conceptual model of a trapezoidal WRB (from Gélinas, 2017).

2.4 In-situ measurements

Several test results indicated that the in-situ backfill samples usually show different characteristics than laboratory prepared samples with higher shear resistance, shear modulus, and less water content during the same curing time (Revell, 2004; Fahey et al., 2011; Thompson et al., 2012). This can be attributed to the impact of the scale, various stress conditions, better field mixing, higher stope temperatures (Grabinsky, 2010), the convergence of walls (Hassani et al., 1998), drainage, and self-weight consolidation of the fill (Fahey et al., 2011).

For successful backfilling applications, the evolution of PWP and the total/effective stresses in stopes and drifts must be evaluated. In-situ instrumentation of stopes is therefore useful to better understand the backfill response in complex field conditions.

In-situ measures could have been used to identify suitable input parameters for numerical modellings, such as an appropriate earth pressure coefficient, cohesion, demonstrate the effects of binder content on backfill stress states, better understand the distribution of pore pressures, and ensure a suitable selection of drained or saturated conditions for backfills (Li & Aubertin, 2009a, b).

Belem et al. (2004) assessed the backfill pressures at the Doyon gold mine during and after the filling in stopes and on barricades. The dimensions of the two stopes were 3m×23m and 22m high, and 12m×21m and 30m high (Fig. 2-20).

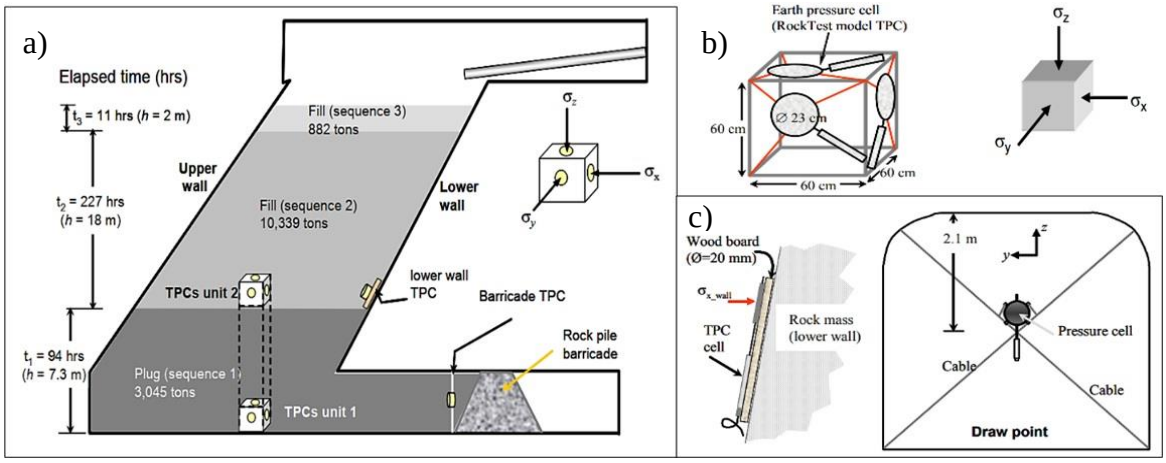


Figure 2-20: a) Basic views of cement paste filling in three sequences; b) Semi-stiff metal unit (box) with three TPCs to measure pressure in three directions; c) Instrumentation of the lower wall of the stope and the drawpoint in front of the barricade (from Belem et al., 2004a)

At different points, eight TPCs have been mounted, including the stope floor, the plug/residual backfill interface, the lower wall, and the barricade. The paste backfills consisted of gold mine tailings blended with 3% (wt) of binder (Portland cement and slag). The stresses were measured in the paste backfill ($\sigma_{\text{longitudinal}} = \sigma_x$, $\sigma_{\text{transversal}} = \sigma_y$, and $\sigma_{\text{vertical}} = \sigma_z$) as well as on the lower wall and the barricade. The pressure recorded indicated that during backfilling, the pressure steadily increased and decreased after 10 days. The internal longitudinal pressure of the paste backfills, presumably due to the arching effect, is greater than the transversal and vertical pressures. When the filling height was approximately 22 m, the lateral pressure measured at the barricade was maximum and remained unchanged when additional fillings were installed (Fig. 2-21).

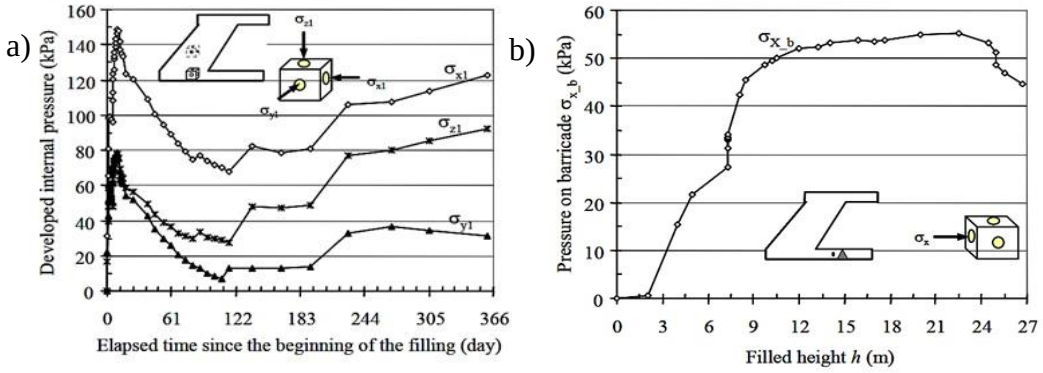


Figure 2-21: a) The internal pressures of the paste backfill at the base of the stope; b) Variation of the lateral pressure σ_{x-b} on the barricade during the filling (after Belem et al., 2004a).

A field investigation into the paste fill of the Golden Giant mine was carried out by Le Roux et al. (2005) to determine the in-situ properties and obtain the information necessary to optimize the mix design. The paste fill consisted of tailings with 1 - 6% binder content (Portland cement and fly ash). A self-boring pressure meter (SBP) was used to measure paste fill field strength (Fig. 2-22). To compare with in-situ results, laboratory tests were also performed with similar laboratory-prepared paste fillings. The result indicated that the undrained shear strength and shear modulus of the field materials (measured by the SBP) varied from 50% to 80% and 100% to 150% respectively, higher than that obtained with laboratory prepared CPB samples. They also reported a higher void ratio and lower cohesion for CPB samples prepared by the laboratory. The friction angles for unsaturated block samples and the laboratory prepared CPB samples were nearly the same (Table 2-2).

Table 2-2: The strength properties of CPB in the field and laboratory (from le Roux et al., 2005).

Strength property	Undisturbed block sample		Laboratory prepared CPB (3% binder at 56 days)
	Saturated	Unsaturated	
Void ratio	1.2	1.2	1
Degree of saturation	99%	92%	99%
ϕ'	19-27	32-37	35
c' (kPa)	55-98	47-60	101
E (MPa)	25-47	12-17	35.9
UCS (kPa)	175-240	110-130	384

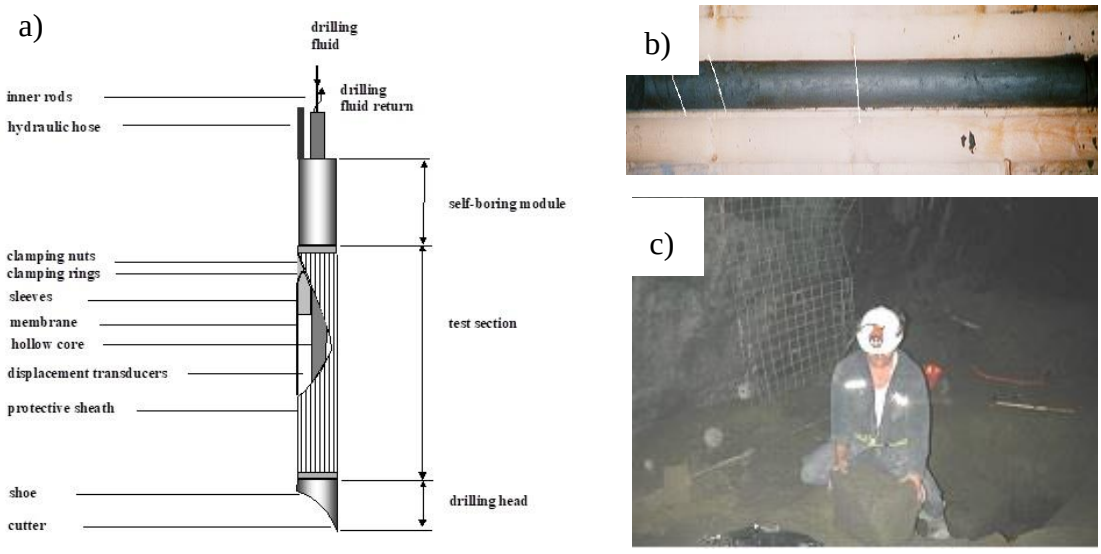


Figure 2-22: a) Self-boring pressure-meter schematics; b) Typical sample quality from thin-walled sampling; c) Excavation of block samples (from le Roux et al., 2005).

Helinski et al. (2010) investigated the evolution of the total vertical stress (σ_v) and pore water pressure (u) during filling of two mine stopes at the Kanowna Belle (KB) mine and Savannah Nickel (SN) mine, Australia. At various locations, the stopes were equipped with earth pressure cells and piezometers (Fig. 2-23). At the KB mine, results demonstrated that the measured value of σ_v was less than the total overburden pressure. The results also showed that σ_v and u initially increased at the same rate as the overburden pressure. After 20 hours, effective stresses started to develop. The effective stress increased due to further consolidation when the supply was stopped (from 34 to 58 hr). The rate of increase in pore water pressure at SNM mine was significantly lower than the rate of total stress increases due to consolidation during placement. The results also indicated that the PWP increased during filling and decreased when the filling finished (at 300 h). PWP magnitude is controlled by the "steady-state" drainage conditions in the fill, which depend on the flow restriction established at the base of a stope due to a reduced flow area through the stope drawpoint.

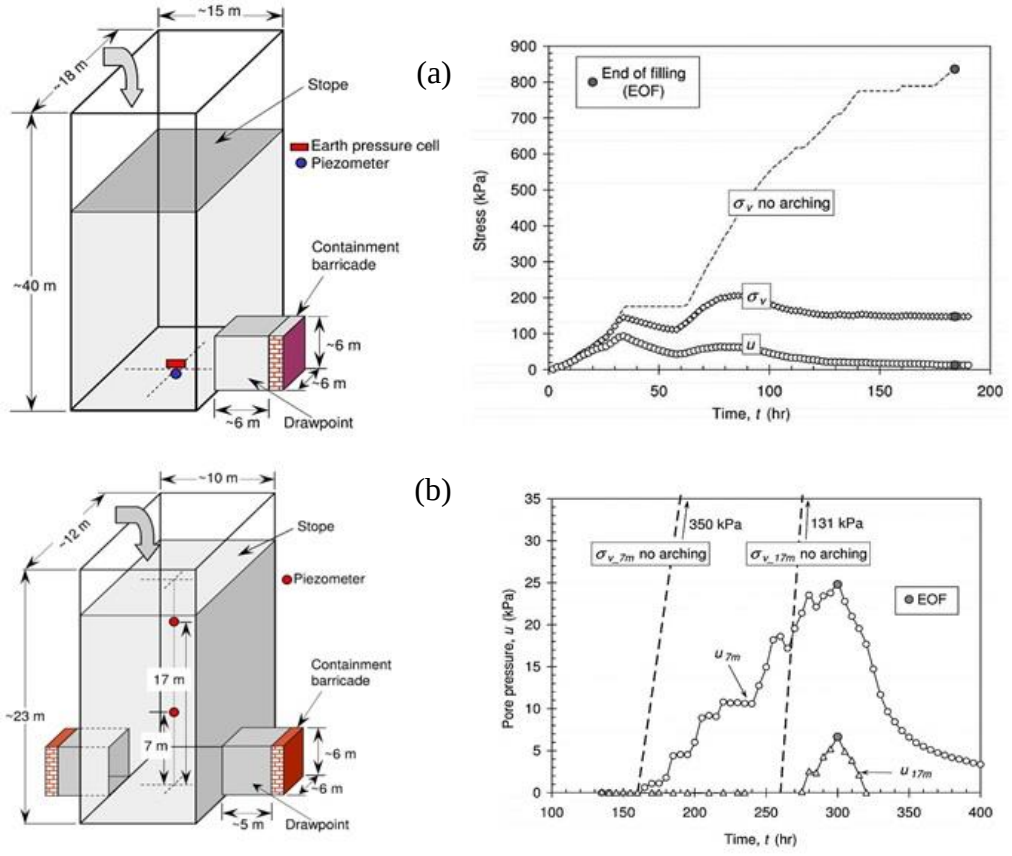


Figure 2-23: Monitoring and in situ measurement of pore water pressure (u) and total vertical stress (σ_v) at the stope: a) in KB Mine, b) in SNM Mine (from Helinski et al., 2010).

Hasan et al. (2014) conducted full-scale monitoring of CPB during and post-filling at the Lanfranchi Nickel mine, Australia (Fig. 2-24). The rising-rate was 0.7 m/h, and the stope can be considered as low and wide.

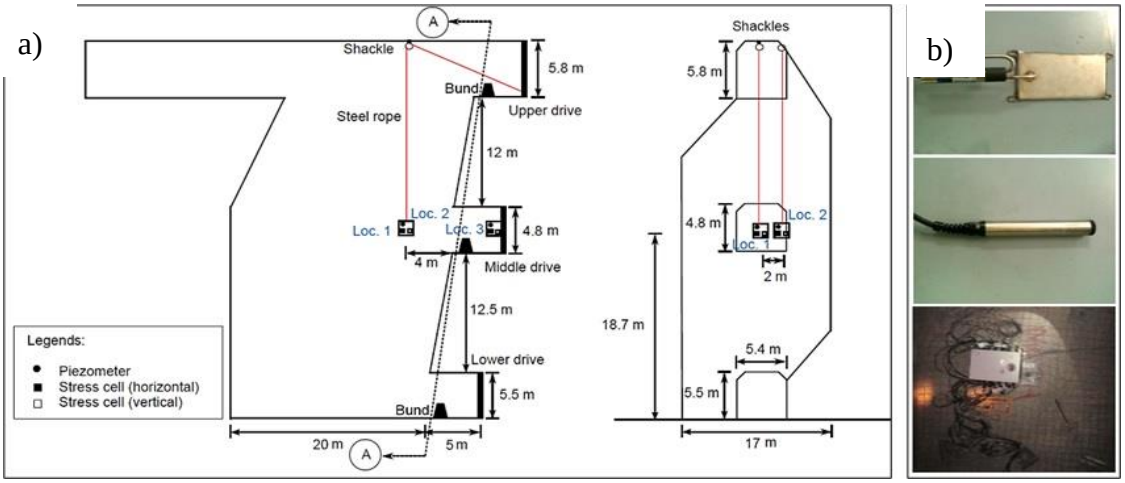


Figure 2-24: a) Stope in Lanfranchi Nickel mine (long section and cross-section); b) Instrumentations (earth pressure cell, piezometer and data-logger) (from Hasan et al., 2014).

Hasan et al. (2014) recorded a decrease in PWP and total stress during the first curing (13 hours) due to self-weight consolidation and hydration of the binder, and when backfilling resumed, total stress and PWP raised again until the second curing period (Fig. 2-25). During the second curing period, total stress began to climb after an initial reduction, while PWPs continuously declined. The increase in pressure during curing is most likely due to the increase in temperature. However, the increase in pressure was not observed in the first curing period, and the temperature was not registered.

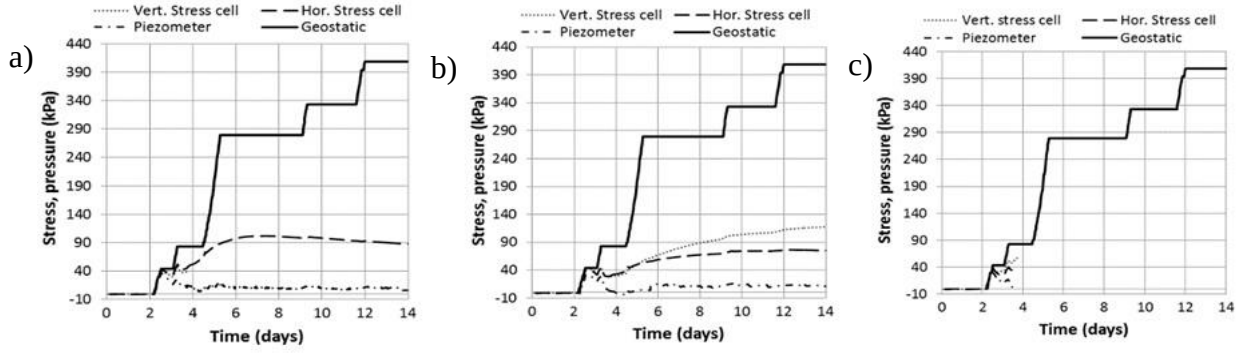


Figure 2-25: Measurement of stresses at a) location 1; b) location 2; c) location 3 (from Hasan et al., 2014).

Thompson et al. (2009) and Grabinsky (2010) studied the evolution of total earth pressure and pore water pressure using instrumented boxes at several locations within backfill stopes and near filling walls. Stress changes at several mines were monitored in Turkey (at the Inmet Cayeli mine) and Canada (at the Kidd mine and the Williams mine). Total Earth Pressure Cells (TEPCs) and piezometers were used to measure total stresses, PWP, and temperature changes during hydration of the fill. All measuring instruments were mounted in a cage attached to a data acquisition system. The stopes with different geometries (stope height and width varied between 15 to 53 m and 8 to 30 m, respectively) were backfilled at various rates. The barricade's height and width were between 5~6 m and 5~10 m, respectively.

Figure 2-26 shows a long-hole stope instrumented by Thompson et al. (2009) at Kidd Mine to monitor the total earth and pore pressure during and after backfilling.

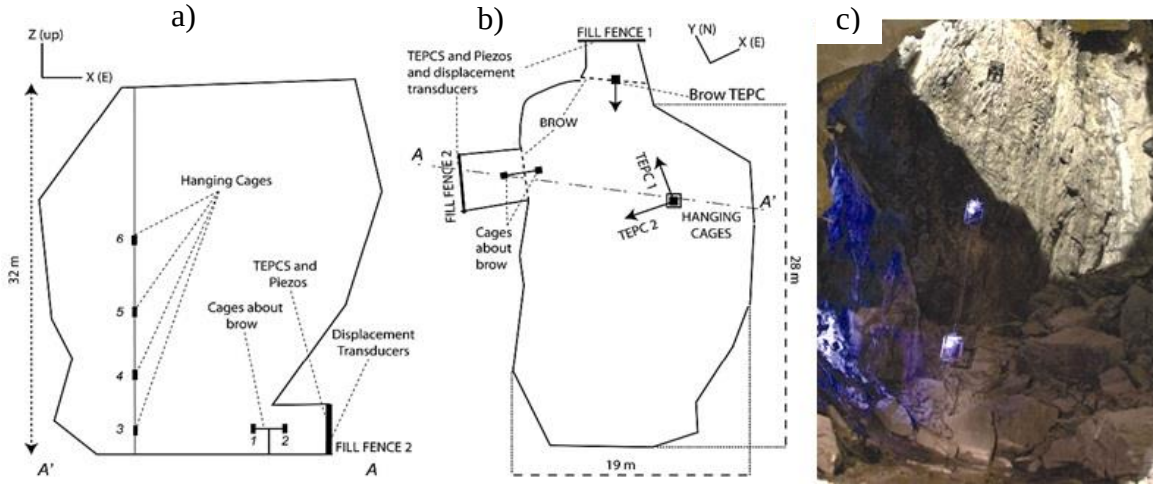


Figure 2-26: a) Cross-section of the stope with locations of instrument cages, b) Plan shows orientations of the TEPCs, c) Cages hanging in the stope (from Thompson et al., 2009).

The highest pressure during the filling was equal to the overburden (545 kPa vertically at 3m above the base of the stope). The pressure measured in a drift located at 2m from the stope brow was 300 kPa acting horizontally and 65 kPa on the fill fence. For both fences, the maximum displacements reported were 0.9 and 0.4 mm. In the plug (4% binder), the pore pressure dropped after less than a day, and the total pressure quickly deviated from hydrostatic pressure, whereas the PWP was equal to the total pressure for two days in the residual part filled with 2% binder. The horizontal stress at

the end of the filling was greatly different from the vertical stress and indicated the development of the arching effect in paste backfill (Fig. 2-27).

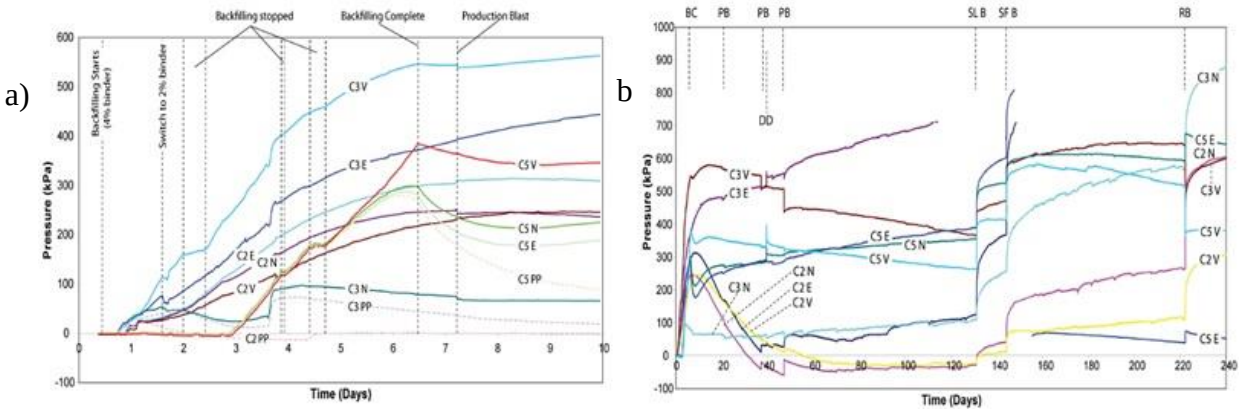


Figure 2-27: a) Total pressure and pore pressure (PP) for 10 days. The TEPCs are either oriented north (N), east (E) or vertically (V) with stope orientation, b) Total pressure over a period of 240 days from the beginning of the backfill (from Thompson et al., 2009).

Figure 2-28 demonstrates the evolution of stress in four TEPCs, placed along the barricade drift. In the first 1.5 days, the stresses were close together and then diverged. The pressure is seen to decrease with a greater distance from the stope brow, indicating the arching effect.

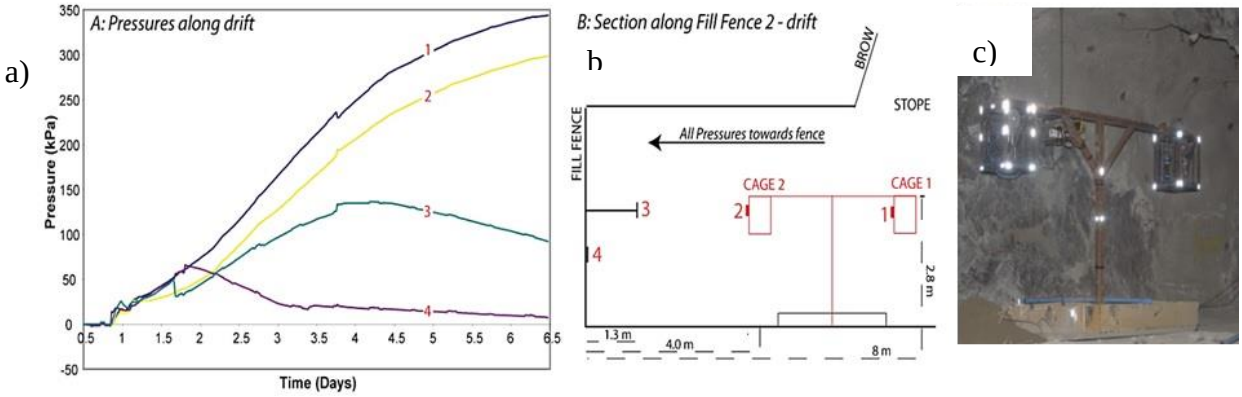


Figure 2-28: a) Total pressures during the filling for TEPCs on the barricade, in the drift and under the brow, b) Plan shows where the instrumented cages are located, c) Cages photo (from Thompson et al., 2009).

Thompson et al. (2012) instrumented two stopes (denoted as 685 and 715) at Cayeli Mine, Turkey. Three cages were installed in the centre of the stope for both stopes, and two cages were put under the stope. TEPCs and piezometers were also provided for the 5-metre-high barricades.

Generally, stopes are backfilled in two stages. Initially, CPB was poured with a height of 8 metres (typical stope height is 15 m), with intervals between 3 and 7 days, depending on the contents of the binder and the undercut mining activities. Filling rates were maintained < 35 cm/h in the undercut, and < 42 cm/h in the main stope. The barricades at drawpoints are made of shotcrete (30 cm thickness), reinforced with vertical and horizontal rebar spars, spaced at intervals of about 1 m.

The 685-stope was 16 m high with a plan section of 25 m by 12.5 m (Fig. 2-29). The average rate of rising was around 0.25 m/h. The binder contents in the plug and residual pours are 8.5% and 6.5%, respectively. The stope was continually filled for 2.85 days, and the plug pour was finished at 1.8 days.

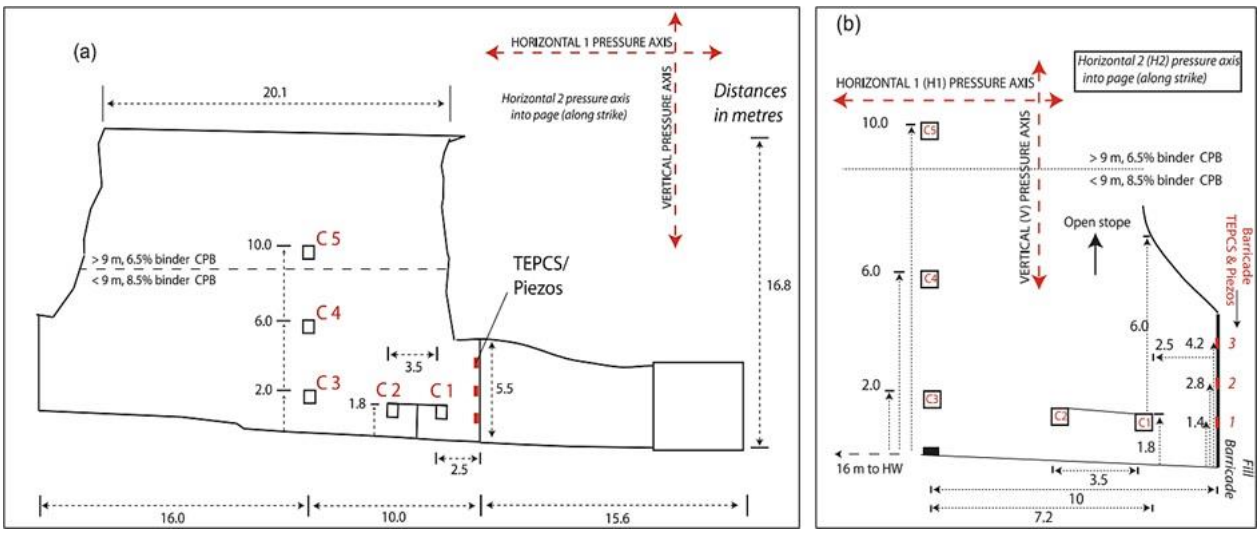


Figure 2-29: a) Cross-section showing instrument locations in the 685-stope, b) Detailed instrument plan–cross-section of the 685-stope (from Thompson et al., 2012).

Thompson et al. (2012) stated that a geostatic loading time was recorded in the plug pour (first placement) from 12 to 15 h and about 20 h in the final pour. The longer geostatic loading of the final casting was due to the slower hydration of the cement due to the lower binder content. They also reported that lower filling rates and a relatively higher content of binders resulted in lower barricade pressure (Fig. 2-30).

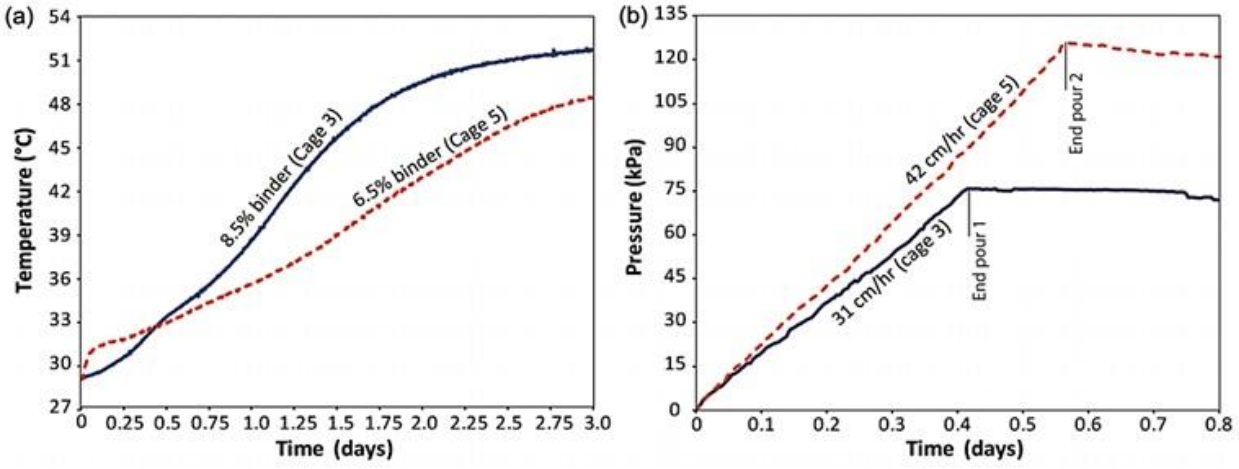


Figure 2-30: a) Temperature history for 8.5% and 6.5% CPB binder content in the 685-stope, b) Pressures for two CPB rise-rates in the 715 stope (from Thompson et al., 2012).

The retaining barricades had TEPCs and piezometers on the backfilled sides (Fig 2-31). Barricade external surfaces were instrumented with potentiometers to measure the deflection (or displacement) during backfilling.

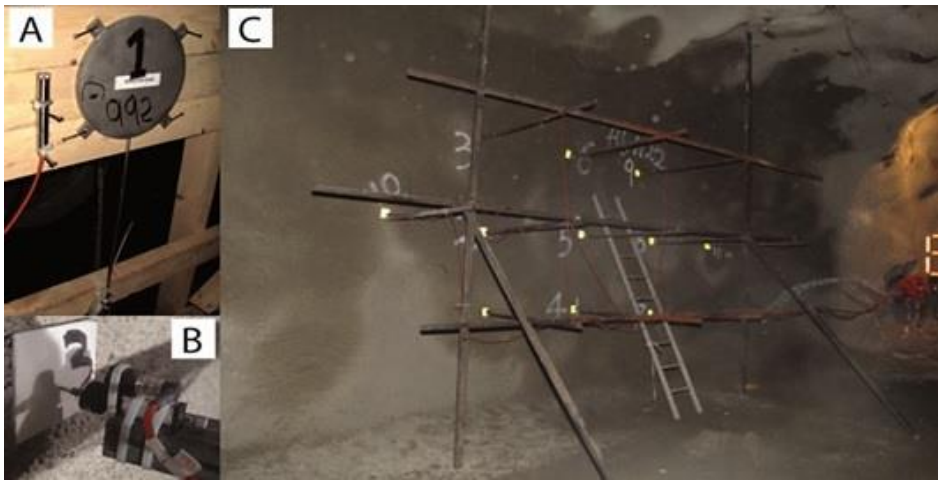


Figure 2-31: a) TEPCs and piezometers directly attached to the barricade; b) Potentiometers mounted to record barricade deflection; c) Barricade external surfaces (from Thompson et al., 2012).

Figure 2-32 shows the evolution of total earth pressure (TEP), pore pressure (PP), temperature, and displacement over the first 5.5 days for the barricade and cage 3. The barricade pressure peaked at 47 kPa after filling. Vertical pressures started to increase considerably more than horizontal pressure for Cage 3 after the geostatic loading period. The PWP at the barricade position is

significantly lower due to the drainage around the barricade. The maximum deflection was 7.8 mm at the barricade center.

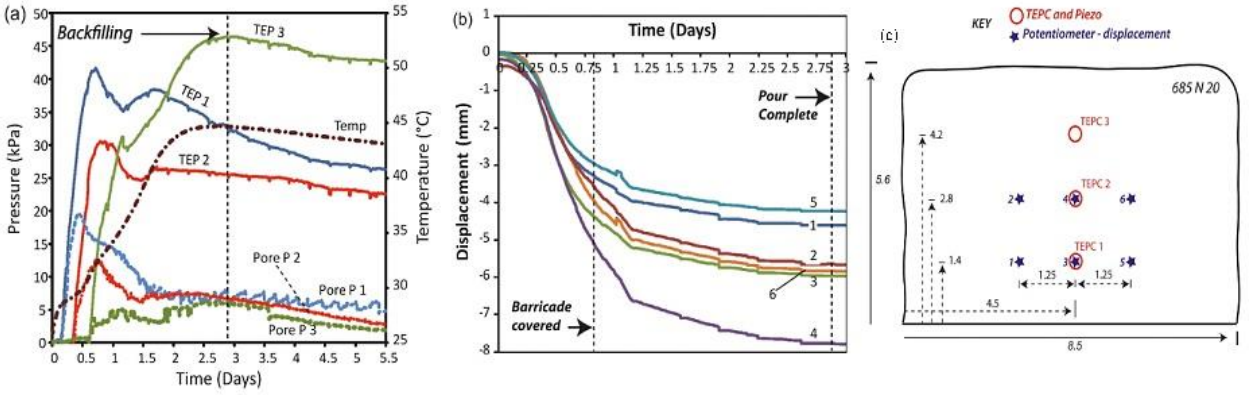


Figure 2-32: 685-Cayeli mine stope: a) TEP, PP, and temperature measurements. The horizontal orientations of the TEP are H1 and H2, and V refers to vertical pressure, b) Displacement of the barricade during backfilling, c) Barricade geometry, TEPCs, piezometer, and displacement array locations (from Thompson et al., 2012).

In conclusion, the measurements vary from one site to another depending on several factors such as the accuracy/type of the measuring tools (pressure cells, piezometers), the properties of the backfill (type and content of the binder, concentration of solids, sulphate content in the tailings), site conditions (temperature, the geometry of the site, the permeability of the rock mass, barricade used, etc.). At some sites, the pressure cells recorded the increase in pressure of each fill, while at other sites, the cell recorded the increase in pressure only after the first layer (equal to that of the overburden). Therefore, the use of small-scale models makes it possible to control the measurement of the state of stress in the different locations inside the stope.

2.5 Small-scale models of mine stopes

Mitchell et al. (1982) conducted several intermediate-scale tests (2m in height) on a physical model made of wood to investigate the stability of exposed cemented backfill (Fig. 2-33). They demonstrated that arching could significantly affect the transfer of stresses inside the stope. They also stated that the required strength of the cemented backfill could be reduced when the walls are closer together. Furthermore, multiple direct shear tests and compressive tests were carried out to assess the properties of the materials used for the creation and testing of a 3D analysis solution.

a) b)

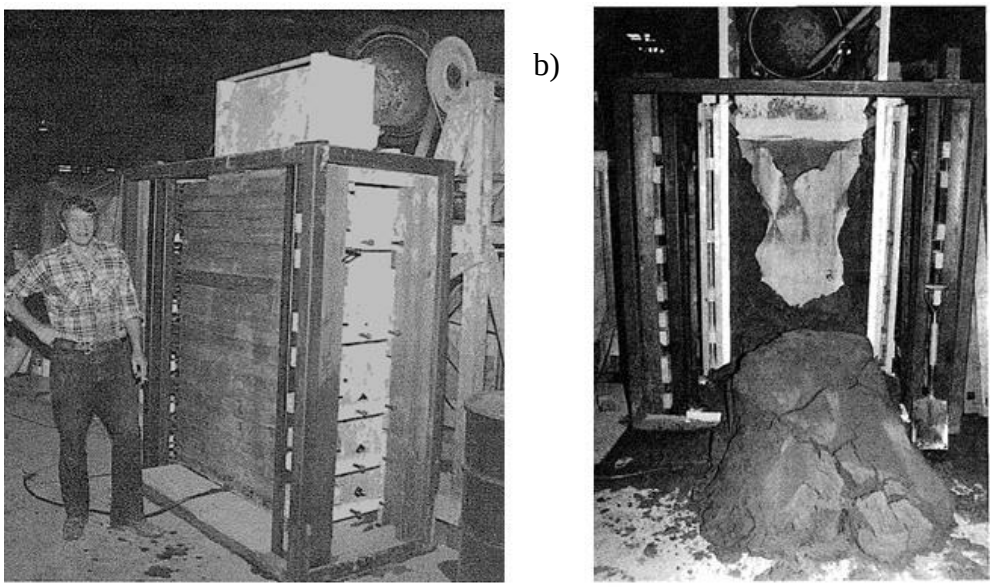


Figure 2-33: General views of a) model fill cast in formwork, b) failure test with a surcharge (from Mitchell et al., 1982).

Several centrifuge tests were performed by Take and Valsangkar (2001) to assess the use of a calibrated flexible earth pressure cell to measure the lateral backfill pressure behind retaining walls. The findings show that the lateral earth pressure is lower than the pressure of the overburden. It was also reported that rougher walls had decreased the lateral earth pressure significantly.

Pirapakaran (2008) constructed a small model for measuring average vertical stress at the base of the stope with considering the different parameters. Two circular and two square models (100 mm and 150 mm width or diameter; 600- and 900-mm height) were built to assess the effects of stope geometry on stress distribution within the hydraulic fills (Fig. 2-34). The arching was established on circular and square stopes and increases with the surface roughness. The laboratory test results were used to validate their 3D analytical solutions. During and after backfilling, the vertical stresses in the circular stopes (for both sizes,100×600 mm and 100×900 mm) were about 85% of the stresses measured in square stopes. It is also stated that the friction angle and interfacial friction angle augmented with the density index I_D.

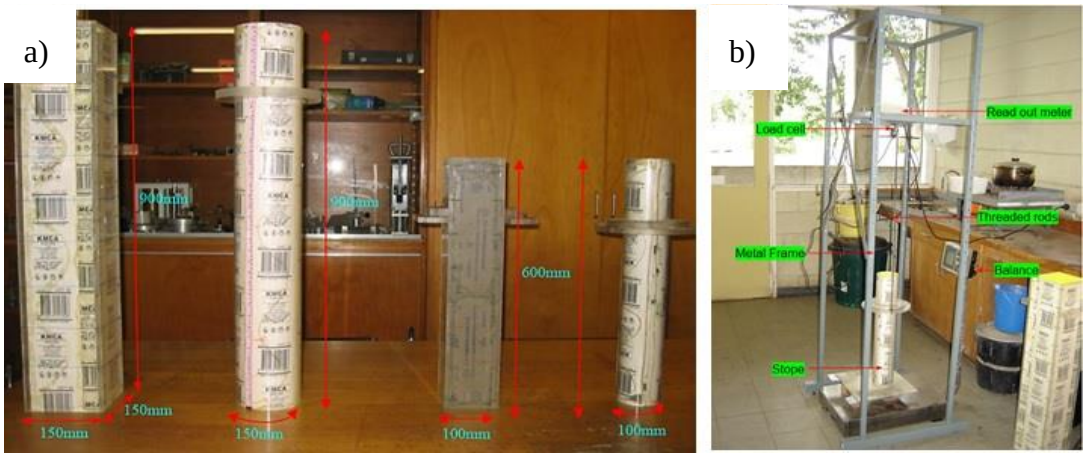


Figure 2-34: a) Stopes geometries with dimensions, b) Photograph of the arching apparatus (taken from Pirapakaran, 2008).

Belem et al. (2016) performed column experiments (3m high) to study the self-weight consolidation and the development of the strength for the cemented backfill at mine backfill plants (Fig. 2-35). Their findings indicated that water drainage and self-weight consolidation settlement occur mostly within the first 48 to 72 hours after the columns are filled. These findings depend on the size and hydraulic characteristics of the cemented backfill column. The accumulated water content drained through the walls and base of the column ranges from 9% (PLD-partial lateral drainage; the middle one in Fig. 2-35b) to 26% (FLD-full lateral drainage; middle one in Fig. 2-35a) of the initial total water in CPB mixture. The associated vertical strains ε_v(%) varied between 2.5 % (CT2-UD column) and 5.5 % (CT2-FLD column). Belem et al. (2016) also stated that at Louvicourt mine, the field-observed volumetric strain of CPB varies from 3.3 % to 5.0 %, implying that in situ backfilled stopes tend to be like full lateral drainage (FLD) or partial lateral drainage (PLD) conditions. It was also reported that the maximum UCS value was observed at the column bottom, presumably due to the highest self-weight consolidation (compactness). The highest strengths of backfill samples were obtained with 50% GU-50% Slag proportioning under equal conditions, regardless of depth.

As observed, previous small-scale physical models did not address waste rock barricades and their interlocking with backfill during placement. There are no experimental parametric studies to study the influence of several factors such as backfill viscosity, binder content, interface friction angles, location of barricades from the brow.

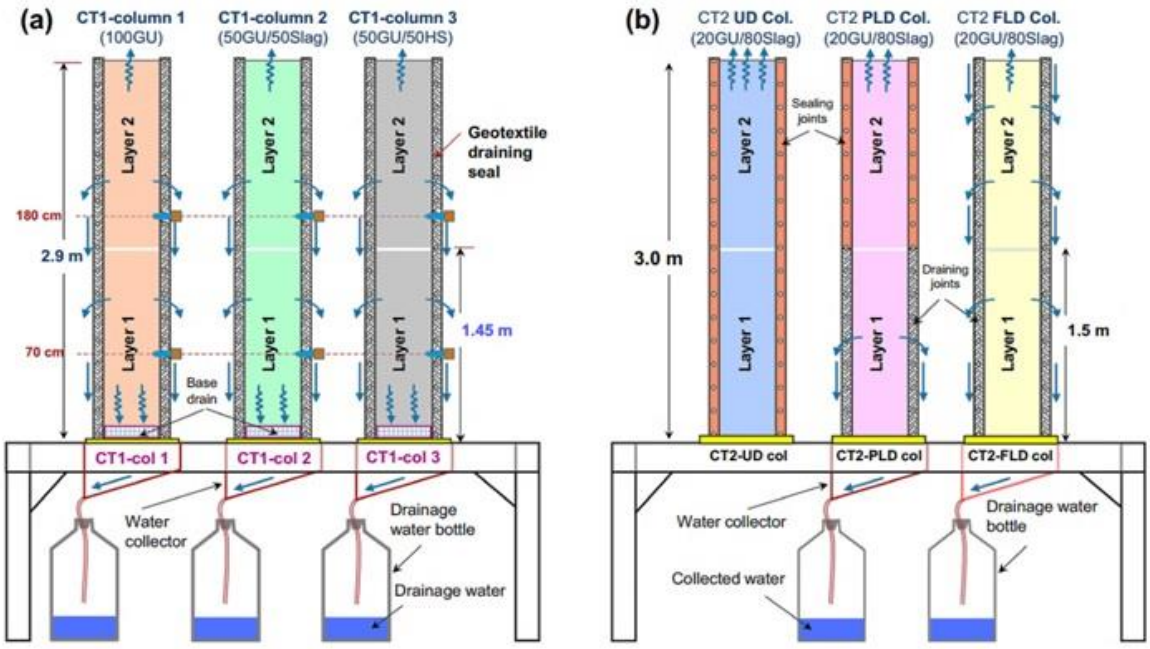


Figure 2-35: Schematic view of the three consolidation columns filled with CPB at a) Laronde (LRD) mine backfill plant, b) Louvicourt (LVT) mine backfill plant (from Belem et al., 2016).

2.6 Numerical simulations for vertical backfilled stope stress evaluation

Numerical simulations can analyze geometric complex shapes, interactions between the fill and the walls, and simulate the most practical conditions. Numerical analyses may also consider complicated questions such as wall convergence, sequential filling, drainages and fill consolidation. Most numerical modelling considers backfill as an elasto-plastic or Mohr-Coulomb material and the rock mass as a linear elastic material unless specified (e.g., Li et al., 2003; El Mkadmi, 2012; Falaknaz, 2014; Yang, 2016). The backfill is usually placed immediately or in layers after the wall convergence has been completed.

Askew et al. (1978) performed simulations using a 2D finite element method (FEM) code. It has been shown that the arching effect is more developed in the cemented backfill compared to the uncemented backfill.

Simulation results obtained on PHASE^2 (RocScience 2002) were presented by Aubertin et al. (2003) to evaluate the stress state in narrow backfilled stopes. The horizontal and vertical stresses were much higher than the overburden stress of the backfill at the mid-height of the stope. This result is partly attributed to the squeeze effect of the inward convergence of the stope walls.

Li et al. (2003) performed numerical simulations to analyze the stress state in narrow backfilled stopes using FLAC (Itasca 2002). The arching effect was noticed in the stope. Their results demonstrate that the uniform distribution of vertical stress along stope walls is not strictly valid in certain analytical solutions (Fig. 2-36).

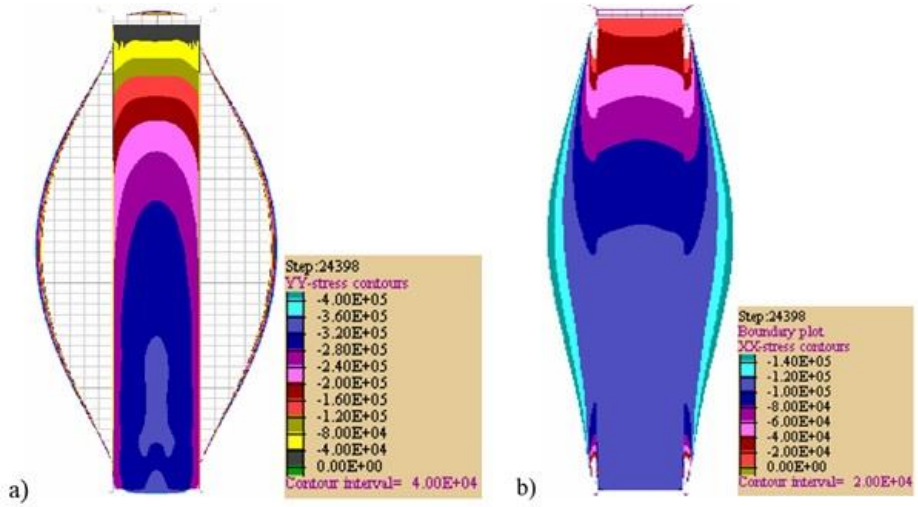


Figure 2-36: Numerical results of the distribution of (a) vertical and (b) horizontal stresses in FLAC (from Li et al., 2003).

Li & Aubertin (2009) used the code FLAC to validate their analytical solutions (see Li & Aubertin, 2009a,b), taking into consideration the influence of water on the stress state. The effective and total stresses of the analytical solution were consistent with numerical simulations for submerged backfill along the vertical centerline (Fig. 2-37).

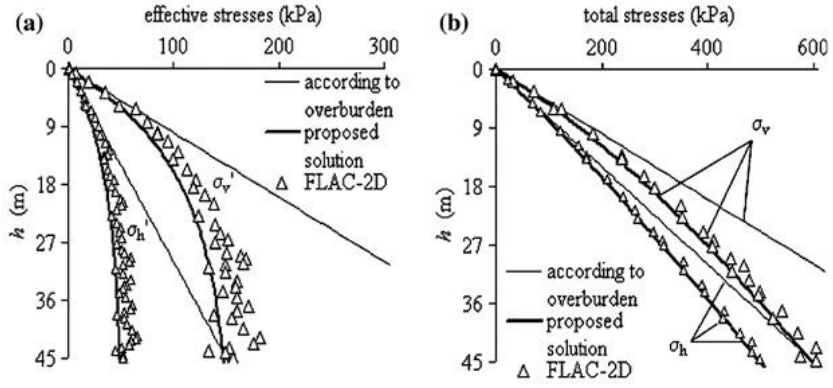


Figure 2-37: Vertical and horizontal stresses along the VCL, obtained from numerical simulations and analytical solution ($K = K_a$): a) effective stresses (b) total stresses (Li & Aubertin, 2009c).

Fahey et al. (2009) conducted simulations for dry (drained) and saturated (undrained) backfill using PLAXIS (version 8.6). They indicated that changing Young's modulus of fill from 10 MPa to 1 GPa has approximately no impact on the state of stress; the horizontal stress increases as Poisson's ratio ν increases for the entire scope; for $\nu < 0.4$, the vertical stress decreases as the ν value increases with reverse relation when ν value differs from 0.4 to 0.499; the greater k value tends to generate smaller final total stresses in-depth, particularly for the total horizontal stress (Fig. 2-38).

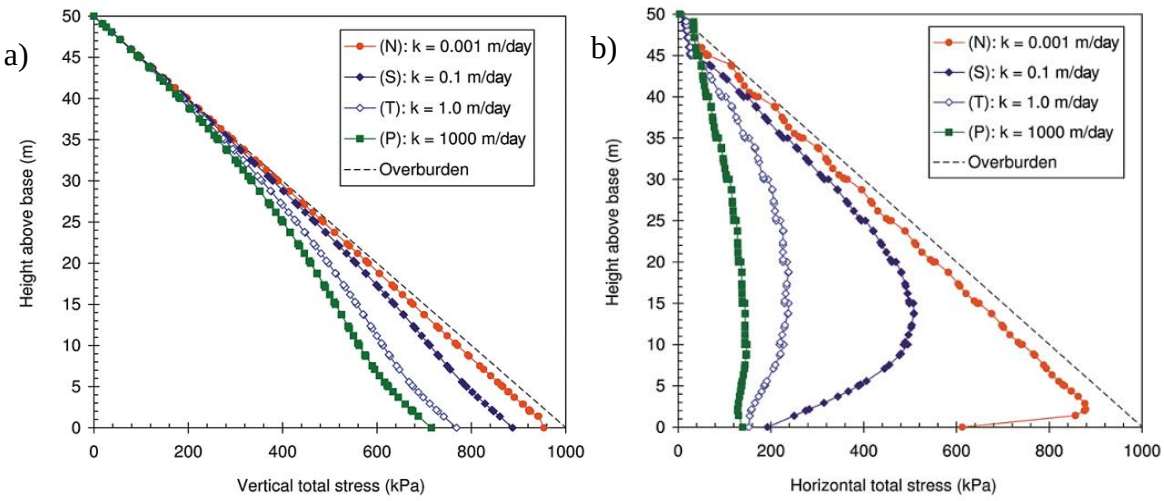


Figure 2-38: a) Vertical total stresses, b) Horizontal total stresses at the end of backfilling for different k values (from Fahey et al., 2009).

Fahey et al. (2009) indicated that the final state of stresses is independent of the type of filling (drained or undrained) and the permeability of the backfill; the saturated fill behaviour is influenced by the hydraulic conductivity relative to the rise-rate. It has also been stated that the evolution of stress depends largely on consolidation in stopes filled with CPB and might take a long time due to low permeability.

To research the 1D consolidation of paste backfill with a non-zero pore pressure boundary condition on the top of the placed layer, Shahsavari & Grabinsky (2014) performed numerical modelling with FLAC^{3D}. The research was based on in-situ measurements that found that non-zero pore pressure at the top of the layer tends to create higher pore pressure.

El Mkadmi et al. (2012) carried out numerical simulations with the finite element code SIGMA/W. They illustrated how the arching effect can evolve and influence the corresponding stress distribution within narrow vertical stopes. The results showed that normal stresses are usually lower

than overburden pressure, ($\gamma_f h$) and the rock-backfill interface characteristics affect the magnitude of stresses in backfilled stopes. Simulations with smooth interface elements tend to produce larger stresses and a better correlation with analytical solutions. The initially saturated backfill was immediately placed into the stope and followed by gradual drainage at the base of the stope (in the right corner). Shortly after deposition, the saturated backfill behaves like a heavy fluid and as PWP is dissipated during the drainage and consolidation process, effective stress increases while total and PWP stresses decrease. The numerical model of the mine stope, evolutions of total and effective vertical stress along the vertical centerline (VCL) and PWP along the stope height are shown in Figure 2-39.

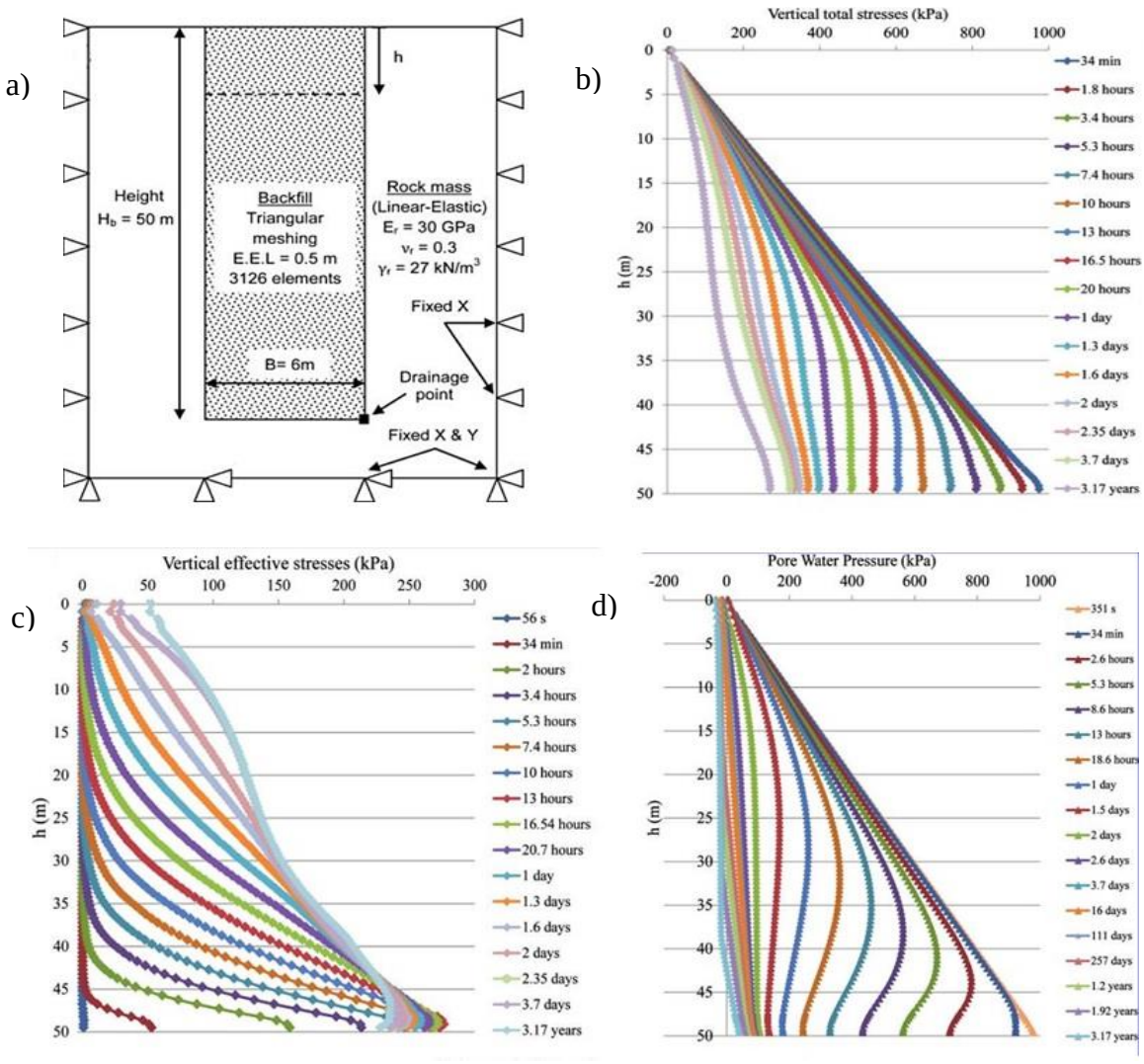


Figure 2-39: a) Model of a backfilled stope. Evolution of: b) total vertical stress, c) effective vertical stress and d) PWPs (from El Mkadmi et al., 2013).

For a sequential deposition with an initially saturated fill, the rise-rate is one of the most influential factors for the stress state in the stope (Fig. 2-40). They also stated that, when the backfill is applied rapidly, PWPs may accumulate when the addition of new layers, thus increasing the total stress at the base of the stope. Low stress, particularly when drainage produces negative PWPs, is observed for slower filling rates.

The effect of cementation has also been modelled by defining the fill characteristics from experimental results such as cohesion, stiffness, and hydraulic functions. They stated that cohesion due to cementation can greatly accelerate the backfill strength gain. They indicated that cementation and cohesion can reduce effective stresses, PWPs, and total stresses in cemented backfill compared to cement-free cases. They also mentioned that the faster filling rate would produce higher total backfill stress.

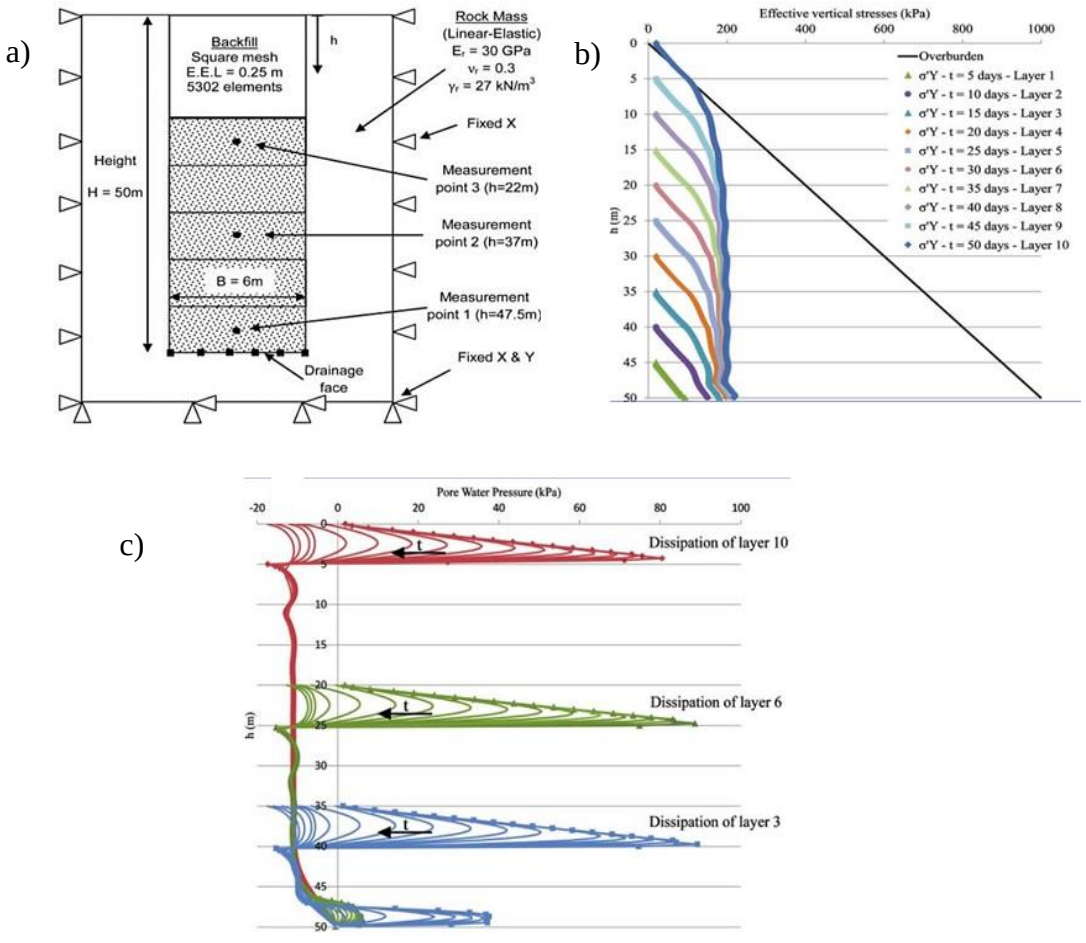


Figure 2-40: a) Sequentially backfilled stope with drainage at the base, b) Evolution of effective vertical, and c) PWP stress for sequential backfilling (from El Mkadmi et al., 2013).

Falaknaz et al. (2014) modelled two adjacent stopes excavated and filled sequentially using FLAC. The stresses in two adjacent stopes obtained at the end of backfilling the second stope are shown in Figure 2-41. Although the arching effect occurs in both adjacent stopes, the distribution of stress was different. The stress state of the first stope was also different from the stress state obtained from a single stope analysis. They attribute the result to the fact that the stresses in the first backfill stope are affected by the excavation and the backfilling of the adjacent stope. They also indicated that the rock mass mechanical behaviour has an influence on the state of stress of the fill (elastoplastic model or linear elastic model), ascribed to the differences in the strains of the backfill and displacements of the rock walls.

a)

b)

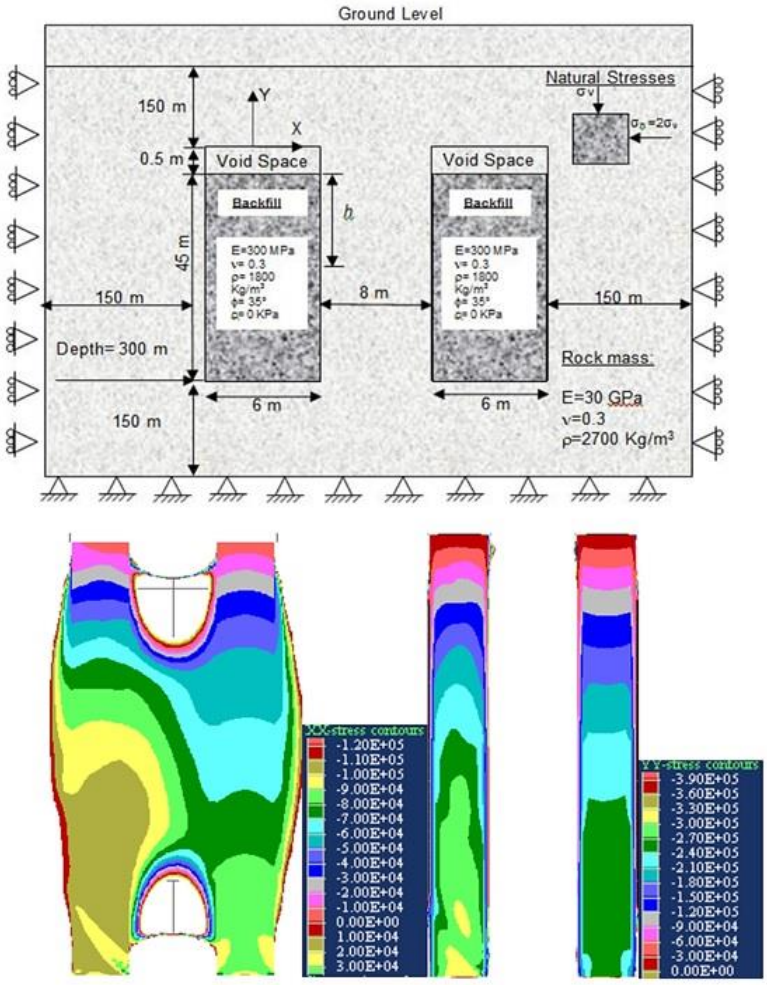


Figure 2-41: a) Illustration of the boundary conditions, dimensions, and materials applied to two backfilled stopes simulations, b) Horizontal (left) and vertical (right) stress distributions at the end of filling for the second stope (from Falaknaz, 2014).

CHAPTER 3 EXPERIMENTAL TESTS ON A SMALL-SCALE MODEL OF A MINE STOPE TO STUDY THE BEHAVIOUR OF WASTE ROCK BARRICADES DURING BACKFILLING

3.1 Introduction

The purpose of mining is to extract minerals from the crust of the earth, which in turn creates voids that alter the existing stress field and lead to instability. Large quantities of waste rock and tailings are produced and stored in waste rock dumps and tailings storage facilities during mining operations. Acid mine drainage (AMD) or contaminated neutral drainage (CND) can occur when these wastes are exposed to atmospheric conditions, resulting in potential pollution of the environment. Underground backfilling offers important economic and environmental benefits for mining operations (Thomas, 1979; Hassani & Archibald, 1998; Potvin et al., 2005; Belem & Benzaazoua, 2008). It also offers a great deal of flexibility and enhances the strategic approach to running. The use of various types of backfills has to do with technical requirements, operating methods, and strategic plans. In general, the geometry of the ore deposit is what determines the method of extraction. The hard rock mining methods that use backfilling as a secondary support system are Open Stope and Cut and Fill (Potvin et al., 2005). The need for backfilling is rising with deeper mining, as the critical span becomes smaller and smaller. Using backfilling as a support strategy to support stope walls will allow reducing their potential movement. Indeed, backfill enhances the stability of the fractured rock mass in two distinct ways: first, restricts the opening of cracks and discontinuations, and second, reduces the convergence of the openings and improves the regional stability (Potvin et al., 2005). Backfill systems are designed according to the required materials and functions, and each operation is regulated by the hydromechanical characteristics of the backfill, the mechanical properties of the rock masses, and the extraction strategies. The paste fill or the cemented paste backfill (CPB) is the most successful and popular of the three different types currently in use in mining (rock fill, hydraulic fill, paste fill). This type of backfill is more homogeneous and provides better strength according to the needs in ground control. The transport of the backfill depends on its fluidity, which could affect its final mechanical performance. The cost of the binder represents nearly 80% of the backfill operation costs.

The understanding of mine backfill requires a multidisciplinary approach, ranging from soil mechanics to geomechanics through fluid mechanics, mineral processing, and other relevant topics.

Understanding the behaviour of the barricades made of waste rock and that must retain the backfill in place in the open stope is essential to ensure their safe use. The main backfill components are full stream tailings (which have a variable source depending on the ore type), mixing water, and binding agent. The tailings contain grains ranging from silt size to clay size and their distribution affects the porosity, wet density, self-weight consolidation, and compressive strength of the resultant CPB. The tailings' mineralogy (e.g., presence of clayey particles) can affect the binder dosage, water retention, and chemical/geochemical stability, which can weaken the backfill (Benzaazoua et al., 2004; Henderson & Revell, 2005). The binder type and proportion also affect the backfill strength development over the curing time (Belem et al., 2000; Potvin et al., 2005; Sivakugan et al., 2015; Walske et al., 2015; Xu et al., 2018). The chemistry of the mixing water can also influence the overall CPB strength, especially when they contain dissolved sulphate salts such as sulfosalt (Hassani & Archibald, 1998; Potvin et al., 2005; Belem & Benzaazoua, 2008; Belem et al., 2018). Acidic water and sulphate salts damage the cement bonds in the backfill, leading to loss of strength, durability, and long-term stability (Mitchell et al., 1982; Benzaazoua et al., 2002; Potvin et al., 2005; Yilmaz, 2010). Underground backfilling of open stopes requires the construction of a barricade placed in the drift (drawpoint) to retain the backfill in the filling chamber (open stope). Serious consequences can occur if barricades fail, such as damage to mining equipment, injuries, or even death of mine personnel. Depending on the type of backfill, the barricade is generally built of permeable brick fibercrete or concrete (hydraulic fill), timber frame (hydraulic and paste fill), shotcrete (hydraulic and paste fill), or waste rock (paste fill) (Belem et al., 2018). Waste rock barricades are efficient and commonly used in several underground mines since they are available through mining production (Belem et al., 2018). These barricades are still poorly documented (Li & Aubertin, 2011; Yang et al., 2016) and must be properly designed to avoid any failure that could slow down mining production. The study of the barricade stability requires a correct estimation of pore water and total pressures in backfilled stopes and on barricades during and shortly after the backfilling (Belem et al., 2018; Zheng & Li, 2020). After backfilling, the total pressures on backfilled stopes and barricades decrease significantly due to several phenomena such as the development of the arching phenomenon, dissipation of pore water pressure (PWP), and cemented backfill hardening (Belem et al., 2004a; Potvin et al., 2005; Belem & Benzaazoua, 2008; Belem et al., 2016; Li, 2019). Numerous analytical approaches, predictive models, and in situ measurements have been suggested through the literature, in which each

investigation has its benefits and limitations, but further investigations are required to determine the critical backfill pressure on the barricade and its design procedure. Several mine stopes were implemented with in situ instrumentation (Belem & Benzaazoua, 2004; le Roux et al., 2005; Thompson et al., 2009; Helinski et al., 2010; Thompson et al., 2012; Hasan et al., 2014) to evaluate the PWP and total/effective stresses in stopes. Also, several reduced-scale physical models of mine stopes have been used to study the distribution of vertical stresses (Sivakugan & Widisinghe, 2013; Widisinghe et al., 2013; Widisinghe et al., 2014; Widisinghe, 2014) or to study the self-weight consolidation settlement of the paste backfill in different drainage conditions (see Belem et al., 2016). Numerical modeling is another approach commonly used to evaluate the stress state in backfilled stopes and to study the influence of different parameters, such as backfill properties, characteristics of the fill/wall interface, the rate of the filling, and pores' water pressures (Li et al., 2003; Li et al., 2007; Pirapakaran & Sivakugan, 2007; Hassani et al., 2008; Li & Aubertin, 2008; Fahey et al., 2009; Li & Aubertin, 2009d, a, c, b, e, 2010; El Mkadmi, 2012; Veenstra, 2013; Emad et al., 2014; Falaknaz, 2014; Doherty, 2015; Pengyu & Li, 2015; Yang, 2016; Cui & Fall, 2017; Suazo & Villavicencio, 2018; Lu et al., 2020). Designing waste rock barricade, however, represents a significant problem, and more research is needed to determine the critical backfill pressure on the barricade.

Two approaches to studying problems in geotechnical engineering are the instrumentation of the actual site/structure and the use of small-scale models. The instrumentation of a full-scale structure makes it possible to validate the results and design methods as well as the calibration of numerical models. In real mining stopes, it is difficult to monitor the barricade–backfill interaction as well as to study the mechanism of the collapse of the waste rock barricades and their ultimate strength. Therefore, small-scale physical models seem to be the plausible way to study such a case. Laboratory testing using these models facilitates the control or modification of material properties and increases stress to failure. Scale model experiments have been conducted for a very long time and under specified conditions. The model must fulfill such requirements to be able to transpose its mechanical behaviour to that of the full structure (Appendix F includes more details). The establishment of similarity laws is based on dimensional analysis, taking into account the invariance of the general equations of mechanics to the unit change (Corté, 1989b). These equations are the general equations of dynamics, the mass conservation equation, and the constitutive laws of various materials. Often, it is challenging to meet all these conditions at the same time, forcing

experimenters to settle for a wider similarity (Niemann, 1995; Garnier, 1997, 2001). Physical modelling can be classified, with regard to similarity conditions, into three main categories: (i) total similarity, if the model simulates all the characteristics of the prototype (full scale), (ii) partial similarity, if the model does not meet certain similarity conditions, in order to improve the prediction of certain aspects of the behaviour of the prototype, and (iii) qualitative similarity, if there is no similarity between the model and the prototype, but with some analogy, the model can accurately predict the behaviour of the prototype. Our research project is classified in the third category, which deals with the qualitative study of a complex phenomenon. In this study, a small-scale model is used to conduct qualitative experiments (at 1/50th of scale length factor) on the stability and failure mechanisms of waste rock barricades during paste backfill placement. This small-scale model, which is made from transparent plexiglass for simulating underground backfilling, allows to visually observe the interaction between the barricade and the backfill. The transparent model also allows the barricade to be monitored during saturation, drainage, and at failure when additional external pressure is applied. This study addressed different issues such as the effect of total pressure induced by the backfill on the barricade, the effect of waste rock particle gradation on the barricade-backfill interaction, and the stability/failure of waste rock barricades.

3.2 Small-Scale Model and Equipment Description

Figure 3-1 shows the small-scale model used with the associated measurement tools. This reduced physical model is designed to simulate underground backfilling operations. A waste rock barricade retains the paste backfill injected in the physical model (longitudinal-type stope) during the filling. This model, with a length scale factor L^* of 1/50 ($L^* = L_{model}/L_{prototype}$), will mimic a typical mine longitudinal stope in the Abitibi region in Quebec (Canada).

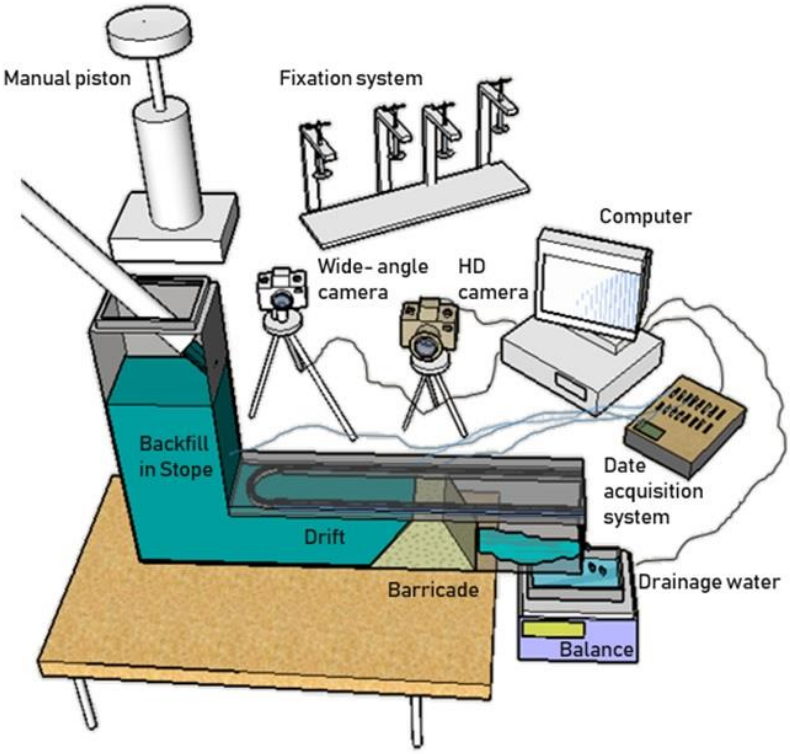


Figure 3-1: A small-scale model of a mine stope made of transparent plexiglass, including the measurement tools.

The small-scale model was built from acrylic glass or plexiglass ((Poly (Methyl Methacrylate) (PMMA)). The PMMA plates of the model have smooth surfaces and may not well reflect the rock wall–backfill interface. Therefore, this research does not address the arching effect phenomenon that can affect the stress state in the backfill. The main feature of this type of PMM is its transparency, which allows monitoring the barricade and its interaction with the backfill during and after placement. The filling chamber (stope) has a horizontal section of 9 × 20 cm and a height of 38 cm (can be increased by another 38 cm to a full height of 76 cm during placement of the second layer). The stope is connected to a drift (called drawpoint), which has a vertical section of 9 × 9 cm and a length of 63 cm. The pressure induced by the backfill on the barricade is measured using mini-pressure sensors positioned at different locations inside the model. The small-scale model is also equipped with a manual external loading system (a piston) to increase the pressure on the barricade until the failure. The small-scale model does not satisfy the first-order similarity due to cost constraints and the inability to achieve some similarity conditions. A high-resolution camera was used to help analyze the barricade displacement and its failure mechanism. A second camera was also used to capture the manipulations during backfill placement (Figure 3-1). The

barricade monitoring is recorded in 2D only through the transparent walls of the drift, assuming that the particles at the core of the barricade will have the same behaviour. Image processing was used to study the failure of the barricade mechanism and its behaviour (see Appendix G for more details). The pressure at different points in the reduced-scale model is measured using two types of pressure sensors (strain gauge transducers) with a capacity of 100 kPa. Assuming that the total stresses are equivalent to the pressures measured by the total earth pressure sensors (TEP), the pore water pressures sensors (PWP) are equal to those measured by the mini-piezometers, and the effective stresses are the difference between their values (TEP – PWP). Two different types of sensors, according to their size and properties, are used to measure the total earth pressure (model PS-D and model DMTY). The PWP is measured using miniature pore water pressure gauges (model DMKY) attached to a data acquisition system that has the same brand (Dan street Nanjing Electronic Technology Co., Nanjing). The earth pressure sensors are ideal for measuring the stress of the soil, mud, and sand. The strained full-bridge circuit can eliminate the influence of temperature changes on the sensor. A high-precision full-bridge strain gauge is pasted inside the sensor's sensing membrane. When external pressure acts on the surface of the sensing membrane, the membrane deforms, causing strain in the strain gauge (Appendix H includes more details). The DMKY sensors are suitable for measuring the pore water pressure (osmotic pressure) inside or around the soil, mud, sand, and model piles in the model test. Table 3-1 shows the characteristics of the sensors used in the experimental tests conducted on the physical model.

Table 3-1: Geometric characteristics of the three types of stress sensors used on the reduced model.

Sensor	**Total Earth Pressure (TEP) Sensors**		**Pore Water Pressure (PWP) Sensor**
Manufacture (brand)	KYOWA	Dan street Nanjing Electronic Technology Co.,	
Model Type	PS-D	DMTY	DMKY
Capacity	50 kPa	100 kPa	100 kPa
Size	6 × 0.6	12 × 4.2 mm	15.8 × 21 mm
Rated Output	500×10^{-6} strain	400×10^{-6} strain	400×10^{-6} strain
Overload	150%	120%	120%
Input/output resistance	350 Ω	350 Ω	10,000 Ω
Exciting voltage	2 V	2 V	2 V

Before using pressure sensors in any application, they must be calibrated under the same conditions as their intended use, and the sensors must be recalibrated periodically to check their response under external loading. Usually, earth pressure cells are calibrated under a uniform loading

condition, called fluid calibration, where a special type of arrangement is used to apply oil pressure only over a cell's sensing area, and this type of calibration is done by the manufacturers (Gade & Dasaka, 2018). Pressure applied to calibrate the sensor is ideally conducted in two cycles of amplitude (loading/unloading). It requires good linearity and a small difference in sensor response between charge and discharge (hysteresis).

In this work, a graduated column of water was used to calibrate the sensors used in the experimental tests. The water pressure on the sensors is calculated by multiplying the unit weight of the water by the height of the column. To calibrate the sensors used, they were fixed to a horizontal plate holding a vertical ruler within a deep-water tank to measure the water column (Figure 3-2).

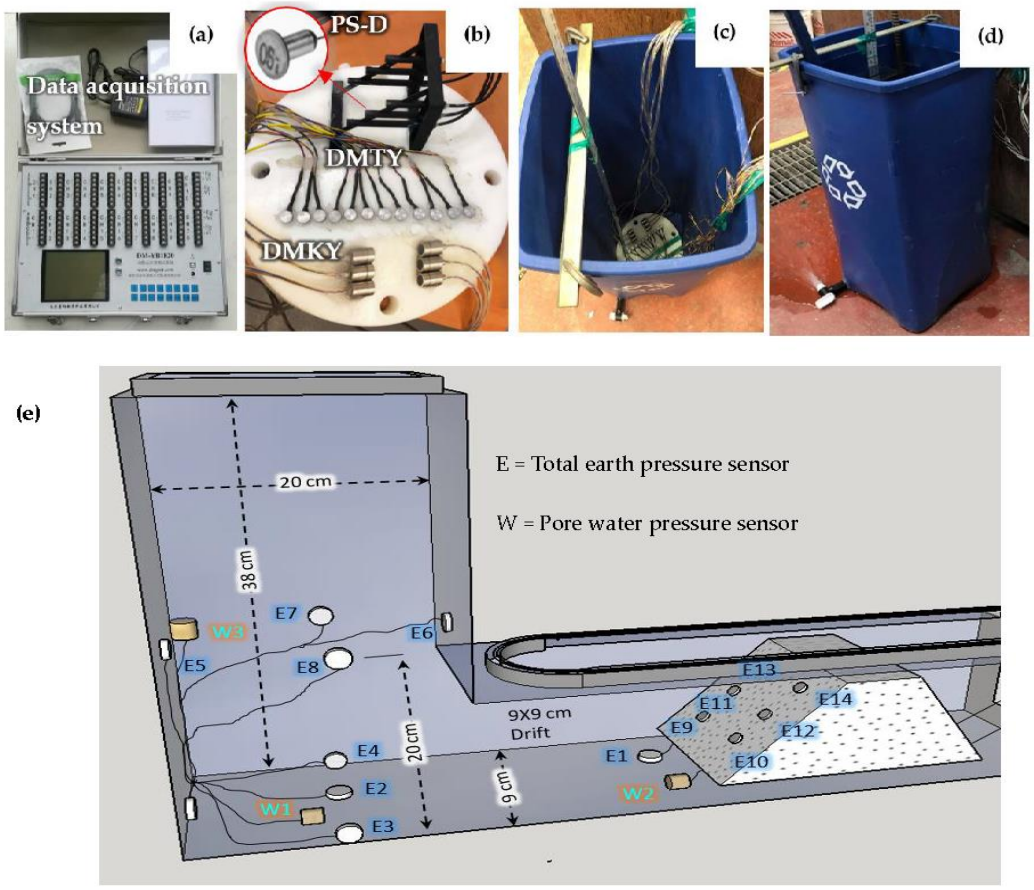
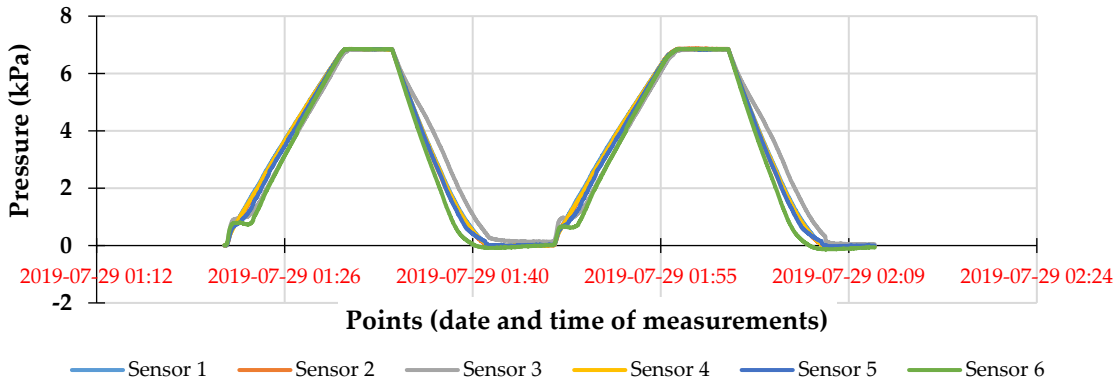


Figure 3-2: Experimental protocol and arrangement: (a) strain gauge data acquisition system (20 channels), (b) all pressure sensors used are installed on a plate before calibration, (c) pressure sensors attached to a plate at the base of a bucket for the calibration, (d) calibration procedure of the pressure sensors using water, and (e) dimensions of the model and the different locations of the pressure sensors.

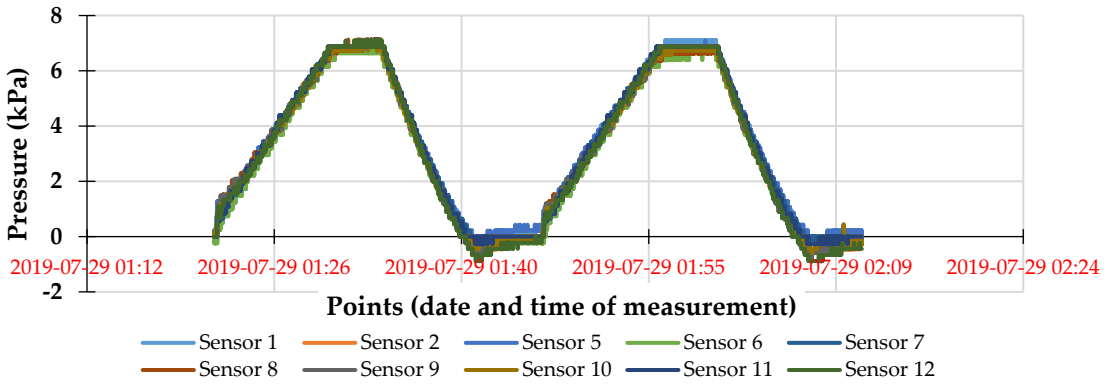
The pressure recorded by the sensors was compared to the pressure of the water column inside the bucket. A calibration factor was calculated for each sensor to correct the pressure measurement. A valve was installed at the base of the tank to empty the water. This procedure allows the pressure on the sensors to increase and decrease during calibration. The calibration of the sensors is done by pouring water until 71 cm height, and the results were satisfactory ($p_{water} = \gamma_w \times h_w = 9.81\ kN/m^3 \times 0.71\ m = 6.96 \approx 7.0\ kPa$).

Figure 3-3 presents the calibration of the sensors of pressure used in the experimental tests. These sensors were calibrated before each test (in loading/discharging) to check the hysteresis of the sensor and correct the calibration factor.

a)



b)



c)

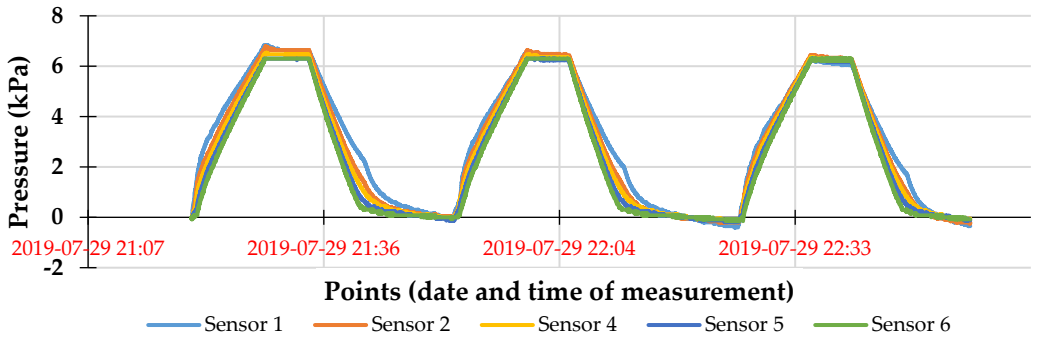


Figure 3-3: Calibration of pressure sensors a) DMKY sensors, b) DMTY sensors, c) the sensors at the face of the barricade (PS-D).

The sensors were positioned at various locations to measure the maximum backfill pressure (vertically and laterally) at the base of the stope and above the drift level. The barricade was also instrumented to determine the backfill pressure (especially on the upper part), and to study the change in stress state during drainage. Several pressure sensors were placed at the base of the model, four sensors at the base of the stope, and two in front of the barricade. Four total earth pressure sensors, E1 to E4 (model DMTY), were used to measure the total backfill pressure (horizontal and vertical) and two-pore water pressure sensors, W1 and W2 (model DMKY), were used to measure the water pressure. On the second level (20 cm above the base of the stope), four total earth pressure sensors (E5 to E8) and one pore water pressure sensor (W3) were installed. Other types of total pressure sensors, E9 to E14 (model PS-D from KYOWA), have been attached to the face of the barricade to measure the backfill pressure on the barricade (Figure 3-2e).

3.3 Material Characteristics

3.3.1 Mine Tailings

Figure 3-4a presents the grain size distribution (GSD) curve of the tailings used (LaRonde mine tailings) for the preparation of the backfill. The GSD curve was determined on a homogenized tailing sample using a Malvern Mastersizer S 2000® (Malvern Panalytical, Malvern, UK) laser particle analyzer. The GSD analysis showed that about 46% of the tailings sample are finer than 20 µm (i.e., ultrafine particles content or $P_{20\mu m}$). The specific gravity of the tailings (G_s) was determined to be 3.32 using a helium pycnometer (AccuPyc 1330, MicroMeritics, Norcross, GA, USA).

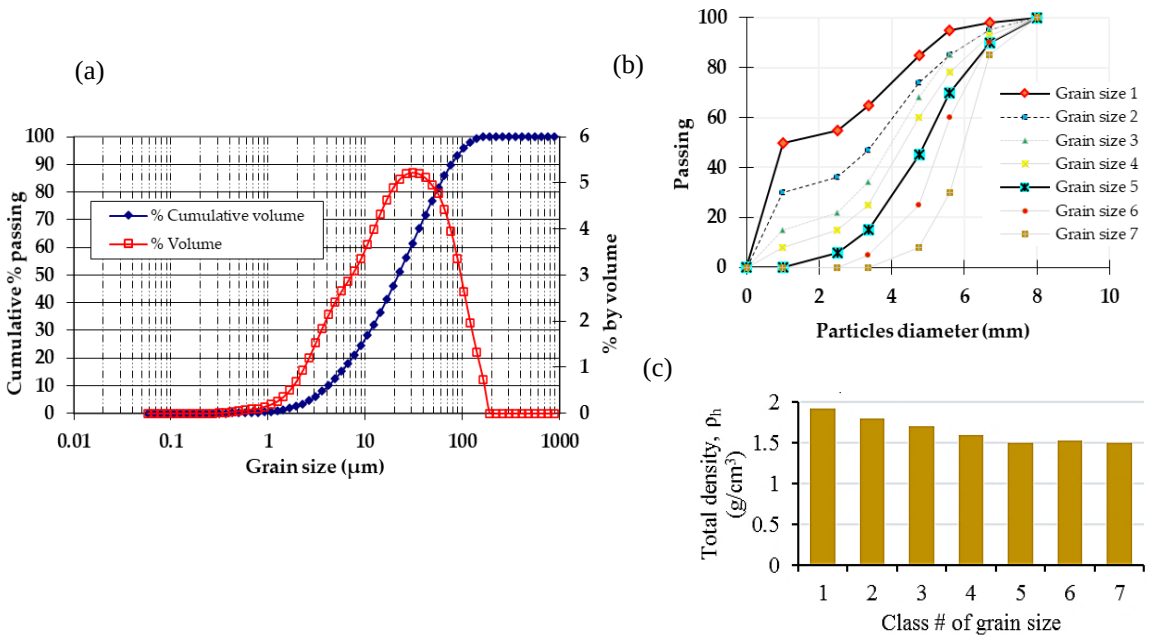


Figure 3-4: Material characteristics: (a) grain size distribution (GSD) curve of the mine tailings sample, (b) particles' size distribution curves of the waste rock barricade, and (c) barricade total or bulk density as a function of the particle size distribution curve number (from #1 to #7).

Besides, other analyses (mineralogical analysis, total sulphur, and carbon content) were conducted. All characteristics of the mine tailings are presented in Table 3-2.

Table 3-2: Characteristics of the mine tailings used in the experimental tests (LaRonde mine tailings).

Physical Characteristics		**Mineralogical Analysis Semi-Quantitative Mineralogical Analysis by X-Ray Diffraction**	
Parameter (Units)	**Values**	**Mineral**	**Values**
Specific gravity, G_s	3.32	Quartz	44.84%
Ultrafine content $P_{20\mu m\ (\%)}$	46%	Pyrite	25.73%
D_{10}, effective particle size (µm)	4.16	Chamosite 1M	4.38%
D_{30}, size of 30 % passing (µm)	11.25	Paragonite 1M	2.98%
D_{50}, average particle size (µm)	21.75	Albite	2.10%
D_{60}, size of 60 % passing (µm)	29.18	Muscovite 2M 1	9.61%
D_{90}, size of 90 % passing (µm)	76.35	Orthoclase	1.56%
$C_U = D_{60}/D_{10}$, coefficient of uniformity	7.02	Labradorite An65	3.09%
$C_C = D_{30}^2/(D_{60} \times D_{10})$, coefficient of curvature	1.04	Microcline	3.66%
Unified Soil Classification System (USCS)	ML (low plastic silt)	Chalcopyrite	0.45%
		Sphalerite	0.16%
		Gypsum	1.45%
Total sulphur analysis and carbon by induction furnace			
$C_{total\ \%}$ p/p (method detection limit, MDL = 0.05)	0.256	$S_{total\ \%}$ p/p (MDL = 0.009)	15.9

3.3.2 Waste Rock Barricade

It is not easy to obtain accurate gradations of waste rock. Different methods, such as sampling and laboratory measurements, in situ determination, and image analysis of photographs (e.g., WipFrag^{TM}), can be used to estimate the particle size distribution (McLemore et al., 2009). Typical waste rock shows a wide gradation curve (from silt to boulders size) with a coefficient of uniformity ($C_U = D_{60}/D_{10}$) of 20 or more (Barbour et al., 2001; Aubertin et al., 2002). The typical angle of repose of waste rock is near to 37° (±3°), which may differ with the physical characteristics of the waste rock (Aubertin, 2013). The size of the waste rock particles can range from 75 μm to about 10 cm and above (Maknoon, 2016). Throughout construction phases, the design of rock waste barricades to maintain fresh paste backfill columns must be carried out carefully (building and forming a pile of waste rocks, compaction using a scoop equipped with a push-plate, and placement of a shotcrete layer) (Belem et al., 2018, Gélinas, 2017). The barricade capacity (resistance) depends on the material used, shape, sizes, and construction quality. The materials used for the construction of the waste rock barricades are the development of waste rocks that are also used for rockfill preparation underground. An experienced operator needs fewer attempts to raise the material and plug the gaps between the barricade and the gallery roof (Gélinas, 2017). It is difficult to evaluate the strength of the waste rock barricade in the drawpoint after the construction. In addition, little information is available on the characteristics of the waste rock barricades (e.g., grain size distribution, shear strength, friction angle, etc.) for an appropriate design purpose. In practice, a layer of shotcrete is used to close the top gap after the barricade construction to avoid any risk of the backfill spill (Belem et al., 2018, Gélinas, 2017).

For this study, seven-grain size distribution (GSD) curves were established, but only three gradations (#1, #2, and #5) were presented in this paper (Figure 3-4b). These different proposed GSD were based on visual and experimental observations in the laboratory in order to study the behaviour, strength, and failure mechanisms of the barricade. The barricade particle diameter varies from 0 to 8 mm in the reduced-scale model, assuming that this particle diameter varies between 0 and 400 mm in the actual-size barricade. The GSD #1 curve represents a barricade made of fine materials (50% smaller than 1 mm), while the GSD #5 curve represents a barricade without fine particles (minimum diameter of 3.35 mm) and other GSDs are in between.

The volume of the trapezoidal barricade used is 1304 cm^3 (25 cm base length, 7.2 cm top length, height = width = 9 cm). The waste rock's apparent dry density ranges from 1.5 to 1.9 g/cm^3 (increases with the increase in fine materials, Figure 3-4c).

3.4 Experimental Setup and Program

Five steps are required to perform the small-scale model testing: (i) setting up the reduced-model, the instruments, and the materials, (ii) calibrating the pressure sensors and verifying the measurements, (iii) starting the test according to the scenario, the material properties, and backfill sequences, (iv) measuring the induced pressures and displacements of the barricade during backfilling, and (v) analyzing the results and varying the particles gradation of the waste rock barricade or the backfill properties for the next test.

3.4.1 Setting up the waste rock barricade

Three steps were used for shaping the barricade in the drawpoint: (i) manufacturing various sizes of trapezoidal moulds for use in building barricades made of crushed waste rock, (ii) placing the mould in the access drift (drawpoint) and then filling it with crushed waste rock (in two compacted layers, each layer is tamped 25 times with a 600 mm-long bullet-nosed metal rod measuring 16 mm in diameter) following a particle diameter scale factor of 1/50 ($d^* = d_{model}/d_{prototype}$), and (iii) lifting the trapezoidal mould after shaping the waste rock barricade. For some test scenarios, several thin, transparent silicone lines are attached to the base of the drift to increase the frictional resistance of the barricade, and to prevent the barricade from sliding. A three-dimensional (3D)-printed plastic frame (Figure 3-2b) was used for attaching the pressure sensors facing the barricade. This frame contains six sensors placed on three levels (at 2.7, 4.5, and 6.3 cm from the base of the model).

3.4.2 CPB Mix Design and Preparation

The required quantities of water and binder to be added to the wet tailings should be calculated before preparing the backfill. The cemented paste backfill ingredients (water, binder, and tailings) can be calculated after knowing the expected backfill volume (V_f) for filling the reduced scale model, the required binder ratio (B_w), and the targeted final solid mass concentration of the CPB (C_{w-f}). The first step is to determine the specific density (ρ_{s-t}) of the tailings and their water

content (w_t) on arrival at the lab. Next, the backfill mix design and proportioning can be done using several equations (see Appendix B for more details).

The required total mass of dry tailings (M_t) in the backfill mixture is given by:

$$M_t = \frac{M_f}{1 + w_f}\left[\frac{1}{1 + B_w}\right] \tag{3-1}$$

Where M_f = the fill mass (g or kg), w_f = the fill water content (decimal; $w_f = (1/C_{w\text{-}f} - 1)$), B_w= ($M_{binder}/M_{tailings} = M_b/M_t$) = the binder rate used (in decimal).

The final solid mass concentration $C_{w\text{-}f}$ of backfill is given as follows:

$$C_{w-f} = \frac{M_t + M_b}{M_f} \tag{3-2}$$

The fill mass to be placed in the model is given as follows:

$$M_f = V_f \times \rho_{h-f} \tag{3-3}$$

Where ρ_{h-f} = bulk or wet density of the fill that is given by the following relationship:

$$\rho_{h-f} = \left[\frac{C_{w-f}}{\rho_{s-f}} + \frac{1 - C_{w-f}}{\rho_w}\right]^{-1} \tag{3-4}$$

Where C_{w-f} is in decimal, ρ_w = density of water (1g/cm^3), and ρ_{s-f} = the specific density of the backfill which is given as follows:

$$\rho_{s-f} = (1 + B_w)\left[\frac{1}{\rho_{s-t}} + \frac{B_w}{\rho_{s-b}}\right]^{-1} \tag{3-5}$$

Where ρ_{s-t} is the density of the tailings solid grains (in g/cm^{3}or kg/m^3) and ρ_{s-b} is the density of the binder.

In mine backfill practice, several types of binding agents are used, but the most common is general use Portland cement (GU), which is usually fractionally replaced by mineral additives with pozzolanic effects, such as fly ash (FA) and smelter ground granulated blast furnace slags (GGBFS)

(Belem & Benzaazoua, 2008). In this case, the binder solid grains density (ρ_{s-b}) is given as follows:

$$\rho_{s-b} = \left[\frac{p1}{\rho_{s-GU}} + \frac{p2}{\rho_{s-FA}} + \frac{p3}{\rho_{s-GGBFS}} + \cdots\right]^{-1} \quad (3\text{-}6)$$

Where $p =$ the proportion of each binder component (1, 2, 3, …).

The mass of binder (M_b) is given as follows:

$$M_b = B_w \times M_t \quad (3\text{-}7)$$

In order to achieve a final target value of $C_{w\text{-}f}$, the total amount of water in the backfill mixture (M_w) is given as follows:

$$M_w = \left(\frac{1}{C_{w-f}} - 1\right)(M_t + M_b) = M_f - (M_t + M_b) \quad (3\text{-}8)$$

Taking into account the amount of water already present in the tailings before the backfill preparation, the amount of water that should be added to the mixture (M_{w-add}) is given in the following relationship:

$$M_{w-add} = M_w - M_t \times w_t \quad (3\text{-}9)$$

At the beginning of the backfill preparation, the water and the binder are first mixed to obtain a slurry before progressively adding the wet tailings ($M_{t\text{-}wet} = M_t\,(1 + w_t)$).

Backfill ingredients are mixed using the Hobart mixer (Figure 3-5a) at a low speed for about 15 min. At the end of mixing, the backfill consistency is determined through the slump test by using the standard Abrams' cone. The backfill was prepared with a 70% solids percentage (except for the final test, $C_{w-f} = 76\%$) and 5% binder (general use Portland cement, or type GU) to allow proper control and easy filling by hand. The fresh backfill is a heavy fluid-like material after mixing, and the measured slump was about 275 mm (10.8 inches). After backfill preparation and shaping the barricade in the drawpoint (Figure 3-5b), the model is filled with the backfill mixture (8136 cm^3 volume) over a short period (approximately 5 min maximum). The stress state of the backfill is recorded during the self-weight consolidation (Figure 3-5c).

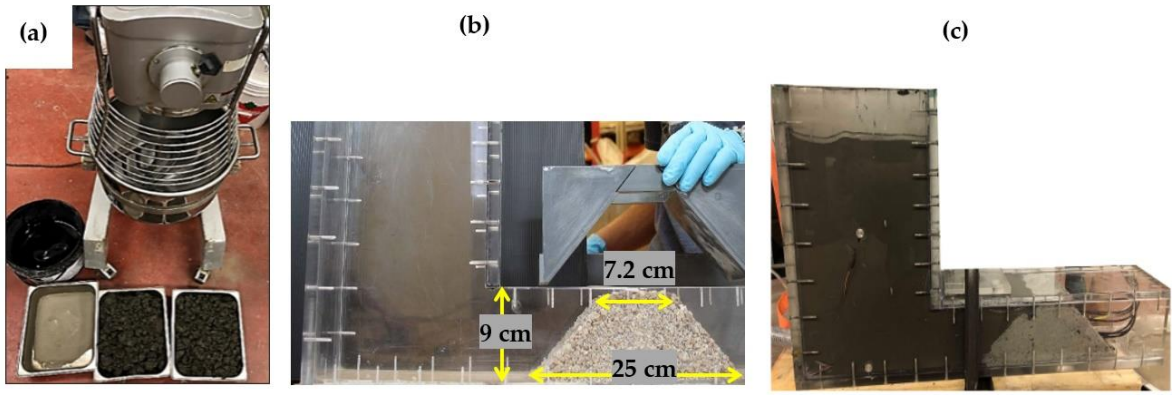


Figure 3-5: Experimental protocol: (a) paste backfill mixture preparation using a Hobart mixer and backfill ingredients (water, tailings, and binder), (b) setting up the barricade in the drawpoint, and (c) the first layer of the backfill after pouring and self-weight consolidation took place.

For the tests conducted to study the failure mechanism of the barricade, the external loading system (piston) is installed once the model is filled. The backfill pressure on the barricade is increased until its collapse (failure or sliding). During this stage, the behaviour of the barricade is monitored using high-resolution cameras.

3.4.3 Program experimental

Two series of tests were performed to study the geomechanical behaviour of the waste rock barricades made up of two different particle size distributions (#1 and #5). The GSD #1 and #5 barricades were examined, and three tests on each gradation were carried out for different purposes. The objective of the first two tests is to study the stress state during a sequential backfill placement in two layers (C_w = 70%). The first backfill was an uncemented backfill (tailings slurry only), while the second backfill contains 5% of Portland cement (GU). The third test was performed to study the strength and failure mechanism of the waste rock barricade by increasing the pressure externally and manually at the top of the stope using the hand piston. Also, only one test was conducted on the GSD #2 to study its mechanism failure and compare it with the GSD #1 and #5. The amount of drainage water collected was determined and the corresponding vertical or volumetric strain of the backfill due to self-weight consolidation (settlement) were calculated.

3.5 Results

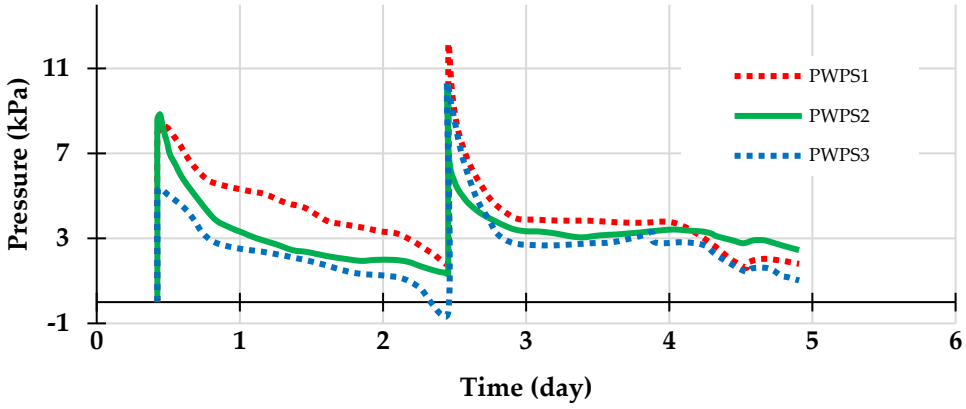
3.5.1 Stress State after the Placement of the Backfill in the Small-Scale Model

3.5.1.1 Uncemented Backfill

The first test is aimed at studying the influence of the barricades' particle gradation (GSD #1 and #5) on the stress state of an uncemented backfill (C_w = 70%) sequentially placed in two layers (one layer every two days). The two types of sensors (TEPs and PWPs) give a pressure equivalent to that of the overburden after the backfill placement, and then the pressures change due to the dissipation of the pore water pressure. The backfill behaves like a heavy fluid during this short phase, and the stress increases linearly with depth (no arching effect). The barricade is usually placed in a dry state in the drawpoint. The barricade containing fine material (GSD #1) started drainage after it was fully saturated, whereas, with the GSD #5 barricade (no fine material), drainage began before full saturation.

The backfill pressures varied in the different locations in the model. It was observed that for both barricade configurations (GSDs #1 and #5), the pore water pressure dissipates rapidly in the middle of the stope and near the barricade (PWPs 2 and 3), compared to the pressure at the base of the stope (PWP 1). For the GSD #1 barricade, the values of water pressures converged after the second layer placement, while pressures for the GSD #5 barricade remained at the same interval (Figure 3-6).

(a)



(**b**)

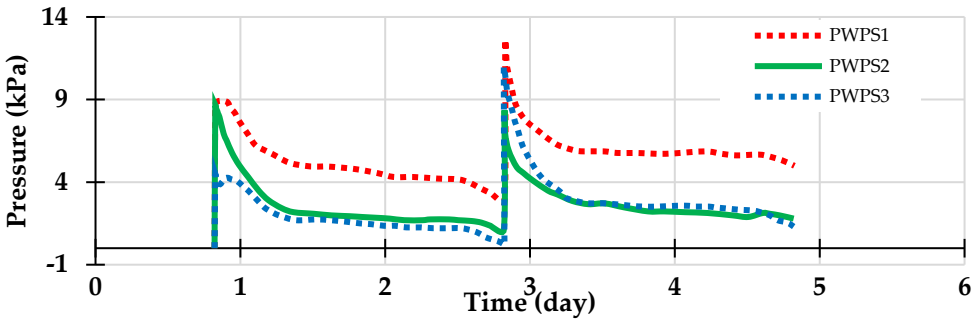


Figure 3-6: Measurement of pore water pressure of uncemented fill at three locations in the model: (a) for the GSD #1 barricade, and (b) for the GSD #5 barricade.

During the sequential placement of the backfill layers, the placement of each last layer induces an excess of PWP in this newly added layer. After the PWPs are dissipated, the stresses become significantly lower than those calculated from the overburden, particularly near the base of the stope. When enough time is allotted before a new layer is added, drainage leads to more pronounced dissipation of PWP, which can then become negative (i.e., suction).

The self-weight consolidation process of a sequential filling in each newly added layer follows a similar trend as the one observed for the instantaneous filling. The volumetric strain ($\varepsilon_v = \Delta V / V_0$) of backfills of the uncemented backfill (C_w = 70%) was about 16.3% for each layer. The mixing water bleeds to the top of the filling chamber after each backfilling installation: this step is accompanied by consolidation and backfill settlement (Figure 3-7). The barricade gradually saturates, and the water level at the stope top drops through drainage. Although pore water pressure sensors indicate a slight pressure and drainage stoppage after four days, the backfill near the barricade remains saturated and can flow if additional pressure is applied. This result highlights the importance of using the binder in the backfill, especially for the first layer.

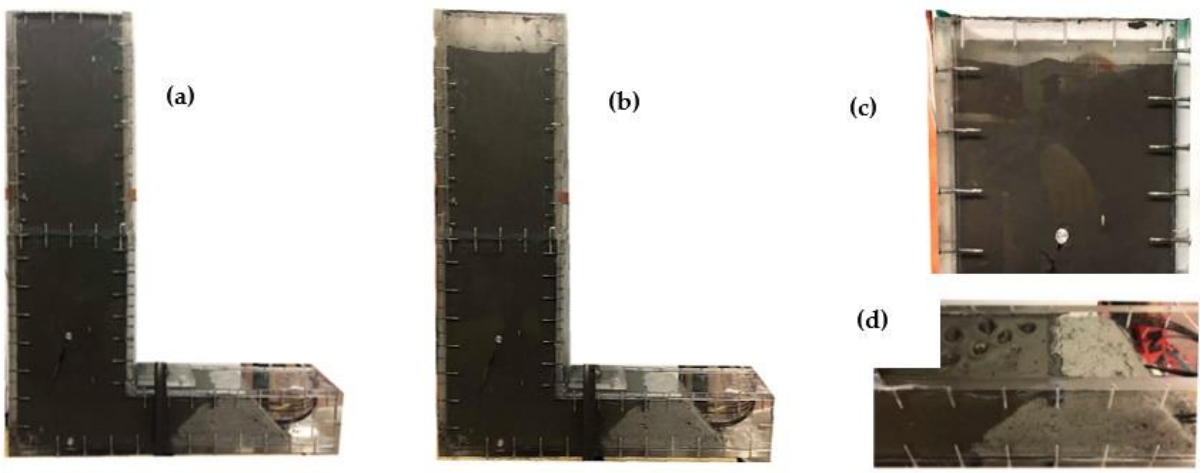
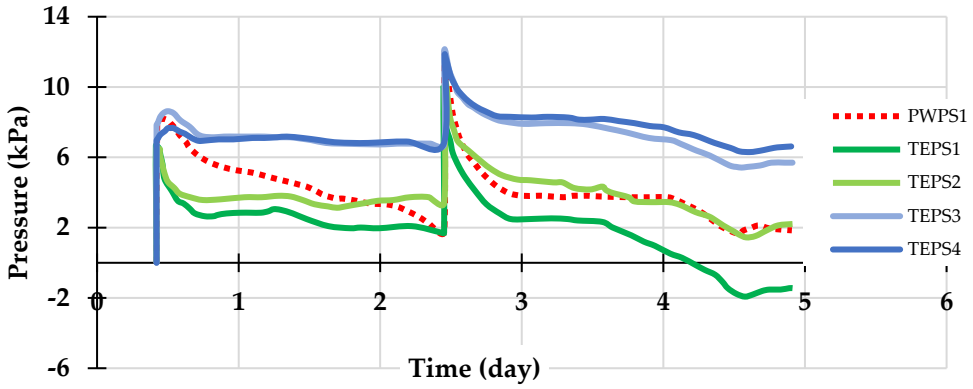


Figure 3-7: Uncemented backfill tests: (a) pouring of the second layer of backfill, (b) the model after self-weight consolidation of the second layer, (c) backfill bleeding water at the top of the filling chamber after each placement of the backfill, and (d) the state of the backfill near the barricade after four days (two layers were continuously poured, once every two days).

The pressure measured by the sensors attached to the base of the model decreases with water dissipation, while the lateral sensors indicated a slight reduction in pressure after backfilling and remained constant even with water dissipation during drainage (Figure 3-8). Drainage tends to reduce these pressures and increase the frictional resistance along the walls. As drainage occurs, the phreatic surface level (where u = 0) drops within the stope, creating an unsaturated zone in the upper part.

(a)



(**b**)

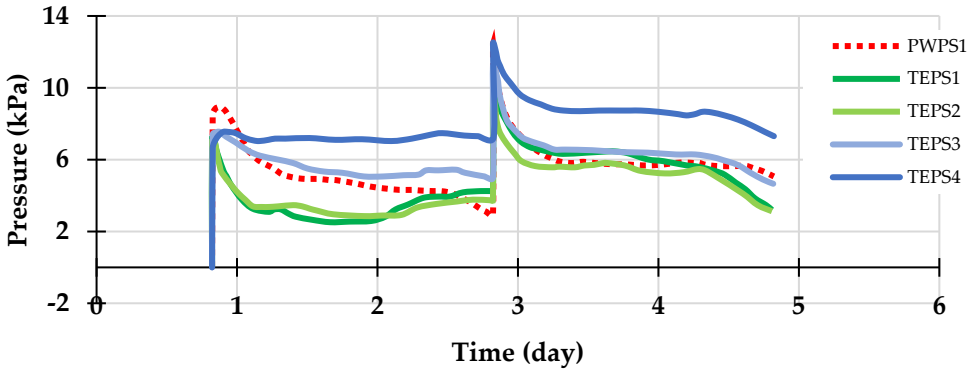
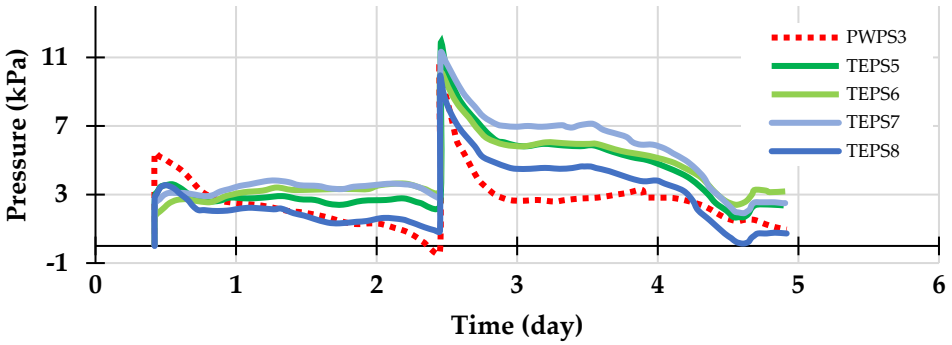


Figure 3-8: The measurement of the backfill pressure at the base of the stope: (a) for the GSD #1 barricade, and (b) for the GSD #5 barricade.

The pressure sensors are affected by atmospheric pressure and air entering during drainage, which can result in negative pressures. The negative pressure value means that the atmospheric pressure around the sensors has been reduced, maybe due to the suction development within the unsaturated zone, compared to the pressure before the test (zero offset point). The lateral sensors used to measure the backfill pressures in the middle of the stope also indicated a slight decrease in pressure relative to the pore water pressure (Figure 3-9). This result can be attributed to the progressive increase in the density of the fill during the self-weight consolidation process. The lateral pressure does not remain stable for a long time during the consolidation process, where it decreases with the dissipation of pore water pressure.

(**a**)



(**b**)

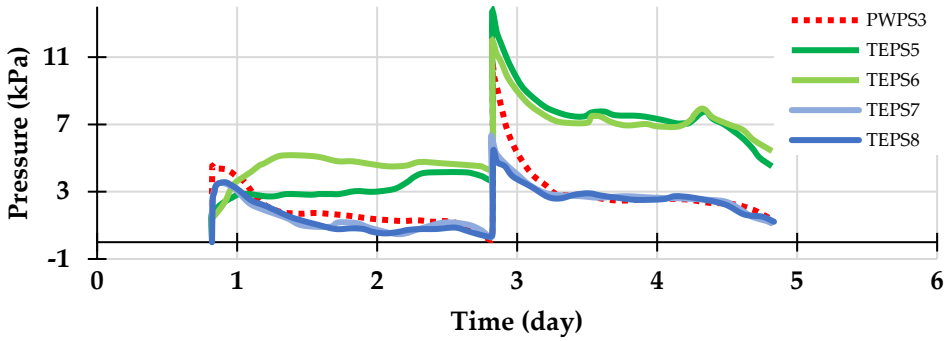
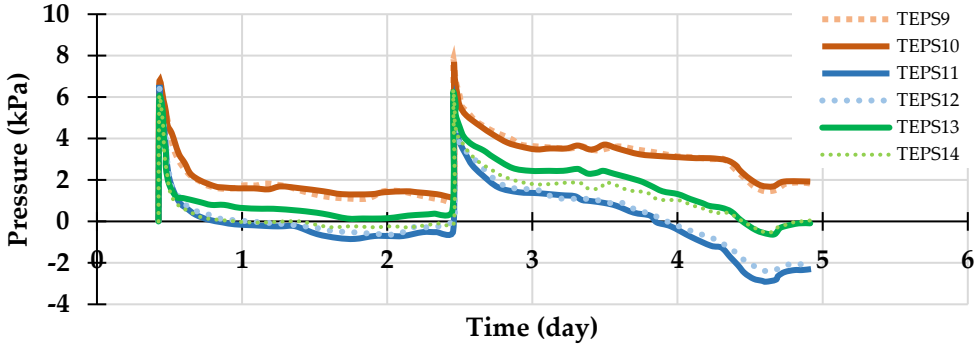


Figure 3-9: The backfill pressure at 20 cm above the base stope: (a) for the GSD #1 barricade, and (b) for the GSD #5 barricade.

The pressure applied to the barricade after the placement of the first layer was equivalent to the overburden pressure, then gradually dropped due to barricade saturation (Figure 3-10). The slope of the decreasing pressure after the second placement of the backfill is different because the barricade has become saturated. The barricade made of fine materials (GSD #1) slowly desaturates from top to bottom so that after the pore water has dissipated, the pressure becomes negative. Whereas the barricade made up of coarse materials (GSD #5) allowed air to enter once the drainage ceased. This observation showed that the characteristics of the barricade would influence the stress state of the backfill after placement.

(**a**)



(**b**)

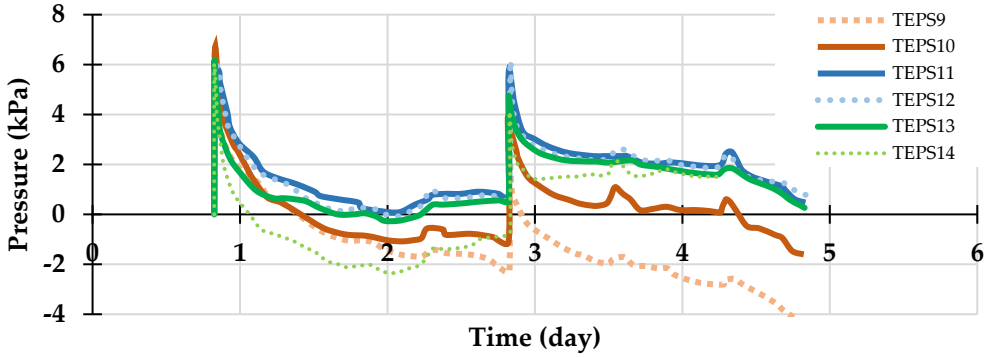


Figure 3-10: The pressure of the backfill on the barricade: (a) for the GSD #1 barricade, and (b) for the GSD #5 barricade.

The drainage water collected and the sensors located in front of the barricade have shown that the barricade that does not contain fine materials (i.e., GSD #5) accelerates the drainage of the backfill water, which rapidly reduces backfill pressure after placement (Figure 3-11). Two days after backfill placement, the pore water pressure at the base of the filling chamber was reduced by 75% and was null on the barricade.

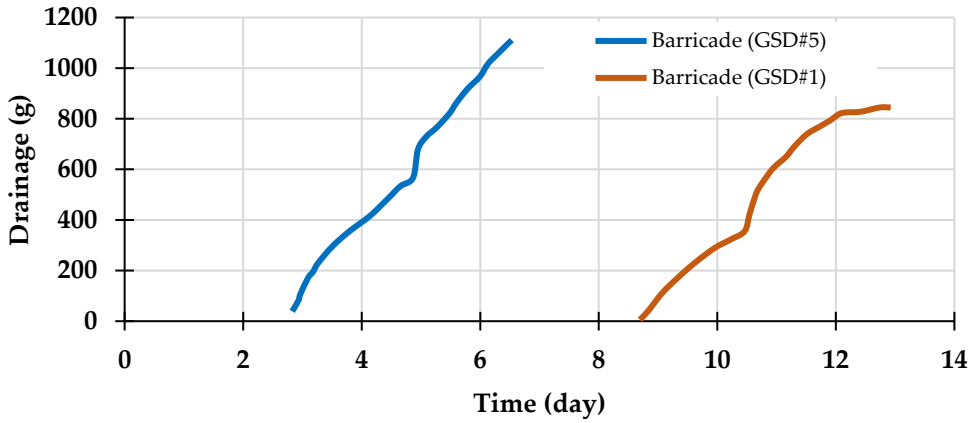


Figure 3-11: The drainage water collected during the tests.

3.5.1.2 Cemented Backfill

This section shows the influence of the grain size distribution of the barricades (GSD #1 and #5) on the stress state of a cemented paste backfill containing 5% of the GU binder (C_w = 70%). The first case for a CPB placed in a single sequence (height of the filling chamber = 76.6 cm and barricade GSD #1), but the measurement was stopped after 5 h due to a power failure. The test presents the backfill stress measurement only in the first few hours after placement. It seems that

the pressures of the cemented fill on the barricade have the same value after backfilling and then differ during drainage (Figure 3-12).

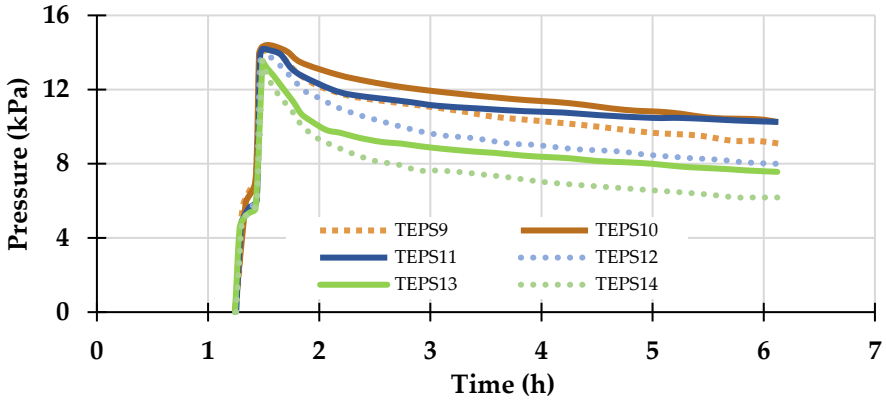
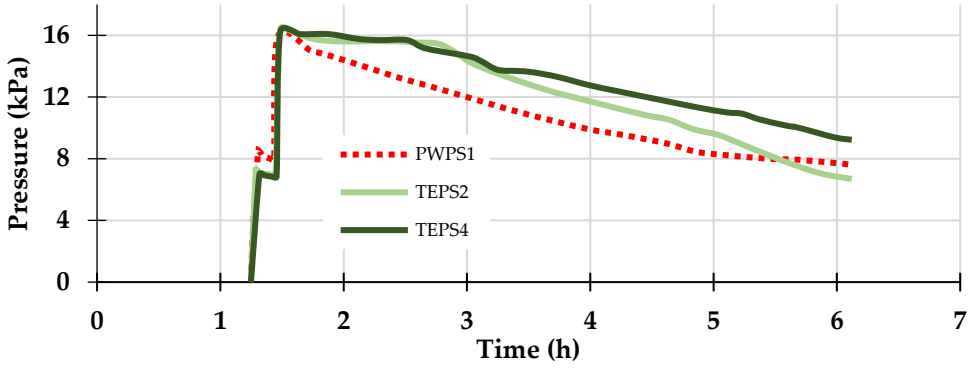


Figure 3-12: The backfill pressure measurement on the upstream side of the barricade.

The sensors (PWPs and TEPs) indicated a pressure equal to that of the overburden after backfill placement (Figure 3-13), except for PWPS3 (above the drift), which was slightly larger.

(**a**)



(**b**)

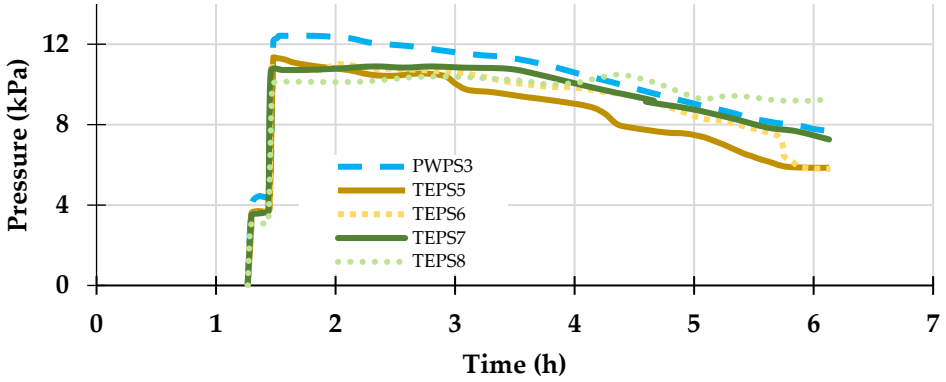


Figure 3-13: Backfill pressure measurement: (a) at the base of the stope, and (b) at 20 cm above the base of the stope.

A pore water sensor was placed inside the barricade (PWPS 4) to measure the water pressure inside the barricade during drainage. The pressure measured inside the barricade increased during its saturation to only about 6% of the pore water pressure at the base of the stope (after 5 h; Figure 3-14). At the end of the CPB self-weight consolidation in the filling chamber (stope), the calculated total volumetric strain was approximately 4.6%. This value is similar to that already observed in situ and during column (physical model) tests (Belem et al., 2016).

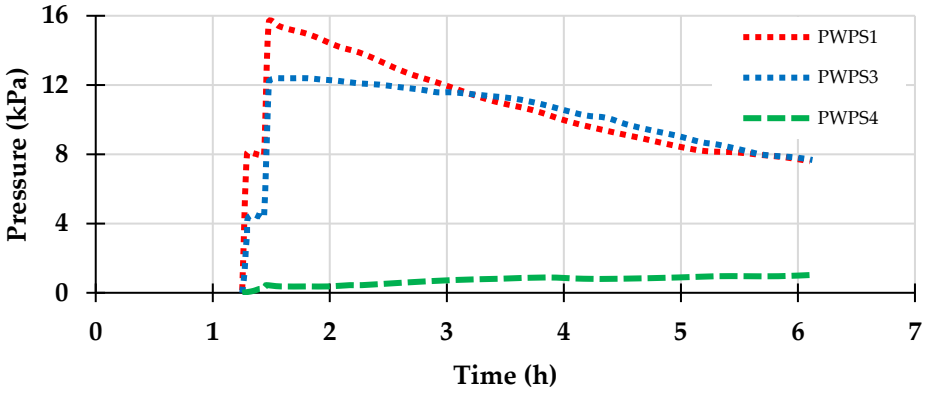
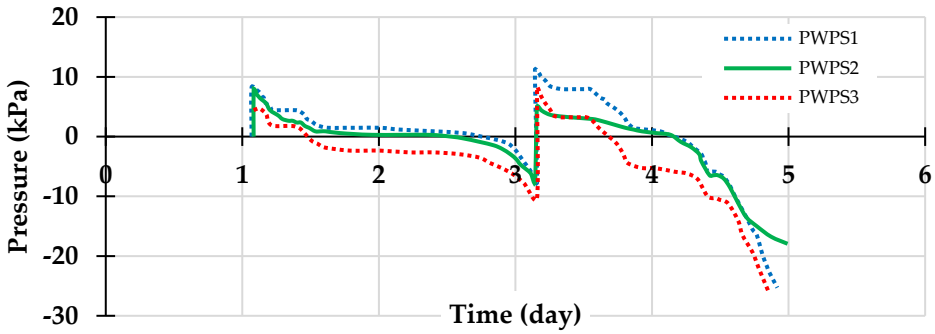


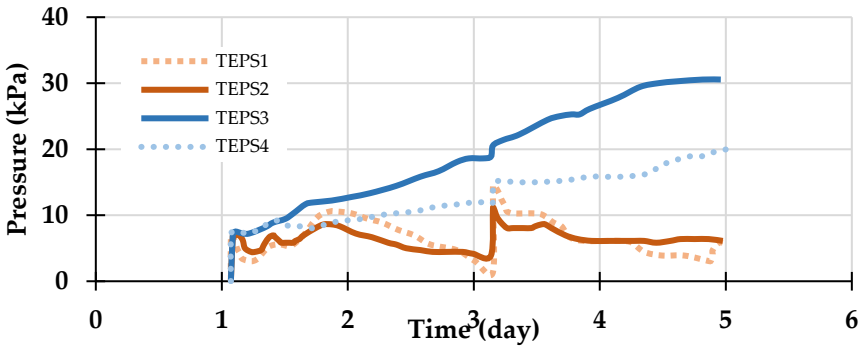
Figure 3-14: The pore water pressure at the base of stope (PWPS1), at 20 cm above the stope (PWPS3), and under the barricade (PWPS4).

The second case is a backfill placed in two sequences (one layer every two days, GSD #5 barricade). The TEP sensors attached to the walls and on the barricade recorded an increase in pressure after half of the day, while the PWP sensors indicated a decrease in pore water pressure (negative values, with the suction development, near the barricade and in the stope middle (PWPS 2 and 3)). When the second layer of backfill was placed, the PWP sensors indicated a jump in pressure values (from negative to positive), while the TEP sensors showed a slight jump and continuing pressure increase as the first layer. The TEP at the base of the stope did not record this pressure increase, and the pore water pressure sensor at this location (PWPS 1) remained positive compared to those placed near the barricade and the stope mid-height (Figure 3-15). These results may require further investigations, but they can be interpreted tentatively by the cement hardening and suction development. It appears that the drainage and the cement hydration consume the water from the backfill, which explains the negative PWP values and the increase in pressure in the TEP sensors after several hours of the backfill placement. These measurements can be useful only in the first few hours after backfilling because the sensors used may be affected by several factors, such as cement hydration, suction, and chemical attack on the sensor surfaces.

(a)



(b)



(c)

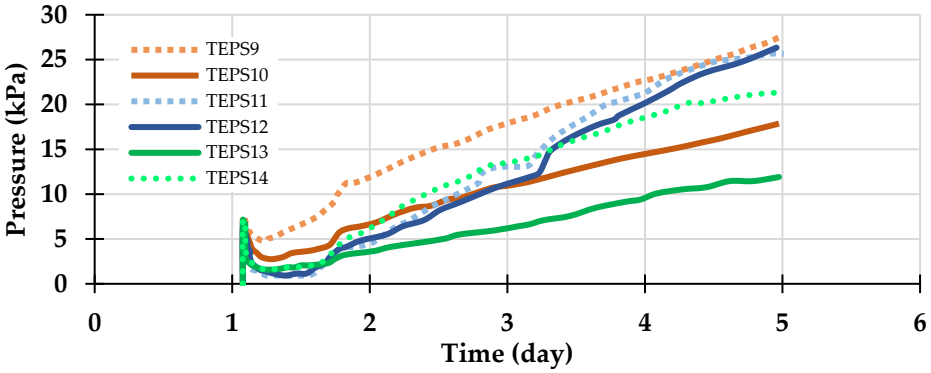


Figure 3-15: Total pressure measurements: (a) The pore water pressure at the base of stope (PWPS1), in front of the barricade (PWPS2), and at 20 cm above the stope (PWPS3). (b) The total pressure at the base of the stope. (c) The backfill pressure measurement on the barricade.

3.5.2 Stability and Failure Mechanism of the Waste Rock Barricades

In order to study the strength and failure mechanism of the waste rock barricades during backfilling, an uncemented backfill (water and tailings mixture with Cw = 70%) was used, assuming that cement hydration does not play any role immediately after backfilling. Barricades with the grain

size distributions #1 and #5 were tested. The model was immediately filled up to the top of the stope, and a manual piston was then used to apply vertical pressure until the barricade collapsed. The barricade–backfill interaction was recorded while increasing the pressure on the barricade. The pressure measured by all sensors (earth and pore water pressure sensors) were varied in different locations inside the model. The test conducted on a barricade made of grain size distribution #1 showed that the fine particles prevent the backfill from penetrating into the barricade pores but seem to give a low shear resistance (internal friction) (Supplementary, video S1). For this type of fine-grain configuration (d < 1 mm), a shear failure was observed when the recorded pressure, using the sensors placed in front of the barricade, reached 120 kPa (Figure 3-16). Several factors can change the shear strength of the barricade during the test, such as the degree of saturation of the barricade before the pressure increase using the piston, the rate of pressure increase, etc. The use of the piston to apply extra pressure strongly pushes the backfill water into the barricade pores (like an injection under pressure).

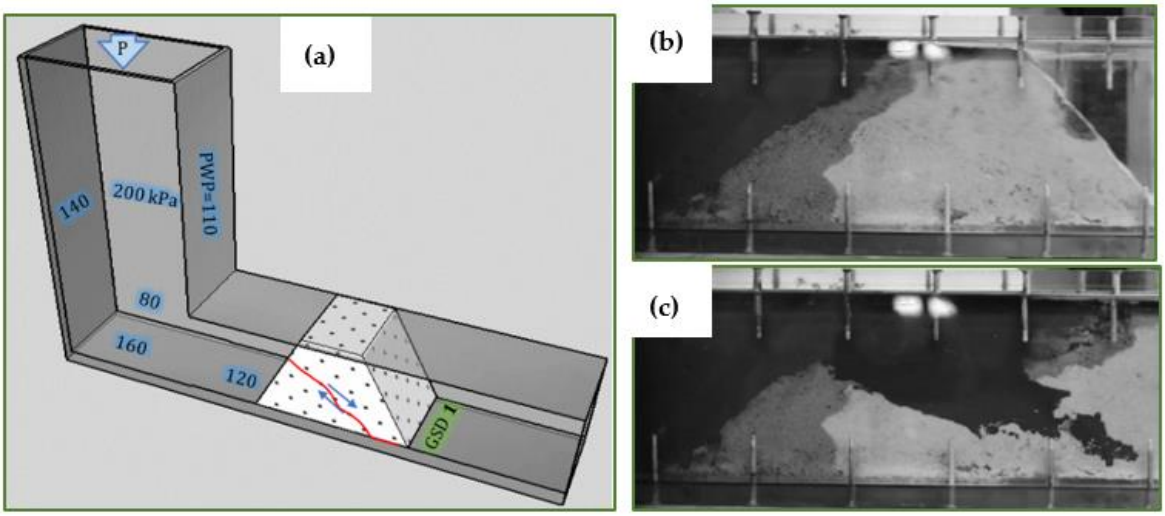


Figure 3-16: The failure mechanism of a waste rock barricade made of GSD #1: (a) the different pressure values in the model at failure, (b) the barricade before the failure (the top largely moved), and (c) the barricade after the collapse.

For the second test (barricade made of GSD #5), the barricade did not contain any fine materials (there are no particles of d < 1 mm), which allowed the backfill to penetrate into the pores of the barricade (see Figure 3-17). When the water of the backfill reached the downstream part of the barricade, the particles began to drift and fall (Supplementary, video S2). It appears that the

frictional resistance of the barricade was sufficient to withstand the pressure, but the drifting of the particles gradually reduces the resistance of the barricade to a value where the pressure can cause the collapse. The pressure at the middle of the stope was lower than that measured in front of the barricade at failure. By comparing this result with the previous test, it can be observed that the barricade made of the fine materials drains slowly, which in turn accumulated the pressure in the stope middle when the piston was used.

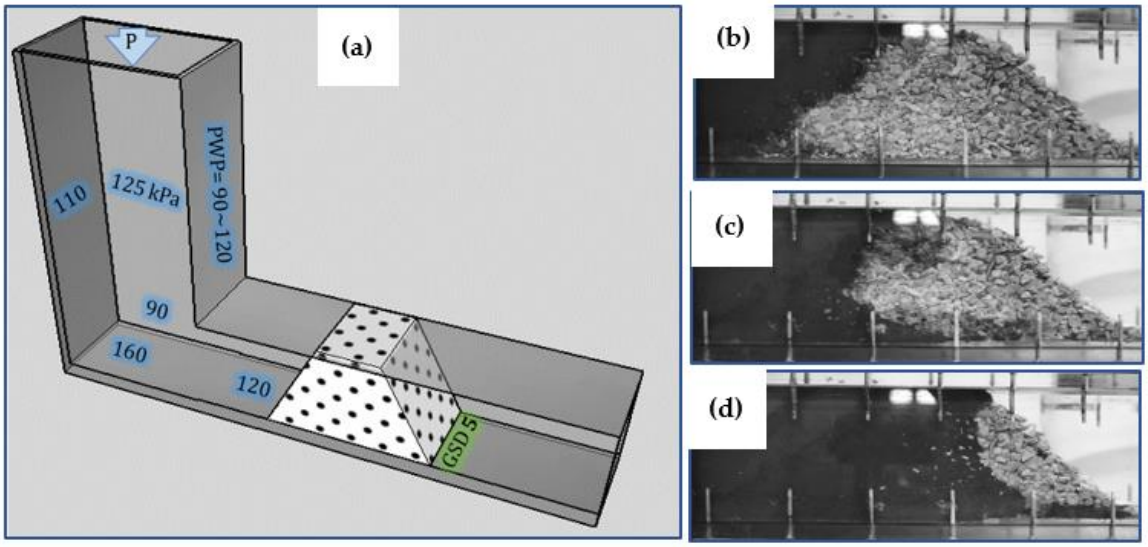


Figure 3-17: The failure mechanism of a barricade made of GSD #5: (a) the different pressure values in the model at failure, (b) the barricade before the failure, (c) the hand piston pushes water from the backfill into the pores of the barricade, and (d) the barricade after using the hand piston.

An intermediate case, between the last two configurations, was tested (GSD #2, 30% of particles of d < 1 mm). The barricade has shown good resistance to pressure and backfill penetration (Figure 3-18). This barricade (GSD #2) has been able to withstand the same pressure as the last test (GSD #5). The barricade did not collapse, but the backfill has been able to flow over the barricade, confirming the need for the application of a shotcrete layer to support the downstream side of the barricade (Supplementary, video S3), or increasing the top length of the barricade. It should be emphasized that, in these tests, the barricades were placed on a number of thin, transparent silicone bars that were fixed at the base of the drift only to increase the frictional resistance between the

barricade and the drift. Future tests are needed to confirm the results by using rough and homogeneous interior surfaces to study the behaviour of the barricade.

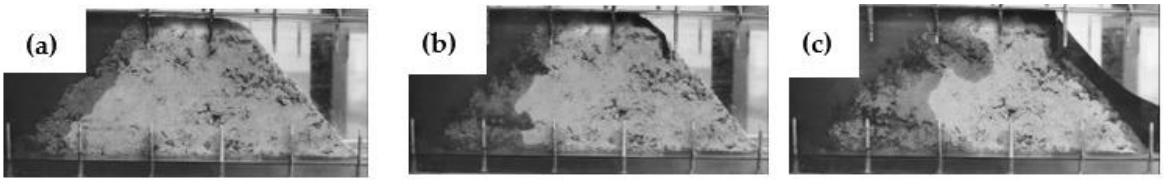


Figure 3-18: Failure mechanism of a barricade made of the GSD #2: (a) after the filling, (b) during the increase of the pressure using the hand piston, and (c) at failure (at the end of the test).

3.6 Concluding Remarks

The results obtained on the small-scale model demonstrated that: (i) the stability of a waste rock barricade depends upon numerous factors, such as the waste rock particles gradation and degree of compaction, as well as the frictional resistance between the barricade and the drawpoint sidewalls, and (ii) for two different types of backfill, cemented and uncemented with 70% of solid, the volumetric strain due to self-weight consolidation of the backfill was 4.5% and 16%, respectively. The consequence of these observations is that a progressive backfilling of the stopes is preferable to dissipate the pore water pressure and to ensure the stability of the barricade.

The use of cameras, as well as other remote monitoring devices, should be considered to supervise the quality of barricades, breather pipes, and paste backfill inlet pipes. The use of binder in the backfilling of the first layer (in the plug), the sprayed concrete layer (behind and around the barricade), and the barricade compaction are essential issues in backfilling operations.

Although these analyses are based on several simplified assumptions, it is desirable to improve future work by using a more realistic filling rate, other types of barricades, and rough inner plexiglass surfaces for the small-scale model. The interior walls of the model will be provided with the appropriate roughness to represent the interface friction of the rock walls. This study will be pursued in different directions: (i) experimental tests on the same reduced model but using high-quality soil pressure transducers (BEC-A 200 kPa, KYOWA), and on an intermediate scale model to study the scale effects and validate the results, (ii) numerical modelling using SIGMA/W code in GeoStudio 2021 suite (version 11.0.1.21429, GEOSLOPE International Ltd., Calgary, AB,

Canada), and (iii) a review of previous in situ studies to be compared to the experimental and numerical parts.

Supplementary Materials: Video S1: Failure mechanism of a barricade made of GSD#1 (https://imgur.com/73WRQr4), Video S2: Failure mechanism of a barricade made of GSD#5 (https://imgur.com/SWqWoAo), Video S3: Failure mechanism of a barricade made of GSD#2 (https://imgur.com/m1niWSm).

CHAPTER 4 ASSESSMENT OF STRESS STATE IN PASTE BACKFILL DURING PROGRESSIVE BACKFILLING: EXPERIMENTS AND MODELLING

4.1 Introduction

The mining industry is an area of the great demand for human development. A reduction in precious minerals near the surface has increased the depth of underground mines. Underground mining of economic resources produces cavities (voids) in various forms, including stope, cellar, and gob shapes. Safety and environmental considerations have forced mining companies to consider backfilling mine waste to avoid mine collapse and other deeper phases of production, subsidence of the ground in the abandoned mine and environmental pollution. Therefore, several methods of backfilling for voids were developed during the historical development of mining technology. Some popular approaches used depending on economic factors and other objectives such as developing or abandoning the mine are the rock backfill, the hydraulic backfill, and the cemented paste backfill (Sheshpari, 2015; Belem et al., 2018). Rockfill (RF) consists of waste rock or quarry material that is carried by truck or conveyor underground. RF can be adjusted by optimizing the grain size (such as crushing or inserting fine-grained materials) and/or adding binders, depending on its use (Hassani & Archibald, 1998; Kuganathan, 2005b). Rockfill is typically used to provide ground stabilization by passive support at the walls of rock. RF is commonly used as a working floor of machinery or when side and base exposures are not necessary because, in the absence of a binder, it has limited ground support capability and negligible self-standing height (Hassani and Archibald, 1998). Hydraulic fill (HF) is known as low solids content slurry ($C_{w\text{-}f}$ varies between 60% and 75%). HF consists of classified mill tailings and/or natural sand, transported through boreholes and pipelines to the underground stopes (Hassani & Archibald, 1998; Potvin et al., 2005). Usually, the fine particles in the hydraulic backfill are removed to create permeability in the backfill, where the particles of less than or equal to 10 μm should be less than 10% (Belem et al., 2018). Cemented paste backfill (CPB) is increasingly being used in backfilling operations, especially when the tailings of the backfill or waste contain a large amount of very fine particles (Potvin et al., 2005). CBP is a non-homogenous material that consists of a mixture of tailings, water, and cement. The amount of solid wastes in the CBP is between 70 and 85%, water used is clean or processed, and the hydraulic binding agent usually is in between 3 and 7% of the total

weight. CPB is a recent rapidly growing waste management in the mining industry that has given economic support and a safe workplace, as well as environmental benefits and the advancement of underground mining (Grice, 2001; Belem & Benzaazoua, 2008).

The backfill needs to be held in the stope by means of a barricade installed at the drawpoint. The barricade is typically constructed of permeable brick fibrecrete, concrete (hydraulic filling), timber frame (hydraulic & paste filling), shotcrete (hydraulic & paste filling) or waste rock (paste filling). A failure or a break of a barricade often led to serious consequences, such as the immobilization or damage of expensive mining equipment, injuries or even death of mine personnel (e.g., Grice, 1998, Sivakugan et al., 2006a, Bussiere, 2007, Helinski et al., 2007, Yumlu & Guresci, 2007, Li & Aubertin, 2009a, Widisinghe et al., 2013, Sivakugan et al., 2015). Waste rock barricades are cost-effective since they are easily accessible and produced underground (access to waste rock development galleries) but are poorly documented in their behaviour and failure mechanisms. Barricade stability analysis requires a correct estimation of pore water and total pressure in the backfilled stopes and on the barricades, particularly at the most critical moments during and shortly after backfilling.

In recent decades, interest in physical modelling has grown considerably due to developments in geotechnical engineering, laboratory testing and in-situ investigations. Proper laboratory testing and in situ measurements can provide accurate and reliable data that can be compared with analytical and numerical solutions. The use of small-scale models is widely used to solve many geotechnical and complex problems because they allow the expected response models to be studied more quickly. The main advantage of physical modelling is that it allows parametric studies, including model geometry, different types or combinations of loads, and soil conditions (Foray et al., 1998). The behaviour of the structure can also be studied at various phases of the building process. The small-scale models of mine stope did not address the waste rock barricades and their interaction with the mine backfill. The models also did not study the stress state of the backfill at different locations in the stope.

Furthermore, numerical modelling, which essentially simplifies real-world problems, is an integral part of any geotechnical analysis and design process. Modelling in geotechnical engineering could vary from constitutive models describing the behaviour of materials to experimental and intelligent models simulating geotechnical systems under different loads and environmental conditions. Complex problems can be studied with numerical methods, including finite differences, finite

elements and discrete element methods. Modelling can involve the stress prediction due to the interactions between the structure (or any civil engineering system) with the ground, the displacements due to imposed loads, and the changes in pore-water pressures and their effects on stability. Since modelling involves simplifications and assumptions, it is very important to know how they are established and their effects.

Geotechnical engineering practice consists of three parts: establishing the ground profile, defining the behaviour of the soil, and modelling. These parts are interlocked and supported by experience consisting of empiricism and precedent (Burland, 1987). These three parts of what is now termed the Burland Triangle (Fig. 4-1).

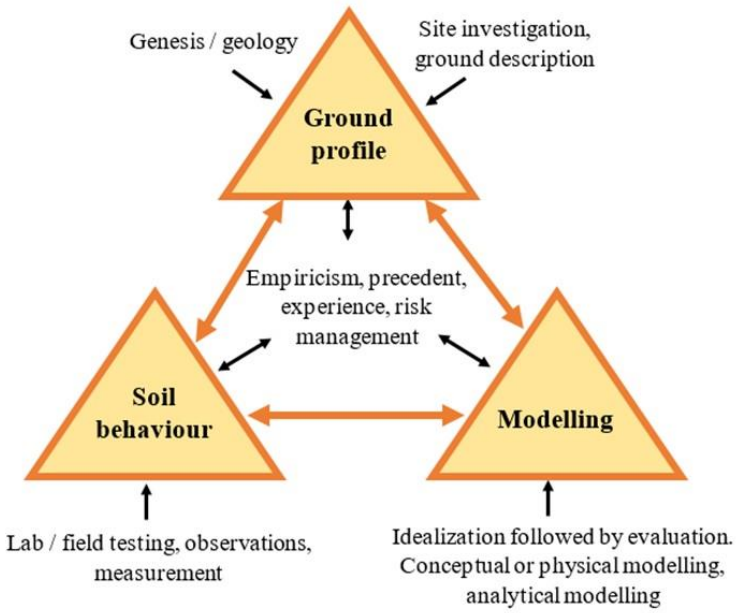


Figure 4-1: Burland Triangle (adapted from Anonymous, 1999).

Several laws of behaviour have been used in geotechnical computation software based on finite element methods. The laws of behaviour express a relation between the tensor of stresses, the tensor of strains and their respective increases, which can imply a criterion of rupture or limit of elasticity (Ti et al., 2009). The choice of a model depends on the behaviour of the material to be studied and the type of analysis that the geotechnical engineer wishes to perform (Wood, 2004). The simplest available stress-strain relationship is Hooke's law of linear (isotropic elasticity). There are four material parameters for an elastic model, the elastic modulus (E), Poisson's ratio (v), bulk modulus (K) and shear modulus (G); and only two are required to fully specify the material (E and v). Generally, the linear elastic model is too simplistic to capture essential soil behavioural features;

however, this model was used to simulate the materials in experimental tests (backfill and barricade). Appendix I includes the fundamentals of numerical modelling along with some of the popular constitutive models used in geotechnical problems.

4.2 Experimental & numerical program

Two experiments of backfilling operations were carried on the reduced model as following:

- An uncemented backfill (70% solids concentration) was backfilled in two layers with 2 days of rest for each layer.
- A backfill contains 5% cement (GU), and 70% of the solid's concentration was filled in a single layer (76 cm high). Unfortunately, the data acquisition of this test was only recorded for six hours due to a power failure.

These two tests were compared to numerical simulations modelled with the finite element code SIGMA/W (GEO-SLOPE 2018 R2)

4.3 Physical & numerical models

4.3.1 Physical model

A small-scale model with a length scale factor of 1/50 was designed to simulate (qualitatively) the backfilling practiced in the underground longitudinal stopes (Fig. 4-2). This model was made of acrylic glass or Plexiglas (transparent). The filling chamber (stope) has a horizontal section of 9 x 20 cm and a height of 38 cm (can be increased 38 cm extra to be full height = 76mm during placement of the second layer).

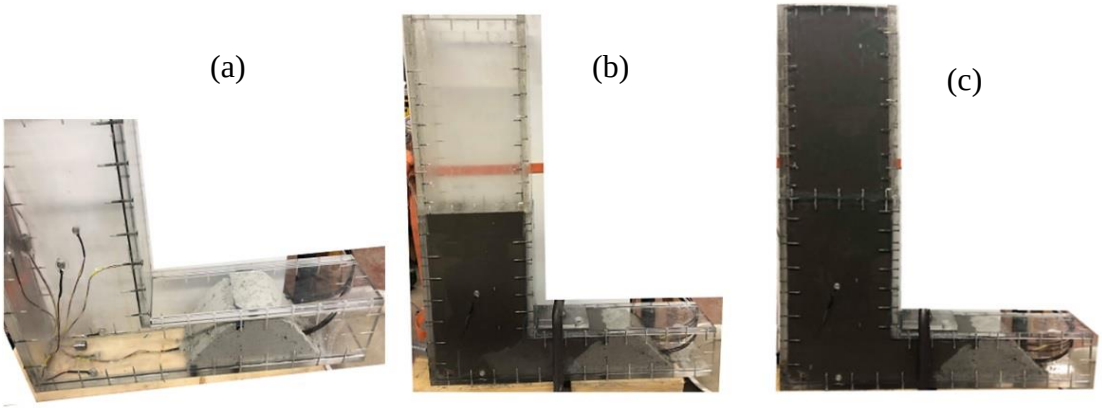


Figure 4-2: Small physical model of the mine stops: a) before backfilling, b) after the first layer is poured, c) after pouring the second layer.

The pressure-induced during the backfilling is measured using mini pressure sensors placed at different locations inside the model (Fig. 4-3).

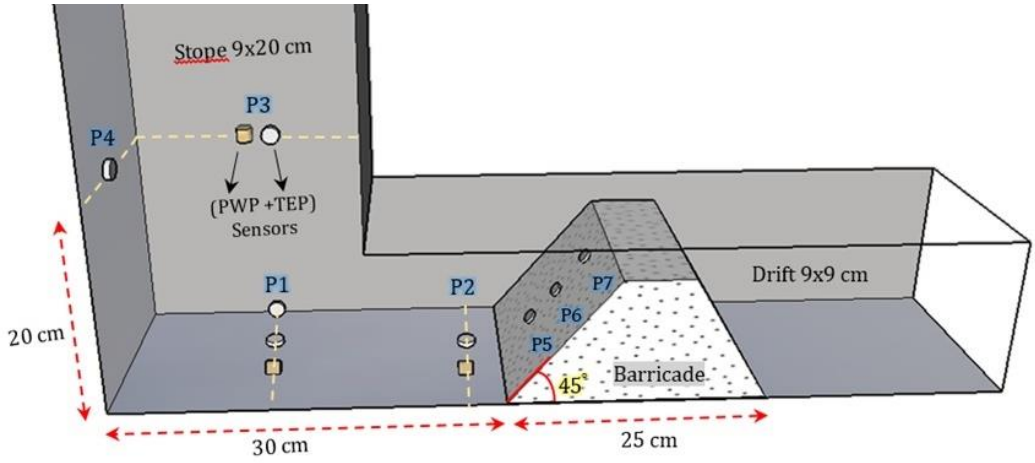


Figure 4-3: Measurement of pressure at different points in the physical model [pore water pressure (PWP) and total earth pressure (TEP)].

Table 4-1 shows the characteristics of the sensors used in the experimental tests conducted on the physical model.

Table 4-1: Characteristics of the pressure sensors used on the reduced model.

Sensor	**Earth total pressure sensors**		**PWP sensor**
Brand	KYOWA	Dan street Nanjing Electronic Technology Co	
Type	PS-D	DMTY	DMKY
Position	(P5, P6 & P7)	(P1, P2, P3 & P4)	(P1, P2 & P3)
Capacity	50 kPa	100 kPa	

To prepare the backfill, the quantities of water and binder to be added to the wet tailings must be determined. The amount of cemented paste backfill ingredients (water, binder, and tailings) can be calculated after estimating the backfill volume (V_f) to fill the stope, the required binder ratio (B_w) and the final target mass content of the CPB (C_{w-f}). The design and dosage of the backfill mixture were performed using several equations (see Belem et al., 2018 and Appendix B for more details). The model is filled with backfill mixture after preparation within a short period of time (approximately 4 minutes). The grain size distribution (GSD) curve of the tailings used (Laronde tailings) for the backfill preparation is presented in Figure 4-4a. The GSD curves were determined on homogenized tailing samples using a Malvern Mastersizer S 2000® laser particle analyzer. The

barricade was constructed of crushed waste rock in trapezoidal form using a mould (see Chapter 3) with 1304 cm^3 of volume (25 cm base length, 7.2 cm top length, height = width = 9 cm). The particle diameters of the barricade vary from 0 to 8 mm on the model (50% smaller than 1 mm). Only a barricade made of fine materials (GSD#1 in Figure 3-4b of Chapter 3) is presented in this work because it is homogenized to be modelled by the software.

Figure 4-4b shows the grain size distribution of the barricade, with a measured bulk density of 1.9 g/cm^3.

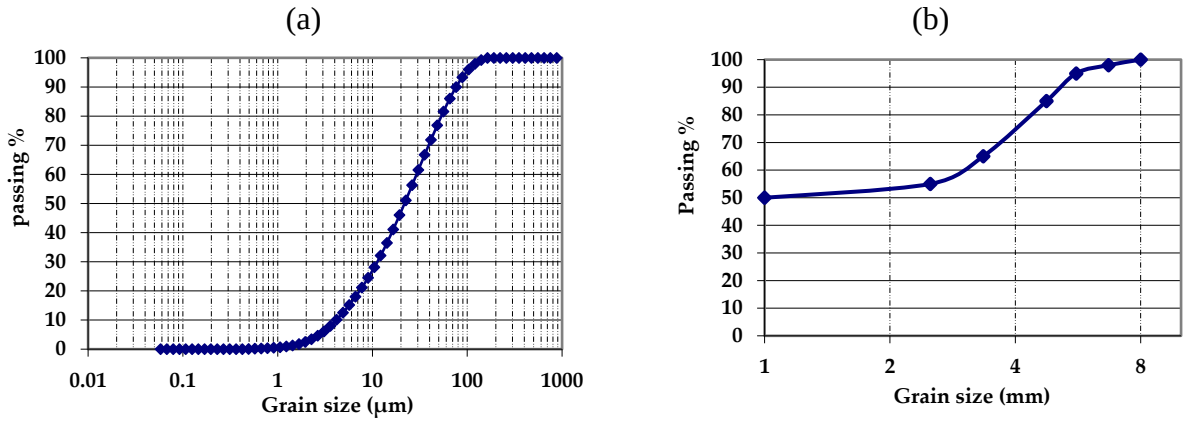


Figure 4-4: Grain size distribution curves of a) tailings from Laronde mine, b) barricade made of crushed waste rock.

4.3.2 Numerical model

Numerical models are very powerful tools that can be very useful in solving complex problems. The different cases simulated in this study are modelled with the finite element code SIGMA/W (GEO-SLOPE 2018 R2). SIGMA/W can be used to perform stress-strain analysis for different types of geotechnical problems, the interactions between soil and structure and simulate sequential construction problems where boundary conditions can change over time (Ltd, 2008).

Figure 4-5 shows a two-dimensional (2D) model of the vertical stope with 76 cm (2 x 38 cm) high and 80 cm wide. An approximate global element size of 1 cm was used (draw mesh). To simulate backfilling, a first step is carried out to reach a state of equilibrium (steady-state) of the model before placing the first layer. This step is important because it ensures that there is no convergence of the model walls when the stope is backfilled (i.e. the elastic displacement of the stressed occurs before backfilling).

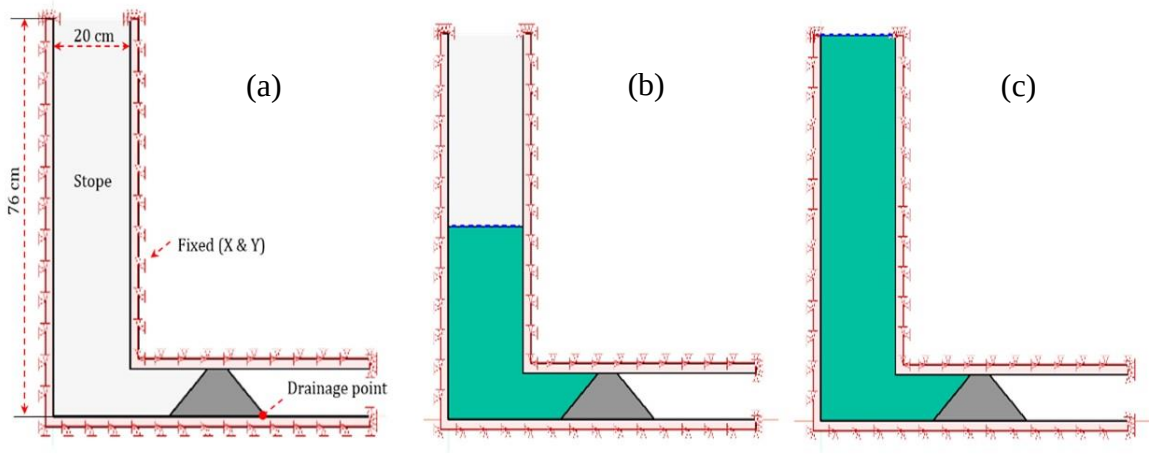


Figure 4-5: Numerical model with the boundary conditions: a) steady state (before the backfilling), b) the placement of the first backfill layer, c) the placement of the second layer of the backfill (water table at the top of each layer).

The reduced Polymethyl-methacrylate (PMMA) model was modelled as a homogeneous material (isotropic and linear elastic behaviour); it has a unit weight of 11.67 kN/m^3, a 3GPa Young module, and a 0.35 Poisson ratio. PMMA is well known under many other names such as acrylic glass, Plexiglas, or Perspex. PMMA properties were given by the manufacture and are available on the internet.

In these simulations, the backfill simulates a very rapid (instantaneous) filling of the stope, followed by progressive drainage. The Backfill was placed in two layers, one layer every two days. 19.2kN/m^3 was the initial unit weight of the backfill measured in the laboratory during physical modelling of uncemented backfill (70% of solid concentration). The water table is placed on the surface of each layer. A coupled analysis (stress-strain and PWP) is then performed for a period of 2 days. For consolidation problems, coupling stress-pore pressure analysis does not necessitate coupling with SEEP/W Software. The calculation of pore pressures is performed for each stress and strain calculation step to determine the change in effective stresses. This analysis requires the definition of hydraulic conditions at the boundaries (groundwater table, drainage, hydraulic flows, etc.) as well as the hydro-geotechnical parameters of materials (water retention curve and the hydraulic conductivity curve as a function of suction).

The conductivity hydraulic and the water retention curve of the backfill (Fig. 4-6) have been taken from previous studies (Aubertin et al., 1996; Belem et al., 2000; Godbout et al., 2004; Godbout et al., 2007; El Mkadmi et al., 2013). A hydraulic conductivity of $k_{sat} = 10^{-7}$ m/s (air-entry and water-

entry values AEV = 15 kPa and WEV = 30 kPa, respectively) was used. A boundary condition corresponds to a zero hydraulic head (hc = 0 m) on the downstream side at the base of the barricade was applied to simulate the flow of water during the drainage (Fig. 4-5a). The backfill (Cw=70%) behaves like a heavy liquid during backfilling, so very small values for the Poisson ratio and Young's modulus of backfill were used, $E_b = 10$ kPa and $v_b = 0.495$, respectively.

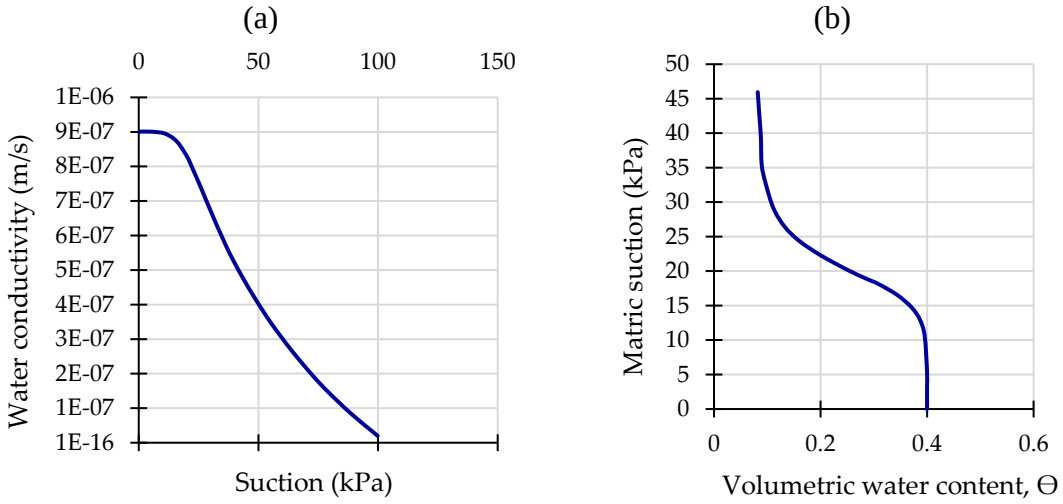


Figure 4-6: Hydraulic properties of the backfill used in the simulations: a) permeability function, b) water retention curve (adapted from El Mkadmi et al., 2013).

The barricade made of sterile waste is modelled as linear elastic (w/PWP change). The hydraulic parameters of the barricade were estimated. The volumetric function of the water content was estimated by the software as a simple function (silty sand) with a saturated water content of 0.35. Also, a saturated hydraulic conductivity of k_{sat} = 10^{-4} m/s was used (estimation method: Van Genuchten). The dry bulk density of the barricade (γ_{wr}) is 18.9 kN/m^3 (measured in the lab). Table 4-2 summarizes the properties of the backfill and barricade used in the simulations.

Table 4-2: Parameters used for the simulations conducted with SIGMA/W (GEO-SLOPE 20١8).

Material parameters	E (kPa)	v	ɣ (kN/m^3)	Saturated WC	K_{sat}	Model type
Backfill	10	0.495	19.2 20.5(CPB*)	0.4	4.5E-08 Clay	Effective parameters, Linear elastic (w/ PWP change)
Barricade	7000	0.37	18.9	0.35	1E-04 (silty sand)	

*CPB: cemented paste backfill

4.4 Results

- **1st test**

After each backfill placement, the pore water pressure sensors indicated a pressure equivalent to the overburden weight of the backfill (or slightly higher). The pore water pressure decreases after pouring the backfill into the stope during the drainage and self-weight consolidation process. The drainage rate or the variation in pore water pressure curve during the dissipation depends on several factors such as the barricade state (dry or saturated), the backfill consistency (solid content), backfill type (cemented or uncemented), the measurement point (location), and the time between the placements (rest time).

Figure 4-7 presents the pore water pressure of the uncemented backfill at the base of the stope, in front of the barricade and the middle of the stope, respectively. Experiments and numerical modelling have produced similar results. The pore water pressure near the barricade was smaller than that at the base of the stope due to water drainage within the barricade. After a period of drainage, negative pore water pressure begins in the upper part of the stope due to the development of suction during desaturation. This consistency between numerical and experimental values shows that it can use the linear elastic model (with PWP change) to simulate uncemented backfill in the first few days after placement. The PWP2 near the barricade was slightly different in the numerical modelling, possibly due to the estimation of the hydraulic parameters of the barricade.

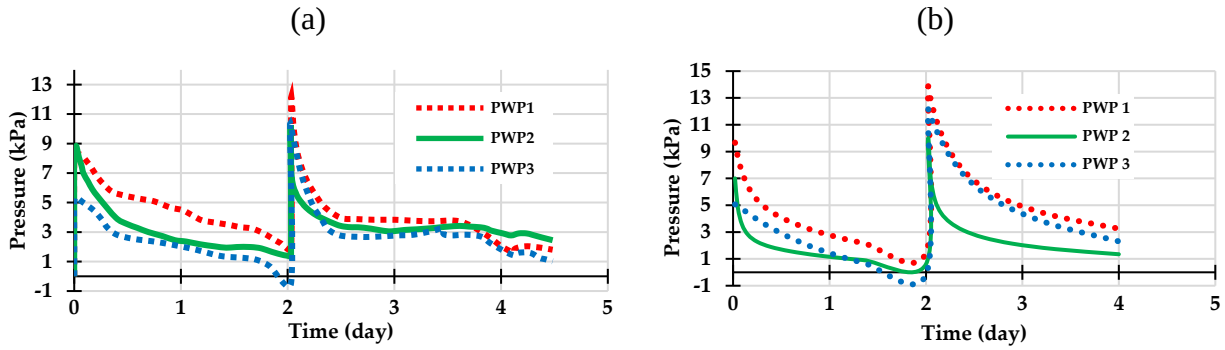


Figure 4-7: Pore water pressures: (a) from the reduced physical model, (b) from the numerical modelling.

Figure 4-8 shows the total pressure of the backfill on the barricade (P5, P6 & P7). The experimental results showed a significant drop in pressure shortly after pouring the first layer of backfill. This result can be attributed to the rapid saturation of the barricade (50 % of particles < 1mm), which

was installed in the drift (drawpoint) in a dry state. But after the second layer was applied, where the barricade was saturated, a gradual decrease in pressure was observed. Experience and numerical modelling have shown negative pressure in the upper part of the barricade several hours after the backfill was placed. Pressure magnitudes may be slightly different between physical model experiments and numerical simulations due to the sensitivity of the high capacity sensors (100kPa).

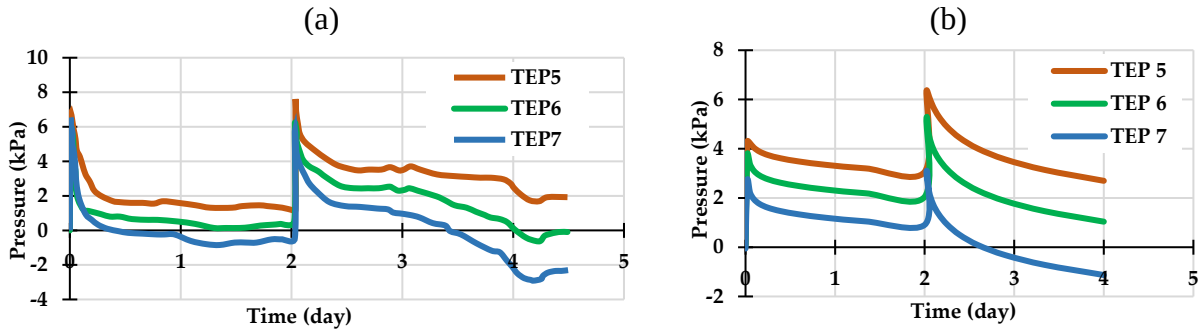


Figure 4-8: Total stresses on the barricade (horizontal direction): a) on the reduced physical model, b) from numerical modelling.

Figure 4-9 shows the total stresses at the base of the stope, P1 was measured in the vertical (Y) and horizontal (X) directions, whereas P2 was measured only in the vertical direction near the barricade. During drainage, the total stresses decrease as the measurement point moves towards the barricade. The pressure gradient during pore water pressure dissipation at these points was similar in the experiment and numerical modelling, with slight variations between them. As observed, the total stress at the base of the stope decreased shortly after the first placement and then remained constant, not like the pore water pressure, which was decreased until another layer was added. In the physical model, the lateral pressure at the base of the stope was higher, which could be due to the accumulation of backfill particles on/and around the sensor during consolidation.

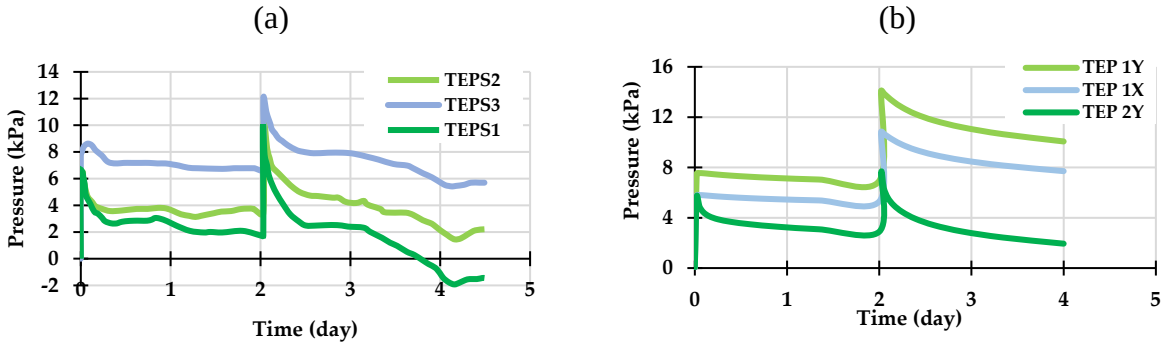


Figure 4-9: Total stresses at the base of stope (horizontal direction, X & vertical direction, Y): a) on the reduced physical model, b) from numerical modelling.

Figure 4-10 shows the stresses in the middle of the first layer (at 20 cm above the base of the stope). As observed, experimental and numerical results indicate that pore water pressure is higher than overburden stress after installation of the backfill. After backfilling, the pore water pressure decreased during drainage to a negative value after several hours, while the total stresses (in the X and Y directions) changed slightly. This result can be explained by two scenarios: either that, with the dissipation of pore water pressure, some of the vertical load is transferred to the walls of the stope, or that consolidation of the fill increases its density and lateral pressure, which may indicate a slight variation.

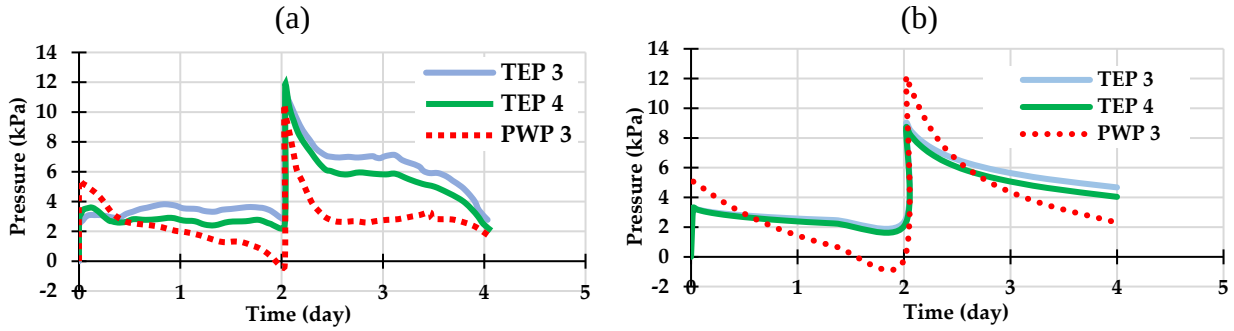


Figure 4-10: Stresses at 20 cm above the base of stope: a) on the reduced physical model, b) from numerical modelling.

Figure 4-11 shows the distribution of stresses and displacement of the backfill from the numerical modelling at the end of the experiment. It should be noted that numerical modelling was not discussed in detail in this work, but rather for a comparison of results with the experimental part. Several researchers have carried out extensive numerical modelling on the backfill by conducting parametric studies (e.g., El Mkadmi, 2012; Falaknaz, 2014; Yang, 2016) but still require additional research and comparisons with experimental tests.

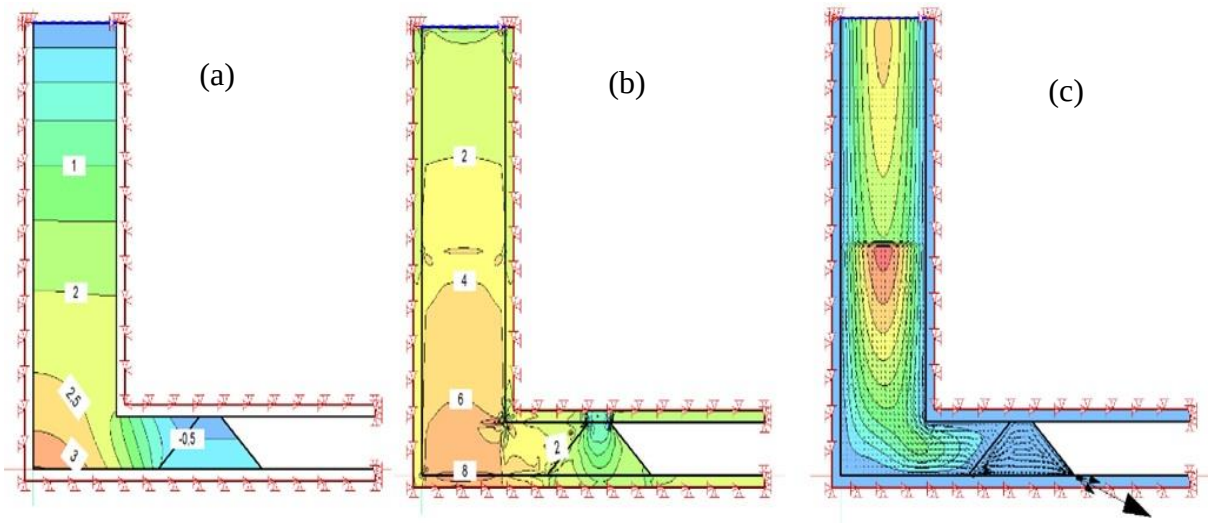


Figure 4-11: Isocontours show the distribution of a) pore water pressure, b) vertical stresses, c) flow and backfill displacements (XY direction) at the end of the tests (after four days).

It is interesting to mention that the inner corners of the model were rough compared to the surfaces due to the use of silicone sealant to provide a water-resistant seal. Due to this roughness, the upper surface of the backfill was curved for each backfill placement after the self-weight consolidation process (Fig. 4-12). This observation shows that the interface friction between the backfill and the walls of the stope affects the stress state of the sequential backfilling. It appears that as the roughness of walls increases, the vertical load of the backfill transferred to the stope walls increases, which in turn reduces the pressure at the base of the stope. In situ, the stope sidewalls formed after blasting are often rough and irregular; thus, shearing tends to take place in the backfill and developing of the arching effect. The use of interface elements between the backfill and rock mass in the numerical models can be used to represent the interface friction (e.g., Li et al., 2003; Li & Aubertin, 2009d).

The viscosity of the backfill and the percentage of the binder used in the backfill can play an important role in the stress state and backfill behaviour after placement. In the sequential backfilling, the properties of the first placement (the plug), which consider a foundation for the layers placed above it, greatly influence the pressure measured at the base of the stope and on the barricade.

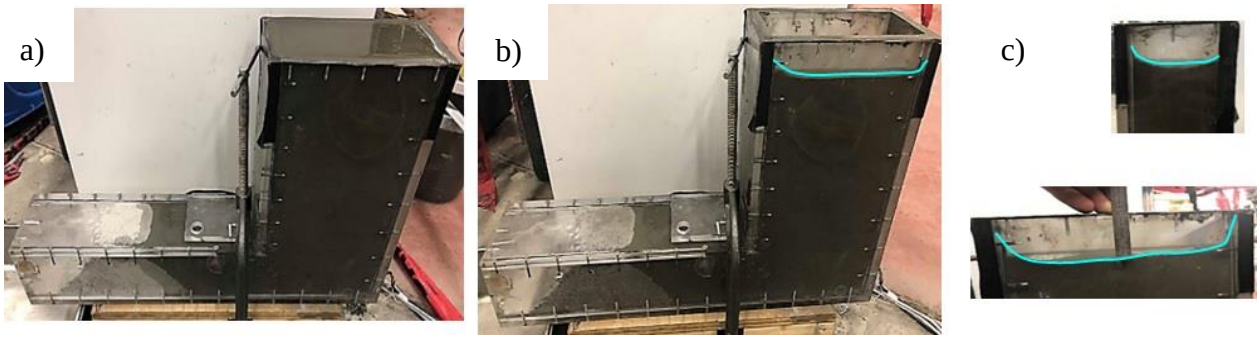


Figure 4-12: The filling chamber (stope) with backfill (C_{w-f} = 70%): a) after backfill placement; b) during self-weight consolidation; c) the front and right views of the top of the stope.

- **2nd test**

The second test involved a single-layer poured backfill containing 5% general use cement (GU), but the pressure measurement was only recorded during the first six hours after placement due to a power outage. The parameters used in the numerical modelling are the same as those used in the previous test for comparison purposes and may require a slight calibration to be similar to the experimental measurement. The pore water pressure appears to be higher in numerical modelling. Young's modulus should be slightly increased for cemented backfill. The interesting things in the figures below are the pressure variation at different locations during pore water pressure. The backfill pressure on the barricade, which appears to have the same value after backfilling (are concentrated at one point) and then differs during drainage (Fig. 4-13). Figures 4-14 & 4-15 present the stresses at the base of the stope (P1) and at 20cm above this level (P3). The pressure variations in the physical and numerical modelling are somewhat similar, with the slight need to modify the backfill parameters on the numerical model. The experimental test could also be influenced by the physical model roughness (made from PMMA). Smooth walls for the reduced model could not reflex the actual behaviour of the backfill during consolidation and shear stress development. In addition, the presence of binders in different percentages in the backfill can considerably modify the behaviour of the backfill during drainage and cement hardening. Therefore, shear stresses and arching effect are not addressed in this work and future tests are needed with the supply of the internal walls of the model by small protrusions to represent the friction resistance (see Chapter 6 for more details). These results showed that the specificity of the cement backfill had to be taken into account in the numerical modelling, even before the effect of the cement begins.

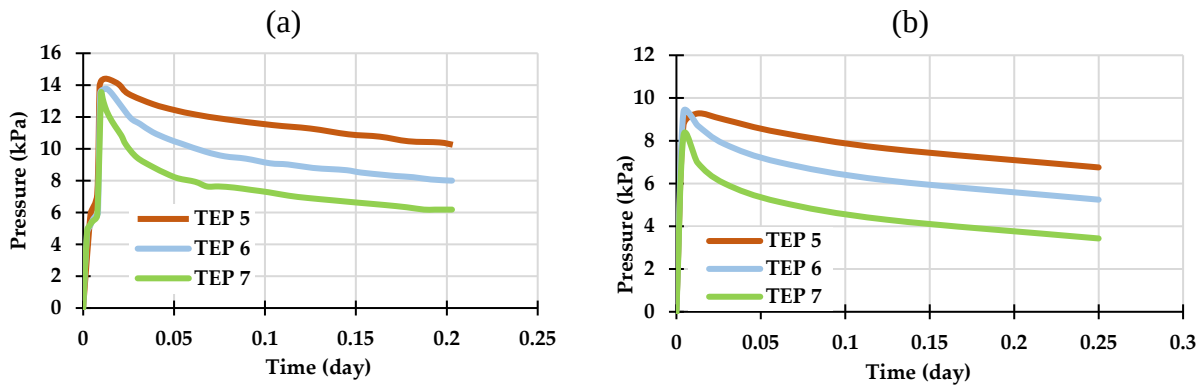


Figure 4-13: Total stresses on the barricade (horizontal direction): a) on the reduced physical model, b) from numerical modelling.

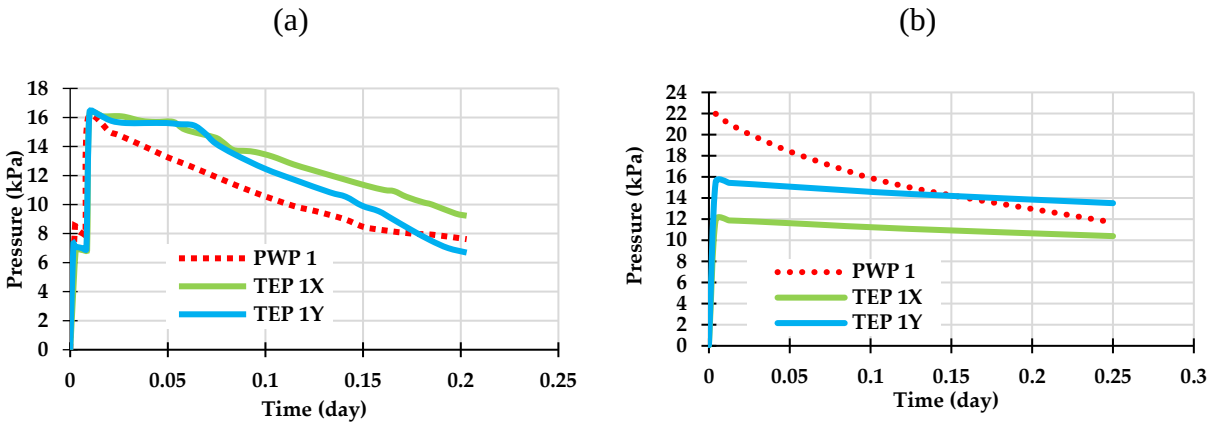


Figure 4-14: Total stresses at the base of stope (horizontal direction, X & vertical direction, Y): a) on the reduced physical model, b) from numerical modelling.

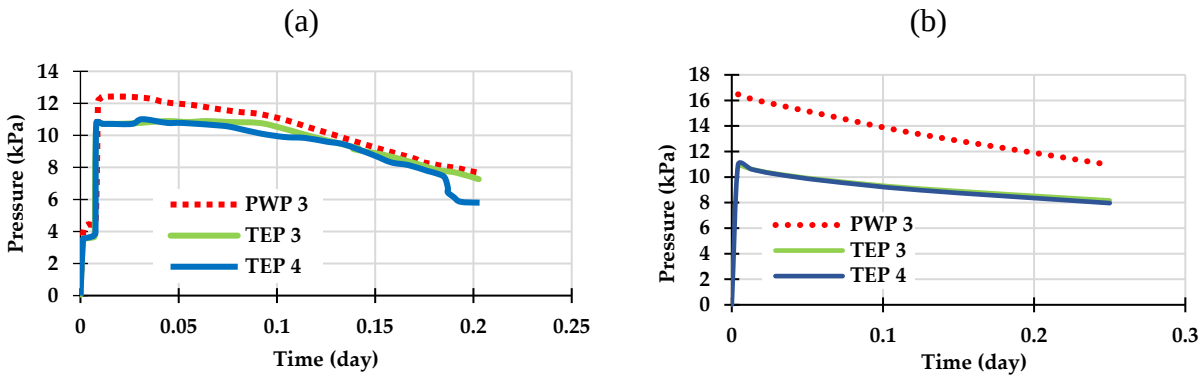


Figure 4-15: Backfill stresses at 20 cm above the base of stope: a) on the reduced physical model, b) from numerical modelling.

During the last years, several authors and their collaborators have carried out extensive studies to estimate the stress in backfilled stopes and on the barricade, which were used subsequently to design the waste rock barricades using the limit equilibrium calculation (e.g., Aubertin et al., 2003; Aubertin et al., 2005; Li & Aubertin, 2008, 2009a, b; Li et al., 2009; Yang, 2016). These studies may work well with uncemented fill, as cemented fill exhibits complex behaviour during the hardening process that may require further investigation. The cemented backfill (5% GU) was placed in two layers every two days. After the installation of the first layer, sensors indicated an increase in pore water pressure, while a slight increase was recorded by the total earth pressure sensors. It seems preferable to develop an adapted law of behaviour for paste fill that simulates the actual behaviour, which changes over time after backfilling depending on the binder content and consistency (see Chapter 3 for more details).

In the progressive backfilling of the cemented backfill, the pressure sensors near the barricade may demonstrate an increase in pressure with each new placement. But, once the backfill becomes self-standing, several hours after the backfilling, the danger that may arise from the collapse of the barricade vanishes. Figure 4-16 shows the importance of the use of binder and compares the condition of the fill at the end of the test for cemented and uncemented fill (Cw=70%). As the backfill begins to gain strength during the hardening of the cement, it correlates the particles of the barricade on the interlocking surface, thus increasing the stability of the barricade. It can also be seen that the upper part of the cemented fill, in contact with the barricade, dries and/or desaturates faster than the lower part, which may accelerate the gain in strength in this important position.

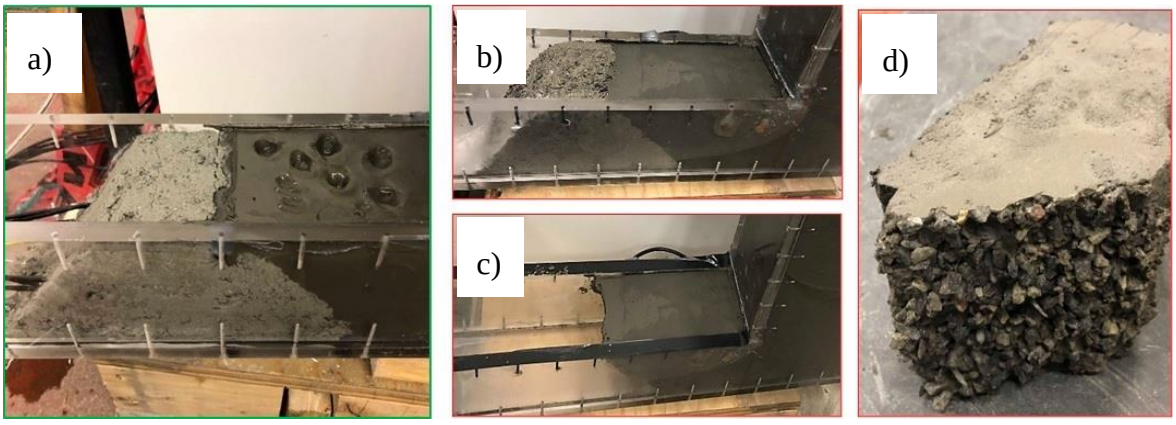


Figure 4-16: State of the backfill near the barricade at the end of the test (after four days) for a) the uncemented backfill, b&c) the cemented backfill before and after removal of the barricade; d) the barricade-backfill interaction.

It was observed that the change in the simulation parameters of the barricade did not have much influence on the stress state of the backfill during dissipation. The hydraulic conductivity of the barricade was not sufficient to describe a barricade made of coarse material (e.g. GSD #5, Chapter 3). This work requires more work to study the sensitivity of the parameters introduced to run numerical simulations and the ability to express the gradations and morphological characteristics of the barricade grains (shape, angularity and surface roughness). The behaviour of these rock barricades remains complex, especially with the interlocking with the paste backfill. It is important to measure in the laboratory all the material parameters necessary for numerical modelling (hydro-geotechnical parameters, modulus of elasticity, shear parameters, unit weights) to obtain a reliable comparison of the results. It is also important to define the behaviour of the paste backfill as a function of time. Where, it is better to define the backfill with elastic behaviour after placement, such as a heavy liquid, but once the consolidation-sedimentation process begins, the backfill behaviour tends to be like silty to clayey soil (before entering the binder effect). Once the cement hardens (depending on the content and type of binder), the behaviour of the backfill changes and the suction develops rapidly. Therefore, further experimental tests are needed on the paste backfill according to the previous remarks. Finally, it is difficult to compare experimental tests with numerical simulations because experimental tests on paste fill can be influenced by temperature and the accuracy of the measuring tools.

4.5 Conclusion

The results of previous preliminary tests have shown that the numerical simulation seems to be more consistent with the experimental tests carried out on the small-scale physical model with the uncemented fill. It has also been seen that the vertical stresses are equal to the total pressure of the overburden just after the instantaneous filling. During this short phase, the stress increases linearly with depth. As drainage occurs, the total stresses progressively decrease as water is expelled from the stope. It was observed that the rate of stress change is initially very rapid but tends to slow down with draining time. After filling the stope (placement of the backfill instantaneously), the PWP is equal to the total overburden stress. This indicates that the water pressure initially supports the entire backfill weight; thus, effective normal stresses are nil. Pore water pressures then decrease progressively over time, while the effective stresses increase proportionally. Consolidation and pore water dissipation takes place over a few days (two days in this test). The drainage of backfill

water increases the effective stresses, and after some time, unsaturated zones appear in the upper part of the backfilled stope and near the barricade due to the development of the suction.

Future tests need to be carried out on backfills (cemented & uncemented) with a high solid concentration (about 76%). The acquisition data, after backfill placement, must be recorded for several days during the consolidation and cement hardening process.

CHAPTER 5 STABILITY ANALYSIS OF WASTE ROCK BARRICADES USING A SMALL-SCALE MODEL OF MINE STOPE AND ANALYTICAL SOLUTIONS

5.1 Introduction

The mining industry is a sector that contributes greatly to Quebec's economic activity. Today, the mining sector is safer, but the fatal accident rate remains the highest among paid workers in Quebec (Li, 2019). Underground backfilling is commonly used in the mining industry to improve field conditions, thereby ensuring a safer workspace for underground mine personnel (Thomas, 1979; Hassani & Archibald, 1998; Potvin et al., 2005; Belem & Benzaazoua, 2008). The use of mine waste materials (tailings and waste rocks) to fill the underground voids (stopes) can also largely decrease their environmental footprint (Bussiere, 2007; Benzaazoua et al., 2008). However, the application of this technique requires the construction of barricades in the entrance galleries at the draw points to hold the backfill in place. However, recent cases of barricade failure indicate that barricades may pose a danger to the health and safety of all mining workers using underground backfilling. Like all other construction structures, the stability of a barricade to hold a backfill in underground stopes depends on its capacity and demand. Capacity varies depending on the materials used, the geometry (shape and dimensions) of the barricade and the construction method.

Several cases of barricade failures related to the paste fill have been reported in Australia, Turkey and Canada (Revell & Sainsbury, 2007; Yumlu & Guresci, 2007; Hughes, 2008). A failure or a break of a barricade often led to serious consequences, such as the immobilization or damage of expensive mining equipment, injuries or even death of mine personnel (e.g., Grice, 1998, Sivakugan et al., 2006a, Bussiere, 2007, Helinski et al., 2007, Yumlu & Guresci, 2007, Li & Aubertin, 2009a, Widisinghe et al., 2013, Sivakugan et al., 2015).

The literature review indicates that the design of barricades is usually carried out by civil engineers using bricks, shotcrete, or concrete blocks. The design of the waste rock barricade and its failure mechanism is often mysterious for a mining engineer (Yang, 2016; Belem et al., 2018; Li, 2019).

A good estimate of the pressure on the barricade (P) requires a clear understanding of the interaction between backfill and containment structures, including rock walls and barricades. This is a complex problem because of the significant contrast between the rigidity and the strength of

the backfill and that of the rock mass. When the backfill is placed in a stope, it tends to settle towards the lower part of the stope and towards the barricade at the drawpoint (drift), whereas the rock walls tend to hold the backfill in place because of the friction that occurs along the interfaces between the backfill and the rock. Part of the backfill weight is thus transferred from the backfill to the rock walls. This load transfer, known as the arching effect, has been demonstrated by some numerical modelling and in situ measurements in backfilled stopes. In latest years, considerable efforts have been made to assess the stress of the backfills placed in stopes (e.g., Aubertin et al., 2003; Li et al., 2003; Pirapakaran & Sivakugan, 2007; El Mkadmi, 2012; Ting et al., 2011; Ting et al., 2012; Ting et al., 2014); there is also a concern in the pressure on barricades established at the base of the stope near the drawpoints (e.g., Mitchell et al., 1975; Kuganathan, 2002; Li & Aubertin, 2009a, b Thompson et al., 2009; Thompson et al., 2010; Thompson et al., 2012; Grabinsky, 2010).

The stability and design of a barricade constructed to retain fill within a construction stope depend on several factors, including the type of fill, water content (often expressed as a percentage of solids), the proportion of cement, backfill rate, geometry, size and material of the barricade (Belem et al., 2018; Li, 2019). Several analytical and numerical solutions were proposed to estimate pressures and stresses in a backfilled stope and on barricades (e.g., Li & Aubertin, 2009a, b, e), however, the solutions developed are often based on certain simplifying assumptions. Observation and consideration of these limits are necessary for the design of barricades. A limitation of these studies is associated with neglecting the effect of cement hydration. It is true that the cement hydration can have an impact on the pressure in the stope and on the barricade, especially during a long waiting period with a cement content such as that commonly used in mines (3 to 7% for side-exposed backfill and 7 to 14% for base-exposed backfill; Li, 2019). Cement hydration leads to water consumption and reduced pore pressures (Helinski et al., 2007). However, the stability of the barricade is mainly related to the behaviour of the fill shortly after it has been poured into the stope. Therefore, the hydration of cement would have little effect on the design of the barricades and neglecting the effect of cement hydration in the design of the barricades would be on the conservative side.

To date, the influence of the percentage of solids in the backfill has not been considered in the calculation of pressures. According to the strict definition of a paste fill, it requires not only a high level of fine particles (at least 15% of particles less than 20 μm) but also a high percentage of solids so that there is no bleeding water, regardless of the deposition time (Li, 2019). Therefore, it is

necessary to take into account the viscosity of the paste backfill in estimating pressures in a backfilled site and on the barricades. The pressures caused by such a backfill on the barricade will be very low; if the barricade is built far enough away from the drawpoint (entrance of the gallery), there may be no contact between the fill and the barricade. In all these cases, the construction of light barricades is sufficient to retain the fill (Hassani & Archibald, 1998).

In many cases of actual mining practice, more water is added to meet the criteria for flow and pipe transportation of backfill, and in some cases, to ensure close contact between the backfill and the roof of the stope. For paste fill, due to the high percentage of fine particles, permeability is often low. The dissipation of excess pore pressure is very slow, and excess pore water cannot escape quickly, and the amount of drainage water is not a reliable indicator of the dissipation of excess pore pressure. Once the pouring or backfilling is complete, and the excess pore pressure reaches the maximum, the drainage and consolidation process begins with the passage of time. The water related to excess pore pressure drains up or down along with the dissipation and decrease of excess pore pressure and increase of effective stress. The total vertical stress and the pore pressure are almost identical and equal to the isogeostatic pressure according to the overburden of the fill. Both decrease with the passage of time due to drainage and consolidation under the self-weight of the fill. To avoid barricade ruptures caused by excessive pressure, backfilling a high stope is often divided into two phases: plug and residual or final. The plug generally contains a higher content of binder to increase the strength of the backfill as a safety factor to prevent the failure of the barricade when the filling is resumed or to open a gallery through the backfill.

The experimental results of Thompson et al. (2012) and the numerical results of El Mkadmi et al. (2012) all showed that there was no arching effect in the stope shortly after the deposition of the paste backfilling. Therefore, pore pressures, total horizontal and vertical stresses are expected to be equal at a given elevation in the stope and within the drift (drawpoint). However, field measurements by (Grabinsky & Bawden, 2007; Thompson et al., 2009) showed that the total stresses in the drift decrease as the measuring points move away from the stope. Rather, these results indicate the occurrence of a horizontal arching effect in the drift shortly after the stope was backfilled.

Due to limitations in the capacity of the backfill production by the backfill plant or in the transport of the backfill by pipes, the backfill speed of a stope is limited. With a typical value of 0.2 m/h for the rate of increase of the backfill height, the complete backfilling of a typical 40 m high

construction stope takes about a week (Li, 2019). In practice, the drainage and consolidation of the cemented paste backfill can take place during the backfilling operation. The construction of the barricades could therefore be too conservative by completely ignoring the drainage and consolidation of the backfill.

Analytical solutions were proposed for the sizing of WRBs (e.g., Li et al., 2009; Li & Aubertin, 2011) under fully drained (no water pressure) and submerged (hydrostatic water pressure) conditions. The design was based on the rectangular shape geometry for the barricade. Yang et al. (2016) modified the original solution proposed by Li and Aubertin (2011) by considering a more realistic geometry. The modified solution discusses the design of trapezoidal WRBs constructed to retain paste backfill during the first few hours after deposition.

In this section, the limit equilibrium calculation was used to evaluate the strength of WRBs using experimental tests on a reduced model. The use of a small-scale transparent physical model allows the failure mechanism to be observed during the tests. The results and observations presented are part of a series of experiments aimed at sizing waste rock barricades in light of the previous work of the researchers mentioned above. The current physical model does not meet all the desired requirements, but another model is being developed for future testing.

5.2 Experimental tests

Two tests were carried out on a physical model made of transparent plates (Fig. 5-1). The objective is to study the strength and rupture mechanisms of a waste rock barricade. A layer of backfill (38 cm high) was injected into the stope, which has a section of 20x9 cm. The distance between the entrance of the drift (drawpoint) and the edge of the barricade at the base is 10cm. The model was designed to study the behaviour of a typical waste rock barricade in the Abitibi-Temiscamingue region (Canada). The model is set up for qualitative experiments because of the difficulty in meeting certain similarity rules (see Appendix F at the end of the thesis for more details).

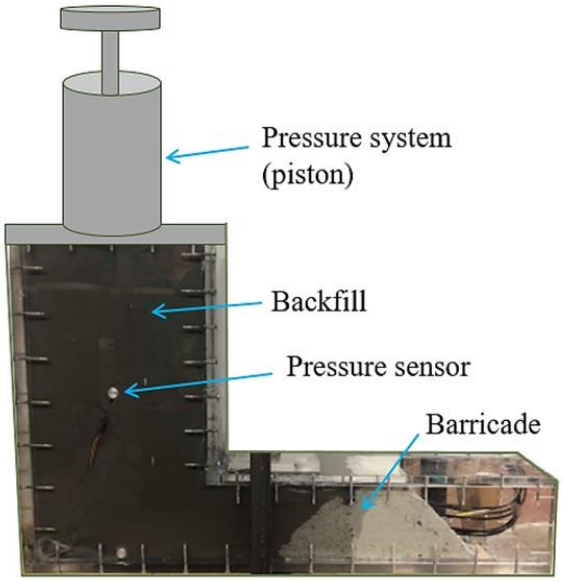


Figure 5-1: A physical model of mine stope designed to study the behaviour of the waste rock barricades in interaction with the paste backfill.

Muck barricades made of development waste rocks are commonly used in Quebec mines as retaining structures located in mining drawpoints. It is not easy to obtain an accurate particle size distribution of waste rock in stacks where heterogeneity, segregation, and the presence of large rocks complicate measurement.

Although the use of waste rock barricades is widely practiced in many Canadian mines, these structures are still poorly documented and require further research to determine their physical and mechanical characteristics. In this work, preliminary tests started on a barricade made of fine materials [GSD1, Fig. 3-6(a)] and further testing will be resumed in the future on different grain size distributions. The volume of the trapezoidal barricade used is 1304 cm^3 (25 cm base length, 7.2 cm top length, height = width = 9 cm). Therefore, the angle of inclination of the barricade on both sides is 45°. The waste rock's apparent density was about 1.9 g/cm^3, and the solid mass concentration of the uncemented backfill was approximately 70%. A high viscosity fill (Cw=70%) is chosen to facilitate filling and compression operations. Pressure sensors placed in front of the backfill were used to measure the total pressure of the backfill that is increased by the manual piston until a barricade failure occurs.

Two tests were carried out on the barricade as follows:

- barricade is placed in drift has smooth surfaces (low fiction).

- barricade is placed on shims (0.2×0.6cm each 5cm) fixed to the base of the drift to increase the interface friction (rough surface at drift base). The shims were formed from lines of silicon sealant that were left to dry before the tests.

5.3 Results

The first case concerns a barricade placed on a smooth surface (without shims at the base of the drift), where the barricade slipped at a pressure of 40 kPa (sliding failure) when the manual piston was used. While in the second case, the barricade placed on shims at the base of the gallery collapsed at a pressure of 120 kPa with an inclined plane (shear failure) emerging at mid-height in the upstream part of the barricade. The volume of the slipping portion in the upper section was about half the total size of the barricade (Fig. 5-3).

The pressure recorded at the failure of the barricade during the backfill pressure increasing is summarized in Table 5-1.

Table 5-1: Pressure recorded at the failure of the barricade during the experimental tests.

Failure type	The pressure at failure (kPa)	Barricade unit weight (γ_{wr})
Sliding failure	40	19 kN/m^3
Shearing failure	120	

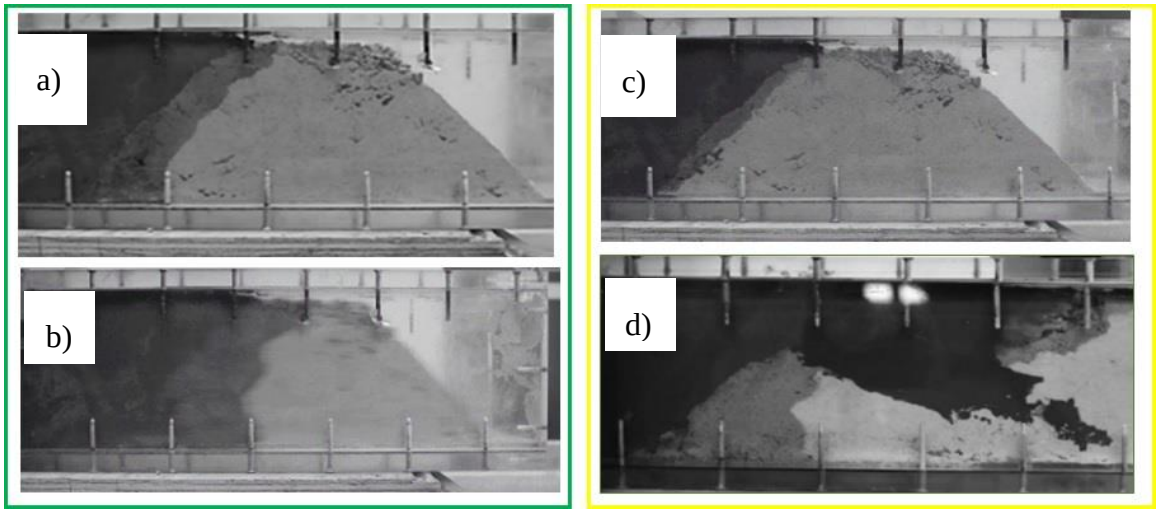


Figure 5-2: Results of the two experimental tests: (a & b) barricade before and at sliding; (c & d) the barricade before and at the collapse of the upper part.

Based on these results, it can be observed that the friction between the barricade and the drift walls controls the instability form of the barricade (sliding or collapse). Analysis of these results using the limit equilibrium calculation is based on several assumptions, including the following:

- The shear strength is ignored between the top of the barricade and the drift roof because there is a gap over the barricade.
- The lateral friction between the barricade and the smooth walls of the drift is ignored for simple calculation.

By the limit equilibrium calculation, the stability of the barricade in the direction of the drift can be analyzed as follows:

1st test (Sliding analysis)

Figure 5-4 shows the acting forces in the first test (sliding case). Where P is the backfill load at failure (kPa) acting at mid-height of the drift (h). L_T is the length of the barricade at the top (m), which is varied in different mines according to the experience of their engineers. Increasing the length of the top increases the overall size of the barricade, which enhances stability. In this analysis, we consider that only the friction at the base of the barricade (F_b) resists the backfill; this friction is generated by the vertical component of the backfill and the weight of the barricade. In order to achieve barricade failure, the additional pressure applied by the piston was so rapid that the backfill water did not have time to dissipate and/or be consumed by the pores of the barricade when the pressure was increased.

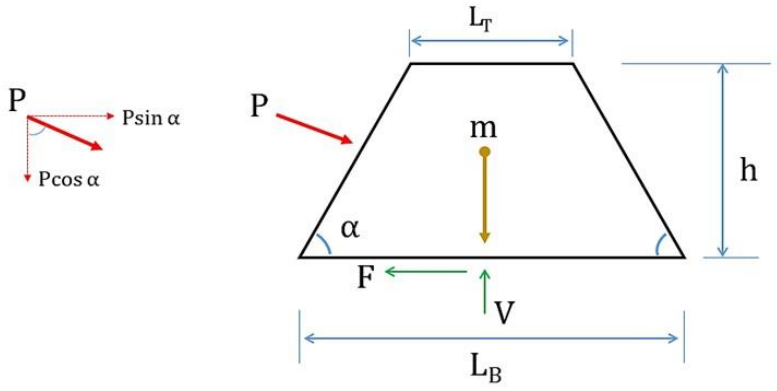


Figure 5-3: Sliding analysis of acting forces.

Since the inclination angles of the upstream and downstream sides are equal (α), the length of the barricade at the base (L_B) can be written as follows:

$$L_B = L_T + \frac{2h}{tan\alpha} \tag{5-1}$$

Where (h) is the height of the drift or the barricade (m). If the force V is the resultant of the vertical forces and δ is the interface friction angle between the barricade and drift walls, the friction force at the base of the barricade (F_b) is given as follows:

$$F_b = V \tan\delta \tag{5-2}$$

The vertical reaction at the base of the barricade is given as follows:

$$V = P\cos\alpha + \gamma_{wr}\left[\frac{1}{2}(L_T + L_B)hW\right] \tag{5-3}$$

Thus, the fiction at the base of the barricade is written as follow:

$$F_b = \tan\delta\left[P\cos\alpha + \gamma_{wr}\left(L_T + \frac{h}{\tan\alpha}\right)hW\right] \tag{5-4}$$

Where W is the width of the drift or the barricade (m); γ_{wr} is the unit weight of the barricade (kN/m^3).

By neglecting the lateral friction between the barricade and smooth walls of the drift, the factor of safety (FS) is given by:

$$FS = \frac{F_b}{P\sin\alpha} = \frac{V\tan\delta}{P\sin\alpha} \tag{5-5}$$

Therefore, the coefficient of friction will be written as follows:

$$\tan\delta = \frac{FS \times P\sin\alpha}{P\cos\alpha + \gamma_{wr}\left[\frac{1}{2}(L_T + L_B)hW\right]} \tag{5-6}$$

By substituting the values obtained in the first test (FS=1, α=45°, h=W=9cm, L_T=7.2cm, L_B=25cm, γ_{wr}=19kN/m^3, p`=40 kPa, and the inclined height of the barricade ($h/\sin\alpha$) to which the fill is applied is 0.1273m) into the previous equation results:

$$\tan\delta = \frac{1 \times (40 \times 0.09 \times 0.1273)\sin 45°}{(40 \times 0.09 \times 0.1273)\cos 45° + 19\left[\frac{1}{2}(0.072 + 0.25) \times 0.09 \times 0.09\right]} = 0.928$$

$$\delta = 42°$$

The Plexiglas plates (PMMA) of the model have smooth surfaces, and the magnitude of the calculated coefficient of friction was not expected to be close to one. This result demonstrated that the lateral resistance friction between the barricade and the drift walls should not be neglected.

If the lateral friction between the barricade and the walls of the drift is taken into account in the calculation of the stability of the barricade, F_L should be added to the friction force at the base of the barricade. The lateral friction force (F_L) can be calculated by multiplying the coefficient of friction ($\tan\delta$) by the compressive force generated from the lateral earth pressure of the barricade as follows (see also Li & Aubertin, 2011; Yang, 2016):

$$F_L = \tan\delta \left[\frac{1}{2} K_a \gamma_{wr} h^2 \left(L_T + \frac{2}{3}\frac{h}{\tan\alpha}\right)\right] \quad (5\text{-}7)$$

Where K_a is the active lateral earth pressure coefficient.

Thus, the Factor of safety (FS = shear strength / applied load) will be given by:

$$F_S = (F_b + 2F_L)/P \sin\alpha \quad (5\text{-}8)$$

2nd test (Shear analysis)

Figure 5-5 analyzes the second barricade test, installed in a drift with shims at the base. The top part collapsed with a slope from the mid-height of the upstream side to the downstream corner (see Figure 5-3d).

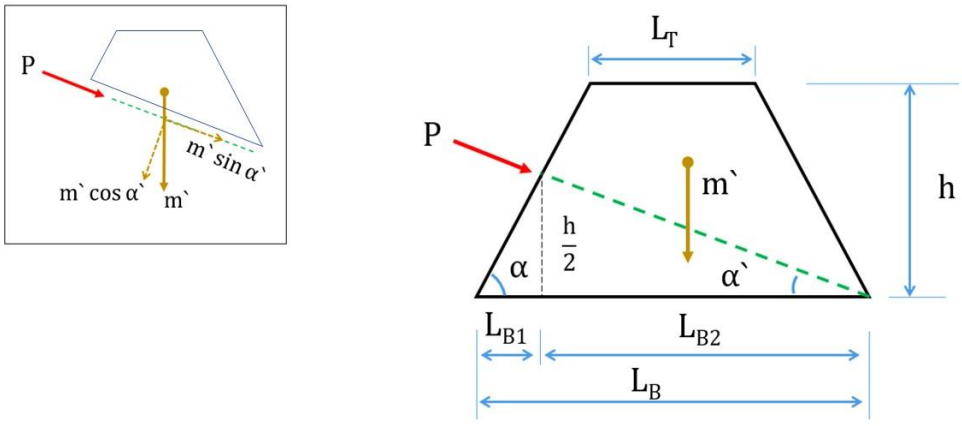


Figure 5-4: Shear analysis for a barricade fixed at the drift base using shims.

In this analysis, we assume that the resultant of the backfill force at failure works on the same breaking line, which is tilted with α` from the horizontal plane (Fig. 5-5). The ultimate pressure at failure is equal to the pressure value recorded using a pressure sensor placed in front of the barricade. Nevertheless, if the engineer/analyst considers that the resultant of the backfill (force) is perpendicular to the barricade surface at the upstream part, it must multiply the force by sinα`.

As shown above, the length of the barricade at the base is given by:

$$L_B = L_T + \frac{2h}{\tan\alpha} = L_{B1} + L_{B2} \tag{5-9}$$

This length (base length of the barricade) is divided into two parts, L_{B1} and L_{B2}. The lengths of the right and left sides are given respectively by:

$$L_{B1} = \frac{h}{2\tan\alpha} \tag{5-10}$$

$$L_{B2} = L_T + \frac{2h}{\tan\alpha} - \frac{h}{2\tan\alpha} = L_T + \frac{3h}{2\tan\alpha} \tag{5-11}$$

Thus, the angle of the failure plane is given by:

$$\alpha` = \tan^{-1}\left[\frac{h}{2} \Big/ \left(\frac{3}{2}\frac{h}{\tan\alpha} + L_T\right)\right] \tag{5-12}$$

By neglecting the lateral friction between the barricade and the smooth walls of the drift, the factor of safety is given as follows:

$$FS = \frac{m`\cos\alpha`\tan\emptyset + c\left(\frac{h}{2}\frac{W}{\sin\alpha`}\right)}{P + m`\sin\alpha`} \tag{5-13}$$

Where $m`$ is the weight of the barricade in the upper part (kN); c is the cohesion along the failure plane (kN/m^2). In the equation above, it has been assumed that the shear resistance force at the failure plane consists of cohesion and internal friction. It may not be correct to pre-determine the failure plane, but this analysis will be performed based on what was observed during the experiment until further testing is conducted (and repeated) to clarify the behaviour of the waste rock barricade in different size distributions.

Therefore, the internal friction angle of the barricade can be written as follows:

$$\emptyset = \tan^{-1}\left[\frac{FS(P + m` \sin\alpha`) - c\left(\frac{hW}{2\sin\alpha`}\right)}{m` \cos\alpha`}\right] \quad (5\text{-}14)$$

To calculate the weight of the slipped portion of the barricade, the A_3 area must be calculated (see Fig. 5-6).

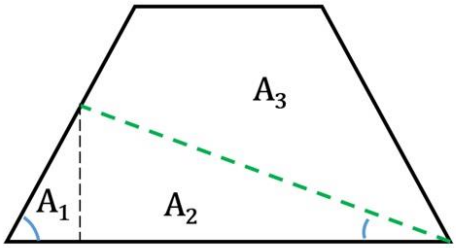


Figure 5-5: Schematic view showing A_3 among the divided areas of the barricade.

The barricade area at the upper part is given by:

$$A_3 = A_T - A_1 - A_2 \quad (5\text{-}15)$$

A_T is the total area of the barricade that is given by the following formula:

$$A_T = \frac{1}{2}h(L_T + L_B) = h\left(L_T + \frac{h}{\tan\alpha}\right) \quad (5\text{-}16)$$

The area of the small triangle at the left in the lower part of the barricade is given as follows:

$$A_1 = \frac{1}{2}\frac{h}{2\tan\alpha}\frac{h}{2} = \frac{1}{8}\frac{h^2}{\tan\alpha} \quad (5\text{-}17)$$

The area of the large triangle at the right in the lower part of the barricade is given as follows:

$$A_2 = \frac{1}{2}\left(\frac{3}{2}\frac{h}{\tan\alpha} + L_T\right)\frac{h}{2} = \frac{3}{8}\frac{h^2}{\tan\alpha} + \frac{h}{2}L_T \quad (5\text{-}18)$$

By substituting A_T, A_1, and A_2 in equation 5-15, the area of the upper part of the barricade (A_3) will be given by:

$$A_3 = hL_T + \frac{h^2}{\tan\alpha} - \frac{1}{8}\frac{h^2}{\tan\alpha} - \frac{3}{8}\frac{h^2}{\tan\alpha} - \frac{h}{2}L_T = \frac{h}{2}\left(L_T + \frac{h}{\tan\alpha}\right) \quad (5\text{-}19)$$

It is noteworthy that the upper section (A_3) is half of the total area of the barricade. The weight of this section ($m`$) is calculated using the following relation:

$$m` = \gamma_{wr} W A_3 = \gamma_{wr} W \frac{h}{2}\left(L_T + \frac{h}{\tan\alpha}\right) \quad (5\text{-}20)$$

Where W is the width of the drift (m); γ_{wr} (kN/m^3) is the unit weight of the waste rock.

By substituting the value of the second test (FS=1, α=45°, h=W=9cm, L_T=7.2cm, L_B=25cm, γ_{wr}=19kN/m^3, p`=120 kPa, and c=0) into the previous equation to calculate the friction angle, we obtain:

$$\alpha` = \tan^{-1}\left[\frac{0.09}{2} / \left(\frac{3}{2}\frac{0.09}{\tan 45} + 0.072\right)\right] = 12.26°$$

$$m` = 19 \times 0.09 \times \frac{0.09}{2}\left(0.072 + \frac{0.09}{\tan 45°}\right) = 0.012466kN$$

$$\emptyset = \tan^{-1}\left[\frac{1 \times (120 \times 0.09 \times 0.12728) + 0.012466 \times \sin 12.26° - 0}{0.012466 \cos 12.26°}\right] = 89.5°$$

This irrational finding (high friction angle, $\emptyset > 45°$) showed that cohesion along the failure plane and lateral friction between the barricade and the drift walls play an important role in resisting the backfill pressure and that it is not correct to neglect them. Nonetheless, the following equation (5-21) may be used to calculate the dimensions of a barricade without considering the lateral friction on both sides (as a safe procedure).

$$L_T = \frac{c\left(\frac{hW}{2\sin\alpha`}\right) - FS \times P}{\gamma_{wr} W \frac{h}{2}(FS \sin\alpha` - \cos\alpha` \tan\emptyset)} - \frac{h}{\tan\alpha} \quad (5\text{-}21)$$

When the lateral friction between the upper part of the barricade and the drift walls is taken into account in the calculation of the shear strength of the barricade (Fig. 5-7), F_L for the upper area must be added as follows:

$$F_L = \tan\delta\left[\frac{1}{2}K_a\gamma_{wr}\int y_{A3}^2 dx\right]\cos\alpha`$$
$$= \tan\delta\left[K_a\gamma_{wr}\left(\frac{L_T h^2}{2} + \frac{h^3}{3\tan\alpha} - \frac{h^3}{48}\left(\frac{1}{\tan\alpha} + \frac{1}{\tan\alpha`}\right)\right)\right]\cos\alpha` \quad (5\text{-}22)$$

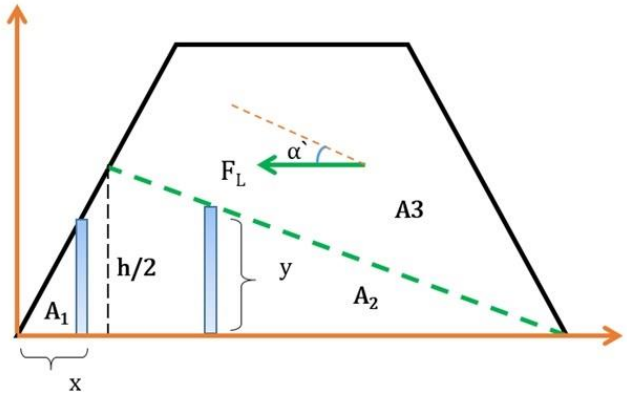


Figure 5-6: Lateral friction calculation between the barricade and drift walls (second test).

Thus, the factor of safety (FS = shear strength/applied load) will be given by the following equation:

$$FS = \frac{m` \cos \alpha` \tan \emptyset + c\left(\frac{h}{2}\frac{W}{\sin \alpha`}\right) + 2F_L}{P + m` \sin \alpha`} \quad (5\text{-}23)$$

The force applied to the backfill after placement can be considered as follows:

$$P = \gamma_b \left(H - \frac{h}{2}\right) hW / \sin \alpha` \quad (5\text{-}24)$$

Where γ_b (kN/m^3) is the unit weight of saturated backfill, and H (m) is the backfill height in the stope.

It should be noted that when the pressure on the barricade of the second test (with chocks at the base of the drift) increased, the upper par was largely displaced before the collapse. Figure 5-8 shows the position of the barricade at the time of the collapse (indicated in yellow) relative to the initial position.

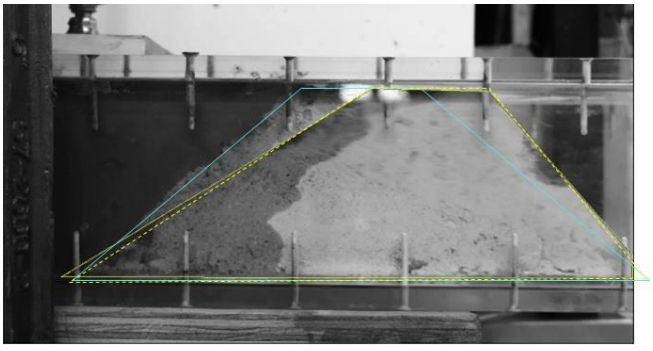


Figure 5-7: Displacement of the upper part of the barricade before the collapse.

It is more appropriate to include the entire surface in the calculation of the lateral friction resistance of the barricade (not just the upper part). At first, the entire mass of the barricade resists the backfill pressure, and then the upper part becomes more effective in resisting the pressure (together with the internal shear resistance) until failure. But to design a safe barricade, it is better to adapt /or ignore the lateral friction in the upper part of the barricade.

It may be important to note that the pressure measured in front of the barricade may not express the actual force that caused the barricade to collapse. Once the backfill touches the surface of the barricade, the pressure drops sharply due to the large difference in hydraulic conductivity between the barricade and the backfill (see PWPS4 in Figure 3-14 in Chapter 3). This observation can be attributed to the rapid passage of water through the barricade pores when the piston was used. This means that the ultimate strength of the barricade may be much lower than the value measured in the experiment. A high backfill consistency (about C_w=76%) may give different results if the same test is repeated as the use of the piston, in this case, will push the pulp of backfill towards the barricade (not just the water).

Many important parameters were not calculated in the previous tests, such as the interface friction angle (δ) between the barricade and the physical model (PMMA), the internal angle of friction of the barricade (Ø) and the cohesion (c) when the barricade contains fine materials. Also, protrusions should be made on the inner walls to represent the friction on all surfaces of the drift (not only at the base of the drift). In addition, to confirm the results and achieve a safe design, the repeatability of barricade tests at different positions and distribution of grain size should be considered. The influence of the percentage of solids in the backfill and all the previous notes will be taken into account in complementary tests on a physical model developed to apply high pressure using a manual or pneumatic piston, as shown in Figure 5-9 (see the recommendations in Chapter 6 for more details).

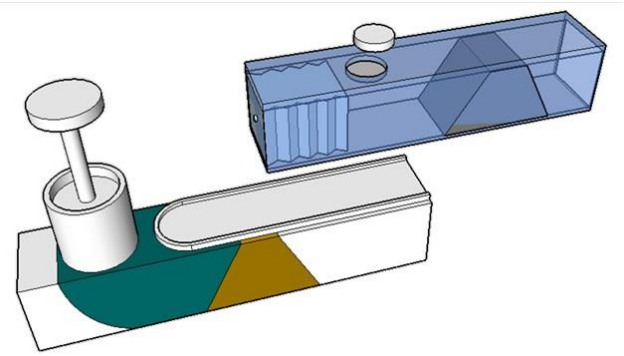


Figure 5-8: Prospective physical model equipped with a piston.

Other tests were carried out on barricades of different grain sizes (varied between 1to 8mm) without achieving complete failure when the backfill (70% solid concentration) pressure was increased (Fig. 5-10).

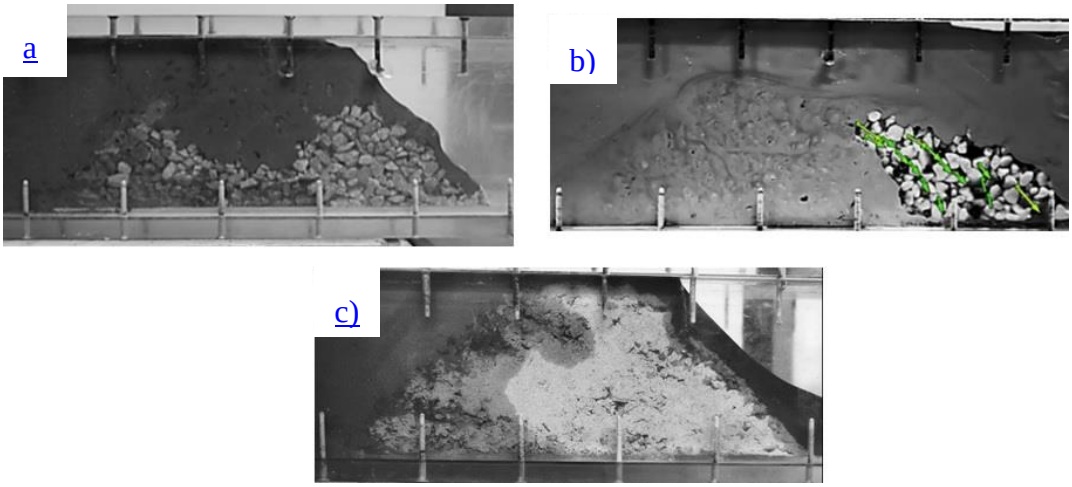


Figure 5-9: Different scenarios for the collapse of the barricade.

These tests have shown that not only is the determination of barricade dimensions sufficient to ensure the safety of the barricade in retaining mine backfill but also that several issues need to be considered. A dense (well-graded) barricade prevents penetration of the backfill and increases its shear resistance. Sealing around the barricade, spatially at the top, during barricade construction plays an important role in preventing the backfill from leaking. The results also showed that the use of the shotcrete layer behind the barricade is beneficial in increasing the safety factor and avoiding unexpected incidents such as tremors due to explosions or earthquakes, or even design errors.

Previous tests conducted on the same model (see Nujaim et al., 2019) to measure the sliding pressure of the barricade (no shims at the base) for all the GSDs in Figure 3-4a. The results showed that the pressure measured when the barricade is sliding varied from 13 to 50 kPa. Intuitively it is possible to suggest that the barricade with higher apparent density (ρ_h) would fail/slide under a total pressure higher than that for barricade with lesser density. In fact, the barricade seems to develop higher frictional resistance generated by its particles in contact with the drift walls. It appeared that the barricade containing about 30% of fine material (diameter < 1 mm) exhibits higher frictional resistance (or sliding resistance) than the other barricade configurations, even if the total density is higher, as can be seen in Figure 5-10.

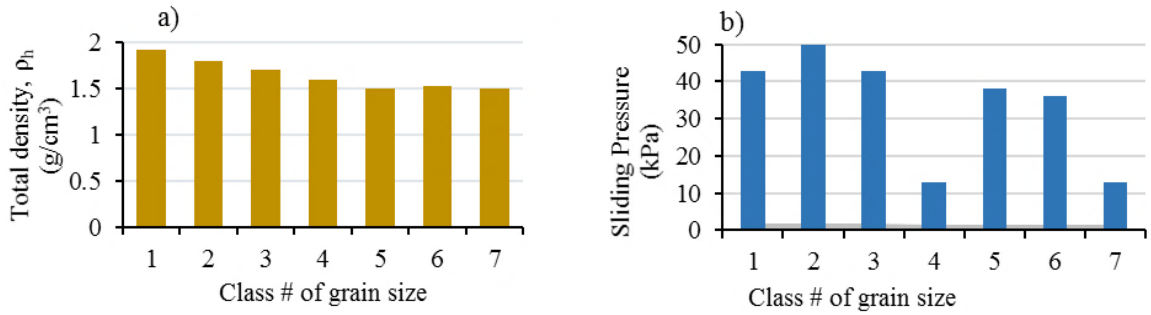


Figure 5-10: a) barricade total density as a function of particle size distribution; b) barricade sliding pressure for all particle size distributions

In addition, the backfill slurry of many other tests takes a slope towards the barricade during backfilling (with drainage). That means that in the actual stopes (in situ) that are progressively filled over several days, there may be a void (unfilled) at the top of the barricade (Fig. 5-11). This unfilled portion may appear depending on several factors such as the barricade position from the brow, the height of the backfilled layer below the level of the drif roof, the viscosity of the backfill, the rest time, the binder content and the permeability of the barricade. Consequently, the sequential filling increases the safety factor and the stability of the barricade, especially in the upper part; these aspects also need to be investigated in future work.



Figure 5-11: a) Tilt of the backfill slurry surface (Cw=70%) during filling, b) Unfilled portion at the top of the barricade after the drainage and sedimentation process; sand (0/400µm) was used instead of the tailings (see Nujaim et al., 2018).

5.4 Concluding and remarks

Experimental results are consistent with a few previous studies (e.g., Li et al., 2009; El Mkadmi, 2012; Yang et al., 2016; Nujaim et al., 2018). The failure mechanism of the waste rock barricade depends on the properties of the interface between the drift walls and the waste rock. Fixing the barricades at the base using some chocks increased the resistance of the barricade three times (from 40kPa for the barricade without chocks to 120 kPa for that has chocks at the base). When the drift walls are smooth, the interface friction angle may be less than the critical angle; the slip failure then governs the design of the barricade. When the drift walls are rough, the design of the waste rock barricade is generally dependent on the shear strength of the barricade specialty at the top. It was also shown that the stresses generated within the barricade in the event of a failure may be much lower than those measured in front of the barricade due to the high hydraulic conductivity of the barricade.

The resultant of the backfill pressure acting on the failure plane accelerates once collapse begins, where part of the sipped weight works in its direction. The results also demonstrated that the quality of the construction for the barricade, the good sealing around the barricade, and experience govern and play an important role in ensuring safety. The viscosity of the backfill (concentration of solid mass), the position of the barricade from the drawpoint, the filling rate, the reset time between layers, the cement content, the arching effect, the particle size distribution of the barricade and the

use of the shotcrete layer are interrelated issues that control the design and safety during the backfilling operation and require further research. Additional tests on an updated physical model will help to develop a general analytical solution that includes both sliding and shearing scenarios depending on the amount of friction between the barricade and the walls of the drift (interface friction angle). If the factor of safety governs the design for continuous backfilling regardless of the size/cost of the barricade, the engineer can consider the worst-case (sliding scenario with the neglect of the lateral friction). The experience of the field engineer plays an important role in the selection of the design type and the insertion and/or neglect of certain parameters depending on the condition of the site. The important question is what is the angle of friction of the interface that moves the barrier failure from slip to shear? With numerical modelling, it can be easy to perform several simulations and use a calibration factor to develop a general solution. But with experimental tests, it is difficult to obtain this factor because we need many tests at different interface friction angles to measure the increase in strength of the barricade until we obtain shear failure. The repeatability of tests on the physical model remains a challenge for this type of experiment.

CHAPTER 6 BRIEF DISCUSSION, CONCLUSIONS AND SOME RECOMMANDATIONS

6.1 Discussion

From the literature review it was suggested the necessity of performing some experimental study on the stability/failure mechanisms of waste rock barricades because there are any physical modeling available. All the results of the tests on reduced-scale models existing in the literature deal with the investigation of exposed backfill free faces, estimation of the average vertical stress at the bottom of a stope, measurement of the self-weight consolidation or the stress state during the backfilling (Mitchell et al., 1982; Sivakugan et al., 2006a; Widisinghe et al., 2013; Sivakugan et al., 2015; Belem et al., 2016, 2016). Indeed, the previous studies using physical models did not address the waste rock barricades and their failure mechanism in relation to different grain size distributions. In addition, no parametric study for the characteristics of the backfill during the backfilling and its interaction with the barricade exist in the literature. Physical modelling using a reduced-scale transparent model was needed for understanding the geomechanical behaviour of waste rock barricades and their failure mechanism. The reduced-scale models are fast, reproducible and can be driven to failure. The choice of material properties is extensive, and various parameters can easily be modified to study their influence. The reduced-scale models must obey similarity laws that guarantee the similarity of the mechanical behaviour between the scale model and its associated prototype. These laws allow applying the solution obtained on the scale model to the problem in real size. To satisfy the different conditions of similarity, the use of a natural gravity model is useless and only allows us to remain within the framework of a qualitative study. Laboratory models are also subjected to large-scale effects that modify/disturb both qualitative results (failure mechanisms) and quantitative ones (displacements versus loads). Besides, the failure of the barricade during the experiment can damage the equipment.

Although waste rock barricades are more economical, they have not yet been studied in detail, so there are very few options for their analysis and design of the optimal size. The behaviour of these barricades must be studied for a secure design to protect equipment and workers and increase the rate of filling. The grain size distributions (GSD) of the waste rock barricade used in the model experiments were not configured according to standard GSD curves. The GSD curves were based

on laboratory observations so that the configurations varied from a fine-grained barricade to a coarse-grained barricade without fine particles.

The use of a reduced-scale model made from transparent PMMA plates (plexiglass) to simulate underground mine stopes backfilling allowed the observation of the interaction between the barricade in the drawpoint and the backfill. The transparent reduced-scale model also allowed monitoring the barricade during saturation, drainage and at failure when the manual piston is used. The results obtained do not necessarily reflect reality since the interior walls of the reduced-scale model must be provided with representative roughness to represent the interface friction with the rock walls. However, the results obtained contribute to an understanding of the behaviour of the waste rock barricade and the backfills (cemented or uncemented). The results also showed that the optimal design of the barricade to support the backfill should be well-graded and compacted.

The numerical and physical modelling have shown that negative pressure can occur in different desaturation zones due to suction. Therefore, it is precautionary of using numerical modelling results in practice because:

i) for the first hours after the placement, it is preferable to model the fresh liquid backfill as a heavy fluid (effective stress analysis, linear elastic with pore water pressure change). These modeling parameters yield results that are close to experimental results compared to other built-in models (e.g. elastoplastic models);

ii) when the backfill is placed in a dry state or partially saturated, it is preferable to define the backfill as soil with constant mechanical parameters (do not change over time);

iii) the cemented backfill behaviour can be modelled, only in the first hours, as a fluid-like material (elastic behaviour and effective stress analysis).

The various software packages used in numerical modelling have been developed for geotechnical problems and may not reflect the complex behaviour of cemented backfill. Comparison between these models was avoided because they were not examined in experimental studies. In this thesis, the numerical simulations were more consistent with the experimental tests for the uncemented backfill than for the cemented paste backfill. It is therefore important to develop a numerical model to simulate the cemented backfill during the cement hydration (hardening) depending on several factors such as the binder ratio, backfill viscosity and shear yield stress, and the tailings properties.

However, numerical modelling is still useful for predicting the cemented backfill pressure few hours after placement (corresponding to the critical phase).

The stability analysis based on limit equilibrium calculation showed that lateral friction between the barricade and the drift walls, as well as the apparent cohesion between the barricade particles (due to clogging of fine particles), play an important role in the overall shear strength of the waste rock barricade. The good quality of barricade construction and the use of shotcrete will increase the stability of the barricade. For the design of the barricade (sliding or shearing failure), it was clarified the importance of the friction between the barricade and the walls of the drift. Placing the barricade on some chocks increased by three times the shear strength of the barricade (from 40 kPa for the barricade without chocks to 120 kPa when using chocks at the base). However, future works are required to develop a general analytical solution (sliding and shearing scenarios) depending on the amount of friction between the barricade and the drift sidewalls (interface friction angle and shear). If the factor of safety (FS) guides the backfilling design irrespective of the size/cost of the barricade, the worst case can be considered by the engineer (sliding scenario with the neglect of the sidewalls friction). It can be easy to perform many simulations using numerical modelling to build a general solution and use a calibration factor to evaluate the interface friction angle that changes the failure of the barricade from sliding to shearing. But it is difficult to get this aspect using experimental testing because numerous tests should be performed on different interface friction angles to assess the increase in barricade shear strength before the failure occurred. For this sort of experiment, the repeatability of experiments on the physical model remains a challenge. One of the objectives of this thesis was to evaluate the existing analytical solutions for the waste rocks barricade design, but due to several shortcomings and restrictions (simplification made on the physical model, time, measurement tools, ...), this part has been left for future work.

6.2 Conclusions

This thesis presents an experimental study on a reduced-scale physical model of a typical longitudinal mine stope, as well as numerical simulations of the geomechanical behavior (evaluation of the stress state in the cemented paste backfill placed in a mine stope) and the interactions between the fresh backfill and the waste rock barricade. The results of this thesis can help to improve the design of underground backfilling systems as well as the sizing of waste rock barricades. The main conclusions of this thesis are as following:

- The high hydraulic conductivity of the waste rock barricades allows rapid drainage of the stope. Indeed, the drainage of the 70% solids paste backfill was quantified through the volumetric deformation (ε_v) due to its self-weight consolidation, whether it is cemented (ε_v = 4.5%) or uncemented (ε_v = 16%).
- The viscosity of the backfill (and its shear yield stress) and its shear parameters influence the state of stresses in backfilled stopes and the time to final consolidations.
- The drainage increases the effective stresses and, after some time has elapsed, zones of desaturation (suction) appear in the upper part of the backfilled stope and near the waste rock barricade.
- The stability of a waste rock barricade depends on many factors, such as the particle size of the waste rock particles, the degree of their compaction, as well as the roughness of the draw-point sidewalls (sliding resistance and/or friction between the barricade and the walls). Indeed, this stability seems to be controlled by the frictional resistance of the interface along the base of the barricade (smooth or rough walls). The overall slip and shear failure were observed during testing.
- The backfill-wall interface of the physical model influences the stress state in the backfill placed. The rougher the wall surfaces, the greater the frictional resistance, and this results in a transfer of some of the backfill weight to the sidewalls.
- The use of a trapezoidal waste rock barricade greatly favors its stability against sliding, depending on the roughness of the walls of the model. Analysis of the test results suggests that special attention should be paid to the upstream face near the top of the barricade for the analysis of overall stability.
- The use of cement for backfilling the first layer (the plug), a layer of shotcrete around the perimeter at the top of the downstream face of the barricade and the compaction of the waste rock from the barricade are important operations which must be well executed when building the rock barricades.
- The results of the numerical simulations were consistent with the tests performed on the reduced-scale physical model, but the orders of magnitude of the pressures measured were different (30% higher in the numerical results).

Since the testing and analysis of the results are based on several simplifying assumptions, it is desirable to improve future work by using a more realistic filling rate, other types of barricade and rough interior surfaces of the reduced-scale model.

6.3 Recommendations for further study

Besides what is presented in the thesis, several aspects require further research for a better assessment of the behaviour of waste rock barricades and cemented paste backfills:

- It would be useful to better investigate the backfill stress in different consistency, cement content, and realistic mining/filling rate and filling sequences.
- To better represent the behaviour of the barricades, it is suggested to carry out experimental tests in different dimensions, positions, and GSDs with sequential filling.
- Further research is required to collect in situ data on the particle size distributions of the waste rock barricades to configure them on the reduced-scale model.
- Experiments should be conducted on the shear box to measure the shear parameters of the waste rock material (c, ϕ) and to find out the frictional resistance generated in the interface between the physical model and the barricade. These parameters shall be calculated, considering the same degree of compaction for the particles in which the barricade is built in the drift. These parameters, as well as the ultimate resistance measured during the experiment, will greatly contribute to the development of an analytical solution for the design of the barricade.
- It will be interesting to study the strength of the waste rock barricade at different stages of saturation (dry, partially saturated, saturated); this can be achieved by using the piston at the targeted saturation point for the barricade.
- the analytical solutions (presented in Chapter 2) proposed for estimating the pressure in the backfilled stopes and on the barricade should be verified according to the results from an upgraded reduced-scale physical model. This procedure will also verify the relationships used for sizing the waste rock barricades.

- More work is required to study the sensitivity of the parameters introduced in the numerical simulations and the ability to express the gradations and morphological characteristics of the grains making up the barricade (shape, angularity and surface roughness).
- In order to obtain good comparisons between numerical modelling and physical model in the laboratory testing, it will be important to calculate all the parameters or functional relationships needed for numerical simulations, such as hydraulic conductivity and water retention curve.
- An important validation step should be taken to compare the results with the in situ measurement data published by some authors (e.g. Alcott et al., 2019; Grabinski et al., 2010; Thompson et al., 2012); it must then be based on the real geotechnical properties of the backfill used, the geometry of the stope and the sequence of backfilling.
- It will be interesting to calculate the time factor (T) to determine whether the backfill placed is classified as non-consolidating or fully consolidating (e.g., Belem et al., 2013; Fahey et al., 2010; Gibson, 1958) and compare the results with the experimental observations.
- It is also suggested to relate the shear parameters and Poisson's ratio ν of the backfill with the consistency of the elastoplastic model or use more realistic constitutive models to better represent its behaviour.

The use of the translucent physical model contributed, even in small part, to the understanding of the behaviour of the backfill after placement in the stope and the understanding of the behaviour of the barricades and their failure mechanics. However, further experiments need to be conducted after the improvements to the model, including the following:

- Provide the internal walls of the model with the representative roughness (by making protuberances) that simulate the actual behaviour on site. The latter will contribute to the understanding of the arching effect, particularly in the case of sequential rather than instantaneous (or continuous) filling, as the casting layers first can serve as a foundation for the upper layers and reduce the weight of the fill measured at the bottom of the stope by transferring it to the sidewalls.

- Install the piston used to increase backfill pressure at the top of the model to gain time during removal and installation and to prevent backfill leakage. The piston must be made of solid materials that can withstand the pressure without breaking.
- The model must also be rebuilt from stronger plates to avoid cracks or collapse due to the use of the piston to overcome the maximum strength of the barricade. Otherwise, the barricade must be made of light particles so that the ultimate strength can be determined at reasonable values using the hand piston.
- It is suggested to redesign the reduced-scale model without screws, but rather use a clamping system to close the roof of the drift (which should contain rubber gaskets) after building the barricade at its location inside the drift.
- One of the sidewalls of the stope must be removable (without screws) so that the model can be easily cleaned after each experiment.
- When the solid content of the backfill exceeds 75%, it is difficult to fill the model stope manually. Thus, it will be easier to use a filling system to obtain a regular filling rate for low viscosity backfill by using, for example, a small pump or conveyor.
- It should be noted here that the sensors used are not designed to measure paste backfill pressure and require additional information from the manufacturer, such as the impact of the cement, the temperature resulting from cement hydration, the effects of sulphate attack (present in the tailings). Therefore, to further analyze the backfill temperature during hydration, a small temperature sensor can also be installed to help evaluating the measurement errors of the pressure sensors due to the increase in temperature and to ensure that the temperature remains within the safe range.
- It is best to make a hollow base below the model to pass the cables of sensors used to measure the pressure. Light films should be used to protect the surface of pressure sensors from the effect of the cement and sulphate involved in the backfill. It is also advisable to locate the sensors places on the model to find the appropriate method for laying the cables.
- In some experimental tests on cemented backfills, during the desaturation and drainage of the water, the pressure measurement increased gradually and significantly after a certain time from the filling. It appears that reduced-scale physical modelling on a cemented

backfill, using current measurement tools, can only give good results a few hours after the filling. This phenomenon was not observed with the uncemented filling. It appears that the hardening of the cemented backfill and the development of shear strength can affect pressure sensors. Hence, it is important to check and find appropriate sensors to conduct long-term monitoring experiments.

- Finally, to facilitate the analysis of the results of long-term experiments, the data acquisition system should permit the recording of pressure measurements at the desired frequency.

REFERENCES

Agarwal, A., & Lang, J. (2005). *Foundations of analog and digital electronic circuits*. San Francisco, CA: Morgan Kaufmann Publishers.

Altaee, A., & Fellenius, B. H. (1994). Physical modeling in sand. *Canadian Geotechnical Journal, 31*(3), 420-431.

Annor, A. (1999). *A study of the characteristics and behaviour of composite backfill material.* (Ph.D. Thesis), McGill University, Montreal, Canada.

Anonymous. (1999). Definition of Geotechnical Engineering. *Ground Engineering Magazine, 32*(11), 39.

Arioglu, E., & Biron, C. (1983). Design of supports in mines: Wiley and Sons, New York.

Askew, J., McCarthy, P., & Fitzgerald, D. (1978). *Backfill research for pillar extraction at ZC/NBHC.* Paper presented at the 12th Can. Rock Mech. Symp. on Mining with Backfill, Sudbury.

Atkinson, J. H., & Bransby, P. (1978). *The Mechanics of Soils: An Introduction to Critical States, Soil Mechanics*: McGraw-Hill.

Aubertin, M. (2013). *Waste rock disposal to improve the geotechnical and geochemical stability of piles.* Paper presented at the In 23rd World Mining Congress; X-CD Technologies Inc, Montreal, QC, Canada.

Aubertin, M., Bussière, B., Bernier, L., Chapuis, R., Julien, M., Belem, T., . . . Li, L. (2002). *La gestion des rejets miniers dans un contexte de développement durable et de protection de l'environnement.* Paper presented at the Congrès annuel de la société canadienne de génie civil, Montréal, Québec, Canada, Montréal, QC, Canada.

Aubertin, M., Bussiere, B., & Chapuis, R. P. (1996). Hydraulic conductivity of homogenized tailings from hard rock mines. *Canadian Geotechnical Journal, 33*(3), 470-482.

Aubertin, M., Li, L., Arnoldi, S., Belem, T., Bussière, B., Benzaazoua, M., & Simon, R. (2003). Interaction between backfill and rock mass in narrow stopes. *Soil and rock America, 1*, 1157-1164.

Aubertin, M., Li, L., Belem, T., Simon, R., Harvey, A., James, M., . . . Bussière, B. (2005). *Méthodes d'estimation des pressions induites dans les chantiers remblayés.* Paper presented at the Proceedings of the Symposium Rouyn-Noranda: Mines and the Environment, Rouyn-Noranda, Que.

Barbour, S., Hendry, M., Smith, J., Beckie, R., & Wilson, G. (2001). A research partnership program in the mining industry for waste rock hydrology. *University of Saskatchewan, Saskatoon, SK, Canada*.

Barbour, S. L., & Krahn, J. (2004). Numerical modelling–Prediction or process. *Geotechnical News, 22*(4), 44-52.

Barrett, J., & Cowling, R. (1980). *Investigations of cemented fill stability in 1100 orebody, Mount Isa Mines, Ltd.* Paper presented at the The IMM Trans Sect A Min Industry, Queensland, Australia.

Bawden, W., Thompson, B., & Grabinsky, M. (2011, 26-29 June). *In-situ Monitoring of Cemented Paste Backfill.* Paper presented at the 45th US Rock Mechanics/Geomechanics Symposium, San Francisco, California.

Belem, T., & Benzaazoua, M. (2008). Design and application of underground mine paste backfill technology. *Geotechnical and Geological Engineering, 26*(2), 147-174.

Belem, T., & Benzaazoua, M. (2004). *An overview on the use of paste backfill technology as a ground support method in cut-and-fill mines.* Paper presented at the In Ground Support in Mining and Underground Construction: Proceedings of the Fifth International Symposium on Ground Support, 28–30 September; Villaescusa, E., Potvin, Y., Eds.; CRC Press: Leiden, The Netherlands, Perth, Australia.

Belem, T., Benzaazoua, M., & Bussière, B. (2000, 15–18 October). *Mechanical behaviour of cemented paste backfill.* Paper presented at the In Proceedings of the 53rd Annual Conference of the Canadian Geotechnical Society Montréal, QC, Canada.

Belem, T., Benzaazoua, M., El-Aatar, O., & Yilmaz, E. (2013, 11th to 15th August). *Effect of drainage and the pore water pressure dissipation on the backfilling sequencing.* Paper presented at the Proceedings of the 23rd World Mining Congress. Canadian Geotechnical Society, Montréal, Canada.

Belem, T., Bussière, B., & Benzaazoua, M. (2001). *The effect of microstructural evolution on the physical properties of paste backfill.* Paper presented at the Proc. of Tailings and Mine Waste, Fort Collins, Colorado, Balkema, Rotterdam.

Belem, T., El Aatar, O., Benzaazoua, M., Bussière, B., & Yilmaz, E. (2007). *Hydro-geotechnical and geochemical characterization of column consolidated cemented paste backfill.* Paper presented at the Proceedings of the 9th International Symposium in Mining with Backfill.

Belem, T., El Aatar, O., Bussière, B., & Benzaazoua, M. (2016). Gravity-driven 1-D consolidation of cemented paste backfill in 3-m-high columns. *Innovative Infrastructure Solutions, 1*(1), 37.

Belem, T., Harvey, A., Simon, R., & Aubertin, M. (2004a). *Measurement and prediction of internal stresses in an underground opening during its filling with cemented fill.* Paper presented at the Proceedings of the fifth international symposium on ground support in mining and underground construction, 28-30 September, Perth, Australia.

Belem, T., Harvey, A., Simon, R., & Aubertin, M. (2004b). Measurement and prediction of internal stresses in an underground opening during its filling with cemented fill. *Ground support in mining and underground construction. Edited by E. Villaescusa and Y. Potvin. Taylor and Francis Group, London*, 619-630.

Belem, T., Mbonimpa, M., & Li, L. (2018). Note du cours de GML6603-Remblais miniers. *UQAT–École Polytechnique de Montréal: Rouyn-NorandaMontreal, QC, Canada*.

Benzaazoua, M., Belem, T., & Bussière, B. (2002). Chemical aspect of sulfurous paste backfill mixtures. *Cement and Concrete, 32, no7*, 1133-1144.

Benzaazoua, M., Belem, T., & Jolette, D. (2000). Investigation de la stabilité chimique et son impact sur la résistance mécanique des remblais cimentés. *Rapport IRSST, IRSST ed., R-260*, 158p + Annexes.

Benzaazoua, M., Bussière, B., Demers, I., Aubertin, M., Fried, É., & Blier, A. (2008). Integrated mine tailings management by combining environmental desulphurization and cemented paste backfill: Application to mine Doyon, Quebec, Canada. *Minerals Engineering, 21*(4), 330-340.

Benzaazoua, M., Fall, M., & Belem, T. (2004). A contribution to understanding the hardening process of cemented pastefill. *Minerals Engineering, 17*(2), 141-152.

Bloss, M. L. (1992). *Prediction of cemented rock fill stability: design procedures and modelling techniques.* (Ph.D. Thesis), University of Queensland, Brisbane, Australia.

Boger, D., Scales, P., & Sofra, F. (2006). Rheological concepts. *Paste and Thickened Tailings-A Guide (Second Edition), Jewell and Fourie (eds), Australian Centre for Geomechanics, Perth, Australia*, 25.

Bolton, M., & Lau, C. (1988). *Scale effects arising from particle size.* Paper presented at the Centrifuge 1988: Proceedings of the International Conference on Geotechnical Centrifuge Modeling, Paris (ed. J.-F. Corté) A.A. Balkema, Rotterdam.

Bowles, J. E. (1978). Engineering properties of soils and their measurement (second Edition). *New York: McGraw-Hill*.

Brackebusch, F. (1994). *Basics of paste backfill systems. Miner Eng 46:1175–1178*.

Brady, B., & Brown, E. (1985). 2004 "Rock Mechanics for Underground Mining" George Allen & Unwin–London.

Britto, A. M., & Gunn, M. J. (1987). *Critical state soil mechanics via finite elements. Ellis Horwood, Chichester, U.K., 488*.

Burland, J. (1987, 31 August - 03 September). *The teaching of soil mechanics–a personal view. The Nash Lecture.* Paper presented at the Proceedings of the 9th European Conference on Soil Mechanics and Foundation Engineering, Dublin, Ireland.

Bussiere, B. (2007). Colloquium 2004: Hydrogeotechnical properties of hard rock tailings from metal mines and emerging geoenvironmental disposal approaches. *Canadian Geotechnical Journal, 44*(9), 1019-1052.

Cai, S. (1983). *A simple and convenient method for design of strength of cemented hydraulic fill.* Paper presented at the Proceedings of International Symposium on Mining with Backfill, AA Balkema, Rotterdam.

Chapuis, R. P., & Aubertin, M. (2003). On the use of the Kozeny Carman equation to predict the hydraulic conductivity of soils. *Canadian Geotechnical Journal, 40*(3), 616-628.

Chen, L., & Jiao, D. (1991). A design procedure for cemented fill for open stoping operations. *Mining Science and Technology, 12*(3), 333-343.

Chen, W.-F., & Zhang, H. (1990). *Structural plasticity: Theory, problems and cae software*. Berlin/New York: Springer-Verlag.

Clayton, S., Grice, T., & Boger, D. (2003). Analysis of the slump test for on-site yield stress measurement of mineral suspensions. *International journal of mineral processing, 70*(1-4), 3-21.

Cooke, R. (2006). *Thickened and paste tailings pipeline systems: Design procedure–Part 1*. Paper presented at the International Seminar on Paste and Thickened Tailings, Limerick, Ireland, April, ACG, Perth, Australia.

Copco, A. (2007). Mining methods in underground mining. *Atlas Copco: Nacka, Sweden*.

Cornelius, K. (1985). *Manual of mineralogy*: John Wiley & Sons.

Corté, J.-F. (1989a). Essais sur modèles réduits en géotechnique. *Rapport général, session, 11*, 2553-2571.

Corté, J. (1989b, 13–18 August). *Model testing-Geotechnical model test. General Report.* Paper presented at the 12th International Conference on Soil Mechanics and Foundation Engineering, Rio De Janeiro, Brazil.

Cowling, R., Grice, A., & Isaacs, L. (1988). *Simulation of hydraulic filling of large underground mining excavations.* Paper presented at the Proceedings of 6th International Conference on Numerical Methods in Geomechanics, Innsbruck, Austria.

Cui, L., & Fall, M. (2017). Modeling of pressure on retaining structures for underground fill mass. *Tunnelling and Underground Space Technology, 69*, 94-107.

Darling, P. (2011). *SME mining engineering handbook* (Vol. 1): SME.

Das, B. M., & Sobhan, K. (2013). *Principles of geotechnical engineering*: Cengage learning, Stamford, USA.

Dismuke, S., & Diment, T. (1996). The testing, design, construction, and implementation of cemented rockfill (CRF) at Polaris. *CIM bulletin, 89*(1005), 91-97.

Doherty, J. P. (2015). A numerical study into factors affecting stress and pore pressure in free draining mine stopes. *Computers and Geotechnics, 63*, 331-341.

Donovan, J. G. (1999). *The effects of backfilling on ground control and recovery in thin-seam coal mining.* (M.Sc. Thesis), Virginia Polytechnic Institute and State University, Blacksburg, Virginia.

Double, D., Hellawell, A., & Perry, S. (1978). The hydration of Portland cement. *Proc. R. Soc. Lond. A, 359*(1699), 435-451.

Douglas, E., & Malhotra, V. (1989). Ground granulated blast-furnace slag for cemented mine backfill: production and evaluation. *CIM Bull, 82*(929), 27-36.

Dubreucq, T., Garnier, J., Favraud, C., & Noblet, S. (1995). Fondation sur sol renforcé par géotextiles: comparaison d'essais sur modèles centrifugés et modèles sous la gravité normale. *Les modèles réduits en Génie Civil*, 123-128.

Duffield, C., Gad, E., & Bamford, W. (2003). Investigation into the Structural Behaviour of Mine Brick Barricades. *AusIMM Bulletin*(2), 44-50.

El Mkadmi, N. (2012). *Simulations du comportement géotechnique des remblais dans les chantiers miniers: effets du drainage et de la consolidation.* (Master's Thesis), Ecole Polytechnique, Montreal Montreal, QC, Canada.

El Mkadmi, N., Aubertin, M., & Li, L. (2013). Effect of drainage and sequential filling on the behavior of backfill in mine stopes. *Canadian Geotechnical Journal, 51*(1), 1-15.

Emad, M. Z., Mitri, H., & Kelly, C. (2014). Effect of blast-induced vibrations on fill failure in vertical block mining with delayed backfill. *Canadian Geotechnical Journal, 51*(9), 975-983.

Fahey, M., Helinski, M., & Fourie, A. (2011). Development of specimen curing procedures that account for the influence of effective stress during curing on the strength of cemented mine backfill. *Geotechnical and Geological Engineering, 29*(5), 709-723.

Fahey, M., Helinski, M., & Fourie, A. (2009). Some aspects of the mechanics of arching in backfilled stopes. *Canadian Geotechnical Journal, 46*(11), 1322-1336.

Falaknaz, N. (2014). *Analysis of the geomechanical behavior of two adjacent backfilled stopes based on two and three dimensional numerical simulations.* (Ph.D.), École Polytechnique de Montréal, Montreal, QC, Canada,.

Fall, M., Adrien, D., Celestin, J., Pokharel, M., & Toure, M. (2009). Saturated hydraulic conductivity of cemented paste backfill. *Minerals Engineering, 22*(15), 1307-1317.

Fall, M., Belem, T., Samb, S., & Benzaazoua, M. (2007). Experimental characterization of the stress–strain behaviour of cemented paste backfill in compression. *Journal of materials science, 42*(11), 3914-3922.

Fall, M., & Benzaazoua, M. (2003, October 12-15). *Advances in predicting performance properties and cost of paste backfill.* Paper presented at the Proceedings of International Conference of Tailings & Mine Waste, Vail, USA, Balkema, Rotterdam.

Farsangi, P. N. (1997). *Improving cemented rockfill design in open stoping.* (Ph.D. Thesis), McGill University, Montreal, Canada.

Foray, P., Balachowski, L., & Colliat, J.-L. (1998). Bearing capacity of model piles driven into dense overconsolidated sands. *Canadian Geotechnical Journal, 35*(2), 374-385.

Gade, V. K., & Dasaka, S. (2018). Calibration of earth pressure sensors. *Indian Geotechnical Journal, 48*(1), 142-152.

Garnier, J. (2001). Modèles physiques en géotechnique: Etat des connaissance et évolutions récentes. *1ère Biennale Coulomb, Paris*, 67.

Garnier, J. (1997, 6–12 September). *Validation des modèles physiques et numériques: problème des effets d'échelle.* Paper presented at the Compte-Rendus du 14eme Conférence International de Mécanique des Sols et des Travaux de Fondations, Hambourg, Germany.

Gélinas, L.-P. (2017). *Caractérisation des propriétés géomécaniques des barricades rocheuses et des chantiers miniers remblayés en vue de leur analyse de stabilité.* (Master's Thesis), Université du Québec en Abitibi-Témiscamingue, Rouyn-Noranda, QC, Canada.

Godbout, J., Bussière, B., Aubertin, M., Belem, T., & Benzaazoua, M. (2004). *Évolution des propriétés de rétention d'eau des remblais miniers cimentés en pâte durant le curage.* Paper presented at the Proceedings of the 57th Canadian Geotechnical Conference and the 5th joint CGS-IAH Conference.

Godbout, J., Bussière, B., & Belem, T. (2007). *Evolution of cemented paste backfill saturated hydraulic conductivity at early curing time.* Paper presented at the 60th Canadian Geotechnical Conference, Ottawa, Canada.

Grabinsky, M. (2010). *In situ monitoring for ground truthing paste backfill designs.* Paper presented at the Proceedings of the 13th international seminar on paste and thickened tailings, Toronto, Canada. ACG.

Grabinsky, M., & Bawden, W. (2007). *In situ measurements for geomechanical design of cemented paste backfill systems.* Paper presented at the Proceedings of the 9th International Symposium in Mining with Backfill, Montréal, Que.

Grice, A. G. (2001). *Recent minefill developments in Australia.* Paper presented at the Minefill 2001: 7 th International Symposium on Mining with Backfill. Minefill 2001, SME, Seatle, Washington.

Grice, T. (1998, 14-16 April). *Stability of hydraulic backfill barricades.* Paper presented at the Proceedings of 6th International Symposium on Mining with Backfill: Minefill, Brisbane, Australia.

Guang-Xu, T., & Mao-Yuan, H. (1983). *Assessment on support ability of the fill mass.* Paper presented at the Proceedings of international symposium on mining with backfill, AA Balkema, Rotterdam.

Hansen, J. B. (1970). A revised and extended formula for bearing capacity. *Danish Geotechnical Institute Bulletin, No. 28*.

Hartman, H. L., & Britton, S. G. (1992). *SME mining engineering handbook* (Vol. 2). Littleton, Colorado: Society for Mining, Metallurgy, and Exploration Denver.

Hasan, A., Suazo, G., Doherty, J., & Fourie, A. (2014, 20–22 May). *In situ measurements of cemented paste backfilling in an operating stope at Lanfranchi Mine.* Paper presented at the Proc. 11th Int. Symposium on Mining with Backfill (Minefill 2014), Perth.

Hassani, F., & Archibald, J. (1998). Mine Backfill [CD-ROM]; Canadian Institute of Mining, Metallurgy, and Petroleum: Montreal, QC, Canada.

Hassani, F., & Bois, D. (1989). Economic and technical feasibility for backfill design in Quebec underground mines. Final report 1/2, Canada-Quebec Mineral Development Agreement. *Research and Development in Quebec Mines. Contract No. EADM, 1992*.

Hassani, F., Fotoohi, K., & Doucet, C. (1998). Instrumentation and backfill performance in a narrow vein gold mine. *International Journal of Rock Mechanics and Mining Sciences, 35*(4-5), 392.

Hassani, F., Mortazavi, A., & Shabani, M. (2008). An investigation of mechanisms involved in backfill-rock mass behaviour in narrow vein mining. *Journal of the Southern African Institute of Mining and Metallurgy, 108*(8), 463-472.

Hedley, D. (1995). Stiff Backfill. *Canadian Rockburst Research Program 1990-1995, Chapler4, CAMIRO Mining Division*, 77.

Helinski, M., Fahey, M., & Fourie, A. (2010). Behavior of cemented paste backfill in two mine stopes: measurements and modeling. *Journal of Geotechnical and Geoenvironmental Engineering, 137*(2), 171-182.

Helinski, M., Fourie, A., Fahey, M., & Ismail, M. (2007). Assessment of the self-desiccation process in cemented mine backfills. *Canadian Geotechnical Journal, 44*(10), 1148-1156.

Henderson, A., & Revell, M. (2005). Basic mine fill materials *In Handbook of Mine Fill; Potvin, Y., Thomas, E.D., Fourie, A., Eds.* (pp. 13-20). Perth, Australia: Australian Centre for Geomechanics.

Henderson, A. M., & Lilley, C. R. (2001, 17-19 Sept). *Backfill selection and experience at the Kanowna Belle Gold Mine, Western Australia.* Paper presented at the Minefill 2001: 7 th International Symposium on Mining with Backfill, Seattle, Washington.

Hill, R. (1950). The mathematical theory ofplasticity. *OxJord tiniuersir)! Press, Oxford*.

Hughes, P. B. (2008). *Performance of paste fill fences at Red Lake Mine*. (Master Thesis), University of British Columbia, Vancouver, Canada.

Hunt, R. E. (1986). *Geotechnical engineering analysis and evaluation. McGraw Hill, New York, 729 pp*.

Kesimal, A., Ercikdi, B., & Yilmaz, E. (2003). The effect of desliming by sedimentation on paste backfill performance. *Minerals Engineering, 16*(10), 1009-1011.

Klein, K., & Simon, D. (2006). Effect of specimen composition on the strength development in cemented paste backfill. *Canadian Geotechnical Journal, 43*(3), 310-324.

Kuganathan, K. (2005a). Geomechanics of mine fill. *Handbook on Mine Fill, Australian Centre for Geomechanics, Perth, Western Australia*, 23-47.

Kuganathan, K. (2002). *A model to predict bulkhead pressures for safe design of bulkheads.* Paper presented at the Filling with hydraulic fills seminar. Section 6, ACG, Perth, Australia.

Kuganathan, K. (2005b). Rock fill in mine fill. *Handbook on Mine Fill, Australian Centre for Geomechanics*, 101-115.

le Roux, K., Bawden, W. F., & Grabinsky, M. F. (2005). Field properties of cemented paste backfill at the Golden Giant mine. *Mining Technology, 114*(2), 65-80.

Leahy, F., & Cowling, R. (1978). *Stope fill developments at Mount Isa.* Paper presented at the The Twelfth Canadian Rock Mecanics symposium on Mining with Backfill, Sudbury, Ontario, Canada.

Lee, D.-S., Kim, K.-Y., Oh, G.-D., & Jeong, S.-S. (2009). Shear characteristics of coarse aggregates sourced from quarries. *International journal of rock mechanics and mining sciences (1997), 46*(1), 210-218.

Lessard, G. (2011). Essais d'infiltration sur la halde à stériles Petit-Pas de la mine Tio, Havre-St-Pierre. *Rapport de maîtrise. Département des génies civil, géologique et des mines. École Polytechnique de Montréal, Canada*.

Li, L. (2019). *Vers une conception de barricades plus sécuritaire dans les mines: Étude de l'interaction entre le remblai et les structures encaissantes*. Montreal, QC, Canada: Institut de recherche Robert-Sauvé en santé et en sécurité du travail.

Li, L., & Aubertin, M. (2010). An analytical solution for the nonlinear distribution of effective and total stresses in vertical backfilled stopes. *Geomechanics and Geoengineering, 5*(4), 237-245.

Li, L., & Aubertin, M. (2009a). Horizontal pressure on barricades for backfilled stopes. Part I: Fully drained conditions. *Canadian Geotechnical Journal, 46*(1), 37-46.

Li, L., & Aubertin, M. (2009b). Horizontal pressure on barricades for backfilled stopes. Part II: Submerged conditions. *Canadian Geotechnical Journal, 46*(1), 47-56.

Li, L., & Aubertin, M. (2008). An improved analytical solution to estimate the stress state in subvertical backfilled stopes. *Canadian Geotechnical Journal, 45*(10), 1487-1496.

Li, L., & Aubertin, M. (2009c). Influence of water pressure on the stress state in stopes with cohesionless backfill. *Geotechnical and Geological Engineering, 27*(1), 1.

Li, L., & Aubertin, M. (2011). Limit equilibrium analysis for the design of backfilled stope barricades made of waste rock. *Canadian Geotechnical Journal, 48*(11), 1713-1728.

Li, L., & Aubertin, M. (2009d). Numerical investigation of the stress state in inclined backfilled stopes. *International Journal of Geomechanics, 9*(2), 52-62.

Li, L., & Aubertin, M. (2009e). A three-dimensional analysis of the total and effective stresses in submerged backfilled stopes. *Geotechnical and Geological Engineering, 27*(4), 559-569.

Li, L., Aubertin, M., & Shirazi, A. (2010). Implementation and application of a new elastoplastic model based on a multiaxial criterion to assess the stress state near underground openings. *International Journal of Geomechanics, 10*(1), 13-21.

Li, L., Aubertin, M., Shirazi, A., Belem, T., & Simon, R. (2007, 29 April–2 May). *Stress distribution in inclined backfilled stopes.* Paper presented at the Proceedings of the 9th International Symposium in Mining with Backfill, Montreal, QC, Canada.

Li, L., Aubertin, M., Simon, R., Bussière, B., & Belem, T. (2003, 21–24 October). *Modeling arching effects in narrow backfilled stopes with FLAC.* Paper presented at the Proceedings of the 3rd international symposium on FLAC & FLAC 3D numerical modelling in Geomechanics, Sudbury, ON, Canada.

Li, L., Ouellet, S., & Aubertin, M. (2009). *A method to evaluate the size of backfilled stope barricades made of waste rock.* Paper presented at the Proc., 62nd Can. Geotech. Conf. and 10th Joint CGS/IAH-CNC Groundwater Specialty Conf., Halifax, Canada,.

Lingga, B. A., Apel, D. B., Sepehri, M., & Pu, Y. (2018). Assessment of digital image correlation method in determining large scale cemented rockfill strains. *International Journal of Mining Science and Technology*.

Liston, D. (2014). *Utilisation of cemented rockfill, cemented hydraulic fill and paste to successfully achieve ore production expansion to 2 Mtpa at Chelopech Mine*. Y Potvin & AG Grice (eds), ACG, Perth, Australia.

Ltd, G.-S. I. (2008). Stress-deformation modeling with SIGMA/W 2007, 4th edn. GEO-SLOPE International Ltd., Calgary, Canada.

Lu, H., Qi, C., Li, C., Gan, D., Du, Y., & Li, S. (2020). A light barricade for tailings recycling as cemented paste backfill. *Journal of Cleaner Production, 247*, 119388.

Maknoon, M. (2016). *Slope Stability Analyses of Waste Rock Piles Under Unsaturated Conditions Following Large Precipitations.* (Ph.D. Thesis), École Polytechnique de Montréal, Montreal, QC, Canada.

Mandel, J. (1962). Essais sur modèles réduits en mécanique des terrains: Etude des conditions de similitude. *Revue de l'Industrie Minérale, 44*.

Marsal, R. (1969). Mechanical properties of rock-fill and gravel materials. *Special Session, 7th. ICSMFE, 3*, 499-506.

Marston, A. (1930). *The theory of external loads on closed conduits in the light of the latest experiments.* Paper presented at the Iowa Engineering Experimental Station, Bulletin No. 96, Ames, Iowa.

Mbonimpa, M., Aubertin, M., Chapuis, R., & Bussière, B. (2002). Practical pedotransfer functions for estimating the saturated hydraulic conductivity. *Geotechnical & Geological Engineering, 20*(3), 235-259.

McCormick, N., & Lord, J. (2010). Digital image correlation. *Materials today, 13*(12), 52-54.

McLemore, V. T., Fakhimi, A., van Zyl, D., Ayakwah, G. F., Anim, K., Boakye, K., . . . Gutierrez, L. A. (2009). Literature review of other rock piles: characterization, weathering, and stability. *Questa Rock Pile Weathering Stability Project. New Mexico Bureau of Geology and Mineral Resources. OF-Report, 517*, 101.

MEHTA, P. K. (1987). Natural Pozzolan. *Suplementary Cementing Materials. Ottawa: VM Malhotra*.

Mercer, J. W., & Faust, C. R. (1981). Ground-water modeling. *National Water Well Association, Worthington Ohio. 1981. 60 p.*

Mitchell, R. (1989a). Model studies on the stability of confined fills. *Canadian Geotechnical Journal, 26*(2), 210-216.

Mitchell, R. (1989b). Stability of cemented tailings mine backfill. *Proceedings of Computer and physical modelling in geotechnical engineering. Edited by Balasubramaniam et al., AA Balkema, Rotterdam*, 501-507.

Mitchell, R., Smith, J., & Libby, D. (1975). Bulkhead pressures due to cemented hydraulic mine backfills. *Canadian Geotechnical Journal, 12*(3), 362-371.

Mitchell, R. J., Olsen, R. S., & Smith, J. D. (1982). Model studies on cemented tailings used in mine backfill. *Canadian Geotechnical Journal, 19*(1), 14-28.

Neville, A. M. (1995). *Properties of concrete* (Vol. 4): Longman London.

Niemann, H. (1995). L'analyse dimensionnelle et son application aux lois de similitude. *Les modèles réduits en Génie, 155*, 3-20.

Note, A. (1998). 078," Strain Guage Measurement-A Tutorial. *National Instrument Corporation. 341023C-01*.

Nujaim, M., Auvray, C., & Belem, T. (2018, 22-26 May). *Geomechanical behaviour of a rock barricade and cemented paste backfill: Laboratory experiments on a reduced-scale model.* Paper presented at the Geomechanics and Geodynamics of Rock Masses, Volume 1: Proceedings of the 2018 European Rock Mechanics Symposium, Saint Petersburg, Russia.

Nujaim, M., Belem, T., & Auvray, C. (2019). *Small-scale model preliminary testing on the interaction between paste backfills and waste rock barricades.* Paper presented at the ISRM 14th International Congress of Rock Mechanics, Foz do Iguassu, Brazil.

Pan, B., Qian, K., Xie, H., & Asundi, A. (2009). Two-dimensional digital image correlation for in-plane displacement and strain measurement: a review. *Measurement science and technology, 20*(6), 062001.

Pashias, N., Boger, D., Summers, J., & Glenister, D. (1996). A fifty cent rheometer for yield stress measurement. *Journal of Rheology, 40*(6), 1179-1189.

Pengyu, Y., & Li, L. (2015). Investigation of the short-term stress distribution in stopes and drifts backfilled with cemented paste backfill. *International Journal of Mining Science and Technology, 25*(5), 721-728.

Peters, W., & Ranson, W. (1982). Digital imaging techniques in experimental stress analysis. *Optical engineering, 21*(3), 213427.

Pierce, M., Bawden, W., & Paynter, J. (1998). *Laboratory testing and stability analysis of paste backfill at the Golden Giant Mine.* Paper presented at the Minefill'98: Proceedings of the 6th International Symposium on Mining with Backfill, Brisbane, Australia.

Pirapakaran, K. (2008). *Load-deformation characteristics of minefills with particular reference to arching and stress developments.* (Ph.D. Thesis), James Cook University, Australia.

Pirapakaran, K., & Sivakugan, N. (2007). Arching within hydraulic fill stopes. *Geotechnical and Geological Engineering, 25*(1), 25-35.

Potvin, Y., Thomas, E., & Fourie, A. (2005). *Handbook on mine fill*: Australian Centre for Geomechanics: Crawley, Australia.

Rankine, K. J. (2005). *An investigation into the drainage characteristics and behaviour of hydraulically placed mine backfill and permeable minefill barricades.* (Ph.D. Thesis), James Cook University, Townsville, Australia.

Revell, M. (2000, April). *Cannington backfill taking the pig out of paste.* Paper presented at the Paste Technology Seminar, Perth, Australia.

Revell, M. (2004, September 19-21). *Paste–How strong is it.* Paper presented at the Proceedings of the 8th International Symposium on Mining with Backfill, Beijing, The Nonferrous Metals Society of China.

Revell, M., & Sainsbury, D. (2007). *Advancing paste fill bulkhead design using numerical modeling.* Paper presented at the International Symposium of MineFill07., Montréal, QC, Canada.

Rosenblum, F., & Spira, P. (1981). *Self-heating of sulphides.* Paper presented at the 13th Annual Meeting of the Canadian Mineral Processors.

Saebimoghaddam, A. (2005). *Rheological Yield Stress Measurements of Mine Paste Fill Material.* (Ph. D. thesis), McGill University, Montreal, Canada.

Schreier, H. W. (1969). *Investigation of two and three-dimensional image correlation techniques with applications in experimental mechanics.* (PhD Thesis), University of South Carolina, Columbia, US.

Sheshpari, M. (2015). A review of underground mine backfilling methods with emphasis on cemented paste backfill. *Electronic Journal of Geotechnical Engineering, 20*(13), 5183-5208.

Simon, D., & Grabinsky, M. (2013). Apparent yield stress measurement in cemented paste backfill. *International Journal of Mining, Reclamation and Environment, 27*(4), 231-256.

Sivakugan, N., Rankine, K., & Rankine, R. (2006a). Permeability of hydraulic fills and barricade bricks. *Geotechnical & Geological Engineering, 24*(3), 661-673.

Sivakugan, N., Rankine, R., Rankine, K., & Rankine, K. (2006b). Geotechnical considerations in mine backfilling in Australia. *Journal of Cleaner Production, 14*(12-13), 1168-1175.

Sivakugan, N., Veenstra, R., & Naguleswaran, N. (2015). Underground mine backfilling in Australia using paste fills and hydraulic fills. *International Journal of Geosynthetics and Ground Engineering, 1*(2), 18.

Sivakugan, N., & Widisinghe, S. (2013). Stresses within granular materials contained between vertical walls. *Indian Geotechnical Journal, 43*(1), 30-38.

Sofra, F., & Boger, D. (2001). *Slope prediction for thickened tailings and pastes.* Paper presented at the Tailings and Mine Waste '01: Proceedings of the 8th International Conference, Fort Collins, Colo, A.A. Balkema, Rotterdam, Netherlands.

Stone, D. (1993). *The optimization of mix designs for cemented rockfill.* Paper presented at the Proceedings of fifth international symposium on mining with backfill, Johannesbourg, South Africa.

Suazo, G., & Villavicencio, G. (2018). Numerical simulation of the blast response of cemented paste backfilled stopes. *Computers and Geotechnics, 100*, 1-14.

Sutton, M. A., Orteu, J. J., & Schreier, H. (2009). *Image correlation for shape, motion and deformation measurements: basic concepts, theory and applications*. New York: Springer Science & Business Media.

Sveinson, S. (1999). *Characterisation of tailings for paste backfill system design.* (master thesis), University of British Columbia, Vancouver, Canada.

Terzaghi, K. (1943). Theoretical soil mechanics. John Wiley & Sons, New York. -.

Thomas, E. G. (1979). *Fill technology in underground metalliferous mines*: University of British Columbia, Department of Mineral Engineering: Vancouver, BC, Canada.

Thompson, B., Bawden, W., & Grabinsky, M. (2012). In situ measurements of cemented paste backfill at the Cayeli Mine. *Canadian Geotechnical Journal, 49*(7), 755-772.

Thompson, B., Bawden, W., Grabinsky, M., & Karaoglu, K. (2010, 3-6 May). *Monitoring Barricade Performance in a cemented paste backfill operation.* Paper presented at the Proceedings of the Thirteenth International Seminar on Paste and Thickened Tailings, Toronto, Ont.

Thompson, B. D., Grabinsky, M., Bawden, W., & Counter, D. (2009, 9–15 May). *In-situ measurements of cemented paste backfill in long-hole stopes.* Paper presented at the ROCKENG09: proceedings of the 3rd CANUS rock mechanics symposium, Toronto, Canada.

Ti, K. S., Huat, B. B., Noorzaei, J., Jaafar, M. S., & Sew, G. S. (2009). A review of basic soil constitutive models for geotechnical application. *Electronic Journal of Geotechnical Engineering, 14*, 1-18.

Ting, C. H., Shukla, S. K., & Sivakugan, N. (2011). Arching in soils applied to inclined mine stopes. *International Journal of Geomechanics, 11*(1), 29-35.

Ting, C. H., Sivakugan, N., Read, W., & Shukla, S. K. (2014). Analytical expression for vertical stress within an inclined mine stope with non-parallel walls. *Geotechnical and Geological Engineering, 32*(2), 577-586.

Ting, C. H., Sivakugan, N., & Shukla, S. K. (2012). Laboratory simulation of the stresses within inclined stopes. *Geotechnical Testing Journal, 35*(2), 280-294.

Van Horn, D., & Tener, R. (1963). *A study of loads on underground structures. Final report. An analytical method for determining loads. part iii (supplement). Gaphical representation of analytical expressions (no. dasa-1406; ad-420528)*. AMes: Iowa State University, Iowa Engineering Experiment Station.

Veenstra, R. L. (2013). *A design procedure for determining the in situ stresses of early age cemented paste backfill.* (Ph.D.), Toronto, ON, Canada.

Walske, M. L., McWilliam, H., Doherty, J., & Fourie, A. (2015). Influence of curing temperature and stress conditions on mechanical properties of cementing paste backfill. *Canadian Geotechnical Journal, 53*(1), 148-161.

Widisinghe, S., Sivakugan, N., & Wang, V. (2014, 20–22 May). *Loads on barricades in hydraulically backfilled underground mine stopes.* Paper presented at the In Proceedings of the Eleventh International Symposium on Mining with Backfill, Perth, Australia.

Widisinghe, S., Sivakugan, N., & Wang, V. Z. (2013, 29-31 May). *Laboratory investigations of arching in backfilled mine stopes.* Paper presented at the In Proceedings of the 18th Southeast Asian Geotechnical Conference (18SEAGC) & Inaugural AGSSEA Conference (1AGSSEA), Singapore.

Widisinghe, S. D. (2014). *Stress developments within a backfilled mine stope and the lateral loading on the barricade.* (Ph.D. Thesis), James Cook University, Townsville, Australia.

Wood, D. M. (2004). *Geotechnical modelling*. New York: Spon Press, Version 2.2, 448 p.

Xu, W., Cao, P., & Tian, M. (2018). Strength development and microstructure evolution of cemented tailings backfill containing different binder types and contents. *Minerals, 8*(4), 167.

Yang, P. (2016). *Investigation of the geomechanical behavior of mine backfill and its interaction with rock walls and barricades.* (Ph.D. Thesis), École Polytechnique de Montréal, Montreal, QC, Canada.

Yang, P., Li, L., Aubertin, M., Brochu-Baekelmans, M., & Ouellet, S. (2016). Stability analyses of waste rock barricades designed to retain paste backfill. *International Journal of Geomechanics, 17*(3), 04016079.

Yilmaz, E. (2010). *Investigating the hydrogeotechnical and microstructural properties of cemented paste backfill using the cuaps apparatus.* (Ph.D. Thesis), Université du Québec à en Abitibi-Témiscamingue, Rouyn-Noranda, QC, Canada.

Yilmaz, E., Kesimal, A., & Ercidi, B. (2004, September 19-21). *Strength development of paste backfill simples at Long term using different binders.* Paper presented at the Conference: Proceedings of the 8th International Symposium on Mining with Backfill, Beijing, China.

Yu, H.-S. (2007). *Plasticity and geotechnics* (Vol. 13). New York: Springer Science & Business Media.

Yu, T. (1992, 15 June). *Mechanisms of fill failure and fill strength requirements.* Paper presented at the Proceedings of 16th Canadian rock mechanics symposium, Sudbury, Ontario, Canada.

Yu, T. (1989). Some factors relating to the stability of consolidated rockfill at Kidd Creek. *Innovations in Mining Backfill Technology*, 279-286.

Yu, T., & Counter, D. (1983). Backfill practice and technology at Kidd Creek Mines. *CIM bulletin, 76*(856), 56-65.

Yumlu, M., & Guresci, M. (2007). *Paste backfill bulkhead monitoring: A case study from Inmet's Cayeli Mine, Turkey*. Paper presented at the Proceedings of the 9th International Symposium in Mining with Backfill, CIM, Montréal, Que, Canada.

Zhang, P., Zhang, Y., Zhao, T., Tan, Y., & Yu, F. (2019). Experimental Research on Deformation Characteristics of Waste-Rock Material in Underground Backfill Mining. *Minerals, 9*(2), 102.

Zhang, X. (2011). *Modélisation physique et numérique des interactions sol-structure sous sollicitations dynamiques transverses.* (Ph. D. thesis), Université de Grenoble, France.

Zheng, J., & Li, L. (2020). Experimental study of the "short-term" pressures of uncemented paste backfill with different solid contents for barricade design. *Journal of Cleaner Production, 275*, 123068.

Zhu, Z. (2002). *Analysis of mine backfill behaviour and stability.* (Ph.D. Thesis), McGill University Libraries, Montreal, Canada.

APPENDIX A – BACKFILL COMPONENTS

Mill tailings, aggregate or waste rock, water, and binder are the principal components of the backfill. In some cases, one or more adjuvants may be added to enhance backfill performance or some of its properties.

1. Tailings

Particles that contain precious minerals require several processes, such as crushing and grinding the extracted ore to be released (separated) from the waste rock particles. The subsequent treatment generates two flows, which are the treated ore and the waste, generally by flotation, separation by gravity, or leaching. The waste stream is normally deposited on the surface in storage facilities (Fig. A-1a) and is called tailings. The tailings vary (in particle size) between clay and fine sand (Fig. A-1b). The use of tailings as backfill eliminates a large part of the tailings generated by underground mining. Not all tailings can be used as backfill its volume produced exceeds the original volume of the underground ore (Potvin et al., 2005)

a)



b)

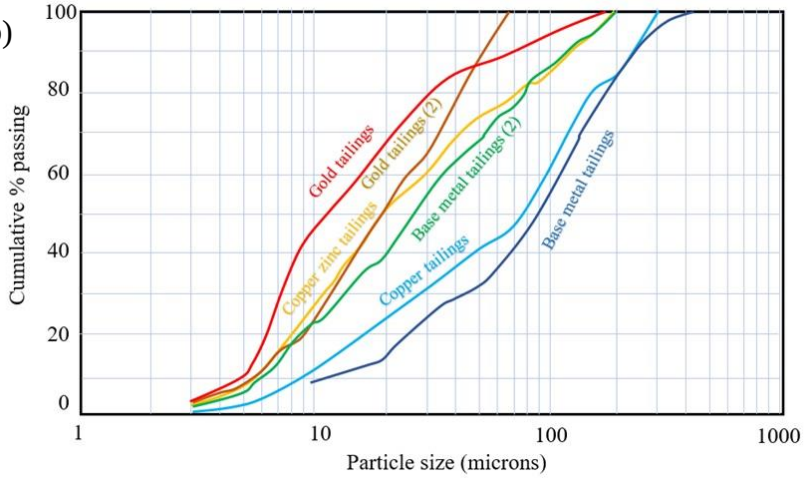


Figure A-1: a) Tailings disposal in ponds or impoundments (from Belem et al., 2018); b) Typical size distribution of mine tailings (adapted from Potvin et al., 2005).

The particle size distribution of the tailings allows for the determination of many ultimate backfill properties, such as void ratio, flow properties, permeability/percolation, and pumpability. Imperial equations (Mbonimpa et al., 2002) have been proposed to predict the k_{sat} of granular soils by taking into account the basic geotechnical properties of the material (grain size distribution parameters and porosity) as following:

$$k_{sat} = c_0 . \frac{\gamma_w}{\mu} . D_{10}^2 . C_U^{1/3} . \frac{e^{3+m}}{1+e} \quad \text{(A. 1)}$$

Where c_0 is a dimensional constant, C_U is the coefficient of uniformity of the particles ($C_U = D_{60}/D_{10}$), γ_w is the unit weight of water (γ_w= 9.81 kN/m3 at 20°C), μ is the dynamic viscosity of water (μ = 10^{-3} Pa.s at 20°C), and m is a parameter introduced to represent the influence of tortuosity (Aubertin et al., 1996).

The mineralogy of the tailings influences several characteristics such as water retention, settling, and the final strength of the fill by influencing chemical reactions (Potvin et al., 2005). When sulphur is exposed to water and oxygen, it begins to oxidize, generating sulphuric acid and heat. Oxidation is manifested by a change in colour, indicating the rusting of the particles. Sulphates released can attack the cementitious bonds in the fill during the hardening time, reducing the strength of the fill. Investigations (Rosenblum & Spira, 1981) have identified the high concentration of pyrrhotite in the tailings may result in self-heating, as was the case at the Brunswick Mine.

2. Rock and aggregate

Many resources that produce the rock aggregates include the waste rock from open-cut operations, underground development, quarried rocks, and coarse gravels. The moisture content of the aggregates must be carefully controlled as it alters the water balance of the fill, posing problems of transportation, drainage, and stability of the fill. Aggregate grading is very important to minimize voids and maximize placed density, which in turn increases the UCS resistance of the fill. Figure A-2 presents the grading of some rock fills taken from Potvin et al. (2005). Besides, attrition must be taken into account during the transport of the fill from the surface to the stope. Attrition reduces the size of the fill particles (up to 50% for a vertical distance of 300m at the Brunswick mine), which influences performance (Yu, 1989).

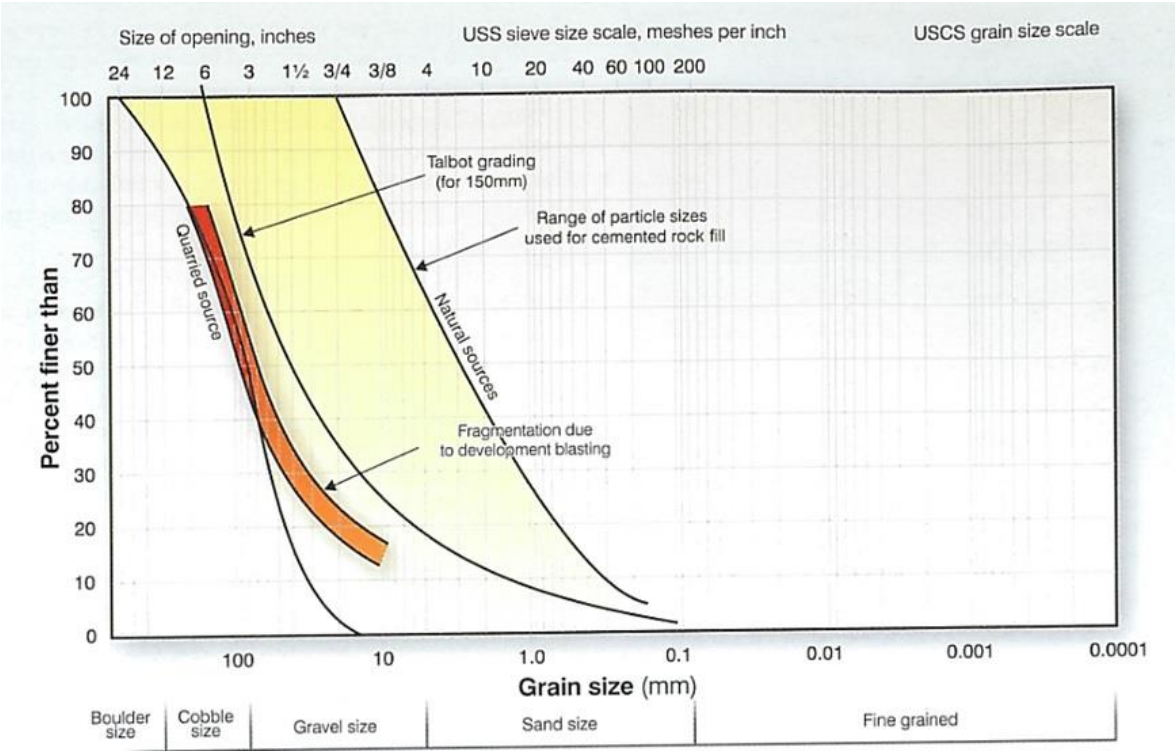


Figure A-2: Grain size distribution of different sources of rock fills (from Potvin et al., 2005).

3. Water

The mixing water used to prepare the backfill is either clean water or mining process water. The presence of salt in the water at sufficient concentrations may affect the development of the strength of the cemented fill. During the curing process, a quantity of salt crystallizes, which inhibits the strength gain of the paste fill by dispersion of cement (Potvin et al., 2005).

4. Cement or binder

Normal or ordinary Portland cement (general-use cement) is the most common type of cement used in mine backfill applications. Ordinary Portland cement is a mixture consisting primarily of cement clinker and calcium sulphate (usually gypsum). Cement clinker is a partially fused product resulting from the combustion of calcareous minerals (limestone) and other argillaceous materials (Potvin et al., 2005). Portland cement contains more than 5% fly ash or blast furnace slag and may contain up to 10% silica fume. The alumina contained in cement plays an important role in preventing sulphate attack.

In cement chemistry, calcium, silicon, aluminum, and iron are represented by C, S, A, and F, respectively. For example, tricalcium silicate ($3Ca.SiO_2$) is represented by C_3S, tricalcium

aluminate is represented by C_3A, and the water (H_2O) is written as H. Table A-1 shows the typical weight proportions of the principal components of Portland cement.

Table A-1: main components of Portland cement.

Portland cement components	proportion
C_3S	60%
C_2S	15%
C_3A	8%
C_4AF	10%

C_3S is responsible for the initial hardening reaction in the first few days, while C_2S reacts more slowly, allowing the cement's strength to develop continuously over months or even years (Double et al., 1978).

$$Calcium\ silicates\ +\ water \rightarrow calcium\ silicate\ hydrates + calcium\ hydroxide$$

Gypsum presence in the cement, C_3A reacts slowly with water to obtain the ettringite ($3CaO.Al_2O_3.32H_2O$). The reaction continues until all the gypsum is consumed. However, in the absence of gypsum, C_3A reacts very quickly (with the water) to be calcium aluminate hydrate ($4CaO.Al_2O_3.19H_2O$), which produces an immediate hardening. This reaction generates links between the calcium silicates reducing their mobility. Many cement particles cannot react as a result of the firm structure of these links producing a weaker concrete.

4.1 The cement contents in mine fill

Several relationships have been proposed to establish the relationship between binder content and backfill strength in light of certain variables that affect strength. The correlation between binder content and fill strength is non-linear, and some laboratory tests are used to measure these variables. 5% of the binder material, of the total dry weight fill, provides a suitable strength for most freestanding fill applications (Potvin et al., 2005). A relation (Henderson & Lilley, 2001) is proposed for the aggregate fill as follows:

$$UCS = 63(c/n)^{1.54} \qquad \text{(A. 2)}$$

Where $c =$ cement content by weight, and $n =$ porosity

4.2 Cement types

4.2.1 Pozzolans

Pozzolans are a broad class of materials based on silicon, silicon, and aluminum, which have little or no cementitious value in themselves, but which react chemically with calcium hydroxide at ordinary temperature and form compounds with cementitious properties in a finely divided form in the presence of water (MEHTA, 1987). Pozzolanic materials can be natural, such as pozzolana, or artificial, such as fly ash and silica fumes (Neville, 1995).

4.2.2 Fly ash

Fly ash is a fine powder with an average particle size of 10 to 15µ. These solid materials are found flying or suspended in the flue gases of the boiler. Chemically, fly ash consists mainly of oxides of silicon, aluminum, and iron, with a low calcium and alkali content. ASTM (American Society for Testing and Materials) classify fly as type C (CaO from 15 to 30%) and type F (CaO 5% or less). The binder used in paste backfill, usually at a dosage of 3-5%, contributes significantly to the cost of backfill. While ordinary Portland cement is the typical binder for paste fillings, there is an increasing trend to substitute OPC in varying proportions for mixed cement, i.e. OPC / slag and OPC / fly-ah, to reduce costs.

4.2.3 Slag

Slag is like cement in its composition but with different proportions. The slag consists of the silicates and aluminosilicates of calcium produced simultaneously with iron in a blast furnace. Slag replaces about 50% of cement in mine backfill applications and reduces the cost of cement backfill by about 60% (Potvin et al., 2005).

4.2.4 Gypsum

Gypsum is a mineral consisting of dehydrated calcium sulphate, with the chemical formula $CaSO_4 \cdot 2H_2O$ (Cornelius, 1985). Calcined gypsum (gypsum partially dehydrated by heat) is more economical to produce than cement because it requires less energy. Petrolito et al. (1998) reported that typical target strength could be achieved with calcined gypsum using 2.5 and 4 times the amount of Portland cement. Other pozzolans may be found in certain backfill applications, such as natural pozzolans.

5. Admixtures

Adjuvants can be applied to increase the performance of the mixture (concrete or mortar) before or after the hydration. Admixtures can improve the physical, chemical, and mechanical properties of the fill, but should never be used without first being tested, taking into account cost and performance (Potvin et al., 2005). The product groups of admixtures that are most effective in certain filling operations can be classified into three categories:

i) rheology modifiers (improve the consistency or the fill placement, reduce the binder usage, and reduce the pressure losses or the pipeline wear rate);

ii) hydration modifiers (accelerate or retard the strength gain in the place fill) and

iii) durability enhancers.

APPENDIX B – PHYSICAL RELATIONS OF MINE FILL

Backfill is a complex subject that includes many disciplines such as soil mechanics, concrete technology, fluid mechanics, and process engineering (Potvin et al., 2005; Belem et al., 2018). This section presents the soil mechanics aspect of mine backfill because it is necessary to understand the coherent soil behaviour to clarify the paste backfills. The definitions and all relationships listed in this section are taken from the Mine Fill Course (Belem et al., 2018) and Handbook on mine fill (Potvin et al., 2005). Tailings deposits and backfill masses are not homogenous media (like soil) and consist of three phases: solids, liquid, and gas. If all three phases are simultaneously present in the tailings, they are classified as unsaturated. However, where only two phases, namely solids and liquids, are present, these tailings are classified as saturated tailings (Fig. B-1).

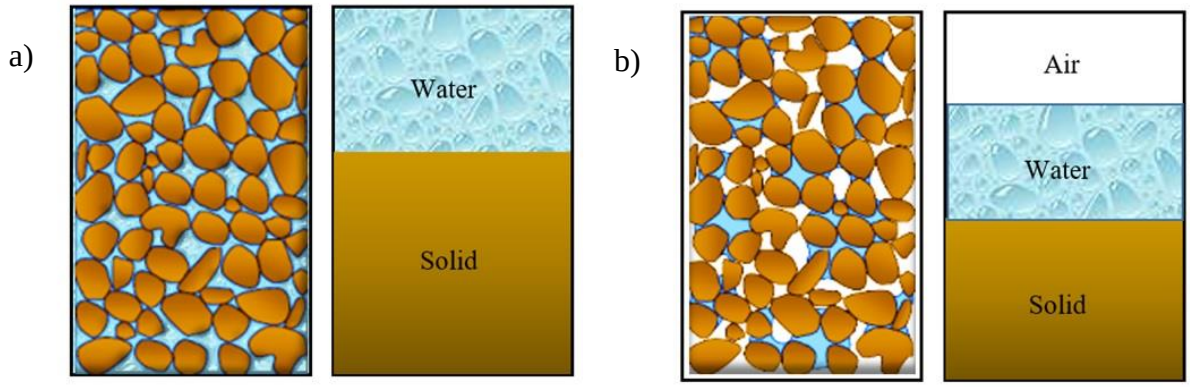


Figure B-1: Soil components: a) a fully saturated soil; b) partially saturated soil (adapted from Belem et al., 2018).

- **Volumetric relationships**

As with soil, to achieve beneficial volumetric relationships, it is necessary to gather all solid grains into a solid mass and all liquids into a liquid mass, as well as all gases into a separate gas volume. After this grouping of the different phases in separate volumes, the original tailings will be represented by three distinct phases (Fig. B-2).

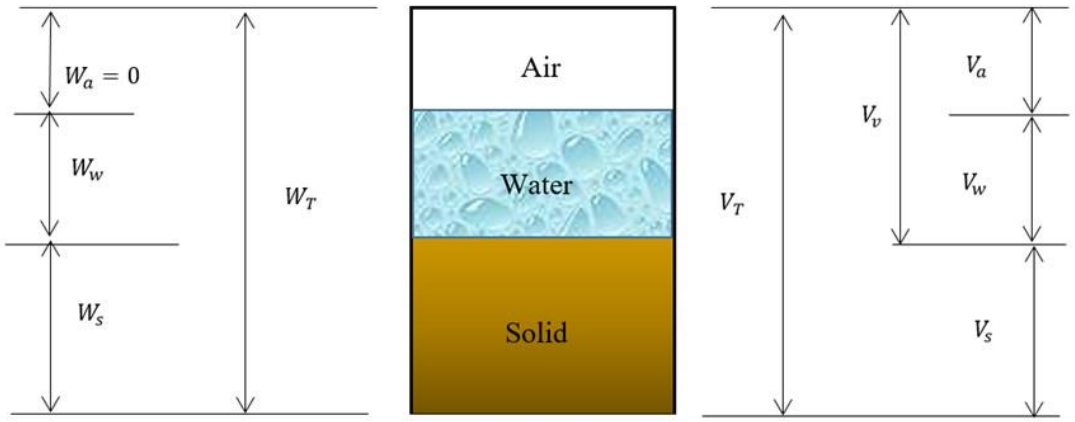


Figure B-2: Phase diagram based on weight and volume (adapted from Belem et al., 2018).

As shown above, the volume of tailings is given by:

$$V = V_s + V_w + V_a \tag{B. 1}$$

Where $V =$ total volume of tailing (all solids volume +all water volume + all air volume); $Vs =$ volume solid of grains; $Vw =$ volume of water contained between grains, and $Va =$ volume of the air between the grains and water film.

The volume of voids (V_v) is given by the following relation:

$$V_v = V_w + V_a \tag{B. 2}$$

Where $Vw = 0$ for dry tailing (no water present); and $Va = 0$ for saturated tailing (absence of air in the medium when all the spaces between the solid grains are filled with water).

The void ratio (e) is the ratio of the volume of all space between the mineral grains to the volume of all the mineral grains and is given by:

$$e = \frac{Void\ volume\ V_v}{Solid\ volume\ V_s} \tag{B. 3}$$

The ratio of the volume of space between the solid grains to the total volume is also a useful property and called porosity (n) and is given by:

$$n = \frac{Void\ volume\ (V_v)}{total\ volume\ of\ fill\ (V)} \tag{B. 4}$$

The relationship between porosity (n) and void ratio € can be deduced as follows:

$$n = \frac{V_v}{(V_s + V_v)} = \frac{V_v}{V_s(1+e)} = \frac{e}{(1+e)} \quad \text{(B. 5)}$$

The unit weight of solids is the weight of a cubic unit of solids if there is no space between the grains when packed in the cubic unit. This is the weight of a cube unit if it is a solid cube and made from the same grain material. The weight of the solids unit is indicated by γ_s. Similarly, the unit of weight of water is the weight of the unit of volume of water and is designated by γ_w. The specific gravity of the solid material is defined as the ratio between γ_s and γ_w and is denoted by G_s.

$$G_s = \frac{\gamma_s}{\gamma_w} \quad \text{(B. 6)}$$

- **Degree of saturation**

Degree of saturation (S_r) indicates the amount of water contained in the voids. It is the ratio of the volume of water inside the voids to the volume of the voids as follows:

$$S_r = \frac{V_w}{V_v} \quad \text{(B. 7)}$$

When $S_r = 100\%$, the fill is completely saturated, and all pores are filled with water.

- **Unit weights of backfill**

The ratio between the weights of the fill sample, including any water in the interstices, to the total volume of the sample of the fill (including the void space), is called the bulk unit weight (γ_b) and is obtained by:

$$\gamma_b = \frac{total\ weight\ of\ fill\ sample\ W_f}{total\ volume\ of\ fill\ sample\ V_f} \quad \text{(B. 8)}$$

When no water present in the pores sample of fill, the unit weight is called dry unit weight in this case (γ_d) and be given by:

$$\gamma_d = \frac{dry\ weight\ of\ fill\ sample\ W_d}{total\ volume\ of\ fill\ sample\ V_f} \quad \text{(B. 9)}$$

- **The water content of backfill**

The fill water content (w_f) is the ratio between the weight of the water present in the sample to the weight of the solid. It can range from 0 (completely dry) to the value of the materials' porosity at saturation and is given by the following relationship:

$$w_f = \frac{weight\ of\ water\ W_w}{weight\ of\ the\ solids\ W_s} \quad \text{(B. 10)}$$

The water content in the material can also be expressed in volume and is called the volumetric water content (θ). It is a ratio between the volume of water in the sample to the total volume of the fill and is given by:

$$\theta = \frac{water\ volume\ in\ the\ sample}{the\ total\ volume\ of\ the\ fill\ sample} = \frac{V_w}{V} = n.S_r \quad \text{(B. 11)}$$

- **The moisture content of backfill**

In mineral processing, the amount of water contained in the tailings is expressed as a portion of the total solid weight and water tighter and is called the moisture content of the sample. It is necessary to know the difference between the water content and the moisture content and to calculate water weights and solids using the appropriate relationship. The moisture content (m) is determined by the following relationship:

$$m = \frac{weight\ of\ water\ W_w}{weight\ of\ solids\ W_s + weight\ of\ water\ W_w} \quad \text{(B. 12)}$$

If W_s is taken as 1, then, the relation between the water content and the moisture content is given as follows:

$$m = \frac{W_w}{(W_s + W_w)} = \frac{W_w}{(1 + W_w)} = \frac{w_f}{(1 + w_f)} \quad \text{(B. 13)}$$

- **The solid content of backfill**

The solid content (C_w) is the ratio between the weight of the solid to the total weight of the fill. It is expressed as a percentage and is given by the following relationships:

$$C_w = \frac{weight\ of\ solids\ W_s}{weight\ of\ the\ solids\ W_s + weight\ of\ water\ W_w} = \frac{W_s}{(W_s + W_w)} \quad \text{(B. 14)}$$

Hence, the solids concertation is given by:

$$C_w = \frac{1}{(1 + w_f)} \tag{B. 15}$$

Also, the moisture content can be given by:

$$m + C_w = 1 \tag{B. 16}$$

- **The volumetric solids concentration**

The volumetric solids concentration (C_v) is the ratio between the volume of solids (V_s) to the total volume of solids and the voids ($V_s + V_v$). The relation between the volumetric solids concentration C_v and the mass solids concentration C_w can be derived as follows:

$$C_v = \frac{V_s}{(V_s + V_v)} = \frac{\frac{W_s}{G_s.\gamma_w}}{\frac{W_s}{G_s\gamma_w} + \frac{W_w}{\gamma_w}} = \frac{W_s}{W_s + G_s\gamma_w} = \frac{1}{1 + G_s w_f} = \frac{1}{1 + G_s \frac{m}{(1-m)}} = \frac{1}{1 + G_s \frac{(1 - C_w)}{C_w}}$$

Hence,

$$C_v = \frac{C_w}{C_w + G_s(1 - C_w)} \tag{B. 17}$$

- **Relative density or density index**

Relative density (D_r) is a measure of the degree of packing achieved in a particle packing and defined as follows:

$$D_r = \frac{(e_{max} - e)}{(e_{max} - e_{min})}\% \tag{B. 18}$$

This parameter can be useful for tailings in tailings ponds and not for backfills because there is no control over their void indices. The relative density can be expressed in term of the dry unit weight of the tailings as follows:

$$D_r = \frac{(\gamma_d - \gamma_{d\,\min})}{(\gamma_{d\,\max} - \gamma_{d\,\min})} \frac{\gamma_{d\,\max}}{\gamma_d}\% \tag{B. 19}$$

Where γ_d = unit weight of the fill at the field condition; $\gamma_{d\,\max}$ = maximum dry unit weight of the fill and $\gamma_{d\,\min}$ = minimum dry unit weight of the fill

Das and Sobhan (2013) summarized the fundamental relationships for the moist unit weight, dry unit weight, and saturated unit weight of soil and several other forms of relationships that can be obtained for γ, γ_d, and γ_{sat} in Table B-1.

Table B-1: Various forms of relationships for γ, γ_d, and γ_{sat} (taken from Das & Sobhan, 2013).

Moist unit weight (γ)		Dry unit weight (γ_d)		Saturated unit weight (γ_{sat})	
Given	**Relationship**	**Given**	**Relationship**	**Given**	**Relationship**
w, G_s, e	$\frac{(1+w)G_s\gamma_w}{1+e}$	γ, w	$\frac{\gamma}{1+w}$	G_s, e	$\frac{(G_s+e)\gamma_w}{1+e}$
S, G_s, e	$\frac{(G_s+Se)\gamma_w}{1+e}$	G_s, e	$\frac{G_s\gamma_w}{1+e}$	G_s, n	$[(1-n)G_s+n]\gamma_w$
w, G_s, S	$\frac{(1+w)G_s\gamma_w}{1+\frac{wG_s}{S}}$	G_s, n	$G_s\gamma_w(1-n)$	G_s, w_{sat}	$\left(\frac{1+w_{sat}}{1+w_{sat}G_s}\right)G_s\gamma_w$
w, G_s, n	$G_s\gamma_w(1-n)(1+w)$	G_s, w, S	$\frac{G_s\gamma_w}{1+\left(\frac{wG_s}{S}\right)}$	e, w_{sat}	$\left(\frac{e}{w_{sat}}\right)\left(\frac{1+w_{sat}}{1+e}\right)\gamma_w$
S, G_s, n	$G_s\gamma_w(1-n)+nS\gamma_w$	e, w, S	$\frac{eS\gamma_w}{(1+e)w}$	n, w_{sat}	$n\left(\frac{1+w_{sat}}{w_{sat}}\right)\gamma_w$
		γ_{sat}, e	$\gamma_{sat}-\frac{e\gamma_w}{1+e}$	γ_d, e	$\gamma_d+\left(\frac{e}{1+e}\right)\gamma_w$
		γ_{sat}, n	$\gamma_{sat}-n\gamma_w$	γ_d, n	$\gamma_d+n\gamma_w$
		γ_{sat}, G_s	$\frac{(\gamma_{sat}-\gamma_w)G_s}{(G_s-1)}$	γ_d, S	$\left(1-\frac{1}{G_s}\right)\gamma_d+\gamma_w$
				γ_d, w_{sat}	$\gamma_d(1+w_{sat})$

- **Important relations developed to design the paste fill**

The relationships in this section assist the calculation of the components of the cemented paste backfill. The amount of water and binder must be determined to be added to wet tailings for fill preparation. Figure B-3 shows the phase diagram of the backfill based on the volume (the right part) and mass (in the left).

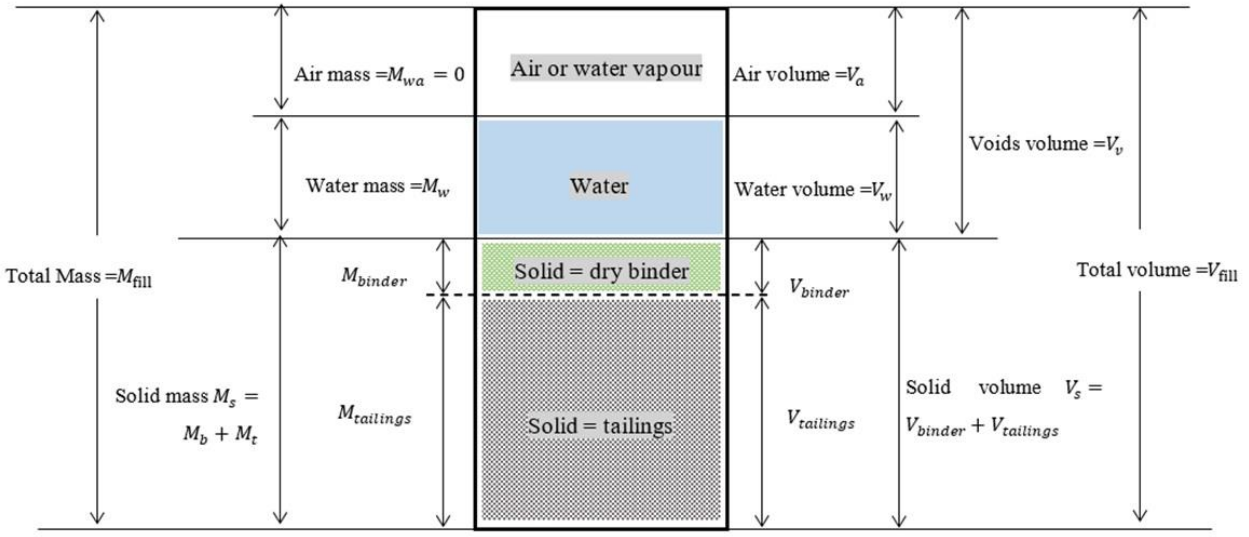


Figure B-3: Cemented paste backfill components (adopted from Belem et al., 2018).

The difference between the fill diagram and the soil diagram is that in the fill diagram, the solid part is divided into two parts, binder, and tailings, to separately determine its mass or volume, as follows:

$$M_s = M_b + M_t \tag{B. 20}$$

$$V_s = V_b + V_t \tag{B. 21}$$

The mass percentage of binder in the fill is the ratio between the solid mass of the binder and the solid mass of the tailings. The mass percentage of the binder is denoted B_w and given by:

$$B_w = \frac{mass\ of\ the\ binder\ M_b}{total\ dry\ mass\ of\ the\ tailings\ M_t} \tag{B. 22}$$

Another useful term called the volumetric percentage of binder (B_v) is given by the following relation:

$$B_v = \frac{volume\ of\ the\ binder\ V_b}{volume\ of\ the\ tailings\ V_t} \tag{B. 23}$$

The relation between B_w and B_v as follows:

$$B_v = B_w \frac{specific\ density\ of\ tailing\ (\rho_{s\ \text{tailings}})}{solid\ mass\ of\ the\ binder\ (\rho_{s\ \text{binder}})} = B_w \frac{\rho_{s-t}}{\rho_{s-b}} \tag{B. 24}$$

The solids mass concentration of the fill is given by:

$$C_w = \frac{the\ solids\ mass\ of\ fill}{the\ total\ mass\ of\ fill} = \frac{M_s}{M_f} = \frac{M_b + M_t}{M_f} = \frac{1}{1 + w_f} = \frac{\rho_d}{\rho_h} = \frac{\rho_s}{\rho_s + eS_r} = \frac{\rho_s}{\rho_s + \theta(1 + e)} \quad \text{(B. 25)}$$

Where M = mass of the substance (in g, kg, or tonne).

The solids concentration (%) can be expressed by the water-to-cement ratio (W/C) as follows:

$$C_{w\%} = \frac{100 \times (100 + B_{w\%})}{100 + B_{w\%}\left(1 + \frac{W}{C}\right)} \quad \text{(B. 26)}$$

Where,

$$\frac{W}{C} = \frac{w_{f\,\%}}{100}\left(\frac{100}{B_{w\%}} + 1\right) = \left(\frac{100 - C_{w\%}}{C_{w\%}}\right)\left(\frac{100}{B_{w\%}} + 1\right) \quad \text{(B. 27)}$$

$w_{f\,\%}$= water content of the final fill mix (in percent).

The equivalent volumetric solids concentration ($C_{v\%}$) is given by the following formula:

$$C_{v\%} = \frac{V_{\text{solid}}}{V_{\text{bulk}}} = \frac{V_s}{V_f} \times 100 = \frac{\rho_d}{\rho_s} \times 100 = 100(1 - n) = \frac{100}{1 + e} \quad \text{(B. 28)}$$

Other formula correlates $C_{v\%}$ with $C_{w\%}$ as follows:

$$C_{v\%} = C_{w\%}\left(\frac{\rho_h}{\rho_s}\right) = \frac{100}{1 + \left(\frac{100}{C_{w\%}} - 1\right) \times \frac{G_s}{S_r}} \quad \text{(B. 29)}$$

Where ρ_h = pastefill bulk density (kg/m^3); ρ_s = pastefill solid particles (tailings + binder) specific density (kg/m^3); n = CPB porosity; e =CPB voids ratio; G_s= paste fill specific gravity; S_r= paste fill degree of saturation (varying from 0 to 1).

To calculate the bulk density of the fill (ρ_h), the following relation is proposed (see Belem et al., 2018):

$$\rho_h = \frac{1}{\frac{C_w}{\rho_{s-f}} + \frac{1 - C_w}{\rho_w}} = \left[\frac{C_w}{\rho_{s-f}} + \frac{1 - C_w}{\rho_w}\right]^{-1} \quad \text{(B. 30)}$$

Where $\rho_{s-\mathrm{f}} =$ the solid density of the fill and is given by the following relation:

$$\rho_{s-f} = \frac{1 + B_w}{\frac{1}{\rho_{s-t}} + \frac{B_w}{\rho_{s-b}}} = (1 + B_w)\left[\frac{1}{\rho_{s-t}} + \frac{B_w}{\rho_{s-b}}\right]^{-1} \quad \text{(B. 31)}$$

The solid density of binder ($\rho_{s\ \text{binder}}$) can be calculated by:

$$\rho_{s-b} = \left[\frac{P_1}{\rho_{s\ \text{cement1}}} + \frac{P_2}{\rho_{s\ \text{cement2}}} + \frac{P_3}{\rho_{s\ \text{cement3}}} + \cdots\right]^{-1} \quad \text{(B. 32)}$$

Where P is the proportion of each cement in the binder.

As can be seen, it is necessary to calculate the solid density of the binder, tailings, and backfill before using the bulk density relationship of the backfill. Three important steps to determine components of the fill (water, cement, and tailings) are the estimation of the expected volume of fill (V_f) to be filled into the stope, the adequate cement ratio (B_w) and the targeted percentage of solid concentration for the backfill (C_{w-f}). It is also necessary to calculate the water content (w_t) and the relative density of the tailings (Gs_{-t}).

The amount of backfill required to fill the entire stope can be calculated using the following relationship:

$$M_f = \rho_{h-f} \times V_f \quad \text{(B. 33)}$$

Then, after determining C_{w-f} (Eq. 28), the water content of the filling should be calculated by the following relationship:

$$w_f = \frac{1}{C_{w-f}} - 1 \quad \text{(B. 34)}$$

Where [C_{w-f}= (M_b + M_t)/M_f)] is the solids mass concentration of the fill

The dry mass of the tailings (M_t) is given by:

$$M_t = \frac{M_f}{1 + w_f}\left(\frac{1}{1 + B_w}\right) \quad \text{(B. 35)}$$

The binder mass required to prepare the backfill is calculated as follows:

$$M_b = B_w \times M_t \quad \text{(B. 36)}$$

The total amount of water in the mixture of the fill is given by:

$$M_w = M_f - M_t - M_b \quad \text{(B. 37)}$$

Before backfill preparation, it is important to consider the amount of water already contained in the wet tailings to determine the remaining mixing water. The amount of water to be added to the mixture (M_{w-add}) is given in the following relationship:

$$M_{w-add} = M_w - M_t \times w_{\mathrm{t}} \quad \text{(B. 38)}$$

Where, w_{t} is the water content of the tailing before the preparation of the fill.

The expected change in the solids percentage for backfill, due to the gradual addition of a certain mass of water to the mixture, can be calculated using the following relationship (see Belem & Benzaazoua, 2008; Belem et al., 2018):

$$C_{w-\mathrm{final}} = \left[1 + \left(\frac{1}{1+B_w}\right)\left(\frac{1}{C_{w-t}} - 1\right) + \frac{M_{w-add}}{M_t}\right]^{-1} \quad \text{(B. 39)}$$

Where $C_{w-\mathrm{final}}$ = the final solid percentage of fill, B_w = binder percentage in the fill, M_{w-add}= the added mixing water, M_t = dry mass of tailings in the mixture, C_{w-t} = the initial solid percentage of thickened or filtered tailings.

APPENDIX C - SHEAR STRENGTH OF THE FILL

- **Effective stresses concept**

Mine backfill is a granular medium (like soil) consisting of a skeleton of solid particles and the inter-particle pore spaces (that are filled with water, air, or both). When the saturated fill is under normal pressure (σ), the solid particle skeleton carries part of this normal stress (σ'), and the rest of the normal stress is carried by the pores of the water (u) as follows:

$$Total\ stress\ (\sigma) = effictive\ stress(\sigma') + pore\ stress(u) \qquad \text{(C. 1)}$$

In partially saturated backfill, water and air fill the inter-particle void. The water is not completely connected in the pore space and can move between the particles during charging. The pores of the fill are compressed when normal stress is added. Due to the surface tension of the meniscus, the pore water pressure is lower than the pore air pressure. In a partially saturated fill, the total stress is given by the following equation:

$$\sigma = \sigma' + X.u_w + (1 - X).u_a \qquad \text{(C. 2)}$$

Where X is the fraction of the total cross-sectional area filled with water; u_w and u_a are the pore water pore and air pressure, respectively.

- **Shear strength components**

Backfill develops shear strength due to frictional resistance between particles, the interlocking of fill particles and cohesion, or any cementing of fill particles at the surface or contact points (Potvin et al., 2005; Belem et al., 2018). The shear resistance developed in the fill is given by the following qualitative question:

$$S_T = S_\mu + S_i + S_c \qquad \text{(C. 3)}$$

Where S_T = total shear resistance; S_μ = shear resistance due to friction; S_i = shear resistance due to interlocking and S_c =shear resistance due to cementation

S_μ and S_i are the components of the shear resistance that are dependent on the normal stress acting across a shearing plane and considered as the frictional component of the shear resistance. They are represented by $\sigma_n' \tan \phi'$ or by $\sigma_{nu} \tan \phi_u$ in terms of effective or total stress, respectively. The

total shear resistance of the fill material can be represented by the Mohr-Coulomb failure strength equation as following:

$$S_T = \sigma_{nu} \tan \phi_u + c_u \qquad \text{in term of total stresses (a)}$$
$$S_T = \sigma'_n \tan \phi' + c' \qquad \text{in term of effective stresses (b)} \qquad \text{(C. 4)}$$

Figure C-1 shows the Mohr-Coulomb strength equation graphically. The Mohr-Coulomb envelope can be plotted in either effective or total stress terms. The total stress parameters obtained from the total stress of the Mohr-Coulomb envelope are the most appropriate to represent the cemented fill mass calculation (Potvin et al., 2005).

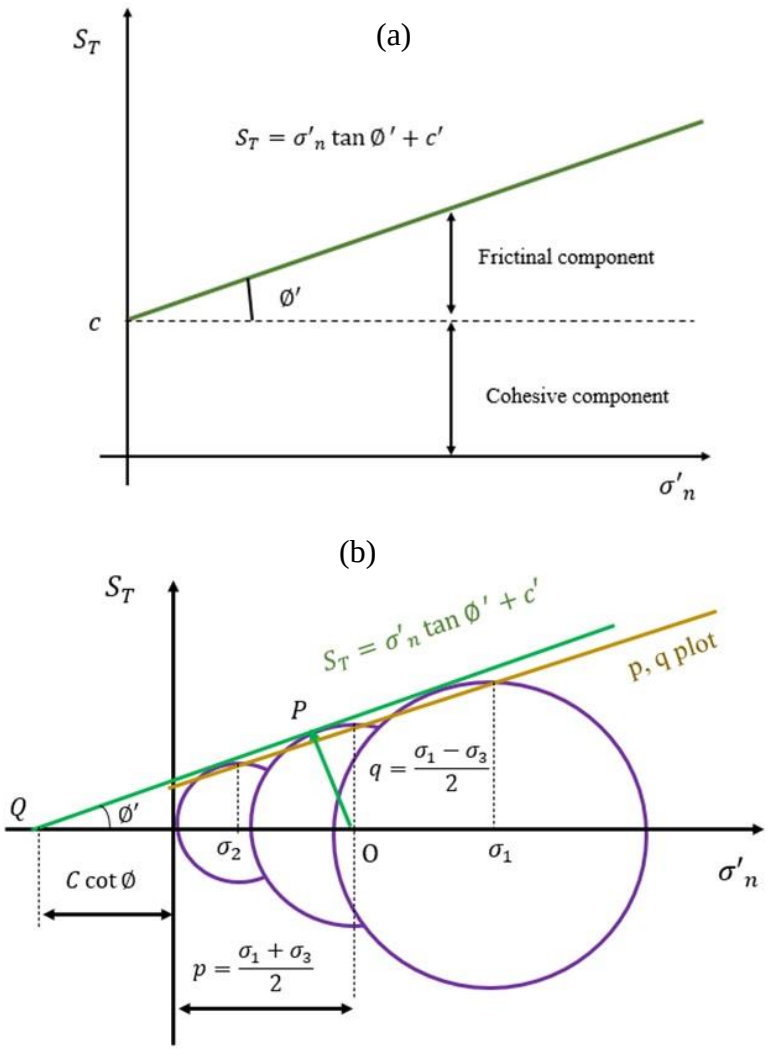


Figure C-1: a) Mohr-Coulomb strength envelope for cemented tailings fill, b) The relationship between Mohr-Coulomb strength envelope and the p, q plot (adapted from Potvin et al., 2005).

Poorly packed fill has low angles of friction (close to zero) and tends to contract during shear. A flat line parallel to the normal stress axis will be in the Mohr-Coulomb strength envelope in this case. Under such conditions, the total shear strength will be provided by the cohesive components. The Mohr-Coulomb failure envelope is obtained by drawing the target to all the Mohr circles obtained by performing axil testing on backfill samples at different confining pressures. The major and minor principal stresses (σ_1 and σ_3) are plotted on the σ_n axis and completing the circles between these two diametrically opposites points. The line that touches the perimeter of the two circles constitutes the envelope of the failure of Mohr-Coulomb. No circle can cross the envelope

or exit above this envelope. Also, the line that connects the highest points on each Mohr circle creates another envelope called p , q plot, where they are defined by:

$$p = \frac{\sigma_1 + \sigma_3}{2} \qquad and \qquad q = \frac{\sigma_1 - \sigma_3}{2}$$

In the effective stresses, the appropriate parameters used are defined by:

$$p' = \frac{\sigma_1 + \sigma_3}{2} - u \qquad and \qquad q' = q = \frac{\sigma_1 - \sigma_3}{2}$$

The relationship between the p, q parameters and the major and minor principal stresses σ_1 and σ_3 can be derived by considering the triangle OPQ, where

$$OP = OQ \sin\phi$$

$$q = \frac{\sigma_1 - \sigma_3}{2} = \left(C \cot\phi + \frac{\sigma_1 + \sigma_3}{2}\right) \sin\phi$$

$$q = p \sin\phi + c \cos\phi \qquad \text{(C. 5)}$$

The relationships between the main stresses in term of effective stresses as follows:

$$\sigma'_1 = \sigma'_3 \tan^2\left(45 + \frac{\phi'}{2}\right) + 2c' \tan\left(45 + \frac{\phi'}{2}\right) \qquad \text{(C. 6)}$$

$$\sigma'_3 = \sigma'_1 \tan^2\left(45 - \frac{\phi'}{2}\right) - 2c' \tan\left(45 - \frac{\phi'}{2}\right) \qquad \text{(C. 7)}$$

With $\tan^2\left(45 + \frac{\phi'}{2}\right) = \frac{1+\sin\phi'}{1-\sin\phi'}$, we get a simple equation as follows:

$$\sigma'_1 - \sigma'_3 = 2c'.\cos\phi' + (\sigma'_1 + \sigma'_3)\sin\phi' \qquad \text{(C. 8)}$$

C. 9

When the angle of the failure plane (θ) is determined (Fig. C-2), it can calculate the tangential (τ_f) and normal (σ'_n) stresses as follows:

$$\theta = 45 + \frac{\phi'}{2} \qquad \text{(C. 10)}$$

$$\tau_f = \frac{\sigma'_1 - \sigma'_3}{2} \sin 2\theta \qquad \text{(C. 11)}$$

$$\sigma'_n = \frac{\sigma'_1 + \sigma'_3}{2} + \frac{\sigma'_1 - \sigma'_3}{2}\cos 2\theta \qquad \text{(C. 12)}$$

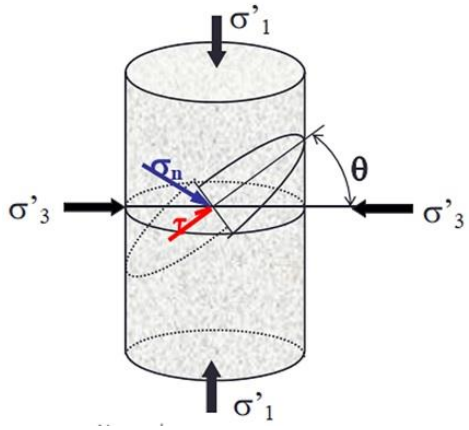


Figure C-2: The normal and tangential stresses on the failure plane (from Belem et al., 2018).

By performing tri-axial consolidated undrained tests (CU tests) with pore water pressure measurements, the total and effective stresses for the sample during the test can be traced to the failure (known as the stress path). Stress paths are very important to describe and study the behaviour of the fill during different loading conditions.

Figure C-3 shows that as the level of binder increases, the shear strength of the cemented fill increase. Similarly, it is observed that the shear strength increases with the curing time of the cemented fill (Potvin et al., 2005).

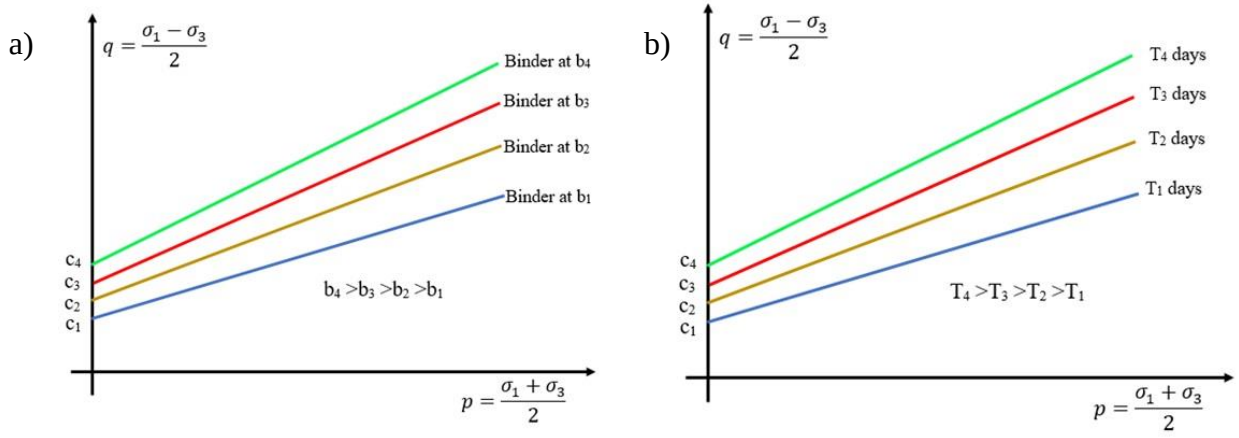


Figure C-3: p, q plot shows the strength gains in cemented tailings fill at a) different binder content and at the same curing time, b) different curing time at the same binder content (adapted from Potvin et al., 2005).

- **Measurement of shear strength**

The triaxial shear test (Fig. C-4a) is the most widely used shearing test in the mine fill applications. In this test, confining pressure and axial loading are applied on a cylindrical sample until failure. Another test is called the unconfined compressive test. The sample is subjected to axial loading without any confining compression applied.

In the triaxial test, both axle load and vertical displacement of the sample are recorded. In some cases, the pressure induced by the water in the pores of the sample must be measured. The results are plotted (the deviator stress ($\sigma_1 - \sigma_3$) versus vertical strain (ε_l)), as shown in Figure C-4b.

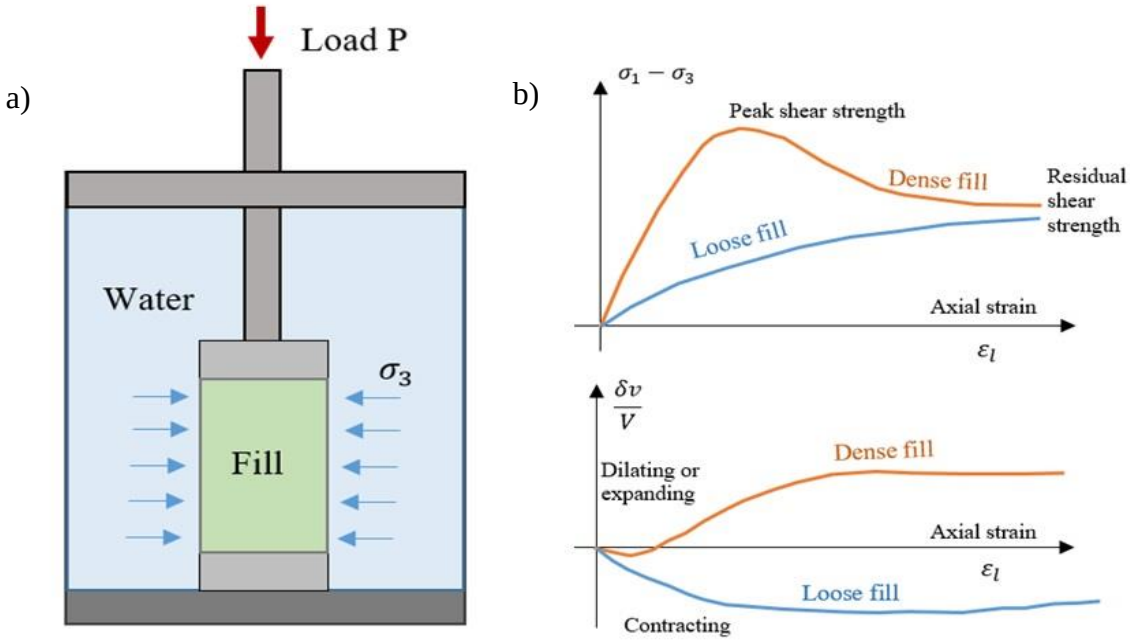


Figure C-4: a) Triaxial test of a cemented fill, b) Strength, and volumetric strain variation of fill (loose and dense samples) (adapted from Potvin et al., 2005).

The shear strength of a dense backfill is mobilized with low axial compression, and the compressive stress reaches a maximum value known as the peak compressive strength at the relatively small axial strain. With further increases in axial pressure (compression), shear resistance begins to decrease. At this stage, almost all the interlocking between particles is overcome. With additional compression, a steady-state shear is achieved with a constant void ratio. At this stage, the dense sand or backfill reaches a constant volume with a void ratio greater than the initial void ratio (called the critical void ratio). For the loose sand, the void ratio is similar or close to the initial void ratio.

The shear strength of the fill is a function of void ratio (e), confining stress (σ_3), loading rate, age of fill, degree of saturation (S_r), size, shape, and grading of the particles (Potvin et al., 2005; Belem et al., 2018). Figure C-5 presents the deviator stresses versus the mean stresses in different curing times.

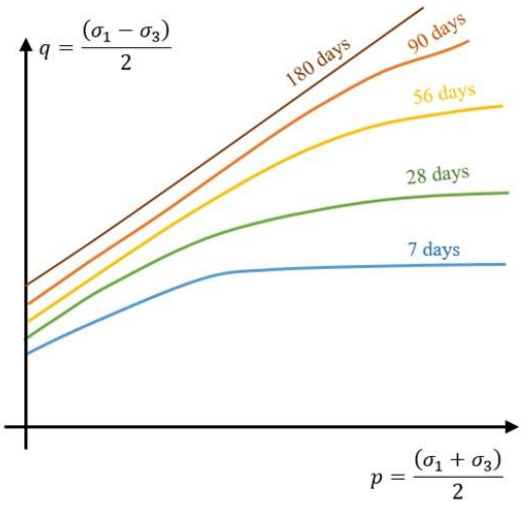


Figure C-5: The effect of curing time on the strength of the cemented fill (adapted from Potvin et al., 2005).

For the short-term stability analysis of mass fill, the total stress parameters are more valid. Nevertheless, the relationship between pore water pressure and total stress can be used to analyze mass fill stability in terms of effective stress. (Potvin et al., 2005).

APPENDIX D - LATERAL EARTH PRESSURE

The lateral earth pressure is related to the shear strength component (or with the friction angle). Consider an element of fill at depth h (Fig. D-1a) is subjected to vertical and horizontal effective stresses (σ'_v and σ'_h, respectively). $\sigma'_h < \sigma'_v$ for fill placed layer by layer if the stresses have been allowed to build up without any disturbance. If the backfill is placed behind a retaining wall and the wall does not move during placement, the relationship between σ'_h and σ'_v is given by:

$$\sigma'_h = K_0 . \sigma'_v \tag{D. 1}$$

Where K_0 is the earth pressure coefficient at rest for normally consolidated soils and given by:

$$K_0 = (1 - \sin \phi') \tag{D. 2}$$

Moving the retaining wall away from the fill (Fig. D-1b) reduce σ'_h but σ'_v remains the same. If the wall continues to move (and the cohesion of the backfill is zero), the backfill will begin to collapse and move towards the wall. The minimum σ'_h necessary to stop the fill failure is smaller the σ'_h at rest and is given by:

$$\sigma'_h = K_a . \sigma'_v = \sigma'_a \tag{D. 3}$$

Where,

$$K_a = \frac{(1 - \sin \phi')}{(1 + \sin \phi')} \tag{D. 4}$$

K_a is called the active earth pressure coefficient. The failure surface slopping at $(45 + \phi'/2)$ to a horizontal plane or with the plane which the major principal stress σ'_v is acting.

When the retaining wall is pushed toward the fill (Fig. D-1c), σ'_h will increase but σ'_v remains the same value. Increasing of σ'_h reaches a maximum value before the fill starts failing by moving upward or heaving. The minimum σ'_h that could initiate such a fill failure is given by:

$$\sigma'_h = K_p . \sigma'_v = \sigma'_p \tag{D. 5}$$

Where

$$K_p = \frac{(1 + \sin \phi')}{(1 - \sin \phi')} \tag{D. 6}$$

K_p is called the passive earth pressure coefficient, and the failure planes make an angle of $(45 - \phi'/2)$ with a horizontal surface.

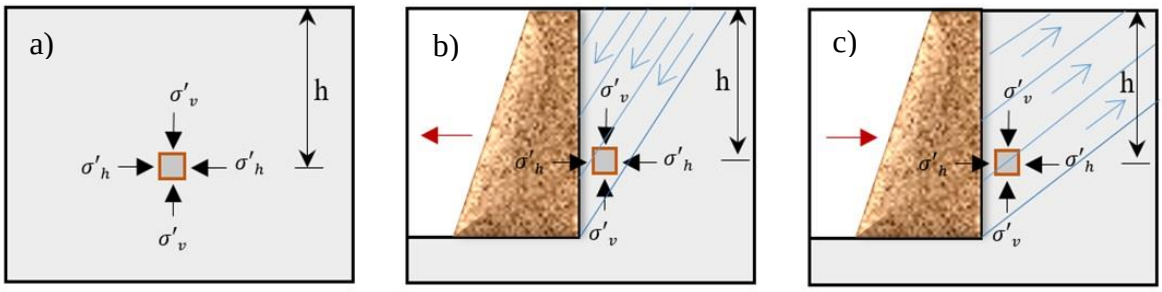


Figure D-1: Mine fill in a) Geostatic stress conditions, b) active earth pressure development, c) passive earth pressure development (adapted from Potvin et al., 2005).

APPENDIX E - CONSOLIDATION OF THE MINE FILL

The backfill consolidation is a process in which saturated backfill particles are forced to move closer together by gravity-related static forces during which pores water escapes from the fill. If pore water cannot escape, there will be no consolidation. An oedometer or triaxial chamber cabin is used to carry out the consolidation test. A backfill sample is subjected to an external pressure that makes it possible to consolidate or contract it. During the test, the change in volume of the fill and the pressure applied are recorded (Fig. E-1).

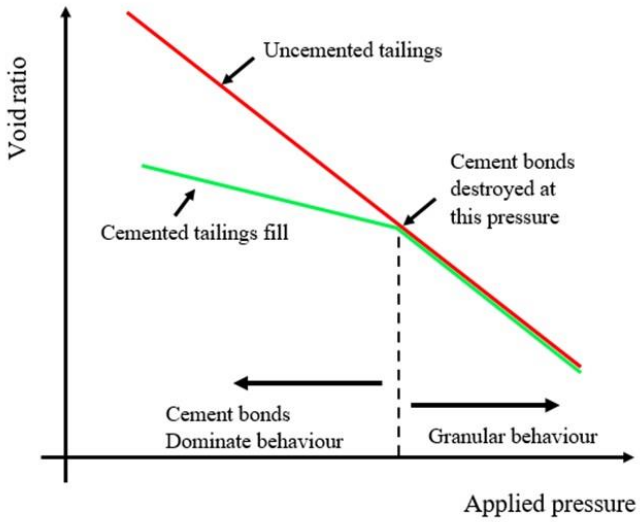


Figure E-1: The ratio of voids to applied consolidation pressure for cemented and uncemented backfill (adapted from Potvin et al., 2005).

To determine whether the backfill at a particular stope is classified as non-consolidating or fully consolidating, Fahey et al. (2010) applied a solution of Gibson (1958) for the consolidation of a layer of sediment increasing in thickness with time. The solution is for 1D self-weight consolidation and assumes a drained base. The solution is expressed in terms of a dimensionless time factor T as follows:

$$T = \frac{m^2 t}{C_v} = \frac{mH}{C_v} \qquad \text{(E. 1)}$$

Where m is the filling rate or rate of rising (in m/h), t is the time of filling (h), H is the total height filled (m), and C_v is the coefficient of consolidation (m^2/h)

According to Fahey et al. (2010), for T $\geq$ 100, the filling is almost completely undrained (non-consolidating), whereas for T $\leq$ 1, the filling is close to fully drained (fully consolidating), with partial drainage occurring for intermediate values of T. They also stated that this solution is only valid until the hydration of the binder begins, because, from that point onwards the stiffness changes due to the binding of the cement, and the self-desiccation mechanism can also begin to produce consolidation.

Belem et al. (2013) published a paper based on the classification system proposed by Fahey et al. (2010; 2011) and Helinski et al. (2010), supported by the results of the mesoscale self-weight consolidation tests and the development of predictive models. They proposed two predictive semi-empirical models of seepage rate and the coefficient of consolidation C_v. These models take into account the tailings grain size gradation, the binder type and amount, the overburden pressure of fill layers, the pre-curing time, and the time elapsed since the beginning of filling.

The seepage rate (q) is given by:

$$q\left(\frac{L}{h}\right) = V_{w0}F_gF_bf_t = \left(\frac{\rho_h}{\rho_w}[1-C_w]V_T\right)\left(\frac{\Delta}{C_UC_C}\right)\left(\frac{\alpha_BD_r}{1+B_w}\right)(0.0263.[t+0.4829]\text{^}(-0.494)\ ) \quad \text{(E. 2)}$$

Where F_g is tailings particle size gradation factor (Δ/C_UC_C); F_b = binder type and amount factor ($\alpha_BD_r/[1+\mathrm{B}w]$); V_{w0} = initial volume of backfill mixing water ($\rho_h/\rho_w[1-C_w]V_T$); ρ_h = total density of CPB; ρ_w = density of water; V_T = total volume of CPB (in L); C_w =solid content of CPB (decimal); Δ = span factor $(D_{90}-D_{10})/D_{50}$; C_U = coefficient of uniformity of tailings (= $\mathrm{D}_{60}/\mathrm{D}_{10}$); C_C = coefficient of curvature of $tailings$ (= $\mathrm{D}_{30}^2/\mathrm{D}_{60}\times\mathrm{D}_{10}$); D_r = relative density of tailings; B_w = binder content in decimal ($M_{binder}/M_{tailings}$); α_B = binder type correction scalar (between 0.2 and 0.55).

The percolation rate (v) can be calculated from the seepage rate as follow:

$$v\ (\mathrm{mm/h}) = q/A_{\mathrm{dp}} \quad \text{(E. 3)}$$

Where A_{dp} = the cross-section of the drawpoint (Belem et al., 2013)

The authors proposed a semi-empirical model for predicting the coefficient of consolidation C_v that is given as follows:

$$C_v = (F_g F_c F_p) f(t_{pc}) = \left(\frac{\Delta}{C_U C_C}\right)\left[\frac{1}{G_s(1 + B_{w\%})}\right]\left(\frac{1}{1 + \sigma_v / P_0}\right)\left(\frac{2.3219}{1 - 0.8410\exp(-0.5929 t_{pc})}\right) \quad \text{(E. 4)}$$

Where σ_v = overburden pressure (kPa), P_0= atmospheric pressure (~100 kPa). The time function $f(t_{pc})$ was obtained through regression analysis on experimental laboratory data.

APPENDIX F - FUNDAMENTALS OF PHYSICAL MODELLING

In the field of geotechnical engineering, two approaches are used to study the problems from an experimental point of view: instrumentation of full-scale structures and laboratory experiments using small-scale models (under normal gravity (lg conditions) or using a centrifuge). Physical models are often very small compared to the structure of the prototype because the testing of a structure on a large scale is expensive, time-consuming, and often impossible (Altaee & Fellenius, 1994). The instrumentation of a real site (prototype) allows validating methods of numerical modelling or experimental tests. The experiments on reduced models have been practiced for a very long time and under satisfactory conditions. Scale relationships have been developed for extrapolating results from small-scale tests to prototype behaviour. The scaling rules indicate the relationships between stress, strain, and displacement for the model and prototype in terms of geometric and stress scale.

- **Rules of similarity**

Similarity rules are the set of conditions to be met by constructing the model and the relationships used to transfer the solution obtained on the reduced-scale model into the full-scale problem (Corté, 1989b). The quest for similarity rules is based on dimensional analysis, taking into consideration the invariance of the solution to the physical problem via unit changes. Vasey's theorem (1927) stated that the final relationship is identical to a relationship between independent dimensionless ratios. The first decrease in solution expression can be achieved, without the need to specifically render the relationships governing the issue by writing its invariance through adjustments in the coherent system of basic units. This results in a set of dimensionless variables (set of similarity conditions).

It is essential to respect the conditions of similarity so that the behaviour of the model reduces as closely as possible the behaviour of the prototype. Frequently, it is very difficult to simultaneously comply with all these conditions, forcing experimenters to be satisfied with a broader similarity (Niemann, 1995). Often not all similarity requirements can be met strictly, and therefore some distortions lead to scale effects.

The system to be studied is characterized by several variables x_i of different dimensions (length, mass, time...). Scale factors x^*_i translate the relationship between the value x_i of the reduced model and that corresponding x'_i of the full-scale prototype as follows:

$$x_i^* = \frac{x_i}{x_i'} \tag{F. 1}$$

The establishment of the laws of similarity is based on a dimensional analysis considering the invariance of the general equations of mechanics to the change of units. These equations are the general equations of dynamics, the conservation equation of mass, and the laws of behaviour of varied materials. Every physical system obeys the indefinite equilibrium equations of continuum mechanics. In the hypothesis of small deformations, they are written as follows:

$$\sum_j \frac{\partial \sigma_{ij}}{\partial x_j} + \rho \left[g_i + \frac{d^2 \xi_i}{dt^2} \right] = 0 \tag{F. 2}$$

Where xj: coordinates, σij= components of the stress tensor, ξi = components of the displacement vector, g_i = components of the gravitational acceleration vector, ρ = unit weight of the material, and $t =$ time.

This equation must be satisfied by the variables of the reduced model and the prototype.

With $x_i^* = \frac{x_i}{x_i'}$, and substituting x_i with $x_i^* x_i'$, we obtain the following equation:

$$\frac{\sigma^*}{L^*} \sum_j \frac{\partial \sigma'_{ij}}{\partial x'_j} + \rho^* \rho' \left[g^* g'_i + \frac{\xi^* d^2 \xi'_i}{t^{*2} dt'^2} \right] \tag{F. 3}$$

For the reduced model to have the same mechanical behaviour as the prototype, the two previous equation (104 & 105) must be formally identical, leading to the following similarity conditions:

$$\sigma^* = \rho^* g^* L^* \tag{F. 4}$$

- **Dimensional analysis**

Vaschy (1892) analyzed the conditions which determine the relation that makes these variables adopt to be independent of the system of units.

If the variable x is a function of n variables x_i, let $x = f(x_1, x_2 \ldots x_n)$, there exist q relations $(q < n)$ between the n scaling factors x_i^*. The relation f can then be replaced by a function F of q dimensionless variables, combinations of n physical quantities x_i.

The q relations between the scaling factors x_i^* are written as power function products:

$$\pi(x_i^*) = \frac{x_i^*}{x_1^{*\alpha} x_2^{*\beta} x_3^{*\gamma} \dots} \quad \text{(F. 5)}$$

The exponents α, β, γ, are computed to render the numbers π dimensionless. It can thus obtain the relationships between scale factors reflecting the similarity to be respected by the scale model. The dimensional analysis method applied to the six variables involved in previous equations allows us to find the following equations:

$$\xi^* = L^* \quad \text{(F. 6)}$$

Therefore, the strain factor is given by:

$$\varepsilon^* = \frac{\xi^*}{L^*} = 1 \quad \text{(F. 7)}$$

Since the length scale factor (L^*) is equal to the scale factor of displacement (ξ^*), the strain (ε) on the reduced model is the same as that of the prototype. In practice, this third condition must be respected in the case of large displacements, when displacements cannot be neglected concerning dimensions (Mandel, 1962). This is the case, for example, for studies on limit loads or failure mechanisms.

- **Relations of behaviour and material selection**

The relations of the mechanical behaviour of materials bring out the characteristics of the parameters that must satisfy the laws of similarity. In order to simplify, it is presented the establishment of laws of similarity with a simple behaviour such as linear elasticity or elastic perfectly plastic with a Mohr-Coulomb criterion.

The generalized Hooke's law is written:

$$\varepsilon_{ij} = -\frac{v}{E} . tr(\sigma_{if}) . \delta_{ij} + \frac{v+1}{E} . \sigma_{ij} \quad \text{(F. 8)}$$

Where ε_{ij} = strain tensor, σ_{if} = stress tensor, δ_{ij} = Kronecker index, v= Poisson ratio, and E = Young's modulus. In the case (linear elasticity), the scale factor of the Poisson's ratio (v^*) = 1 and for the stress $\varepsilon^* E^* = \sigma^*$

The criterion of Mohr-Coulomb is written as follows:

$$\tau = c + \sigma \cdot tan\phi \quad \text{(F. 9)}$$

Where $\tau =$ shear stress; σ = normal stress, $c =$ cohesion, and $\emptyset =$ friction angle

A similar manner for the other units, the scale factors are: $\phi^* = 1,\ \tau^* = \sigma^*$, and $c^* = \sigma^*$

Therefore, when the simulation is conducted under a normal gravity ($g^* = 1$), with the length scale factor ($L^* = 1/n$), and the material used in the prototype is the same real material or equivalent material having approximately the same density ($\rho^* \approx 1$), it can obtain the following relation:

$$\sigma^* = c^* = L^* = 1/n \quad \text{(F. 10)}$$

This means that the stiffness and cohesion of the reduced model materials must be n times smaller than that of the prototype. Therefore, it is interesting to use the same material of the prototype to reproduce the scenarios or the experiments on the model.

In soil mechanics, one particularity lies in the fact that their behaviour is closely related to the level of stress to which they are subjected. Sand at a given density can, for example, expand under low stress but contract under high stress (Zhang, 2011). The effect of the stress state can also result in qualitatively different phenomena leading to changes in failure mechanisms (Dubreucq et al., 1995). Therefore, the first necessary condition for the realization of realistic physical models is the respect of the level of stress ($\sigma^* = 1$). Moreover, in the absence of equivalent materials with the same rheological properties, we are most often forced to use real soils ($\rho^* = 1$). The simultaneous respect of relations finally leads to $\sigma^* = 1/L^*$. If a reduction coefficient *n* ($L^* = 1/n$) is applied on the lengths, the condition imposing similarity on the stresses implies that the scale model must be tested under an acceleration *n* times greater than that of gravity ($g^* = n$). Different methods have been considered to produce these macro-gravity fields such as shock tables, additional masses, friction tables, hydraulic gradient method, or centrifugation. The latter has established itself as one of the major physical modelling methods. When the models are tested under normal gravity with real soils, the condition becomes $\sigma^* = L^*$. In this case, as the level of stress is no longer respected, scale effects may occur. Scale factors to be respected for models under normal gravity are summarized in Table F-1.

Table F-1: Scale factors for models under normal gravity (1g).

Physical quantities	Scale factors
Density	$\rho^* = 1$
Length	$L^* = 1/n$
Displacement	$\xi^* = 1/n$
Deformation	$\varepsilon^* = 1$
Stress	$\sigma^* = 1/n$
Strength	$F^* = 1/n^3$
Dynamic time	$t^* = 1/\sqrt{n}$
Frequency	$f^* = \sqrt{n}$
Acceleration	$g^* = 1$
Angle of friction	$\emptyset^* = 1$
Young's module	$E^* = 1/n$
Poisson ratio	$v^* = 1$

Corte (1989) reported that in the case of linear elastic strains if the prototype soil mass is homogeneous and isotropic, the conditions for producing an equivalent material are decreased to the equality of Poisson's ratios. If the soil consists of several layers, the elasticity modulus ratios of these layers should also be preserved. The similarity may be obtained with different materials on the condition of a homothetic transformation of the intrinsic curves in the same ratio σ^*, of the coefficients of elasticity in the same ratio $E^* = \sigma^* \varepsilon^{*-1}$, and of the densities in the same ratio ρ^* for all the layers.

Corte (1989) also stated that for a diphasic medium (soil + fluid), it is required to conserve the behaviour of each phase and the interactions between phases. For laminar flows in a porous medium, the interaction between fluid and soil is defined using the laws of Terzaghi and Darcy. The validity of the latter rule may be defined roughly by a Reynolds number less than 10. For steady-state turbulent flows, the size of the elements must be decreased in the ratio 1/n for the flow velocity to be the same in the model as in the prototype structure.

The physical rules that govern the behaviours of the different phases of a substance and their interactions involve the time factor in various forms that lead to multiple conditions of similarity. Similarity conflicts arise as soon as several phenomena occur at various speeds (Corté, 1989a).

Table F-2 shows the different times scale factors for tests under normal gravity (1g) and in the centrifuge, when the stresses, strains, and materials of the full-scale problem are conserved.

Table F-2: Time scale factors (t^*) for different phenomena (from Corte, 1989).

	Centrifuge tests	1 g tests
Inertia	$t^* = L^*$	$t^* = \sqrt{L^*}$
Laminar Flow Consolidation Diffusion	$t^* = L^{*2}$	$t^* = L^*$
Creep	$t^* = 1$	$t^* = 1$

In the case of granular, a decrease in grain size is inevitable. Usually, the same material is used for the model, translating the particle size range and conserving the shape of the elements. The particle size distribution and shape factor are issues that must be taken into consideration. However, this approach is not enough to ensure good similarity, as the crushing strength of the blocks is generally not conserved (Marsal, 1969). The fragmentation of the prototype problem blocks is governed by discontinuity networks or geometrical details of the shape, having a characteristic dimension that is practically always larger than the size of the model blocks (Bolton & Lau, 1988).

APPENDIX G - IMAGE ANALYSIS

Displacement and strain are critical parameters for building and engineering projects. Nonetheless, it takes an incredibly difficult choice between traditional techniques to calculate these parameters because precision, simplicity, and cost must be balanced. Digital Image Correlation (DIC) is a non-contacting optical method of measuring deformation and displacement. DIC is simple to use and cost-effective compared with other techniques such as speckle interferometry, and more precise and subjective than manual measurement techniques, opening a variety of applications (McCormick & Lord, 2010). DIC operates in different stages by comparing digital photos of a part or test specimen. The system can track surface displacement and create complete 2D and 3D deformation vector fields and strain maps by following pixel blocks. To be efficient, DIC must have random and unique pixel blocks with different levels of contrast and intensity. It does not need special lighting, and the structure or component's natural surface in several cases has enough image texture for DIC to work without having to prepare special surfaces (Sutton et al., 2009). Software methods were introduced to obtain subpixel resolutions and enable the algorithms to be executed efficiently. Images can be obtained from a wide range of sources, including digital consumer cameras, high-speed video macro-scopes, electron scanning and atomic force microscopes. DIC was first developed in the 1980s by a group of researchers at South Carolina University (Peters & Ranson, 1982). The DIC method has advantages as well as inconveniences. The most influencing factors on the precision of this method are experimental conditions and the algorithm (Pan et al., 2009). In order to capture the digital images of the test specimen surface, before and after deformation, a simple experimental setup with only one fixed camera is required (Fig. G-1). If the surface of the specimen has no random distribution, it is possible to simply spray the paint on the sample surface (Schreier, 1969).

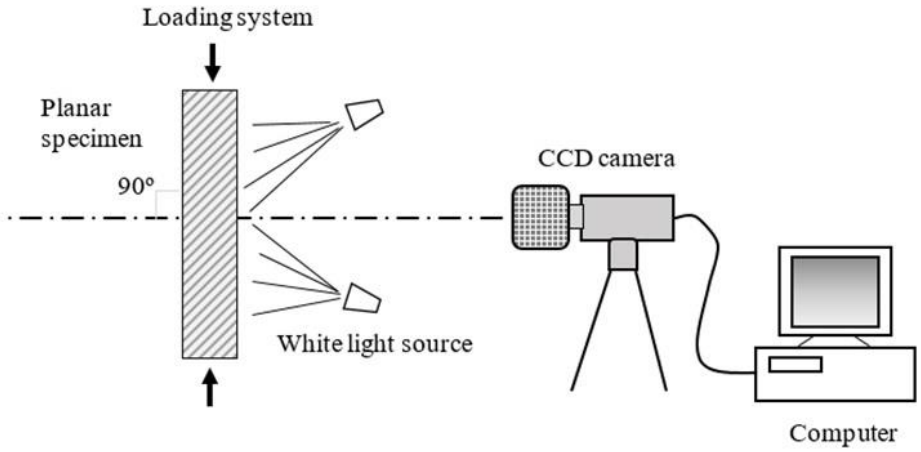


Figure G-1: Typical 2D DIC optical image acquisition system (adapted from Pan et al., 2009).

After recording the digital images of the surface of the specimen before and after deformation, the DIC calculates the displacement of each image point by comparing the digital images of the test object surface in different states. DIC generates displacement data by comparing the difference in the location of the point of interest based on two different photos taken in the global coordinate system from the same location.

Figure G-2 shows the working method of the DIC. The area of computation of the reference image must be specified or defined, which itself is divided into regularly spaced virtual grids (Fig. G-2a). The displacements are calculated at each point of the virtual meshes to acquire the deformation in full-field (Fig. G-2b). The fundamental principle of DIC is to track (or match) the same points (or pixels) between the two pre- and post-deformation photos, as shown in Figure G-2(c & d). In order to obtain the displacements of point P, a square reference subset of $(2M + 1) \times (2M + 1)$ pixels centred at point P(x0, y0) from the reference image is selected and used to track its corresponding location in the deformed image.

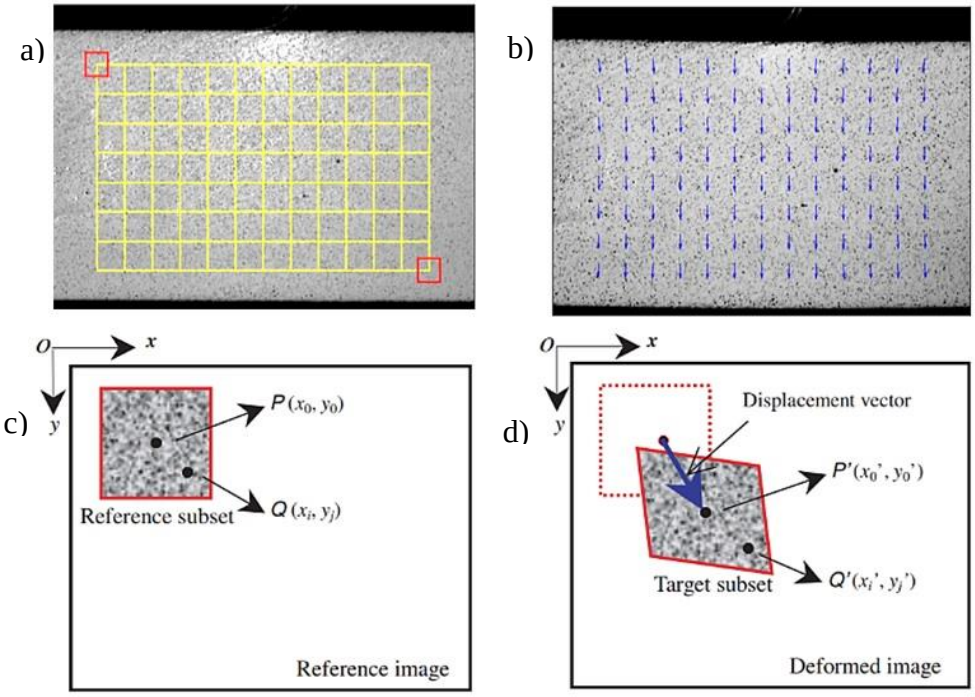


Figure G-2: a) Reference image, The red square imposed is a subset used for the motion tracking of its central point, and the yellow grid cross-section points indicate the points to be computed; b) the computed displacement vectors imposed on the deformed image; c) a reference square subset before the deformation; d) the targeted subset after deformation (from Pan et al., 2009).

The non-contact method by 3D-DIC is appropriate to be used for a large-scale specimen like the cemented rockfill (CRF) elastic properties determination. It is also not recommended that strain gages be placed on a CRF sample surface to measure its total deformations. The strain gages are restricted by internal limitations and external influences, such as the small ring size of the compressometer-extensometer, the temperature effect, and the gage's length limitation.

Lingga et al. (2018) recently conducted several unconfined compressive strength (UCS) tests on CRF specimens. The samples were made sufficiently large to keep a high ratio between the sample's diameter and the total size. The UCS test was carried out for six CRF samples with a cement content of 4.5% and a diameter of 304.8 mm (aggregate waste rock size < 50.8 mm). During the test, the DIC system recorded the deformations using VIC-3D software. Two fixed mounted LVDTs (linear variable differential transformer) and three string potentiometers were recording the lateral and axial deformations (Fig. G-3). Before testing, samples were cured for 28 days indoors so that the backfill could reach its target compressive strength values. The specimens were

completed by capping the top and bottom surfaces and spraying the white and black speckles on the sample surface to track the deformation of multiple points painted on the surface of the specimen.

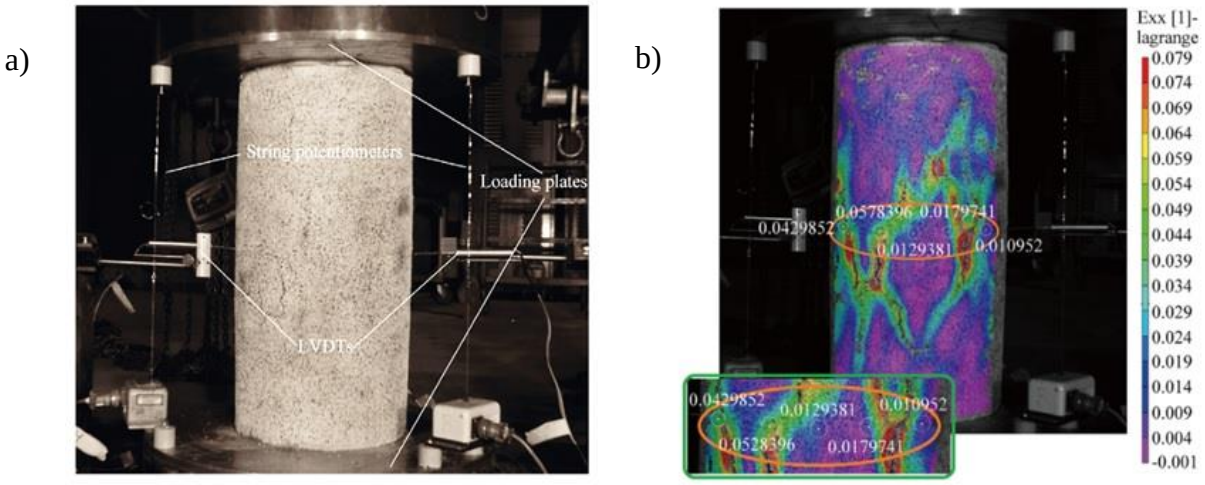


Figure G-3: a) Prepared specimen and installation of LVDT and string potentiometer, b) Strain measurement using 3D-DIC (taken from Lingga et al., 2018).

Their result indicated that the 3D-DIC and contact method strain follow the same trend up to about 70% of the peak strength. The strains of all interest points generally show coherence and conformity with the method of contact until the specimen leaves the elastic zone. Then the deviation gets larger, particularly when the peak strength passes. The location of points of interest greatly influences the elastic properties produced by the 3D-DIC. Average differences of 5.1 and 14.5% were found for lateral and axial deformations, respectively.

APPENDIX H - USE OF STRAIN GAUGES FOR MEASURING PRESSURE

The pressure is defined as a uniform force over a specified area. Only the reference pressure differentiates the different pressures (Fig. H-1). Pressure zero that is available in the air-free universe is the simplest reference pressure. A pressure associated with that reference pressure is called absolute pressure (P_{abs}). Atmospheric pressure (P_{amb}) is the air weight that surrounds the earth to a height of approx. 500 kilometres. Up to this altitude, at P_{abs} = zero, the amplitude of the atmospheric pressure reduces continuously. The difference between the two pressures is defined as the differential pressure ($\Delta p=p_1-p_2$). The gauge pressure (overpressure) is the difference between absolute pressure and the relevant atmospheric pressure ($P_e=P_{abs}-P_{amb}$). A positive overpressure exists if the absolute pressure exceeds atmospheric pressure. Conversely, if the overpressure is less than the atmospheric pressure, the negative overpressure is referred to.

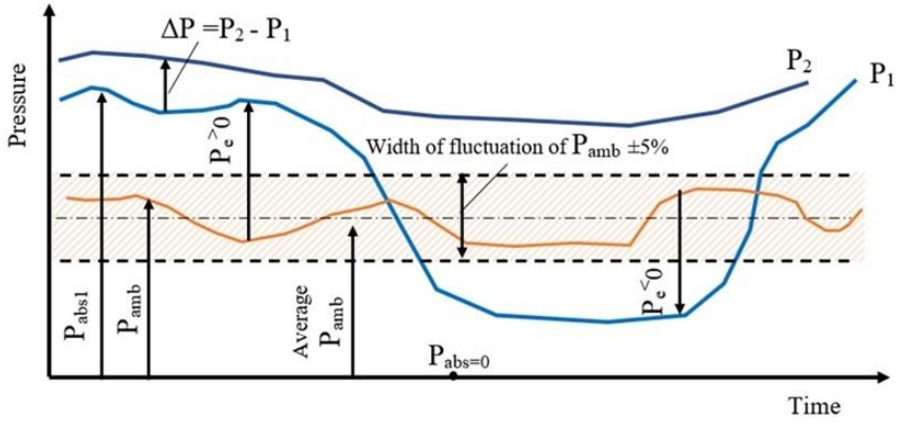


Figure H-1: Types of pressure: absolute pressure, gauge pressure, differential pressure (adapted from en.wika.com).

- **strain gauges**

In small-scale laboratory tests, pressure sensors are used for the measurement of pressure (mechanical energy form) and translating it into an electric signal displayed on a remote gauge (Agarwal & Lang, 2005). A load cell is a transducer used to create an electrical signal whose magnitude is proportional to the measured force. There are different types of charging cells, such as strain gauge cells, piezoelectric load cells, hydraulic load cells, pneumatic load cells and vibrating wire load cells.

In the load cell of the strain gage, the load action deforms a strain gauge by a mechanical arrangement. The strain gauge measures the deformation as a change in the electrical resistance, which is a measure of the strain and, therefore, the applied load. The working principle of the strain gauge sensor is that the strain gauge contracts when its material deforms. The load acting on them is then converted into electrical signals. The strain proportionality changes the electrical resistance of the gauges as the load increases. The precision of a pressure sensor can be divided into a few components, which are linearity, hysteresis, short-term repeatability, temperature errors, hysteresis, long-term stability and zero and span offsets. Strain gages are sensitive to changes in temperature and should be arranged in such a manner that compensates for temperature effects.

Strain (ε) is the quantity of deformation of an object due to the force exerted and is described as the fractional length change. The strain may be either positive (tensile) or negative. The strain is dimensionless; however, it can sometimes be expressed in units (such as in/in or mm/mm). In practice, the strain is quite small and is often expressed as micro-strain ($\mu\varepsilon = \varepsilon \times 10^{-6}$).

The metal strain gauge is made of a thin wire or metallic foil placed in a grid pattern. The grid enhances measuring the strain in the parallel direction (Fig. H-2a). The cross-sectional area of the grid is reduced in order to reduce the effect of the shear strain. The grid is connected to a thin layer (called the carrier). This backing is attached directly to the test specimen during strain measurement. The strain is transferred to the strain gauge, which reacts with a linear change in the electrical resistance. Strain gauges are available on the market with nominal resistance varies from 30 to 3000 Ω. The most common values are 120, 350, and 1000 Ω. A basic parameter of the strain gauge is its responsiveness to strain, expressed quantitatively as the gauge factor (GF). Gauge factor represents the ratio of fractional change in electrical resistance to the fractional change in length (strain), and is given by the following equation:

$$\mathrm{GF} = \frac{\Delta \mathrm{R}/\mathrm{R}}{\Delta \mathrm{L}/\mathrm{L}} = \frac{\Delta \mathrm{R}/\mathrm{R}}{\varepsilon} \qquad \text{(H. 1)}$$

The metallic strain gauge Factor is usually about two (Note, 1998). Both strain gauge and sample respond to temperature changes. Manufacturers seek to minimize temperature sensitivity by manipulating the gauge material to compensate for the thermal expansion of the test sample for which the gauge is designed. In order to measure these small variations in resistance and to account for temperature sensitivity, strain gages are almost always used in a bridge configuration with a

source of voltage or current excitation. The Wheatstone bridge comprises four resistive arms with an excitation voltage (V_{EX}) connected to the bridge (Fig. H-2b).

The output voltage of the bridge (V_o) is given by:

$$V_o = \left[\frac{R_3}{R_3 + R_2} - \frac{R_2}{R_1 + R_2}\right] \quad \text{(H. 2)}$$

When $R_1/R_2 = R_4G_1/R_3G_2F$, the voltage output (V_o) equals zero. It is said that the bridge is balanced in such conditions. Any change in resistance in any bridge arm can result in an output voltage that is nonzero. If the arm R_4 is replaced by an active strain-gauge (Fig. H-2c), any change in the resistance will unbalance the bridge and generate a non-zero output voltage. If the strain gauge's nominal resistance is referred to as R_G, the strain-induced change in resistance (ΔR) may be expressed as:

$$\Delta R = R_G \times GF \times \varepsilon \quad \text{(H. 3)}$$

Assuming $R_1 = R_2$ and $R_3 = R_G$, the above bridge equation may be rewritten to express the ratio (V_O/V_{EX}) as a strain function as follows:

$$\frac{V_O}{V_{EX}} = -\frac{GF \times \varepsilon}{4}\left(\frac{1}{1 + GF \times \frac{\varepsilon}{2}}\right) \quad \text{(H. 4)}$$

The term $1/(1+GF\times\varepsilon/2)$ implies that the quarter-bridge output is nonlinear in relation to strain.

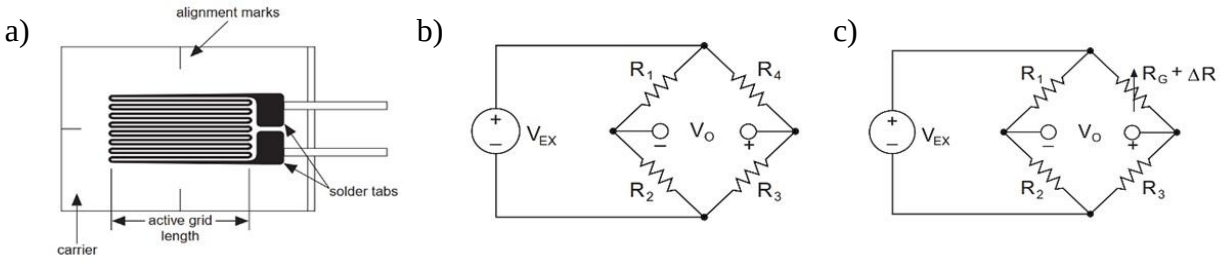


Figure H-2: a) Metallic Strain Gauge; b) Wheatstone Bridge; c) Quarter-Bridge Circuit (from Note, 1998).

The effect of temperature may be prevented by using two strain gauges in the bridge (half-bridge configuration: a second gauge is mounted transversely to the strain applied). A Full-bridge circuit

can be used to maximize circuit sensitivity by making all four bridge arms active strain gauges (mounting two tension gauges and two compression gauges).

Finally, using any type of sensor to measure pressure in laboratory experiments, on a small model or other application, requires reading the technical instructions for these devices to understand the principle of their operation, accuracy, and sensitivity.

APPENDIX I - FUNDAMENTALS OF NUMERICAL MODELLING

Modelling, which basically simplifies real-world problems, is an essential portion of all methods of geotechnical engineering analysis and design. Geotechnical engineering modelling may range from constituent models of soil defining material behaviour to experimental and intelligent models that model geotechnical systems under different mechanical and environmental conditions. Difficult issues can be studied using numerical methods such as finite difference, finite element, and discrete element methods. Modelling may include predicting stress produced by interactions between civil engineering structures and the soil, displacements due to loads imposed, development of pore water pressure, and its effects on stability. Since modelling requires simplifications and assumptions, it is very important to be careful about how these are established and the nature and implications of these assumptions.

- **Numerical modelling methodology**

The practice of geotechnical engineering involves mainly three parts: the ground profile establishment, the definition of ground behaviour and modelling, all linked and supported by empirical and precedent experience (Burland, 1987). These three parts of what is now known as the Burland triangle (Fig. I-1).

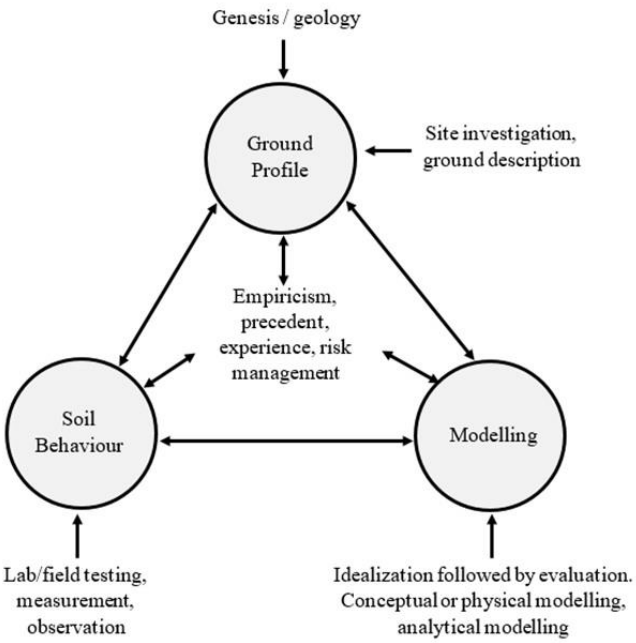


Figure I-1: Expanded Burland Triangle (adapted from Anonymous, 1999).

The main objectives of all geotechnical designs often refer to one of three general types of behaviour (and characteristics): deformation (compressibility), stability (strength), and drainage or groundwater flow (conductivity hydraulic). Every such process is significantly complicated, and the mathematical definitions of this behaviour often lead to non-linear numerical solutions (Barbour & Krahn, 2004). A typical modelling methodology was proposed (by Mercer & Faust, 1981) for groundwater modelling. This methodology comprises four steps as follows:

1) *Observe – Establish the conceptual model:* it is necessary to define the main purpose of the model, to begin collecting existing general data on the site (in-situ information and measurements) and to develop a conceptual model (not very complicated at the start of use) of the geology and hydrogeology of the site (excavation depths, loads, the sequence of construction, etc.).

2) *Measure – Define the theoretical model:* the main material behaviours must be identified using the constitutive relations describing these processes with which material properties are associated. The solution requires us to use these theoretical descriptions to establish solvable resolution equations, subject to suitable material properties and boundary conditions. Field monitoring can become an important source of information to identify material behaviour.

3) *Explain-Develop and validate the analytical or numerical model:* after analyzing and conceptualizing the physical reality and describing the relevant processes logically and mathematically, it can check them by committing them to a mathematical solution. It must first define a domain (geometry) in which it will look for the solution to a set of equations governing. The equations are solved according to a set of boundary conditions applied to the domain and in concert with the material properties. The solution process may be diverse, involving analytical solutions, graphical techniques, or numerical solutions such as finite difference techniques and finite elements. Selecting more than one solution method like an analytical solution and a numerical solution is important. The complexity of the model will ultimately demand the use of a numerical model like a software package. The user must be aware of the characteristics and specific features to use the software correctly (input/output). Since numerical problems can occur, it is important to establish confidence in the limits of the solution with numerical models.

4) *Verify – Interpret, calibrate, validate against physical reality:* The results must be cautiously compared to the physical reality when the mathematical solution is obtained. Conceptual and mathematical models are adjusted using field data until a successful agreement is achieved between the physical and mathematical systems. Sensitivity analysis helps us to understand and interpret which components of the conceptual and theoretical models are particularly important for field performance (e.g. material properties, boundary conditions). There is no definitive solution, though, and the outcomes would depend largely on experience, technical judgement, and reasonableness.

- **Constitutive Models**

Many behaviour laws were used in geotechnical computing software based on finite element methods. The laws of behaviour describe the relationship between the stress tensor, the strain tensor and their corresponding increases, which can imply a rupture or elasticity criterion (Ti et al., 2009). The choosing of a model depends upon the behaviour and type of analysis of the material being studied by the geotechnical engineer (Wood, 2004). Here, only three common models are presented among the many models used in geotechnical numerical simulations: linear elastic, elastoplastic Mohr-Coulomb (EP-MC), and modified Cam-Clay (CCM).

1. Elastic linear model

A simple common model is used to describe the relationship stress-strain is Hooke's law of linear (isotropic elasticity). Four parameters for this elastic model are the elastic modulus E , Poisson's ratio v, bulk modulus K, and shear modulus G. Only two material parameters are needed to fully define the materials are E and v. Using such a simple model, the linear elastic model is generally very primitive to obtain defining features of soil behaviour. In this model, the stresses are proportional to the deformations (Fig. I-2) by the generalized Hooke’s equation as follows:

$$\begin{Bmatrix} \sigma_x \\ \sigma_y \\ \sigma_z \\ \tau_{xy} \end{Bmatrix} = \frac{E}{(1+v)(1-2v)} \begin{bmatrix} 1-v & v & v & 0 \\ v & 1-v & v & 0 \\ v & v & 1-v & 0 \\ 0 & 0 & 0 & \frac{1-2v}{2} \end{bmatrix} \begin{Bmatrix} \varepsilon_x \\ \varepsilon_y \\ \varepsilon_z \\ \gamma_{xy} \end{Bmatrix} \qquad \text{(I. 1)}$$

For a two-dimensional plane strain analysis, ε_z is zero. σ_x represents the vertical stress, σ_y the horizontal stress, σ_z the stress in the direction perpendicular (to the sheet), τ_{xy} the shear stress, and γ_{xy} the shear strain.

The shear stress τ_{xy} is related to the shear strain γ_{xy}, and is given by:

$$\tau_{xy} = G \times \gamma_{xy} \tag{I. 2}$$

G denotes the shear modulus and can be determined as a function of module Young E and the Poisson's ratio ν according to the following equation:

$$G = \frac{E}{2(1+\nu)} \tag{I. 3}$$

It is important to keep in mind that Hooke's law is sometimes unsuitable for soils because they do not behave linearly or isotopically. However, it is useful to utilize this law for small displacements to determine the elastic deformations generated by stresses applied to the ground.

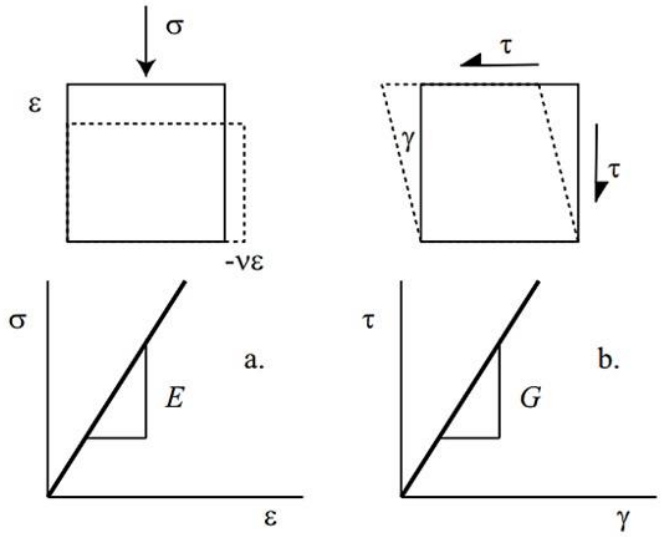


Figure I-2: Linear relationship between stress and strain for (a) compression and (b) shearing of the elastic element (taken from Wood, 2004).

It is well known that the behaviour of the soil is non-linear and anisotropic, and it is often represented as an elastoplastic material, although the actual behaviour can be even more complex.

2. Elastoplastic model

A typical stress-strain curve of the elastic- perfectly plastic model is shown in Figure I-3. Stresses are proportional to strains until attaining the yield stress point. The stress-strain curve is completely horizontal beyond the yield-point.

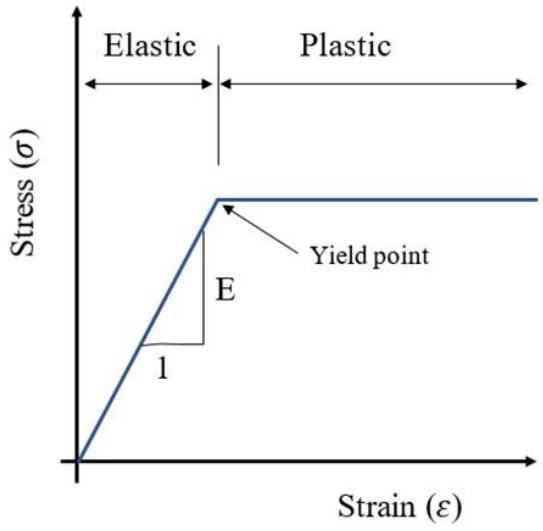


Figure I-3: Elastic-perfectly plastic constitutive relationship (adapted from Ltd, 2008).

Coulomb's plasticity criterion is expressed in terms of shear stress τ and the normal stress on a plane. The plasticity begins when the shear stress satisfies:

$$\tau = c + \sigma \tan \emptyset \tag{I. 4}$$

Also, the Mohr-Coulomb criterion can be expressed with the stress invariants I_1, I_2 and θ. The yield function, F, can then be written as follows (see Chen & Zhang, 1990):

$$F = \sqrt{J_2}\sin\left(\theta + \frac{\pi}{3}\right) - \sqrt{\frac{J_2}{3}}\cos\left(\theta + \frac{\pi}{3}\right)\sin\phi - \frac{I_1}{3}\sin\phi - c\cos\phi \tag{I. 5}$$

$$I_1 = \sigma_x + \sigma_y + \sigma_z \tag{I. 6}$$

$$J_2 = \frac{1}{6}\left[\left(\sigma_x - \sigma_y\right)^2 + \left(\sigma_y - \sigma_z\right)^2 + \left(\sigma_z - \sigma_x\right)^2\right] + \tau_{xy}^2 \tag{I. 7}$$

$$\theta = \frac{1}{3}\cos^{-1}\left(\frac{3\sqrt{3}J_3}{2J_2^{\frac{3}{2}}}\right) = the\ lode\ angle \quad \text{(I. 8)}$$

$$J_3 = \sigma_x^d \sigma_y^d \sigma_z^d - \sigma_z^d \tau_{xy}^2 \quad \text{(I. 9)}$$

WhereJ_2, J_3 the second and third deviatoric stress invariants, I_1, I_2 are the first and the second variants.

The deviatoric stress in direction i can be defined as:

$$\sigma_i^d = \sigma_i - \frac{I_1}{3} \quad \text{(I. 10)}$$

Where i = x, y or z.

When the elasticity threshold is crossed, the plastic strain can be calculated by the following equation (Hill, 1950):

$$d\varepsilon_{ij}^p = \lambda \frac{\partial g}{\partial \sigma_{ij}} \quad \text{(I. 11)}$$

Where λ is a plastic scaling factor, and g represents the plastic potential function that is given by:

$$g = g(\sigma_{ij}) = 0 \quad \text{(I. 12)}$$

3. Cam-clay model

The Cam-clay indicates the critical state and is a model of hardening elastic-plastic (Geoslope, 2008). Figure I-4a shows plots of the change in volume during applying pressure for a soil with a normal consolidation line and an over-consolidation line (swelling line). The stress state will shift along the over-consolidation lines towards the normal consolidation line if stress is increased. If any additional stress increase crosses the intersection of the two lines, the stress state will move down the normal consolidated line.

Figure I-4b shows the stress-strain curve (elastic-hardening plastic). The line of over-consolidation corresponds to the initial linear elastic portion, whereas the line of normal consolidation corresponds to the hardening plastic portion of the stress-strain relation.

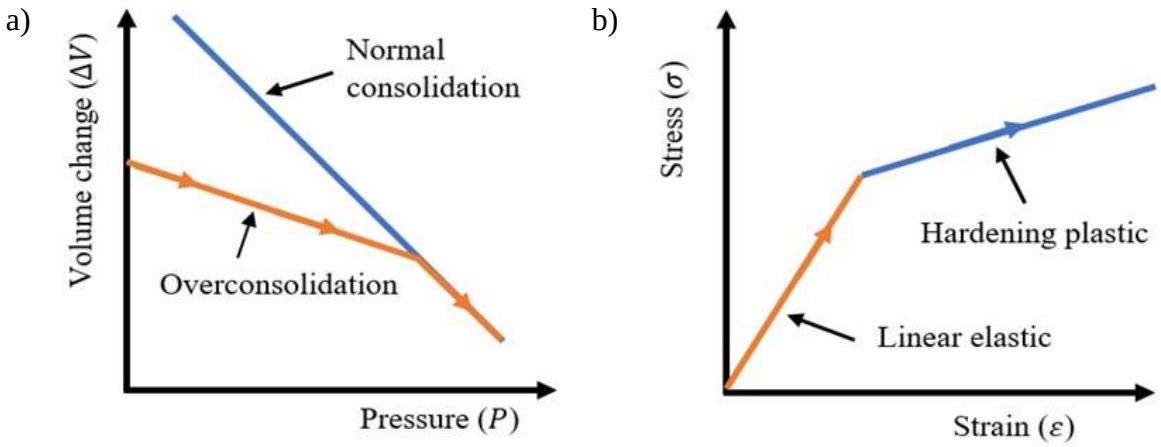


Figure I-4: Cam-Clay model with the relationships between a) volume and pressure, b) stress and strain (adapted from Ltd, 2008).

The most commonly used version of the Cam-clay model for geotechnical applications is called the modified Cam-Clay model (Wood, 2004). The Cam-clay (effective stress model) demands the following soil properties (see Fig. I-5):

- M the critical state line slope in the $p' - q$ plane
- Γ Specific volume at the critical state when p' is 1.0 (or, ln (p') is 0)
- κ Slope of the isotropic over-consolidation (swelling) line
- λ Slope of the isotropic normal consolidation line
- $v = (1 + e)$ Specific volume
- $p' = p - u$, where u is the pore water pressure
- $p = (\sigma_1 + \sigma_2 + \sigma_3)/3 = I_1/3$
- $q = \sigma_1 - \sigma_3 = \sqrt{3.j_2}$
- $j_2 = (1/3)I_1^2 - I_2$
- $I_1 = \sigma_1 + \sigma_2 + \sigma_3$, and $I_2 = \sigma_1\sigma_2 + \sigma_2\sigma_3 + \sigma_3\sigma_1$

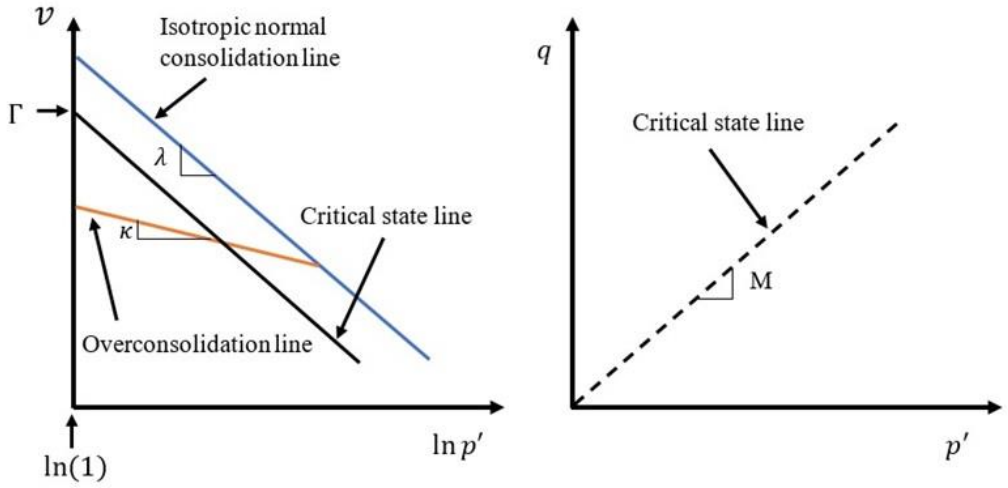


Figure I-5: Parameters of the Cam-Clay model (adapted from Ltd, 2008).

The model of Cam-clay requires the parameters Γ, λ, and κ. Such properties of the material can be obtained from some parameters such as $\phi'$and the compression index C_c. M is the slope of the critical state line, which is associated with the soil's internal friction angle. In triaxial compression cases, M may be expressed as:

$$M = \frac{6 \sin \phi'}{3 - \sin \phi'} \tag{I. 13}$$

It is common to obtain the soil pressure characteristics from the uniaxial consolidation test. The compression index Cc is obtained from a plot of void ratio (e) versus $\log_{10} p$. The compression indices Cc are related to the slope λ and κ by the following relationship:

$$\lambda = \frac{C_c}{\ln 10} \tag{I. 14}$$

$$\kappa = \frac{C_r}{\ln 10} \tag{I. 15}$$

Where Cr is the recompression index. The parameters λ and κ can also be obtained from a plot of the void ratio (e) versus ln(p).

The yield function for Cam-clay can be described in terms of stress invariants p' and q as follows (Atkinson & Bransby, 1978):

$$F = \frac{q}{Mp'} + \ln\left(\frac{p'}{p'_x}\right) - 1 \qquad \text{(I. 16)}$$

Where p'_x is the peak mean stress, and its value of p' at the critical state line (see Fig. I-6).

p'_x is related to the pre-consolidation pressure (p'_c), and is given by the following equation:

$$\ln p'_x = \ln p'_c - 1 \qquad \text{(I. 17)}$$

The modified Cam-clay model resembles the Cam-clay model, except that the yield function is in the form of an ellipse rather than a teardrop (Ltd, 2008). The yield curves for both models (modified Cam-clay model and the Cam-clay) are shown in Figure I-6.

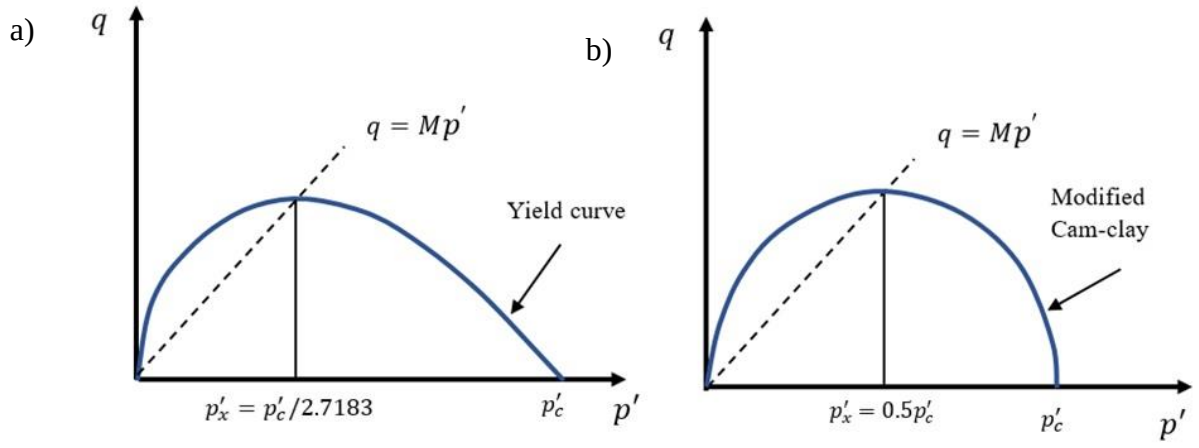


Figure I-6: Yield function of a) Cam-clay; b) modified Cam-clay (adapted form Geoslope 2018).

The yield function of the Modified Cam-clay model is given by the following equation (Britto & Gunn, 1987):

$$q^2 = M^2 p' p'_c - M^2 p'^2 \qquad \text{(I. 18)}$$

Where p'_c = pre-consolidation pressure.

The peak mean stress, p'_x, represents the isotropic pressure when the soil attains its critical state (Fig. 83). The shear stress, q, at this point (the critical state) is written by the following equation:

$$q = Mp'_x \qquad \text{(I. 19)}$$

Substituting q into the modified yield function equation gives:

$$p_c' = 2p_x' \tag{I. 20}$$

Therefore, the yield function for the modified Cam-clay can be written as follows:

$$F = \frac{q^2}{p'} + M^2 p' - 2M^2\, p_x' \tag{I. 21}$$

Finally, there are many models used to study soil behaviour, but it should be noted that there is no single constitutive soil model that can fully describe the complex behaviour of real soils under all conditions (see Wood, 2004; Yu, 2007).

APPENDIX J - DESIGN AND OPTIMIZATION OF THE PASTE BACKFILL

▪ Optimizing paste backfill mix designs

Before designing the filling mixture, it is necessary to know or determine the required resistance of the filling depending on the purpose of its use. Once the required strength has been determined, the mixing variables must be optimized to produce the mixture that reaches the target strength at the least binder use. Mixing variables include binder content B_w% (from dry tailings mass) and binder type (GU, slag, fly-ash,..), tailings particle size distribution (PSD) and mineralogy, solids concentration by mass (C_w %) or volume (C_v %), and mixing water geochemistry (sulphate concentration, pH, Eh, electrical conductivity). Variables need to be adjusted to produce an optimal mix design (UCS_{design}) (Stone, 1993; Belem et al., 2000; Kesimal et al., 2003; Yilmaz et al., 2004). Backfilling costs vary depending on the service required, which must be economical. CPB operating costs range from 10% to 20% of the overall mine operating costs; binding agents are responsible for up to 75% of backfilling costs (Grice, 1998; Fall & Benzaazoua, 2003).

Figure J-1 shows the main elements that influence the quality of the paste backfill, where each factor plays an important role in the transportation and delivery, long-term hardening, and placement of the backfill (Benzaazoua et al., 2002).

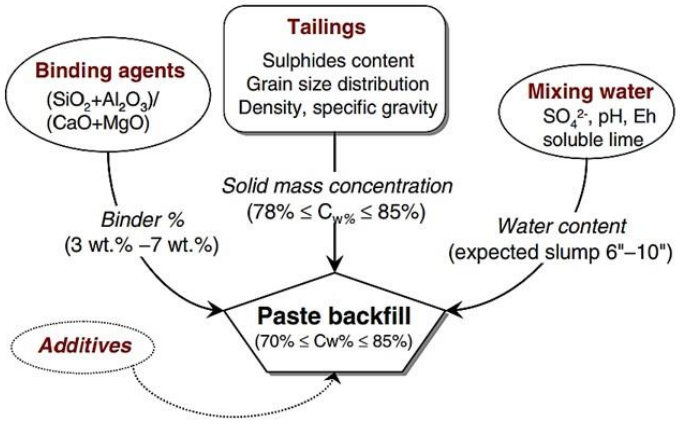


Figure J-1: Principle components affecting the quality of paste backfill (from Benzaazoua and Belem 2000).

- **Binder types and content**

Bonds are formed between fill particles at grain contact points during the hardening of CPB. Several types of binders are used, and the most common binder is the ordinary Portland cement (CEM I, OPC, Type 10, or Type I). Pozzolanic admixtures are often used to reduce the cost of the Portland cement required, such as pulverized fly ash (PFA) and ground granulated foundry blast furnace slag (GGBFS) (Douglas & Malhotra, 1989). The admixtures can be used alone or in combination with OPC to activate reactivity (Belem & Benzaazoua, 2008).

The binder content $B_w = (M_b/M_t)$ ranges from 3% to 7% (by dry mass of tailings). Figure J-2 shows that the UCS of the paste backfill is proportional to the binder content for given curing time (Benzaazoua et al., 2000).

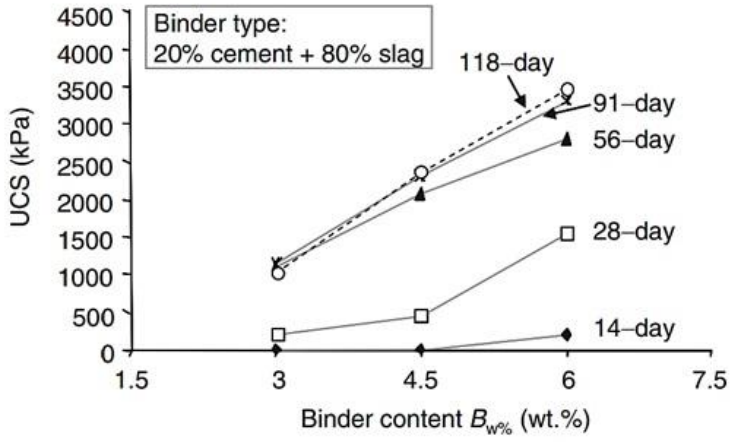


Figure J-2: Backfill UCS versus binder content at different curing times (from Benzaazoua et al., 2000).

- **Mixing water and quality**

Water is necessary to ensure proper hydration of the binding agents. Besides, since more water is generally required to pump the backfill into the underground stopes, the water content of the paste backfill still far exceeds the hydration requirements (Belem & Benzaazoua, 2008). Acidic water and sulphate salts attack the cementitious bonds in the fill, resulting in loss of strength, durability, and stability (e.g., Mitchell et al., 1982; Benzaazoua et al., 2002; Potvin et al., 2005). Benzaazoua et al. (2002) showed that the hardening of CPB (5% binder of 30% OPC+70% Slag) is slow for

three types of waters at 14-day curing. After 28 days of hardening, the UCS of the backfill reaches a maximum value for sulphate-free waters (Fig. J-3).

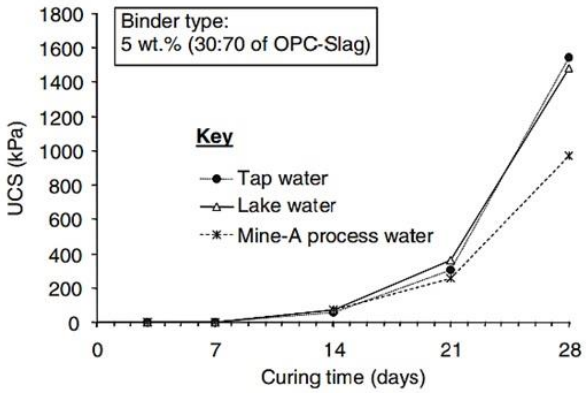


Figure J-3: Effect of mixing water on the strength of paste backfill (from Benzaazoua et al., 2002).

- **Binder Hydration Process**

A linear regression equation has been derived in order to calculate the percentage of dissolved binder D_b (by weight, wt.%) as a function of the water-to-cement ratio (see Belem et al., 2007). The equation was based on dissolution test data on general-purpose Portland cement (Type I) and blast furnace slag (see Benzaazoua et al., 2004) and is given by :

$$D_b(\%) = 3.125 \times (w/c) + 3.3125 \quad \text{(J. 1)}$$

Hardening of the paste backfill occurs in two main stages: dissolution/hydration & hydration/precipitation (Fig. J-4).

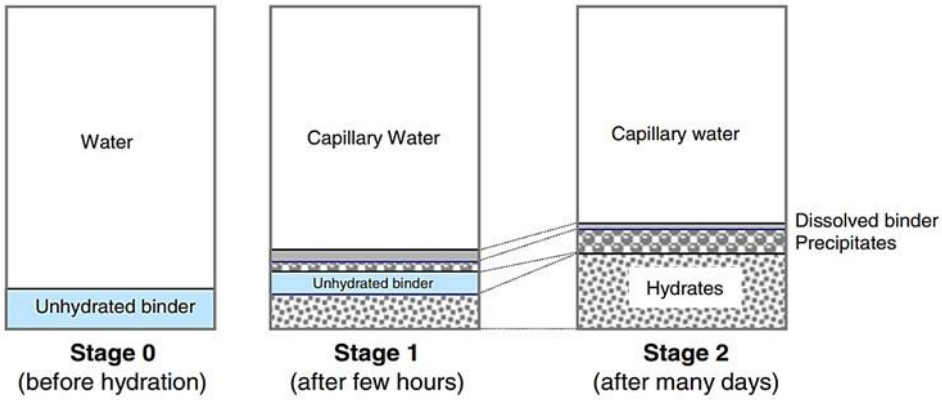


Figure J-4: Hardening process of paste backfill (from Belem & Benzaazoua, 2008).

Figure J-5 shows a diagram of the hydration process of a paste backfill with tailings containing sulphide minerals (e.g., pyrite, pyrrhotite). The OH^- anions are released after mixing the paste with the binder, which buffers the solution at a pH between 12 and 13. Consequently, the dissolution/hydration and hydration/precipitation phases take place successively. The process of hardening first involves the formation of primary ettringite, and then the formation of portlandite. C-S-H phases are formed during medium- and long-term hydration, which significantly contributes to the development of the backfill strength (Belem & Benzaazoua, 2008). Depending on the initial sulphate content, the portlandite formed may eventually react to gypsum. The presence of sulphates in the mixture plays various other roles, depending on the concentration (Benzaazoua et al., 2004). Oxidation of sulphide minerals (e.g., pyrite, pyrrhotite, and arsenopyrite) has been shown to lead to increased acidity (decrease in pH), remobilization of minerals, releasing of sulphate ions, and dissolution of the atoms formed. If the pH < 12 (portlandite stability limit), the possible consequences are the partial or complete dissolution of portlandite [Ca(OH)2], the release of calcium from the formed hydrates (decalcification of the CSH phases), and micro- and mesoporosity increase.

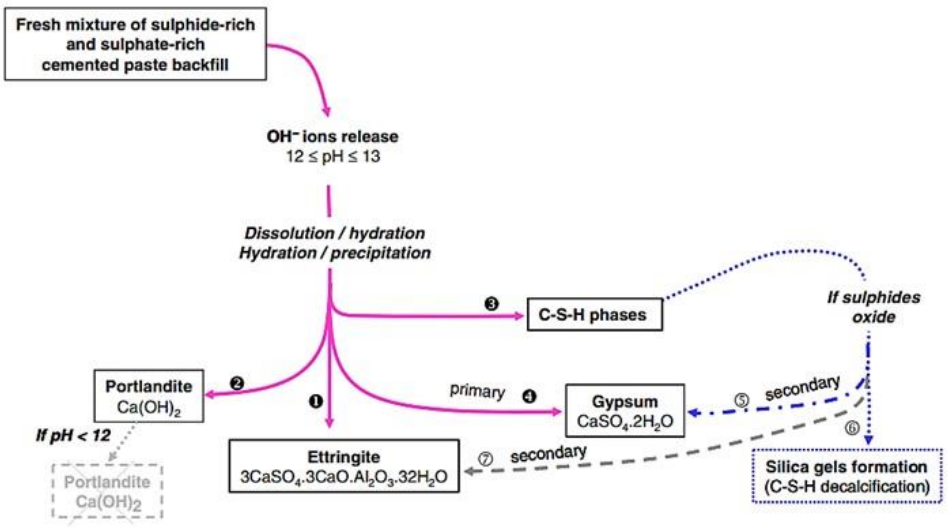


Figure J-5: Paste backfill hydration process (from Belem & Benzaazoua, 2008).

- **CPB Preparation at a Backfill Plant**

Belem & Benzaazoua (2008) reported that wide types of backfill ($C_{w\%}$varies from 63 to 85%) can be produced depending on the initial solid particle density of the tailings ($2.8 \leq \rho_{s\,\text{tailing}} \leq 4.7$), binder content ($B_{w\%}$), and water-to-cement ratio (W/C). They showed that considering the range

of variation in $C_{w\%}$ and $B_{w\%}$ (from 3 wt.% to 7 wt.%) in the mining industry, W/C varies from 2.7 to 20.2 (compared to the approximately 0.5 W/C used in the concrete industry). Figure J-6 shows the influence of the W/C ratio for different binder contents commonly used in the mining industry as well as the typical variation of volumetric solids concentration ($C_{v\%}$) with solids concentration by mass ($C_{w\%}$).

a) b)

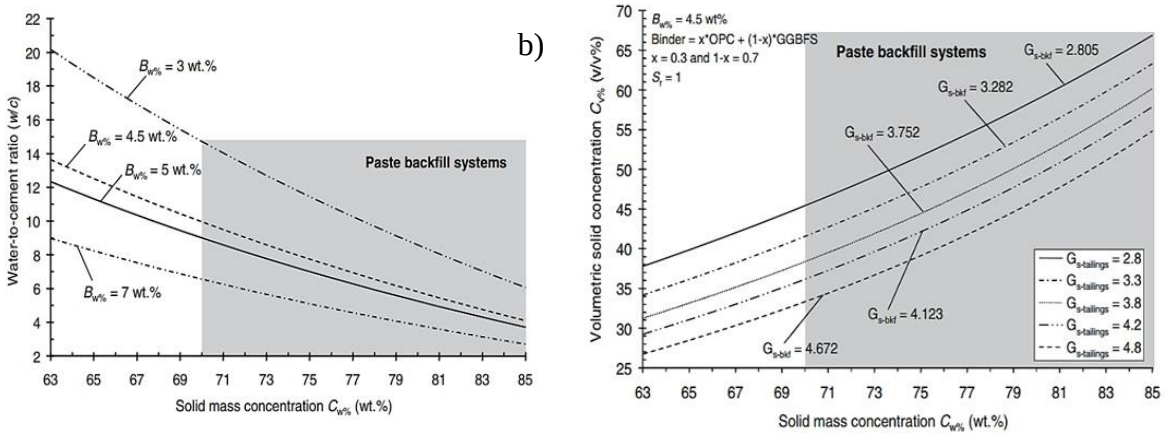


Figure J-6: a) Typical variation of w/c with (C_w%) of paste backfill; b) Typical variation in (C_v%) with (C_w%) (from Belem & Benzaazoua, 2008).

Figure J-7 shows a typical flow chart for a backfill plant. The final mill tailings are fed into a high-capacity thickener to increase the concentration of solids from about 35% to about 55-60% (Belem & Benzaazoua, 2008). The thickened tailings are then pumped from the thickener to a large storage tank (after cyanide destruction). The thickened residues are conveyed by gravity to disc filters to produce a filter cake with a solid concentration of about 70 to 82%. The filter cake is then unloaded on a belt conveyor and transported to a screw feeder for weighing. Finally, the batches of filter cakes are mixed in a spiral (or screw) mixer with binder and water added for about 45 seconds to produce a paste with a specific consistency or a slump height value.

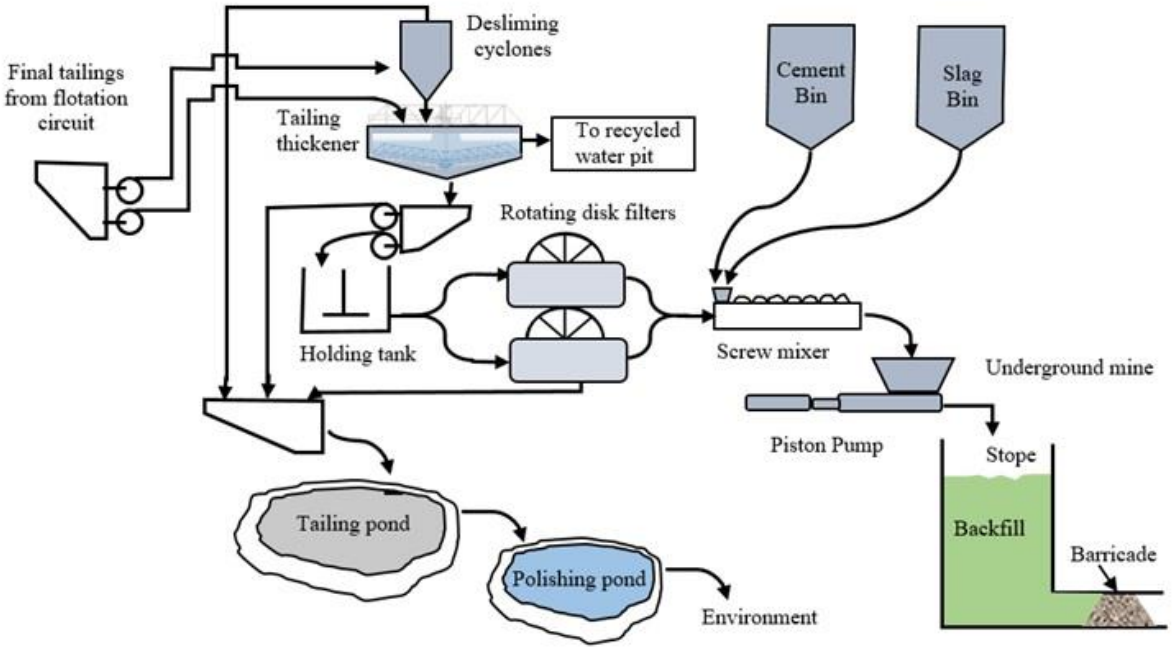


Figure J-7: Paste backfill plant flow sheet (adapted from Clayton et al., 2003).

During the excavation of the site, a slight variation in the grain density of the tailings may occur due to metrological changes in the ore body. Using data taken from Benzaazoua and Bussiere (1999) and Benzaazoua et al. (2000), Belem & Benzaazoua (2008) estimated this variation after knowing total sulphur content ($\%S$) using a regression equation given by:

$$\rho_{s\ \text{tailings}} = \frac{19.5674}{1 + 6.0094 \exp\left(-0.0072 * \%S\right)} \qquad \text{(J. 2)}$$

Where $\rho_{s\ \text{tailings}}$ in (g/cm^3) and $\%S$ = sulphur content (wt.%)

They indicated that to take into account the variation in tailings solid grains specific density in the mix design, adjusted binder content $B_{w\% - adj}$ (i.e., actual binder proportion used, not constant binder content, $B_{w\% - init}$) must be calculated using the following formula:

$$B_{w\%-\text{adj}} = \frac{B_{w\%-\text{init}} \times \rho_{s\ \text{tailings}-\text{init}}}{\rho_{s\ \text{tailings}}} \qquad \text{(J. 3)}$$

Where $B_{w\%-\text{init}}$ = initial constant binder content by dry mass (wt.%); $\rho_{s\ \text{tailings}}$= current tailings solid particles density; $\rho_{s\ tailings-\text{init}}$ =initial tailings solid particles density.

Figure J-8 shows that a decrease in the initial solid grain density of the tailings ($\rho_{s\ \text{tailings}-\text{init}}$) results in a lack of binder content (loss of profit) relative to the adjusted binder content ($B_{w\%-\text{adj}}$), which leads to an under-portioning of the binder in the final paste backfill mix.

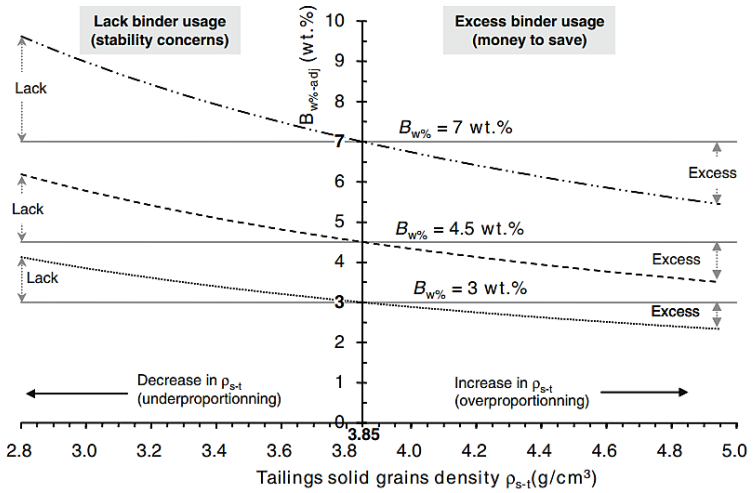


Figure J-8: Variation in adjusted binder content with tailings grains density for different binder contents (from Belem & Benzaazoua, 2008).

- **Rheological Models for Paste Backfill**

The flow of pasty backfill in pipelines is controlled entirely by its rheological properties (Belem & Benzaazoua, 2008). Paste fill behaves like a non-Newtonian fluid, which means that it requires an applied force to begin flowing (Fig. J-9a). Because backfill paste has a higher viscosity, it has a plug flow when transported in a pipe. The outer parts of the slurry shear against the sidewall of the pipe while the central core moves like a plug (Grice, 1998), as shown in Figure J-9b.

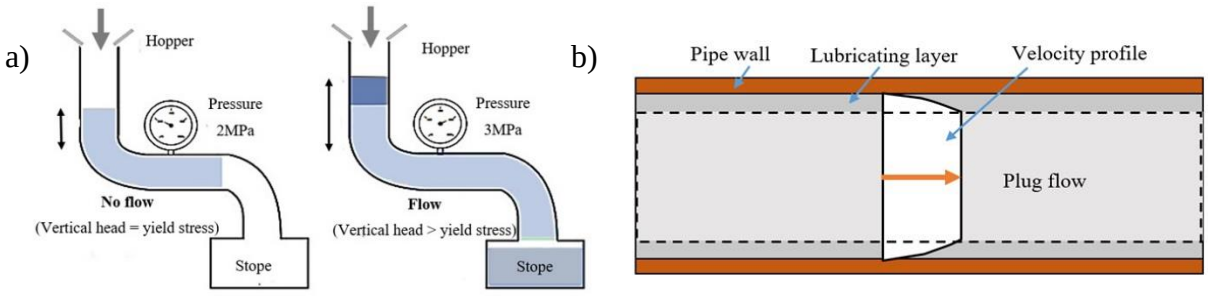


Figure J-9: a) Yield stress in paste backfill flowing through a pipeline (adapted from Revell, 2000); b) Plug flow velocity profile (adapted from Potvin et al., 2005).

Most of the materials classified as true solids or fluids can be studied by mechanics of materials or fluid mechanics. However, there are other materials, such as paste fill, without a clear classification, for which rheology is a key element in their description and understanding.

Viscosity is a measure of the resistance to flow, related to the internal friction of a material. The basic unit of viscosity measurement is "poise". The materials that have a proportional relationship between shear stress and shear rate (constant viscosity) are termed Newtonian materials. However, the materials that reveal an inconstant τ/γ relationship are named as non-Newtonian materials. There are different types of flow behaviours, which are determined by how the fluid viscosity varies in response to changes in the shear rate. Figure J-10 shows some substances that require a certain amount of shear to start the flow. This critical shear stress is denominated by yield stress. For stresses applied below the yield point, the fluid deforms elastically, with complete recovery of the strain when the stress is removed. The material shows viscous liquid behaviour once the yield stress is exceeded (Boger et al., 2006)

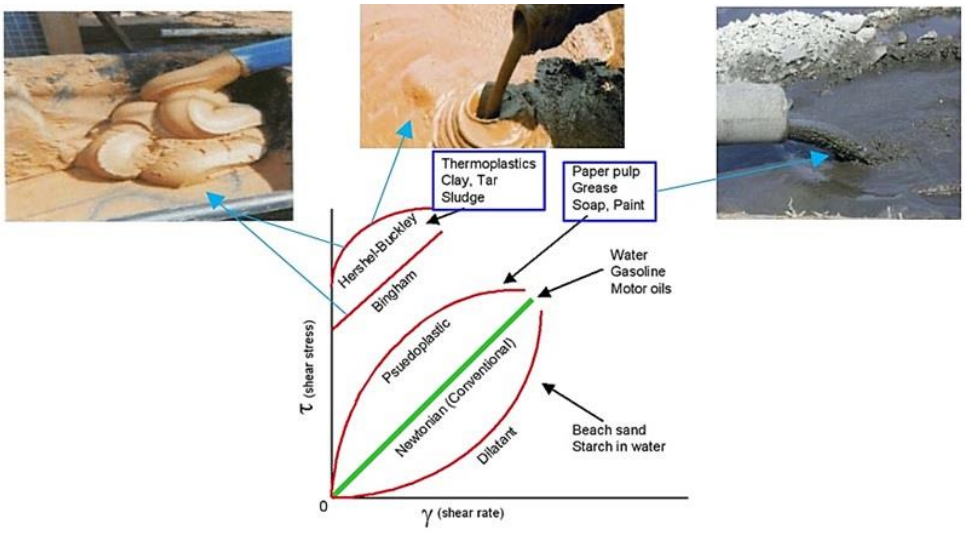


Figure J-10: Shear stress vs shear rate of non-Newtonian fluid flow (from Belem et al., 2018).

The non-Newtonian fundamental models, most frequently used to describe the behaviour of simple flows, are the Power-Law model, Bingham's model, and Herschel-Bulkley's model.

a) Power-law or Ostvald-de Waele Model

One of the most general non-Newtonian constitutive laws is the Power-law model (or Ostvald-de Waele), or two-parameter model, expressed as:

$$\tau_w = \eta_{app}\left(\frac{dV}{dr}\right)^a = \eta_{app}(\dot{\gamma})^a \qquad \text{(J. 4)}$$

Where τ_w = wall shear stress (Pa); η_{app} = non-Newtonian apparent viscosity defining fluid consistency (Pa.s); $(dV/dr) = \dot{\gamma}$ = shear rate (s^{-1}) or velocity ratio V(m/s); and a = power-law model constant indicating the degree of non-Newtonian behaviour. This model does not account for the yield stress. When $a = 1$, a Newtonian fluid is obtained. If $a < 1$, a shear-thinning (or pseudoplastic) fluid is obtained, characterized by a progressively decreasing apparent viscosity with increasing shear rate. When $a > 1$, a shear-thickening (or dilatant) fluid is obtained (the apparent viscosity gradually increases as the shear rate increases).

b) Bingham Plastic Model

The ideal Bingham model is one of the simplest models covering viscoplastic fluids that exhibit such a yield response. This model is described as follows:

$$\tau_w = \tau_y + \eta_B \frac{dV}{dr} = \tau_y + \eta_B \dot{\gamma} \qquad \text{(J. 5)}$$

Where τ_y = shear yield stress (Pa); η_B = Bingham plastic viscosity (Pa s); and $\dot{\gamma}$ =shear rate (s^{-1})

Bingham model illustrates the fluid viscosity characteristics when viscosity is independent of shear rate (Fig. J-11). Therefore, this model (Bingham plastic) cannot account for the shear-thinning characteristics of general non-Newtonian fluids. Many concentrated particle suspensions and colloidal systems, such as mortar, concrete, and possibly paste fill, exhibit Bingham's behaviour at low shear rates (Potvin et al., 2005; Cooke, 2006; Belem & Benzaazoua, 2008).

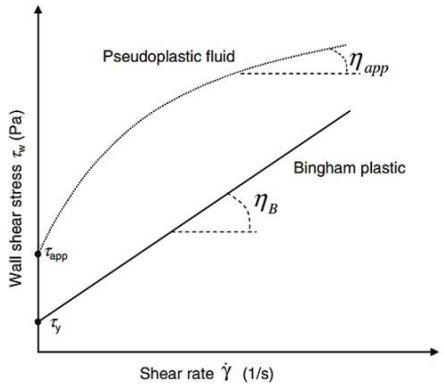


Figure J-11: Time-independent fluids (from Belem & Benzaazoua, 2008).

c) Herschel–Bulkley Model

The Herschel–Bulkley model is a three-parameter model that describes viscoplastic materials exhibiting yield response with a shear-thinning relationship above yield stress and is expressed by the following relationship:

$$\tau_w = \tau_{app} + \eta_{app}\left(\frac{dV}{dr}\right)^n = \tau_{app} + \eta_{app}(\dot{\gamma})^n \quad \text{(J. 6)}$$

Where τ_{app} = constant interpreted as apparent shear yield stress (Pa); η_{app} =consistency index or apparent viscosity (Pa s); $\dot{\gamma}$ = shear rate (s^{-1}); and n = flow parameter indicating the degree of non-Newtonian behaviour. When $n = 1$, the Herschel-Bulkley model is reduced to the Bingham model. If $n < 1$, a pseudoplastic (or shear-thinning) fluid is obtained. If $n < 1$, a dilatant (or shear-thickening) fluid is obtained. These parameters are obtained from rheometer tests (capillary, extrusion, or rotational rheometer) using different tool geometries (Belem & Benzaazoua, 2008).

▪ Paste backfill placement in a mine stope

Once all transport parameters have been accurately determined, the paste fill is transported to the underground openings via pipelines. According to Thomas et al. (1979), three possible techniques that can be used to transport the backfill from the surface to underground stopes are gravity/pumping, gravity, and pumping/gravity systems (Fig. J-12a).

Figure J-12b presents a typical backfilled stope with the various components (fill, rock mass, and barricade). The mine stope is usually filled in three steps. The first step is to place the first layer (called plug) in the stope, which reaches a few meters above the level of the drift, with a backfill containing a high percentage of binder ($B_w = M_b/M_s$ =5 to 7%). A cure period of 3 to 7 days is usually required for mechanical strength after the filling of the plug. The second step is to fill another layer with a lower binder content (B_w from 2 to 5%) compared to the first layer (the plug). The height of the second layer depends on the mechanical strength of the plug, the production sequence, and the geometry of the stope. Height between 20 to 30 m is often encountered in underground mines with a rising rate ranging from 2 to 10 m/day (Cowling et al., 1988; Belem et al., 2004b; El Mkadmi, 2012). In paste fill practice, a rising rate of 0.2 to 0.4 m/h has been reported depending on the flowrate of the backfill (into stope) and section area of the stope (Thompson et al., 2012). The maximum placement rate is often determined by the supply of tailings from the mill

(Potvin et al., 2005). A curing period of 2 to 4 days is also necessary to allow the backfill to consolidate and develop strength (Belem et al., 2004b, Bawden et al., 2011). The third step is to complete the backfilling of the stope up to the top, then place waste rocks so that the machines can move over the backfill. Drainage and settlement are conducive to CPB hardening (see Belem et al. 2001, 2002, 2018). Also, the fill mass achieves stability due to the development of arching effects depending on stope dimensions. The demands on the fill mass are often closely related to the time between completion of ore extraction in the stope to be filled and commencement of adjacent stopping. Preparation of stope is necessary before backfilling, such as the construction of retaining barricades in the drawpoints. Other activities may be required after the completion of the stoping, such as the installation of instrumentation or pre-reinforcement.

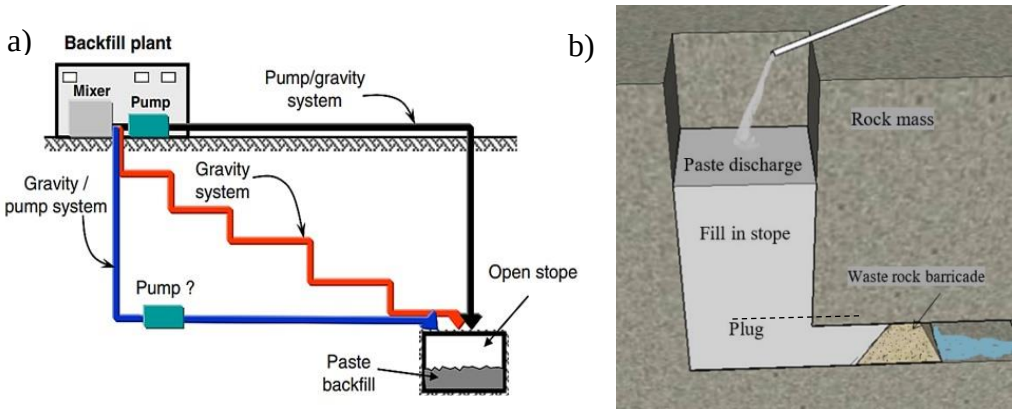


Figure J-12: a) Paste backfill distribution systems (from Belem & Benzaazoua, 2004); b) Schematic diagram of a backfilled stope.

It is generally preferable to fill the gaps (voids) as quickly as possible to maintain the stability of the excavation or to allow quick access to secondary stopes. For paste fillings generated directly from mill tailings, the maximum instant supply rate will be governed by the mill's tailings supply and binder. When faster filling rates are required, additions of other materials such as crushed rock, sand, and other waste can be used to increase the volume placed per hour. However, the addition of these materials results in less tonnage of mill waste overall underground (Potvin et al., 2005). Besides, there is a significant influence of the filling rate on the stress state in the stope and on the pressures acting on the barricades. The rapid rise in rates generates higher PWPs and produces greater stresses on the barricade, while the slow rise in the rate, allowing the dissipation of excess PWP, leads to increased effective stress and the development of the arching effect (Potvin et al., 2005; Belem et al., 2018; Li, 2019).

▪ Design of paste backfill for underground mine applications

While backfilling is somewhat expensive, it is indispensable for most underground mines, as it provides important ground support to protect mines and mining operations (Belem & Benzaazoua, 2008). The paste backfill supports the pillars and walls to avoid caving or roof falls and enhances pillar recovery, which in turn improves productivity. After the placement of the backfill, many effects can be seen, such as self-weight consolidation settlement (Appendix E for more details), shrinkage, wall convergence, and the arching effect. Arching decreases vertical stress and rises horizontal stress distribution within the fill mass. Many UCS design models are developed to predict and determine the horizontal stresses on the stope walls.

a) Design of horizontal pressure on filled stope sidewalls

The traditional design is a free-standing wall requiring a uniaxial compressive strength (UCS) equal to the overburden stress (γh) at the base of the stope. In many mines, depending on stope dimensions, the vertical stress at the stope bottom is less than the weight of the overlying fill (Belem & Benzaazoua, 2008). This phenomenon, named the arching effect, occurs due to frictional and cohesive interaction between backfill and wall rock (Marston, 1930; Terzaghi, 1943). In the case of deformation of pillars or stope walls, the backfill supports them (passive resistance). Passive resistance is described as the state of maximum resistance mobilized when a force pushes against a backfill, and the backfill resists the force (Hunt, 1986). Various analytical solutions are proposed to predict the pressure transferred horizontally such as Martson's model, Terzaghi's model, Van Horn's model and Belem et al model.

1) Martson's Cohesionless Model

Marston (1930) proposed a solution to predict horizontal pressure (σ_h) at the base of an excavated trench (kPa), which is as follows:

$$\sigma_h = \frac{\gamma B}{2\mu'}\left[1 - exp(-\frac{2K_a\mu' H}{B})\right] \quad \text{(J. 7)}$$

where σ_v is the vertical pressure at the bottom of the excavation; $K_a =$ active earth pressure coefficient $(\sigma_h/\sigma_v) = \tan^2(45° - \frac{\phi}{2})$; $\gamma =$fill bulk unit weight (kN/m^3);

B = stope width (m); H =fill mass height (m); $\mu' = tan\delta$= sliding friction coefficient between $\phi/3$ and $2\phi/3$, and ranging from 0° to 22°, and ϕ =fill internal friction angle (°).

2) Modified Martson's Cohesionless Model

Aubertin et al. (2003) suggested a modified version of Martson's two-dimensional arch solution, defined using active earth pressure (Ka) and sliding friction of the wall. The prediction of effective horizontal pressure (σ'_{hH}) along pillar sidewalls at a depth H corresponding to the stope bottom is given as follow:

$$\sigma'_{hH} = \frac{\gamma B}{2\tan \emptyset'_{\mathrm{f}}}\left[1 - \exp\left(-\frac{2KH\ \tan \emptyset'_{\mathrm{f}}}{B}\right)\right] \quad \text{(J. 8)}$$

The effective vertical pressure σ'_{vH} at the bottom of the stope is given as follow:

$$\sigma'_{\mathrm{vH}} = \sigma'_{\mathrm{hH}}/\mathrm{K} \quad \text{(J. 8b)}$$

Where, γ =fill bulk unit weight (kN/m^3); B= stope width (m); H= backfill height (m); $\emptyset'_{\mathrm{f}}$ =fill internal friction angle (º); and K= earth pressure coefficient.

The three states for K are: earth pressure coefficient at rest ($K_0 = 1 - \sin \emptyset'_{\mathrm{f}}$), active earth pressure coefficient ($K_a = tan^2(45° - \emptyset'_{\mathrm{f}}/2)$), and the passive earth pressure coefficient ($K_p = tan^2(45° + \emptyset'_{\mathrm{f}}/2)$). Another relation is proposed to estimate the earth coefficient at rest by Jaky's (1944). The relation is given by $K_0 = v/(1 - v)$ and used for loose sand and perfectly elastic materials, where v = Poisson's ratio of the backfill (between 0.3 and 0.4) but is difficult to obtain for paste backfill materials (Belem & Benzaazoua, 2008). Booker and Ireland (1965) proposed a relation to approximate the earth coefficient at rest for the clay normally consolidated ($K_0 = 0.95 - \sin \emptyset'$). In the field, the dominant earth pressure is likely to be at rest or passive pressure only because the backfill has insufficient internal pressure to push out the stope walls. K_0 varies from 0.4 to 0.6; K_a varies from 0.17 to 1.0; and K_{p} must vary from 1.0 to 10 (Belem & Benzaazoua, 2008). Appendix D includes more information about the earth pressure coefficient.

3) Terzaghi's Cohesive and Cohesionless Material Models

A two-dimensional arch theory has been proposed by Terzaghi (1943) to predict the horizontal pressure (σ_h) along the pillar walls. This relation is given for a cohesive material as follow:

$$\sigma_h = \frac{(\gamma B - 2c)}{2\ \tan\phi}\left[1 - \exp\left(-\frac{2KH\ \tan\phi}{B}\right)\right] \quad \text{(J. 9)}$$

The vertical pressure at the stope bottom is given as follow:

$$\sigma_v = \sigma_h / K \quad \text{(J. 9b)}$$

$$K = \frac{1 + \sin^2\phi}{\cos^2\phi + 4\tan^2\phi} = \frac{1}{1 + 2\tan^2\phi} \quad \text{(J. 9c)}$$

Where K =earth pressure coefficient; γ =fill bulk unit weight (kN/m^3); c= fill cohesive strength (for a cohesion less material c=0, kPa); B= stope width (m); H= depth below fill toe (m); tan ϕ= fill internal friction coefficient; and ϕ = fill internal fiction angle (°).

4) Three-dimensional predictive models

- **Van Horn Model**

A 3D model (by Van Horn & Tener, 1963) is proposed for vertical stress at a depth *h* below the backfill surface. The vertical stress is given as follows:

$$\sigma_v = \frac{\gamma}{2k_r \tan\delta}\left(\frac{BL}{B+L}\right)\left[1 - \exp\left(-2k_r \tan\delta \frac{2h(B+L)}{BL}\right)\right] \quad \text{(J. 10)}$$

γ = fill bulk unit weight (kN/m^3); h =fill hight in the stope (m); L= stope length (m);B= stope width; δ = interface friction angle between backfill and stope wall (°); and $k_r = \sigma_h/\sigma_v$.

- **Belem et al**

Another model is proposed (by Belem et al., 2004a) to predict the horizontal pressure in the stope of mine. This model takes into account the arching effect implicitly and is given as follows:

$$\sigma_h = \omega\gamma H\left(\frac{H}{B+L}\right)\left[1 - exp\left(-\frac{2H}{B}\right)\right] \quad \text{(J. 11)}$$

The vertical pressure at the stope bottom $\sigma_v (= \sigma_z)$ is given as follows:

$$\sigma_v = \sigma_z = 0.185\gamma H\left(\frac{H}{B+L}\right)\left[1 - exp\left(-\frac{2H}{B}\right)\right] \quad \text{(J. 12)}$$

Where γ =fill bulk unit weight (kN/m^3); H =fill height in the stope (m); B =stope width; L= strike length of stope (m); and ω =directional constant (1 for pressure across ore body ($\sigma_x = \sigma_h$) and 0.185 for pressure along ore body($\sigma_y = \sigma_h$)).

b) Paste backfill required strength design

UCS is commonly lower than 1 MPa for free-standing fill application (Stone, 1993). However, at least 5MPa of uniaxial (unconfined) compression strength (UCS) is needed for the backfill to provide sufficient ground support (Belem & Benzaazoua, 2008). Several studies indicated that the UCS of the backfill mass differs from 0.2 MPa to 4 MPa while surrounding rock mass UCS varies from 5 MPa to 240 MPa (Grice, 1998; Revell, 2000).

1) Vertical Backfill Support

Previous research and in-situ experiments have indicated that the backfill only works as a secondary support system and is unable to support the total weight of the overburden (Cai, 1983). The elasticity modulus of the backfill changes from 0.1 GPa to 1.2 GPa, whereas the surrounding rock mass elasticity varies from 20 GPa to 100 GPa. As deliberated by Donavan (1999), vertical loading is assumed because of roof deformation (Fig. J-13), and the design UCS can be predicted by the following relation:

$$UCS_{\text{design}} = \left(E_p\varepsilon_p\right)FS = E_p\left(\frac{\Delta H_p}{H_p}\right)FS \quad \text{(J. 13)}$$

Where E_p = elastic modulus of rock mass or pillar; ε_p = axial pillar strain; ΔH_p = strata deformation; H_p = strata initial height (m); and FS= Factor of Safety.

The overall load is unlikely to exceed the total weight of the overlying deformed strata if the stope walls deform before the stope is filled (Donovan, 1999), and design UCS can be estimated as follow:

$$UCS_{\text{design}} = k(\gamma_p H_p)FS \quad \text{(J. 14)}$$

Where k=scaling constant (between 0.25 and 0.5); γ_p =strata unit weight (kN/m^3); H_p =strata height below the surface (m); and FS= safety factor.

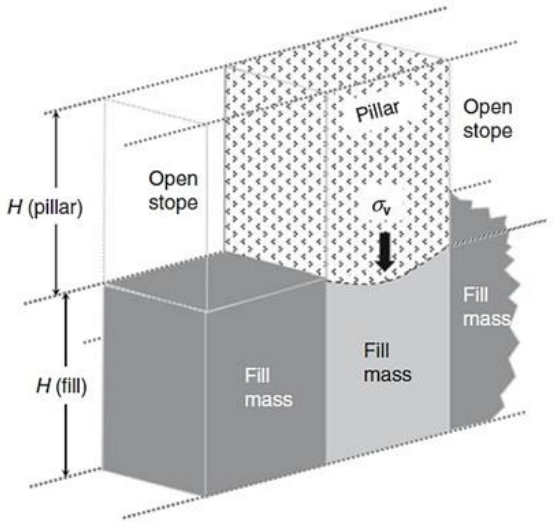


Figure J-13: Vertical loading on the backfill (from Belem & Benzaazoua, 2008).

2) Development opening through backfill mass

Safe design criteria must be applied if new ores are to be accessed by opening a gallery through the backfill (Fig. J-14). A conservative design considers the fill mass as more than two contiguously exposed faces after blasting adjacent pillars or stopes. The walls confining the fill are therefore extracted, and the fill is subjected to gravity loading equivalent to the uniaxial compression test in a simple laboratory (Yu, 1992). The relationship used to estimate the UCS design may be given through:

$$USC_{\text{design}} = (\gamma_{\text{f}} H_{\text{f}}) FS \qquad \text{(J. 15)}$$

Where γ_{f} = fill bulk unit weight (kN/m^3); H_{f} =Fill height (m); and FS = factor of safety.

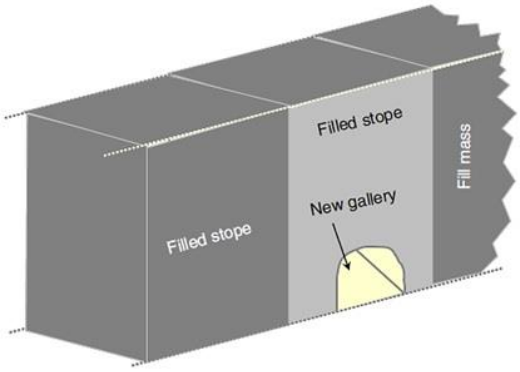


Figure J-14: Opening a gallery in the mass of paste backfill (from Belem & Benzaazoua, 2008).

3) Pillar recovery

It is quite usual to recycle pillars after primary ore recovery to obtain maximum ore recovery. As a result, large vertical surfaces may be exposed to the backfill. The fill must, therefore, be secure when free-standing wall faces are exposed at sufficient strength to withstand the blasting effects during pillar recovery (Fig. J-15).

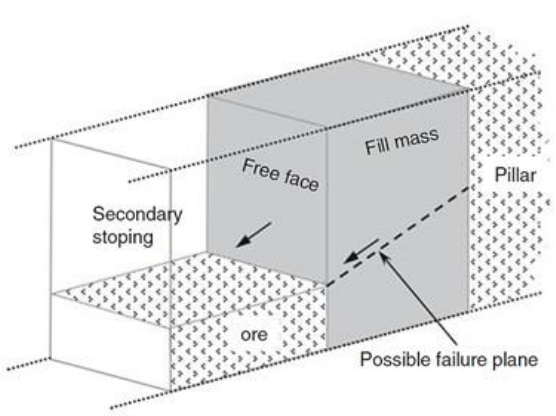


Figure J-15: Secondary stope extraction (from Belem & Benzaazoua, 2008).

In recent years, 2D and 3D empirical models have been developed to account for arching effects, cohesion, and friction along sidewalls (Mitchell et al., 1982; Mitchell, 1989a, b; Arioglu & Biron, 1983; Chen & Jiao, 1991; Yu, 1992). Such methods of design employ the concept of a confined fill block surrounded by wall rock.

- **More than two exposed faces**

The same equation used to open a gallery through the backfill should be used when more than two adjacent pillars are exposed (Fig. J-16, Belem et al., 2008).

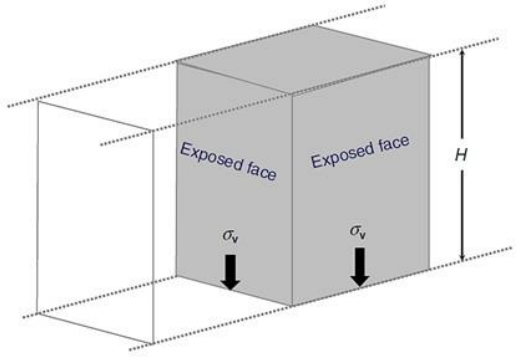


Figure J-16: Backfill mass with three exposed vertical faces (from Belem & Benzaazoua, 2008).

- **Case of narrowly exposed fill face**

Askew et al. (1978) proposed a relation to determine the compressive design strength of a narrowly exposed fill face (Fig. J-17). It is based on modelling 2D finite elements as follows:

$$UCS_{design} = \frac{1.25B}{2K\tan\emptyset}\left(\gamma - \frac{2c}{B}\right) \times \left[1 - exp\left(-\frac{2HK\tan\emptyset}{B}\right)\right] FS \qquad \text{(J. 16)}$$

Where B= stope width; K= fill pressure coefficient; c = fill cohesive strength (kPa); $\emptyset$ =fill internal fiction angle (°); γ =fill bulk unit.

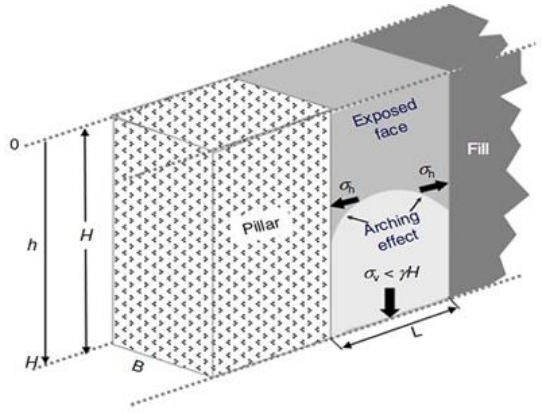


Figure J-17: Schematic illustration of a narrowly exposed fill face (Belem & Benzaazoua, 2008).

- **Case of exposed frictional fill face**

Mitchell et al. (1982) proposed a relationship for a backfill exposed in two opposite sides (Fig. J-18) as follows:

$$UCS_{\text{design}} = \frac{(\gamma L - 2c)}{L}\left[H - \frac{B}{2}\tan\left(45° + \frac{\emptyset}{2}\right)\right] \times \sin\left(45° + \frac{\emptyset}{2}\right) FS \qquad \text{(J. 17)}$$

Where γ =fill bulk unit weight (kN/m^3); c=fill cohesive strength (kPa); L= stope strike length (m); B= stope width (m); H=total fill height (m); $\emptyset$ =fill internal friction angle (°); FS= factor of safety.

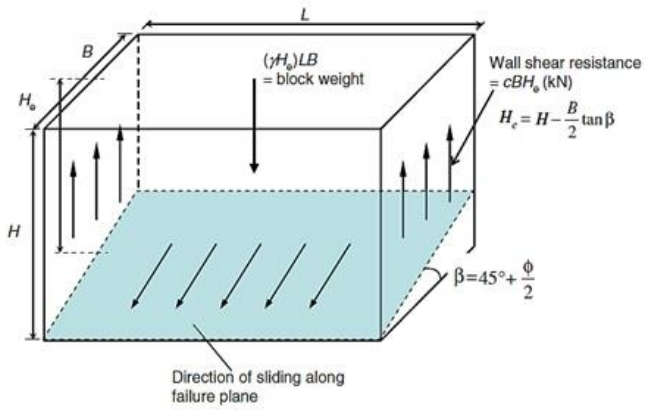


Figure J-18: Confined block with the mechanism of shearing resistance (from Belem & Benzaazoua, 2008).

- **Case of exposed frictionless fill face**

Mitchell et al. (1982) proposed the relationship for a frictionless material, considering that the compressive strength of the fill is only produced by the binding agents and that any strength added by the friction is negligible (Fig. J-19) as follows:

$$UCS_{\text{design}} = \frac{\gamma L\left(H - \frac{B}{2}\right)}{\frac{L}{FS\sin 45°} + \left(H - \frac{B}{2}\right)} = \frac{\gamma L\left(H - \frac{B}{2}\right) FS\sqrt{2}}{2L + \left(H - \frac{B}{2}\right) FS\sqrt{2}} \qquad \text{(J. 18)}$$

Mitchell (1983) proposed a formula derived from the last equation (B=0) as follows:

$$UCS_{\text{design}} = \frac{(\gamma LH)FS}{L + H} = \frac{(\gamma H)FS}{(1 + \frac{H}{L})} \qquad \text{(J. 19)}$$

Where γ =fill bulk unit weight (kN/m^3); c= fill cohesive (kPa); B= stope width (m); L=stope strike length (m); H= fill height (m); and FS= safety factor.

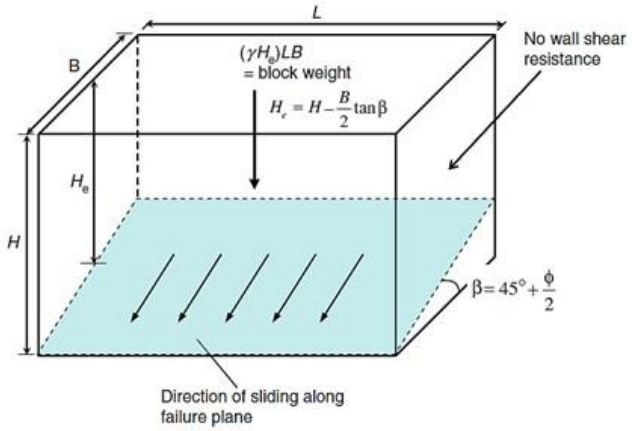


Figure J-19: Confined block without frictionless fill mechanism (form Belem & Benzaazoua, 2008).

4) Ground support

Post filling, compressive strength increases in the surrounding pillars (Fig. J-20). This growing pillar strength is due to mobilizing the fill's passive resistance. The following equation can be used to determine the increase provided by the fill (Guang-Xu & Mao-Yuan, 1983):

$$UCS_{cp} = UCS_{up} + [(\gamma_{\mathrm{f}} H_{\mathrm{f}}) K_{\mathrm{a-f}}] K_{\mathrm{p-p}} \qquad \text{(J. 20)}$$

Where, UCS_{cp} =confined pillar compressive strength (kPa); UCS_{up} = unconfined pillar strength before stope filling (kPa); γ_{f} =fill bulk unit weight (kN/m^3); H_{f} =paste fill height (m); $\emptyset_{\mathrm{f}}$ =fill internal friction angle(°); $\emptyset_{\mathrm{p}}$ =pillar internal friction angle(°); $K_{\mathrm{a-f}} = \tan^2(45° - \emptyset_{\mathrm{f}}/2)$ fill active pressure coefficient; $K_{\mathrm{p-p}} = \tan^2(45° + \emptyset_{\mathrm{p}}/2)$ = pillar passive pressure coefficient.

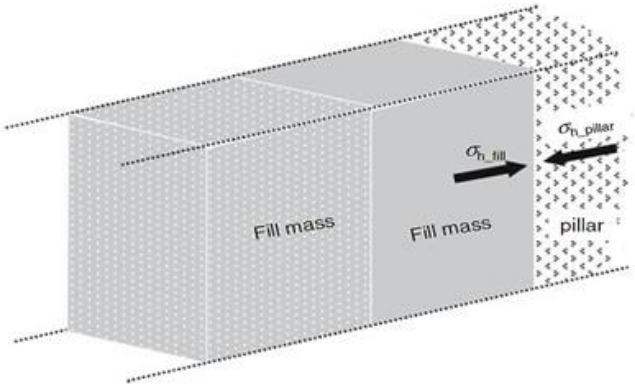


Figure J-20: Strengthening the confined pillar by filling (from Belem & Benzaazoua, 2008).

5) Working platform

In most filling operations, fill typically requires high strength development in the short term to be used as a worker and equipment platform (Fig. J-21). For this type of backfill, a standard bearing capacity relationship developed for shallow foundation design using civil engineering methods would be sufficient (Belem & Benzaazoua, 2008). The bearing capacity of the fill at the top surface Q_{f} (kPa) is determined using Terzaghi's expression, modified by Craig (1995), as follows:

$$Q_{\mathrm{f}} = 0.4BN_{\gamma} + 1.2cN_{c} \tag{J. 21}$$

Bearing factors N_{γ} (developed by Hansen, 1970) and N_{c} are given by the following relation:

$$N_{\gamma} = 1.8(N_{q} - 1)\tan\emptyset \tag{J. 22}$$

$$N_{c} = \frac{(N_{q} - 1)}{\tan\emptyset} \tag{J. 23}$$

$$N_{q} = \tan^{2}(45° + \emptyset/2)\exp(\pi\tan\emptyset) \tag{J. 24}$$

Where N_{γ} = unit weight-bearing capacity factor; N_{c} = cohesion bearing capacity factor; N_{q} surcharge bearing capacity factor; γ =fill bulk unit weight (kN/m^3); c=fill cohesive strength (kPa); B=width of square footing at surface contact position (m); and $\emptyset$ =fill internal friction angle (°).

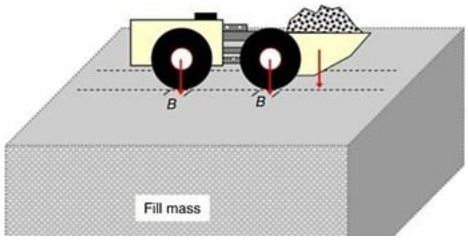


Figure J-21: Fill serves as a working platform (from Hassani & Bois, 1989).

Q_{f} equation supposes that a square footprint of a mine vehicle tire supports the backfill bearing (Hassani & Bois, 1989; Hassani & Archibald, 1998). Contact width B is the width of the tire contact that is given by:

$$B = \sqrt{\frac{F_{t}}{p}} \tag{J. 25}$$

Where F_{t}= tire loading force (kN); and p = tire air pressure (kPa)